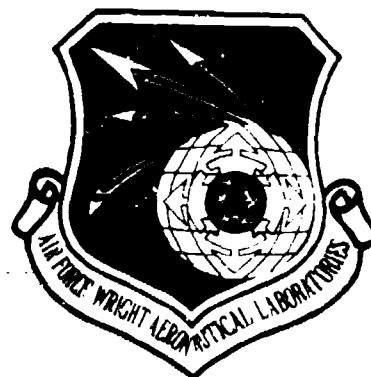


AD A 096827

AFWAL-TR-80-1171

CHARACTERIZATION OF ION-IMPLANTED SEMICONDUCTORS



J. E. Ehret
Y. K. Yeo, Ph.D.
K. K. Bajaj, Ph.D.
E. T. Rodine, Ph.D.
G. Das, Ph.D.

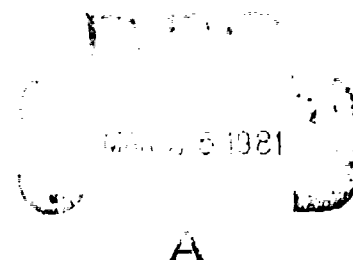
Research Applications Division
Systems Research Laboratories, Inc.
2800 Indian Ripple Road
Dayton, Ohio 45440

November 1980

TECHNICAL REPORT AFWAL-TR-80-1171
Final Report for Period 7 May 1976 - 9 May 1980

Approved for public release; distribution unlimited.

AVIONICS LABORATORY
AIR FORCE WRIGHT AERONAUTICAL LABORATORIES
AIR FORCE SYSTEMS COMMAND
WRIGHT-PATTERSON AIR FORCE BASE, OHIO 45433



81 3 24 008

DTIC FILE COPY

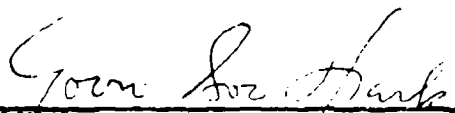
**Best
Available
Copy**


NOTICE

When Government drawings, specifications, or other data are used for any purpose other than in connection with a definitely related Government procurement operation, the United States Government thereby incurs no responsibility nor any obligation whatsoever; and the fact that the government may have formulated, furnished, or in any way supplied the said drawings, specifications, or other data, is not to be regarded by implication or otherwise as in any manner licensing the holder or any other person or corporation, or conveying any rights or permission to manufacture use, or sell any patented invention that may in any way be related thereto.


This report has been reviewed by the Office of Public Affairs (ASD/PA) and is releasable to the National Technical Information Service (NTIS). At NTIS, it will be available to the general public, including foreign nations.

This technical report has been reviewed and is approved for publication.


YOUN SOO PARK
Program Manager
Electronic Research Branch


PHILIP E. STOVER, Chief
Electronic Research Branch
Avionics Laboratory

FOR THE COMMANDER


WILLIAM J. EDWARDS, Chief
Electronic Technology Division
Avionics Laboratory

"If your address has changed, if you wish to be removed from our mailing list, or if the addressee is no longer employed by your organization please notify AFWAL/AADR, N-PAFB, ON 45433 to help us maintain a current mailing list".

Copies of this report should not be returned unless return is required by security considerations, contractual obligations, or notice on a specific document.

(14) SRW-6913

SECURITY CLASSIFICATION OF THIS PAGE (When Data Entered)

19 REPORT DOCUMENTATION PAGE		READ INSTRUCTIONS BEFORE COMPLETING FORM	
1. REPORT NUMBER (18) AFWAL-TR-80-1171	2. GOVT ACCESSION NO. AD-A096827	3. RECIPIENT'S CATALOG NUMBER	
4. TITLE (and Subtitle) (6) CHARACTERIZATION OF ION-IMPLANTED SEMICONDUCTORS		5. TYPE OF REPORT & PERIOD COVERED (9) Final Technical Report 7 May 76 - 9 May 80	
7. AUTHOR(s) J. E. Ehret Y. K. Yeo, Ph.D. K. K. Bajaj, Ph.D.		6. PERFORMING ORG. REPORT NUMBER 6913 Final	
9. PERFORMING ORGANIZATION NAME AND ADDRESS Systems Research Laboratories, Inc. 2800 Indian Ripple Road Dayton, Ohio 45444		8. CONTRACT OR GRANT NUMBER(s) (15) F33615-76-C-1166	
11. CONTROLLING OFFICE NAME AND ADDRESS Avionics Laboratory (AFWAL/AADR) Air Force Wright Aeronautical Laboratories (AFSC) Wright-Patterson AFB, Ohio 45433		10. PROGRAM ELEMENT, PROJECT, TASK AREA & WORK UNIT NUMBERS 61102 (16) 3306-R2-13 (17) R2	
14. MONITORING AGENCY NAME & ADDRESS (if different from Controlling Office) (10) James E. Ehret Y.K. Yeo K.K. Bajaj Edward T. Rodine Gopal Das		12. REPORT DATE (11) Nov 1980	
		13. NUMBER OF PAGES (12) 242	
		15. SECURITY CLASS. (of this report) Unclassified	
		15a. DECLASSIFICATION/DOWNGRADING SCHEDULE	
16. DISTRIBUTION STATEMENT (of this Report) Approved for public release; distribution unlimited			
17. DISTRIBUTION STATEMENT (of the abstract entered in Block 20, if different from Report)			
18. SUPPLEMENTARY NOTES			
19. KEY WORDS (Continue on reverse side if necessary and identify by block number) Ion implantation, GaAs, Hall effect, electrical resistivity, Mg-implanted GaAs, Ge-implanted GaAs, dual implantation, silicon-nitride deposition, deep-level-transient spectroscopy (DLTS), native defects, implantation defects, FET-like structures, device-grade GaAs, magneto-optics, InP, excitons, multiexciton complexes, acceptors, localized vibrational modes, donors.			
20. ABSTRACT (Continue on reverse side if necessary and identify by block number) This report discusses studies conducted on III-V semiconductors. Analysis and characterization of the specimens were carried out by means of photoluminescence, electrical measurements, capacitance-voltage profiling, far-infrared absorption, transmission electron microscopy, and transient-capacitance studies.			

DD FORM 1 JAN 73 1473

EDITION OF 1 NOV 65 IS OBSOLETE

SECURITY CLASSIFICATION OF THIS PAGE (When Data Entered)

409172

OK

100

Accession For
NTM 78881
DEPT OF THE ARMY
U.S. ARMY
3-1-60

RECEIVED
JAN 1960

SIDE 1

A

TABLE OF CONTENTS

SECTION		PAGE
1	INTRODUCTION	1
2	MACHINE AND ASSOCIATED APPARATUS	2
	2.1 ION MACHINE	4
	2.2 ENCAPSULATION	6
	2.3 AUTOMATED HALL-EFFECT/SHEET-RESISTIVITY MEASUREMENT SYSTEM	25
3	ELECTRICAL PROPERTIES OF ION-IMPLANTED GaAs	30
	3.1 SAMPLE PREPARATION	30
	3.2 ELECTRICAL MEASUREMENTS	31
	3.3 ELECTRICAL PROPERTIES OF Mg-IMPLANTED GaAs	34
	3.4 ELECTRICAL PROPERTIES OF Ge-IMPLANTED GaAs	59
	3.5 ELECTRICAL PROPERTIES OF CARBON DUAL-IMPLANTED GaAs	82
4	TRANSMISSION ELECTRON MICROSCOPY (TEM)	88
	4.1 Si ⁺ -IMPLANTED Cr-DOPED GaAs	88
	4.2 ANNEALING STUDIES OF S ⁺ IMPLANTS	90
5	DEEP-LEVEL-TRANSIENT SPECTROSCOPY (DLTS)	97
	5.1 INTRODUCTION AND EXPERIMENTAL TECHNIQUE	97
	5.2 SAMPLE PREPARATION, TEST PATTERNS, AND PRELIMINARY TESTING	109
	5.3 RESULTS	111

TABLE OF CONTENTS (Concluded)

SECTION	PAGE
6 OPTICAL STUDIES	145
6.1 MAGNETO-OPTICS OF FREE EXCITONS IN GaAs and InP	145
6.2 BOUND MULTIEXCITON COMPLEXES IN GaAs	161
6.3 LOCALIZED VIBRATIONAL-MODE ABSORPTION OF CARBON-IMPLANTED GaAs	169
6.4 EMISSION SPECTRA FROM GaAs FET-LIKE STRUCTURES	175
REFERENCES	192
APPENDIX A: AUTOMATED LUMINESCENT TOPOGRAPHIC SYSTEM	197
APPENDIX B: DETERMINATION OF CONCENTRATIONS OF DONORS AND ACCEPTORS IN GaAs BY AN OPTICAL METHOD	202
APPENDIX C: GLOW-DISCHARGE OPTICAL SPECTROSCOPY MEASUREMENT OF B-, Ge-, AND Mg- IMPLANTED GaAs	206
APPENDIX D: COMPUTER PROGRAM OF ELECTRICAL DEPTH PROFILING	213
APPENDIX E: DEFECT STUDIES IN MULTILAYER EPITAXIAL GaAs BY TRANSIENT CAPACITANCE	223

LIST OF ILLUSTRATIONS

FIGURE		PAGE
1	Ion-Implantation Accelerator	3
2	Si_3N_4 Pyrolytic Deposition System	8
3	Thickness of Si_3N_4 as a Function of Deposition Temperature (2 samples each temperature)	12
4	Index of Refraction of Si_3N_4 as a Function of Deposition Temperature (2 samples each temperature)	13
5	Cold-Wall Reactor for Pyrolytic Deposition of Si_3N_4	14
6	Si_3N_4 Plasma-Enhanced Deposition (PED) System	17
7	Plasma-Enhanced-Deposition-System Reactor Chamber	19
8	Block Diagram of Automated Hall-Effect/Sheet-Resistivity Measurement System	27
9	Schematic Diagram of the Hall-Measurement System for the van der Pauw Configuration	32
10	Dependence of Sheet-Carrier Concentration (N_S) and Hall Mobility (μ_H) upon Annealing Temperature (T_A) for GaAs:Mg Sample with CVD Si_3N_4 Cap	36
11	Dependence of Sheet-Carrier Concentration (N_S) and Hall Mobility (μ_H) upon Ion Dose (ϕ) for GaAs:Mg Samples with CVD Si_3N_4 Cap	37
12	Dependence of Electrical Depth Profile upon Annealing Temperature for GaAs:Mg Samples with CVD Si_3N_4 Cap	42
13	Dependence of Electrical Depth Profile upon Ion Dose for GaAs:Mg Samples with CVD Si_3N_4 Cap	43
14	Depth Profiles of Hole, Acceptor, Donor, and Ionized-Impurity Concentrations for GaAs:Mg	45
15	Dependence of Sheet-Carrier Concentration (N_S) and Hall Mobility (μ_H) upon Annealing Temperature (T_A) for GaAs:Mg Samples with PED Si_3N_4 Cap	49

LIST OF ILLUSTRATIONS (Cont'd)

FIGURE		PAGE
16	Dependence of Electrical Depth Profile upon Ion Dose for GaAs:Mg Samples with PED Si ₃ N ₄ Cap	52
17	Dependence of Electrical Depth Profile upon Annealing Temperature for GaAs:Mg Samples with PED Si ₃ N ₄ Cap	55
18	Dependence of Electrical Depth Profile upon Annealing Time for GaAs:Mg	57
19	Dependence of Sheet Resistivity upon Laser Annealing Energy	60
20	Dependence of Sheet-Carrier Concentration (N_S) and Hall Mobility (μ_H) upon Annealing Temperature (T_A) for GaAs:Ge	63
21	Dependence of Sheet-Carrier Concentration (N_S) and Hall Mobility (μ_H) upon Ion Dose (ϕ) for GaAs:Ge	65
22	Dependence of Sheet-Carrier Concentration (N_S) and Hall Mobility (μ_H) upon Annealing Temperature (T_A) for GaAs:Ge + Ga	69
23	Dependence of Sheet-Carrier Concentration (N_S) upon Ion Dose (ϕ) for GaAs:Ge + Ga	71
24	Dependence of Sheet-Carrier Concentration (N_S) and Hall Mobility (μ_H) upon Annealing Temperature (T_A) for Lower-Dose Samples of Both GaAs:Ge and GaAs:Ge + Ga	72
25	Dependence of Sheet-Carrier Concentration (N_S) and Hall Mobility (μ_H) upon Annealing Temperature (T_A) for Higher-Dose Samples of Both GaAs:Ge and GaAs:Ge + Ga	73
26	Dependence of Sheet-Carrier Concentration (N_S) and Hall Mobility (μ_H) upon Annealing Temperature (T_A) for GaAs:Ge + As	76
27	Dependence of Sheet-Carrier Concentration (N_S) upon Ion Dose (ϕ) for GaAs:Ge + As	78
28	Dependence of Sheet-Carrier Concentration (N_S) and Hall Mobility (μ_H) upon Annealing Temperature (T_A) for Lower-Dose Samples of Both GaAs:Ge and GaAs:Ge + As	80

LIST OF ILLUSTRATIONS (Cont'd)

FIGURE		PAGE
29	Dependence of Sheet-Carrier Concentration (N_S) and Hall Mobility (μ_H) upon Annealing Temperature (T_A) for Higher-Dose Samples of Both GaAs:Ge and GaAs:Ge + As	81
30	Profiles of Single and Dual C^+ -Implanted GaAs	86
31	(a) Electron Micrograph Showing Point-Defect Clusters, Precipitates, and Dislocations in Cr-doped GaAs Implanted with Si^+ Ions (120 keV) at Room Temperature at a Total Dose of 3×10^{15} ions/cm ²	
	(b) (c) Selected-Area Diffraction Pattern and Its Schematic Diagram Showing Presence of Extra Spots (x) due to Precipitates. Foil orientation near (100).	89
32	Bright-Field Electron Micrograph (a) Showing Mottled Microstructure Due to the Presence of Amorphous Layer as Evidenced by Diffuse Rings in the Diffraction Pattern (b) in Cr-Doped GaAs Implanted with S^+ Ions (120 keV) at Room Temperature to a Total Dose of 10^{15} ions/cm ²	92
33	Elimination of Inner Diffuse Ring and Formation of Streaking along Two Mutually Perpendicular Directions around (002) and (220) Diffraction Spots of GaAs as a Result of <u>In Situ</u> Annealing at 330°C for 5 min. inside an Electron Microscope in Cr-Doped GaAs Implanted with S^+ Ions (120 keV) at Room Temperature to a Total Dose of 10^{15} ions/cm ² . Foil orientation near (100).	93
34	Observation of Dislocation-Loop Formation during <u>In Situ</u> Annealing at 730°C for 5 min. inside an Electron Microscope in Cr-Doped GaAs Implanted with S^+ Ions (120 keV) at Room Temperature to a Total Dose of 10^{15} Ions/cm ² . Foil Orientation near (100).	95
35	(a) Same Area as in Previous Figure. Annealing Temperature and Time are 860°C and 5 min., Respectively	
	(b) Selected-Area Diffraction from Area (a)	96

LIST OF ILLUSTRATIONS (Cont'd)

FIGURE		PAGE
36	Schematic Diagram of Pulse Sequence, Charge Injection, and Transient-Capacitance Signal for Fast-Capacitance Experiment	100
37	Temperature Dependence of Transient-Capacitance Signals	102
38	Simplified Schematic of DLTS Experiment	104
39	Example of Peak Shift with DLTS Emission-Rate Window	105
40	Typical Plot of Thermal-Emission Rate as a Function of Peak Temperature	106
41	FET-Like Test Pattern for DLTS Measurements	110
42	Epitaxial Wafer and Bonded Device for DLTS Experiment	112
43	Typical I-V Characteristics of an Epitaxial DLTS Sample	113
44	Example of N-W Variations on a Particular Wafer (R19) between Different Dies (30 vs 6) as Determined by C-V Profiling	114
45	DLTS Spectrum of "As-Grown" VPE GaAs	116
46	DLTS Data for Profile Measurements in As-Grown VPE GaAs	117
47	Carrier-Concentration Profiles from C-V Measurements and Trap-Concentration Profile from DLTS Measurements	118
48	DLTS Spectrum after 1-MeV Electron Irradiate Yields 1% Carrier Removal	120
49	DLTS Spectrum after 1-MeV Electron Irradiate Corresponding to 2% Carrier Removal	121
50	DLTS Spectrum of As-Implanted VPE GaAs:Ar	122
51	DLTS Spectrum of GaAs Implanted to 10^{15} cm^{-2} , No Annealing	123
52	Thermal-Activation-Energy Plots of Native Defects and Ion-Implanted Peaks	124

LIST OF ILLUSTRATIONS (Cont'd)

FIGURE		PAGE
53	DLTS Spectrum of Ar-Implanted GaAs Annealed at 300°C	126
54	DLTS Spectra from Ar-Implanted GaAs Annealed to 700°C	127
55	DLTS Spectrum for Ar-Implanted GaAs Annealed to 700°C	128
56	DLTS Spectrum of Ar-Implanted GaAs Annealed to 850°C	129
57	DLTS Spectrum of GaAs Implanted with As and Annealed to 700°C. Pulse to Zero Bias	131
58	DLTS Spectrum of GaAs Implanted with As and Annealed to 700°C. Pulse to + 2 V	132
59	DLTS Spectrum from FET-Like Test Pattern on Device-Grade Material R43	134
60	DLTS Spectrum from FET-Like Test Pattern on Device-Grade Material R44	135
61	DLTS Spectrum from FET-Like Test Pattern on Device-Grade VPE GaAs Irradiated with 1-MeV Electrons	137
62	N-W Profiles of FET-Like Test Pattern on Device-Grade VPE GaAs	138
63	Activation-Energy Plot of FET-Like Test Pattern on Device-Grade VPE GaAs	139
64	DLTS Spectrum for Undoped GaAs (initial data)	141
65	DLTS Spectrum from Electron-Irradiated VPE GaAs (slow emission rate, moderate reverse bias)	143
66	DLTS Spectrum from Electron-Irradiated VPE GaAs (moderate emission rate, high reverse bias)	144
67	Variations of Energy Shifts of σ^+ and σ^- Lines in GaAs as a Function of Reduced Magnetic Field γ	156

LIST OF ILLUSTRATIONS (Cont'd)

FIGURE		PAGE
68	Variations of Energy Shifts of σ^+ and σ^- Lines in GaAs as a Function of Reduced Magnetic Field γ	157
69	Variations of Energy Shifts of π^+ and π^- Lines in GaAs as a Function of Reduced Magnetic Field γ	158
70	Variations of Energy Shifts of σ^+ and σ^- Lines in InP as a Function of Reduced Magnetic Field γ	159
71	Variations of Energy Shifts of σ^+ and σ^- Lines in InP as a Function of Reduced Magnetic Field γ	160
72	Photoluminescence Spectra for GaAs High-Purity Epitaxial Specimen Taken at 2°K with 1 min. and 3 min. Exposures. The proposed electronic transition scheme for complexes composed of one and two excitons bound to the neutral zinc acceptor is illustrated and is discussed further in the text.	164
73	Relative Transmission and Annealing Temperature as a Function of Energy for Three Different GaAs Crystals. All data shown here were taken with the samples at -82°K.	173
74	(a) Typical GaAs Structures Investigated (b) Photoluminescence Mechanisms; Pump Photon Absorption (~10 Å Deep), Carrier Formation and Diffusion ($> 1 \mu\text{m}$ Diffusion Length for Holes), Pair Recombination in a Diffusion-Doped High-Purity Interface Region beneath the Active Layer	176
75	Equipment Schematic	179
76	Photoluminescence Spectra of Typical Donor-Bound Exciton-Dominated Shallow Structure	183
77	Photoluminescence Dominated by Complex Lines	184
78	Magnetic-Field Behavior of Sulfur and Silicon-Bound Exciton Lines	186

LIST OF ILLUSTRATIONS (Concluded)


FIGURE		PAGE
79	Linear Zeeman Splitting of Sulfur and Silicon-Bound Exciton Lines	187
80	Magnetic-Field Behavior of Complex Lines A and B	188
81	Linear Zeeman Splitting of the Line B (1.514538 eV) at 41.3 kG Applied Field	189
82	Diamagnetic Shift of Various Sharp Lines as a Function of Transition Energy	190

LIST OF TABLES

TABLE		PAGE
1	RESULTS OF VARIATIONS IN NITROGEN FLOW RATES AND RF POWER UPON PED NITRIDE, ALL OTHER PARAMETERS BEING HELD CONSTANT	22
2	RESULTS OF VARIATIONS IN TEMPERATURE AND RF POWER UPON PED NITRIDE, ALL OTHER PARAMETERS BEING HELD CONSTANT	23
3	RESULTS OF VARIATIONS IN TEMPERATURE AND SILANE FLOW RATE UPON PED NITRIDE, ALL OTHER PARAMETERS BEING HELD CONSTANT	24
4	RESULTS OF VARIATION IN RF POWER AND TIME UPON PED NITRIDE, ALL OTHER PARAMETERS BEING HELD CONSTANT	24
5	EQUIPMENT IDENTIFICATION OF AUTOMATED HALL-EFFECT/SHEET-RESISTIVITY MEASUREMENT SYSTEM	28
6	SHEET RESISTIVITY ρ_s , EFFECTIVE HALL MOBILITY μ_{eff} , AND THE SHEET-HOLE CONCENTRATION P_s FOR VARIOUS SAMPLES ANNEALED AT 700°C FOR 15 MIN	84
7	COMPARISON OF ELECTRICAL PARAMETERS FOR SINGLE AND DUAL IMPLANTS ANNEALED AT 900°C FOR 15 MIN	84
8	MEASURED d-SPACINGS FROM EXTRA REFLECTIONS AND THEIR ASSIGNMENT BASED UPON THE SiAs ₂ STRUCTURE	91
9	COMPARISON OF MEASURED AND CALCULATED ANGLES (BASED UPON THE SiAs ₂ STRUCTURE) OF DIFFERENT PLANES DUE TO PRECIPITATES	91
10	VALUES OF THE BAND-STRUCTURE PARAMETERS OF GaAs	154
11	VALUES OF THE BAND-STRUCTURE PARAMETERS OF InP	154
12	SAMPLE CHARACTERISTICS	178


Section 1

INTRODUCTION



The purpose of this program was to investigate the controlled doping of compound semiconductors by means of ion implantation. This effort has encompassed 1) the study of the physics of the ion-implantation process, 2) characterization of the as-grown, implanted, and annealed specimens, and 3) optimization of specimen preparation, implantation, and post-implantation treatment for the application of these techniques to electron-device fabrication.

In the sections that follow, studies of III-V semiconductors will be described in detail. The analysis and characterization of the specimen by means of photoluminescence, electrical measurements, capacitance-voltage profiling, far-infrared absorption, transmission electron microscopy, and transient-capacitance studies will be discussed. Some of the characterization techniques represent new developments in experimental capabilities. The fabrication of the apparatus as well as the experimental methods used in their application will be treated in detail.



Publications resulting from the research using photoluminescence topography are included in Appendices A and B.

The results of this research form the basis for a continuing advancement of the state-of-the-art of ion implantation in compound semiconductors.

Section 2

MACHINE AND ASSOCIATED APPARATUS

The importance of ion implantation as a semiconductor doping technique is derived from the degree of control available over the implantation process and from the fact that any ion can be implanted into any solid. The three main parameters over which control is exercised are implantation depth, fluence, and impurity species. The depth of penetration of an impurity ion into a host material is dependent upon the host material, the mass and charge of the impurity ion, and the accelerating potential. For a specific host and ion, the penetration depth is directly controlled by the accelerating potential. The fluence or number of impurities implanted per cm^2 is dependent upon the implant area, the impurity beam current at the target, and the amount of time during which the target is exposed to the beam. For a given implant area and beam current, the fluence is directly controlled by exposure time. Selection of the implant species is accomplished by mass analysis of the ion beam. Only that constituent in the ion beam which has the mass-energy product passes through the analyzing magnet and impacts the target.

The ion-implantation apparatus located in AADR is a ten-year-old 150-kV accelerator that SRL personnel have maintained and operated for three and one-half years. The major elements of the machine are shown in Fig. 1. Included in the high-voltage terminal are focusing and extraction elements for the different ion sources available. An rf source is used to produce ions from gases such as Ar, N_2 , O_2 , and H_2 . A hot-cathode source is used

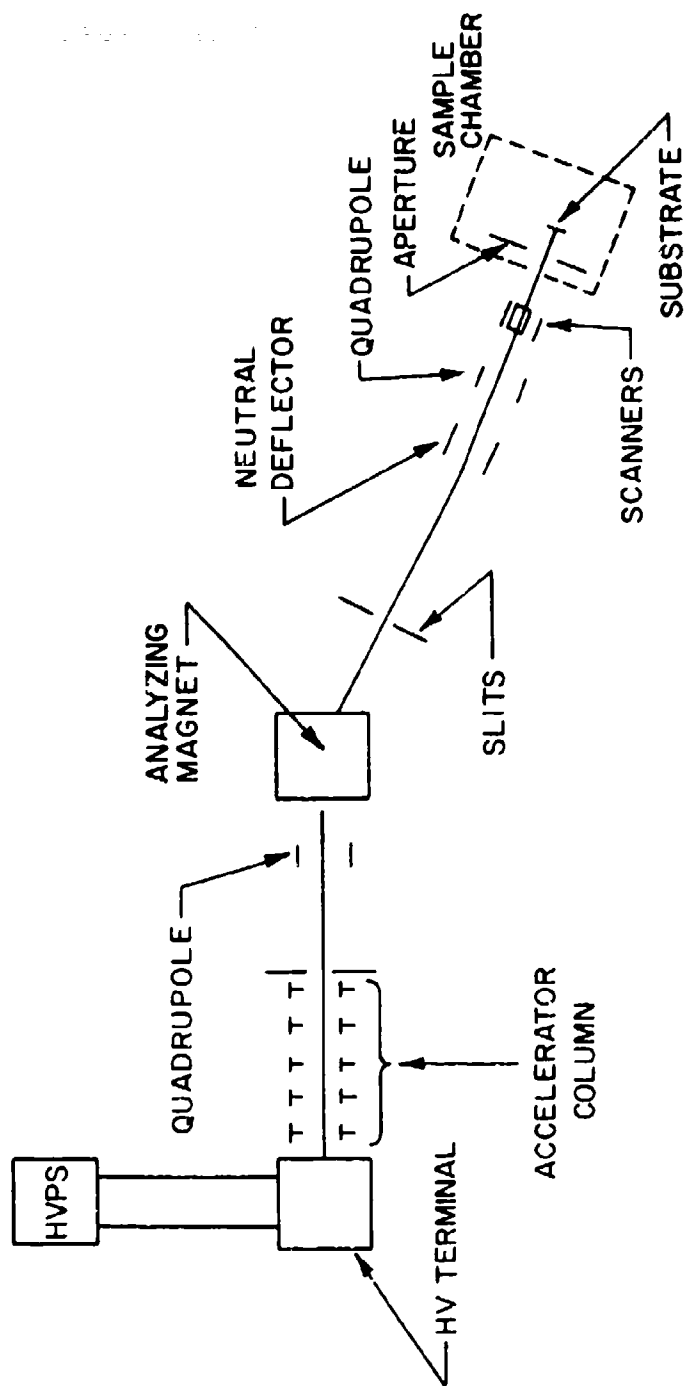


Figure 1. Ion-Implantation Accelerator.

to generate metallic ions such as Ge, Mg, and As from appropriate solid sources. Once the ion beam is generated and accelerated, it passes through the analyzing magnet. The magnetic field divides the beam into its various mass components at the output port. By selecting the proper field, the desired ion beam passes through the magnet to a set of mechanical slits which may be used to adjust (reduce) the beam current. From the slits, the beam passes through the neutral deflector, which is a 5° bend in the beam line. The beam is deflected around the bend by an electrostatic field. Since only charged particles are affected by the field, any neutral atoms that may be contaminating the beam fail to make the bend and impact the beam line wall. The next element in the beam path is a quadrupole which serves as the final focusing element for the ion beam. The scanners are used to deflect the beam across the target surface in an asynchronous manner. This ensures uniform implantation over the entire target area determined by the aperture in the sample chamber. In the present setup, the aperture also serves as a suppressor for secondary electrons emitted during the implantation process.

2.1 ION MACHINE

Three modifications were made to the ion machine during the contract period. A 200-ℓ/sec Perkin-Elmer Ultek ion pump equipped with a titanium sublimator was installed on the target chamber in place of a turbomolecular pump. The ion pump was installed to eliminate sample contamination caused by back-streaming oil from the turbo pump. Four target plates capable of holding 2-in.-diam. wafers for implantation were designed and installed in the target chamber. Previously, the maximum sample size that could be implanted was 1 in. in diam. The last improvement was the addition of a third ion

source--a cold cathode--to the other two sources used for ion-beam production. The cold cathode requires a negative high-voltage supply for its operation. A negative supply does not exist at the source end of the machine. Instead of adding a new supply to the already crowded top end of the accelerator, an existing power supply--the probe supply for the RF source--was modified so that it could be switched easily from positive to negative. The negative discharge potential and the carrier gas pressure are the only parameters on a cold-cathode source. Both must be adjusted for optimum ion current while the source is running. This required installation of a remote control for the carrier-gas metering value. (A remote control for the discharge of potential existed.)

The cold cathode was installed to be used as a Be source since it was constructed with a Be canal. This canal is sputtered by the discharge during source operation, and a small Be ion beam is produced. Since Be is a very toxic material and dangerous to handle, this is a safe means of producing a Be beam. The source did produce a Be beam, and samples were implanted. In addition to low beam currents, another problem with the cold cathode is that because of the energy dispersion of the beam, ion beams cannot be resolved as well as with the other sources. This is not a severe problem for low-mass ions such as Be since it is widely separated from the possible contaminants hydrogen and carbon. These two problems limit the usefulness of the source.

The Be implants were done for use in the initial setup of a new technique, Glow Discharge Optical Spectroscopy (GDOS), to be used for profiling implants. Unfortunately, the Be implants were never identified by GDOS. This was not

the case for three other implanted ions. B, Mg, and Ge implants were successfully profiled using GDOS (see Appendix C for publication on this subject). In addition to the GDOS implants, Ge and Mg also were implanted for a detailed investigation into their electrical properties. The results of this work will be discussed later in this report as will the results of dual implants of C and Ga into GaAs.

2.2 ENCAPSULATION

Radiation damage is an inevitable consequence of ion implantation. Bombardment by high-energy ions creates point defects such as vacancies and interstitials, clusters of point defects, and dislocation loops. The amount of damage generated depends upon the ion species, ion dose, dose rate, and the energy and temperature of the substrate. Unfortunately, some damage sites may act as unwanted traps for holes and electrons or may form vacancy complexes. In addition, all of the as-implanted ions do not settle into substitutional lattice sites and, hence, all of the ions do not become electrically active. Therefore, thermal annealing is required to bring the dopant onto electrically active sites and to remove the unwanted radiation damage. Generally, annealing temperatures in the range 600 - 900°C are required to achieve maximum electrical activation of the implanted ions. Annealing at this high temperature usually removes the majority of the implanted damage. However, it is known that As can be lost from the surface of GaAs at a temperature as low as 400°C. Since the decomposition temperature of GaAs is ~ 630°C, some means of surface protection is required during high-temperature annealing.

Usually the surface of the implanted layer is encapsulated, using a thin dielectric film as a protective cap. An effective encapsulant should reliably protect the implanted GaAs surface from decomposition at temperatures up to at least 900°C. It should also prevent outdiffusion of the implanted species. The encapsulant must be easily depositable as a homogeneous layer which adheres well and does not diffuse into or react chemically with GaAs. It must also be mechanically stable and able to withstand high temperatures without blistering, crazing, or creating strain at the interface.

Among the presently known dielectric caps, Si_3N_4 has been demonstrated to be comparable and in many cases superior to the other encapsulants for annealing GaAs. Even with this cap, however, the implantation results have shown a strong dependence upon the deposition method and the particular parameters used. Two nitride deposition systems were perfected over the period of this contract--a chemical-vapor-deposition system and a plasma-enhanced deposition system. Figure 2 is a block diagram of the chemical-vapor-deposition (CVD) system used to encapsulate GaAs with Si_3N_4 . The system was copied from Lincoln Laboratory which assisted in its initial set-up. Lincoln Laboratory did the encapsulation for the implantation work accomplished during the previous contract. The establishment of an in-house encapsulation facility was necessitated by the increased ion-implantation effort of this contract. The reactor construction was already in progress at the start of this contract. This type of system is also known as a "pyrolytic" system since it uses high temperature to initiate the reaction needed to produce the Si_3N_4 . Although high temperature is employed, this is a "cold-wall" reactor. The CVD system uses two reactive

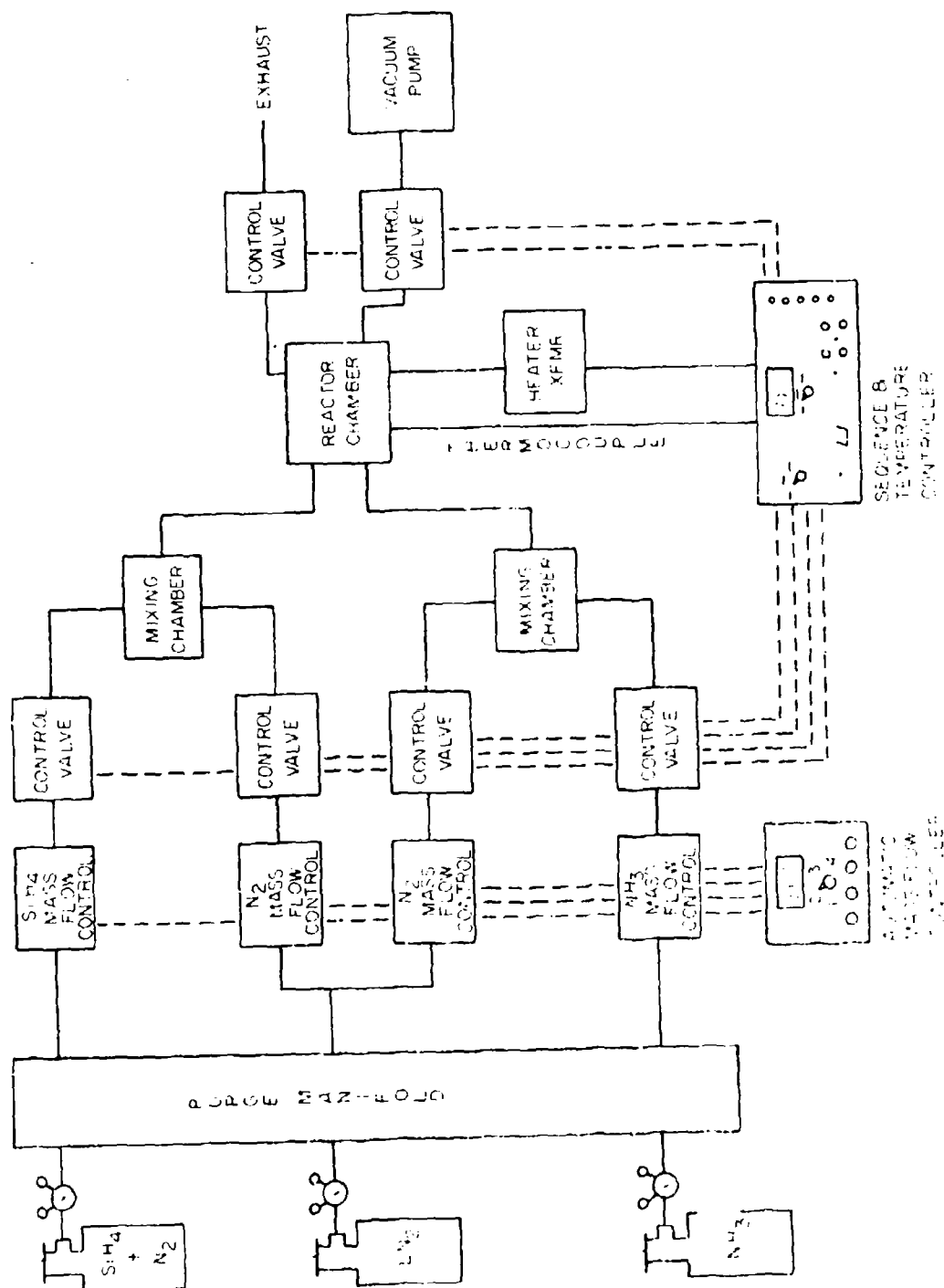


Figure 2. Si_3N_4 Deposition System.

gases--silane and ammonia--and a third diluting gas which is nitrogen. The silane used is a 5% mixture of silane and nitrogen. The other reactant gas is anhydrous ammonia. The nitrogen gas used for diluting and backfilling is obtained from liquid nitrogen in a pressurized storage Dewar. A liquid source for nitrogen was not used in the early stages of the system development. Rather, a standard high-pressure gas cylinder was used. The liquid-nitrogen source was implemented when, in the course of investigating potential reasons for cap failure during annealing, an analysis of the gas in the nitrogen cylinder showed the presence of a substantial amount of helium. It was discovered that the nitrogen cylinder had previously contained helium. Whether or not the helium contributed to the cap failure is unknown, but the incident did dramatize the need for an easily obtainable, reliable, and pure source of nitrogen. A purity problem does not exist for the reactant gases since they must be bought commercially.

Examining the block diagram, one sees that from the source cylinders, the gases are plumbed through a purge manifold. The manifold is designed to permit the backfilling and purging of the entire system with nitrogen. The next elements in the system are the gas-flow controllers. For the first year of operation, flow control was accomplished manually by means of metering valves and mass-flow meters. Constant monitoring was required during a run, and reproducibility suffered. The manual controls were essential for initial set-up, however, since it was necessary to establish gas-flow parameters and the final flow ranges could not be determined. Once the various flow requirements for optimum nitride deposition were established, properly ranged automatic Tylan mass-flow controllers were installed. From the controllers each gas line passes through an electrically operated valve.

These valves, and similar ones located on the exhaust and vacuum pump lines, are operated by the sequence controller and are actuated at different times during the capping cycle. When the system is "standing-by," the valves in both nitrogen and exhaust lines are opened to allow continual nitrogen flow through the reactor chamber. Once a sample is loaded, the system is evacuated. All valves are closed except the one on the vacuum line which is opened to allow evacuation of the chamber and all supply lines up to the other valves. The system is evacuated to less than 1 Torr. At this point the vacuum valve closes, the two nitrogen valves open, and the system is backfilled with nitrogen. The system next enters a purge mode. The nitrogen valves close and the silane, ammonia, and exhaust valves open. The heater temperature is raised to 200°C just prior to introducing silane. This procedure was recommended by Lincoln Laboratory,¹ where it was observed that the silane could react at room temperature with trace amounts of oxygen still present in the reactor chamber and could deposit on the sample. This predeposition can be eliminated if the sample is heated to 200°C. The chamber purge lasts for ~1 min., after which the nitrogen valves open and the reactant gases are diluted in the mixing chambers. From the mixing chambers the diluted reactants flow to the reactor where they are dispersed and mixed. The flow rates for the different gases are as follow:

5% silane in nitrogen	220 sccm
nitrogen-silane dilutant	500 sccm
ammonia	200 sccm
nitrogen-ammonia dilutant	500 sccm

After ~3 min. of mixing, the heater temperature is raised to the deposition temperature of 725°C. This rapid rise is accomplished in ~8 sec. with

minimal overshoot. The sample will remain at this temperature until the desired thickness of Si_3N_4 is deposited. The deposition rate at the above temperature with the above flows is between 30 and 40 $\text{\AA}/\text{sec}$. When the desired film thickness is reached (approximated by the film's color), a system clear button is pressed to deactivate the heater and close the reactant gas valves. Nitrogen continues flowing to flush the chamber and cool the sample. The deposition rate of the nitride is directly dependent upon temperature and gas-flow parameters. The temperature dependence can be seen in Fig. 3. With fixed gas parameters the higher the temperature, the thicker the deposited film. Unfortunately, the index of refraction of the nitride film also varies with deposition temperature, as shown in Fig. 4. The broken line of Fig. 3 and related Fig. 4 represents the early day-to-day non-reproducibility of the system. Each segment of Figs. 3 and 4 was accomplished on a different day. The dependence of deposition rate upon flow parameters can be seen in Fig. 3 by the star in the upper left corner of the graph. The star plots the thickness of the film which results when the silane flow is increased to 220 sccm and the other flows are unchanged. The corresponding index of refraction is plotted on Fig. 4 by the star. The parameters associated with the star are those which were used in connection with some of the implantation work detailed later in this report.

Figure 5 shows the pyrolytic reaction chamber, detailing the dispersion arms for the diluted reactants, the thermocouple for temperature measurement and control, and the heater on which the sample rests. The heater is a low-mass graphite strip 2 in. long \times 7.8 in. wide. Only a 5.8 in.-square area in the center is usable for capping. The heater has holes drilled through it on either end to ensure more uniform current (heat) distribution

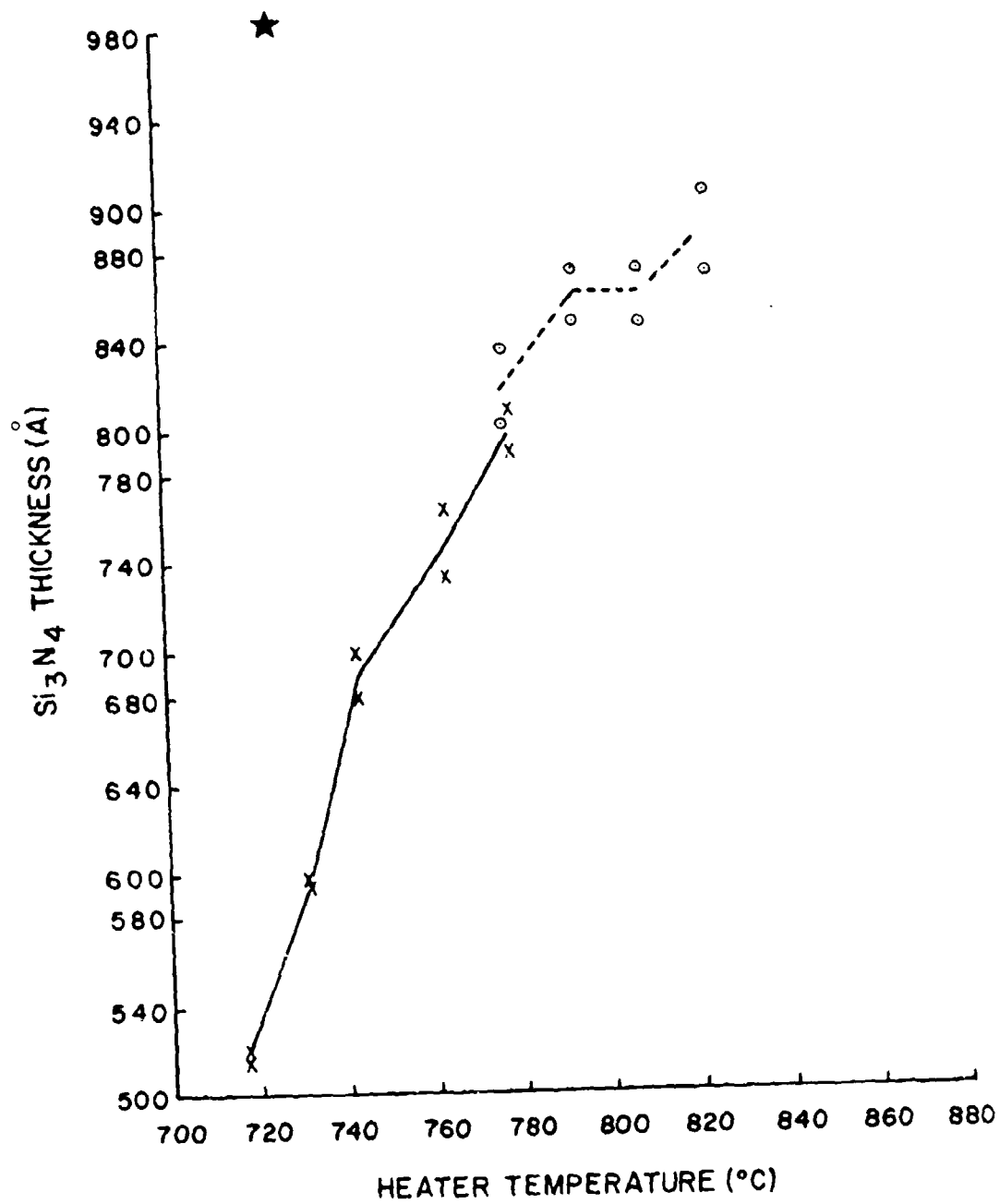


Figure 3. Thickness of Si₃N₄ as a Function of Deposition Temperature (2 samples each temperature).
 Flow parameters: Silane - 80 sccm, Silane Dilutant - 500 sccm,
 Ammonia - 200 sccm, Ammonia Dilutant - 500 sccm
 star indicates thickness when silane flow is changed to 220 sccm.

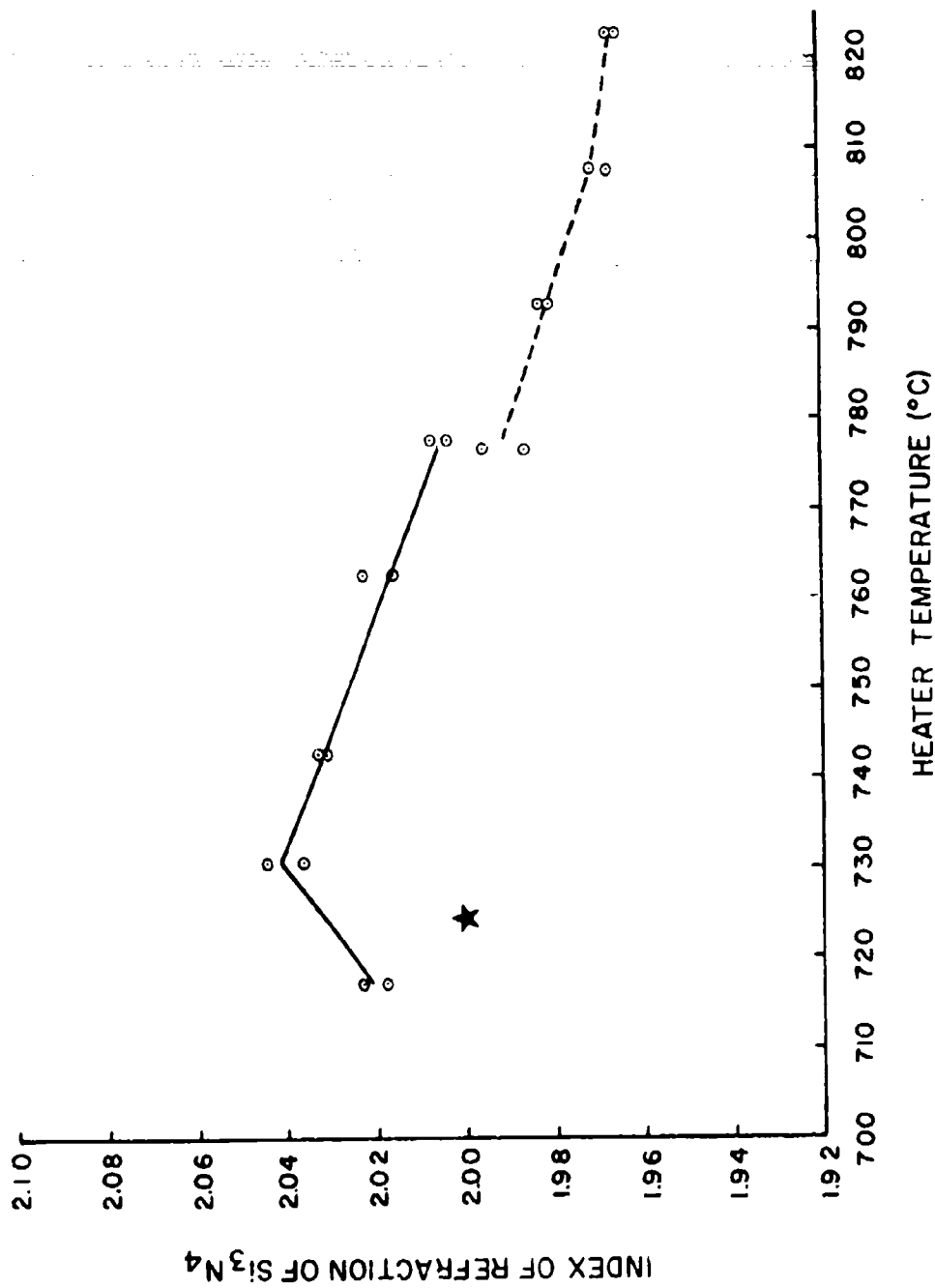


Figure 4. Index of Refraction of Si_3N_4 as a Function of Deposition Temperature (2 samples each temperature).

Flow parameters: Silane - 80 sccm, Ammonia Dilutant - 500 sccm,
 Ammonia - 200 sccm, Ammonia Dilutant - 500 sccm,
 Star indicates thickness when silane flow is changed to 220 sccm.

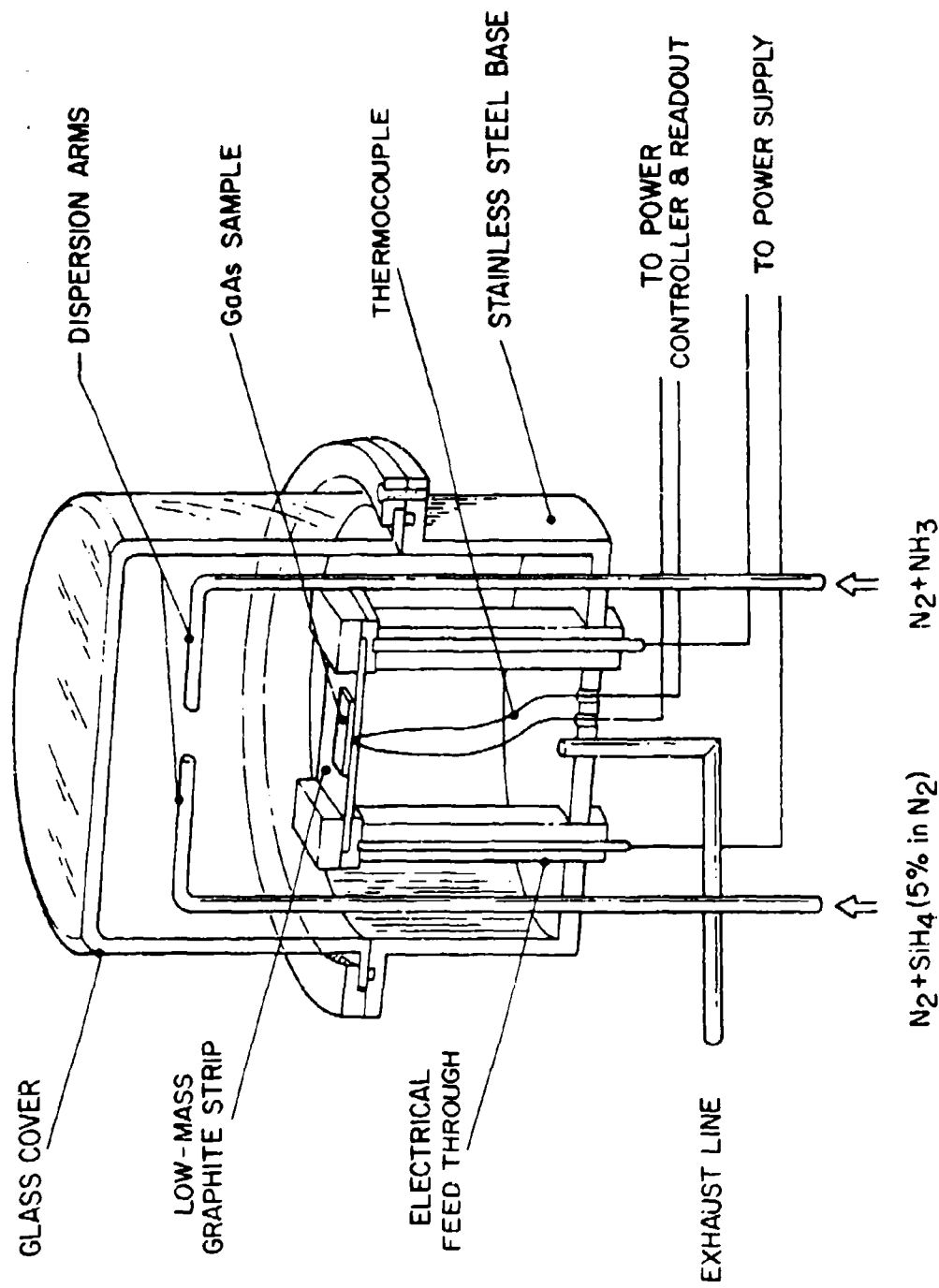


Figure 5. Cold-Wall Reactor for Perovskite Deposition of Si_3N_4 .

and to reduce the heat loss from the strip to the supporting feedthroughs. The heater is connected across the output of a 1.5 kVA transformer, an arrangement which allows the rapid rise to the deposition temperature. The importance of the rapid rise is apparent when one considers that the capping temperature is higher than the decomposition temperature ($\sim 630^{\circ}\text{C}$) of GaAs. The thermocouple is inserted into the side of the graphite strip. It was originally placed in a small indentation in the bottom of the heater, but that arrangement proved to be unacceptable for two reasons. First, the gas flows were sufficiently high to randomly dislodge the small thermocouple bead during a cycle. When the heater was energized, the temperature would rise far above the set point and destroy the sample. Secondly, after repeated runs, the bead would become encrusted with nitride and produce erroneous temperature readings. One additional problem associated with the thermocouple was discovered in the original design. The thermocouple was mechanically attached to a feedthrough in the chamber. It was discovered that the junction of the thermocouple and feedthrough was generating an EMF as the ambient temperature of the system increased with each additional run. This EMF represented an increasing temperature measurement error. Once the problem was identified, the solution was simple. The feedthrough was removed, and the thermocouple leads were continued through the chamber wall intact and connected to a terminal that remains at room temperature. The high temperature associated with the pyrolytic reactor limits its versatility. It is impossible to encapsulate large samples, and some materials of interest such as InP cannot withstand the high temperature required for deposition. In order to solve both of these problems, a low-temperature, large-area encapsulation method was sought. A plasma-enhanced deposition (PED) system fulfilled both the temperature and area

requirements. A system of this type was purchased by AADR from LFE Corp. in January of 1978. A block diagram of the present modified system is shown in Fig. 6. The modifications made to the original system were extensive.

Through the development of the CVD system it already was known that oxygen contamination either from a leak or from residual water vapor in the system would render the nitride useless. Upon examination of the PED system, the internal plumbing was found to be copper and plastic. Helium leak checking confirmed suspicions that this arrangement was not and could never be leak tight. All the plumbing was replaced with stainless steel tubing and fittings. The inadequate flow controls were also replaced with quality metering valves and flow meters. Even after these modifications, the quality of the Si_3N_4 did not match that of the CVD system.

Dr. Streetman's group at the University of Illinois was claiming good results with its home-made PED reactor. A visit was made to Dr. Streetman to observe his procedures and obtain some of his nitride caps. The visit proved to be both beneficial and discouraging. It was discouraging because every one of the 17 University of Illinois caps blistered within a week of encapsulation. The visit was beneficial in that important system modifications were discovered. The first modification was the addition of a cold trapped diffusion pump (a high vacuum system) for evacuating the reactor bell jar. The second modification was the installation of a shutter. Part of the Illinois procedure was to "clean" the bell jar with a nitrogen plasma prior to deposition in an attempt to remove any oxygen or water vapor that might remain even after the chamber had been evacuated to $\sim 3 \times 10^{-6}$ Torr. A moveable shutter was used to shield the sample from exposure to the plasma. A stainless steel leaf shutter was designed and added to the reactor chamber,

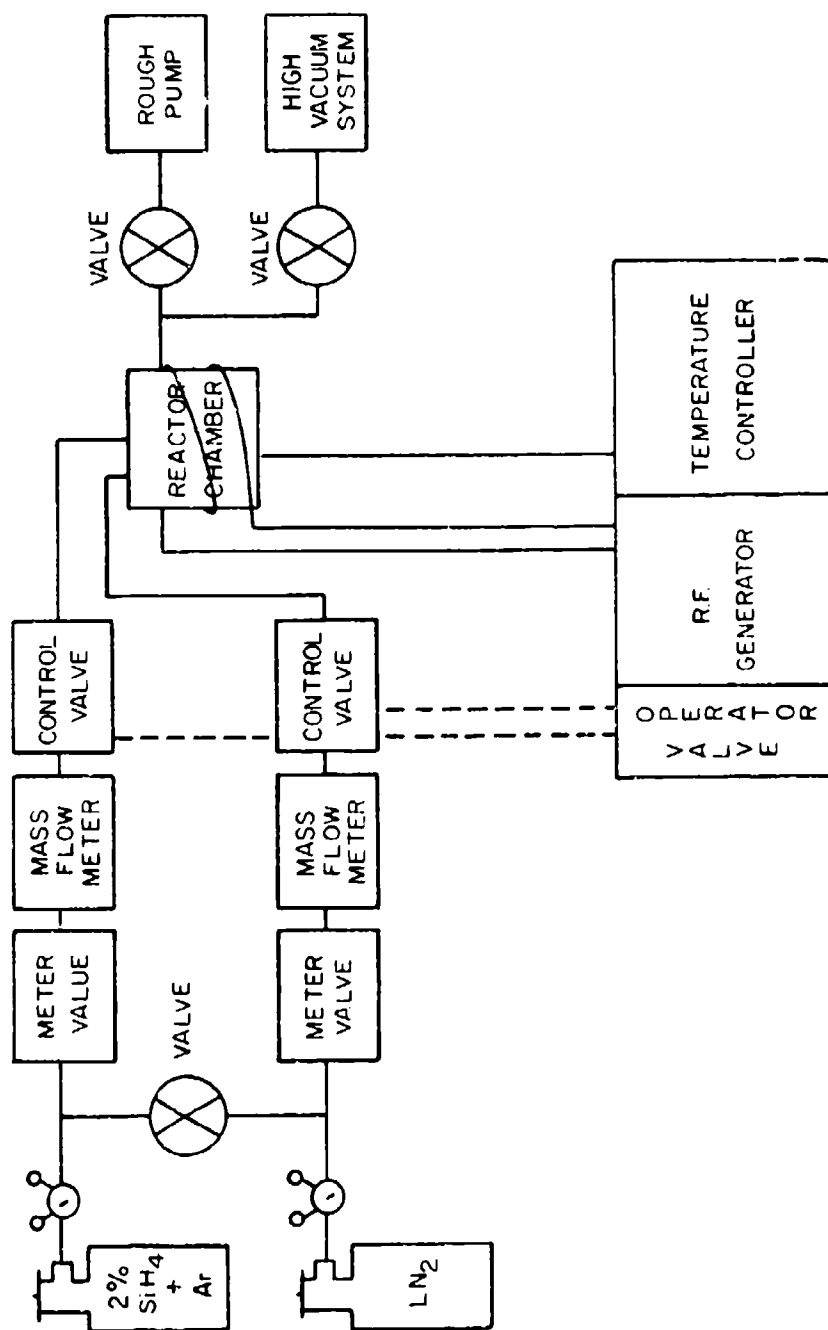


Figure 6. Si_3N_4 Plasma-Enhanced Deposition (PED) System.

as shown in Fig. 7. In order to implement the plasma cleaning procedure on the LFE reactor, the logic and timing had to be disabled. In addition, electrically operated control valves were installed in the gas supply lines. Essentially, the system operation was made completely manual.

In the course of system operation and evaluation, many problems were discovered and modifications made. The silane mixture was changed from that used in the CVD system to a mixture of 2% silane in Ar. This allowed the silane-to-nitrogen ratio to assume any desired value. A new stainless steel shower was designed to replace the existing glass shower. The holes in the glass shower were irregular and did not give a uniform deposition pattern. The glass base-plate of the reactor also was replaced with stainless steel. The original glass plate used o-ring seals for the heater and thermocouple feedthrough. The combination of poor construction of the base plate and the feedthrough's exposure to high temperatures led to frequent o-ring failure which resulted in leaks. The o-rings were not easily replaced because the entire chamber had to be dismantled. With the stainless steel base plate, the feedthroughs were "substrated" in and thus ceased to be a source of leaks. The heater also was replaced. The original heater was a diffusion-pump heater drawn against two aluminum rings, which proved to be a major problem. When a monitoring thermocouple was mounted on the top aluminum plate (where the sample rests), a temperature difference of at least 100°C from the indicated temperature was measured, and this difference fluctuated. Because of the poor thermal contact between the layers of the heater, the temperature difference was dependent upon time and the system pressure. When the system was evacuated, the temperature would decrease, with the amount of decrease depending on the time required for system evacuation. When gas was flowing

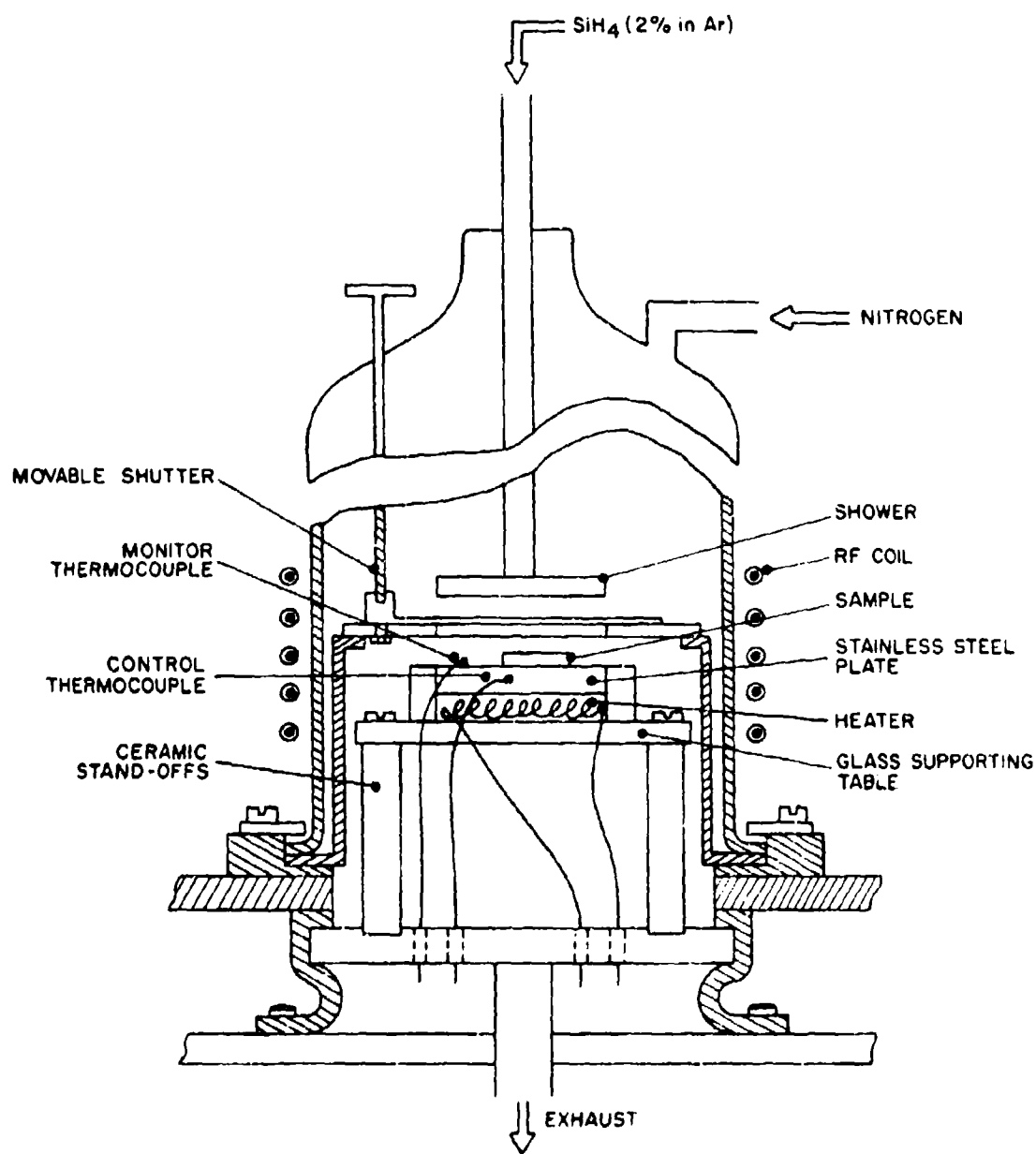


Figure 7. Plasma-Enhanced-deposition-system Reactor Chamber.

the temperature would rise, with the amount of increase depending on how far it previously had dropped and how long the gas flowed. The heater element was encased in metal but it was not sealed, which made it a source of contamination and leaks.

A new heater was designed with the criterion that it must be clean and simple. A spring was fashioned out of nichrome wire for the heating element. The spiral element was positioned on a quartz supporting table and loosely covered with a stainless steel disk. The disk rests on the quartz spacers which prevent the element from shorting. The controlling thermocouple is inserted into the edge of the steel disk, and a monitoring thermocouple is mounted on top of the disk. This arrangement functions quite well and has the advantage of being completely and easily cleanable.

Paralleling the evolution of the system hardware was the evolution of an operating procedure. A sample is placed on the stainless steel disk which is at the desired temperature. The shutter is closed and the chamber is sealed and rough-pumped to less than 10^{-5} Torr. Once below 10^{-5} Torr the rough pump is valved off, and the gate valve to the diffusion pump is opened. The chamber is further evacuated to a range of 10^{-6} Torr. The gate valve is closed, and the chamber is backfilled with nitrogen. The roughing valve is opened and a 200-W plasma is excited. This is the cleaning plasma used at Illinois. The nitrogen flow is stopped, and the system is allowed to rough back to 10^{-5} Torr. RF power is removed, and again the chamber is evacuated to a range of 10^{-6} Torr. As before, the chamber is backfilled and a 200-W nitrogen plasma is excited. This time the shutter is opened, and the sample is exposed to the plasma for at least 30 sec. What is actually accomplished

with this step is not known, but experiments have shown it to be beneficial--possibly it conditions the sample surface for better adherence of the nitride. Following the exposure the shutter is closed and silane is introduced into the chamber. Time is allowed for mixing and stabilizing before the deposition plasma is excited. Once this plasma is excited, deposition begins as soon as the shutter is opened and proceeds until the desired film thickness is deposited. At this time the shutter is closed, the rf power removed, and the gas flows stopped. The system is allowed to rough out before the roughing valve is closed, and the system is backfilled with nitrogen prior to sample removal.

Six parameters affect the nitride deposition--silane flow rate, nitrogen flow rate, rf power, temperature, time, and the distance from the shower to the heater. Although the last parameter has an effect on the composition of the deposited film, its major effect is on the uniformity and size of the area over which the deposition occurs. Tables 1 - 4 record the index of refraction and thickness of the deposited Si_3N_4 , obtained by varying the different parameters. All other affecting parameters were held constant. From the tables it is possible to order the various parameters according to their degree of effect upon the deposited nitride. The parameter having the greatest effect upon the nitride is the silane flow rate. This means that a small change in the silane flow results in a large change in the nitride composition and that good control of the silane flow is required if the system is not to suffer reproducibility problems. The silane flow rate is followed closely by rf power, time, temperature, and finally nitrogen flow rate. The tables also show that the PED system is capable of depositing a wide variety of nitride film compositions. Furthermore, if a specific index

TABLE 1

RESULTS OF VARIATIONS IN NITROGEN FLOW RATES AND RF POWER UPON PED
NITRIDE, ALL OTHER PARAMETERS BEING HELD CONSTANT. SILANE FLOW -
100 sccm, TEMPERATURE - UNKNOWN, TIME 2 MIN.

<u>Nitrogen Flow</u> <u>(sccm)</u>	<u>RF Power</u> <u>(W)</u>	<u>Index</u>	<u>Thickness</u> <u>(Å)</u>
10	25	2.27	600
	50	2.24	790
	75	2.14	870
	100	2.1	830
	125	1.93	1050
15	25	2.28	550
	50	2.22	650
	75	2.06	645
	100	2.00	960
	125	1.90	1240
22	150	2.02	1020
	25	2.28	570
	50	2.17	700
	75	2.06	720
	100	1.92	1007
	125	1.97	1000
	150	1.95	1000
44	175	2.02	935
	25	2.28	600
	50	2.14	617
	75	2.08	600
	100	1.95	748
	125	1.92	800

TABLE 2

RESULTS OF VARIATIONS IN TEMPERATURE AND RF POWER UPON PED NITRIDE,
ALL OTHER PARAMETERS BEING HELD CONSTANT. SILANE FLOW - 100 sccm,
NITROGEN - 22 sccm, TIME - 2 MIN.

<u>Temperature</u> (°C)	<u>RF Power</u> (W)	<u>Index</u>	<u>Thickness</u> (Å)
100	25	2.05	600
	75	1.97	685
	125	1.90	800
150	25	2.13	480
	75	2.09	630
	125	1.95	920
200	25	2.16	510
	75	2.16	550
	125	1.92	965
250	25	2.39	530
	75	2.23	600
	125	2.04	1000
300	75	2.13	625
	125	2.02	875
350	75	2.25	805
	125	1.99	920

TABLE 3

RESULTS OF VARIATIONS IN TEMPERATURE AND SILANE FLOW RATE UPON PED NITRIDE, ALL OTHER PARAMETERS BEING HELD CONSTANT. NITROGEN FLOW - 22 sccm, RF POWER - 10 WATTS, TIME - 5 MIN.

Temperature (°C)	Silane Flow* (sccm)	Index	Thickness (Å)
155	44	1.91	725
	48	2.00	710
	52	2.10	680
210	42	1.86	815
	48	2.02	755
	54	2.02	650
255	39	1.90	845
	43	2.01	865
	48	2.08	720

* Flow Rates are for the Mixture of 2% Silane in Ar.

TABLE 4

RESULTS OF VARIATION IN RF POWER AND TIME UPON PED NITRIDE, ALL OTHER PARAMETERS BEING HELD CONSTANT. SILANE FLOW - 16 sccm, NITROGEN FLOW - 22 sccm, TEMPERATURE - 300°C.

RF Power (W)	Time (min)	Index	Thickness (Å)
20	2.5	2.01	160
	5	2.07	330
25	2.5	1.98	180
	5	2.05	360
	7.5	2.08	600
30	2.5	1.83	200
	5	1.97	425
	10	2.04	900

film is sought, the tables indicate it can be produced by several different parameter combinations. The choice of combination is dictated by the final results sought.

The modifications and procedures described in the preceding discussion on the CVD and PED encapsulation systems were guided by the necessity to minimize the surface conversion of semi-insulating GaAs during high-temperature anneals. This surface conversion results in the formation of a conductive skin on the sample surface. The skin formation is a function of both cap and material. With identical caps, different substrates convert differently and vice-versa, which made the task of establishing a viable encapsulation system doubly difficult. After processing, if electrical measurements indicated sample conversion, it was not immediately clear whether the cause was the substrate, the cap, or some combination of both. Many different deposition parameters, operating procedures, and substrate materials were investigated in the effort to eliminate the cap as a contributor to surface conversion. The success of this effort is evident by the implantation efforts which will be described later.

2.3 AUTOMATED HALL-EFFECT/SHEET-RESISTIVITY MEASUREMENT SYSTEM

Hall-effect and sheet-resistivity measurements form an important part of the characterization study of both ion-implanted and undoped semiconductors. Important information obtained by the electrical measurements include conductivity type, sheet resistivity, sheet-Hall coefficient, sheet-carrier concentration, Hall mobility, dopant profile, diffusion coefficient, compensating level, ionization energy, and effective density-of-state mass.

Single Hall-effect measurements generally are easy to carry out manually. However, a computer-controlled system becomes very useful when the process must be repeated many times and sophisticated data must be analyzed in the measurement process, such as occurs when measuring electrical dopant profiles and investigating temperature dependences. A block diagram of the automated Hall-measurement system, which was established by SRL during the present contractual period, is shown in Fig. 8. All equipment identifications in this figure are given in Table 5. Current control is affected by setting a range and percentage of range, in a constant current source, through the current control board and a D-A converter, respectively. The seven possible ranges in the K725 current source are 10^{-7} , 10^{-6} ... 10^{-1} A, and the D-A converter allows choices within a given range from 0.1 to 99.9%, in 0.1% increments. Thus, currents are available from 0.1 to 99.9 mA. Current is read by means of the digital-electrometer interface, in conjunction with the digital-electrometer control board. These latter instruments also allow control of the various digital-electrometer functions.

Each voltage contact is interfaced with an electrometer and operated as a unity-gain amplifier. To minimize the effective cable capacitances--and thus avoid long response times--the inner shield of the triaxial cable is connected to the unity-gain output of the electrometer.² The particular contact arrangement shown in Fig. 8 is the standard van der Pauw configuration.³ The voltage is read by a K6900 digital multimeter, with BCD output. The Model 55 General-Purpose Interface Bus (GPIB) provides an interface function between the DVM and the bus conforming to the IEEE Standard 488.

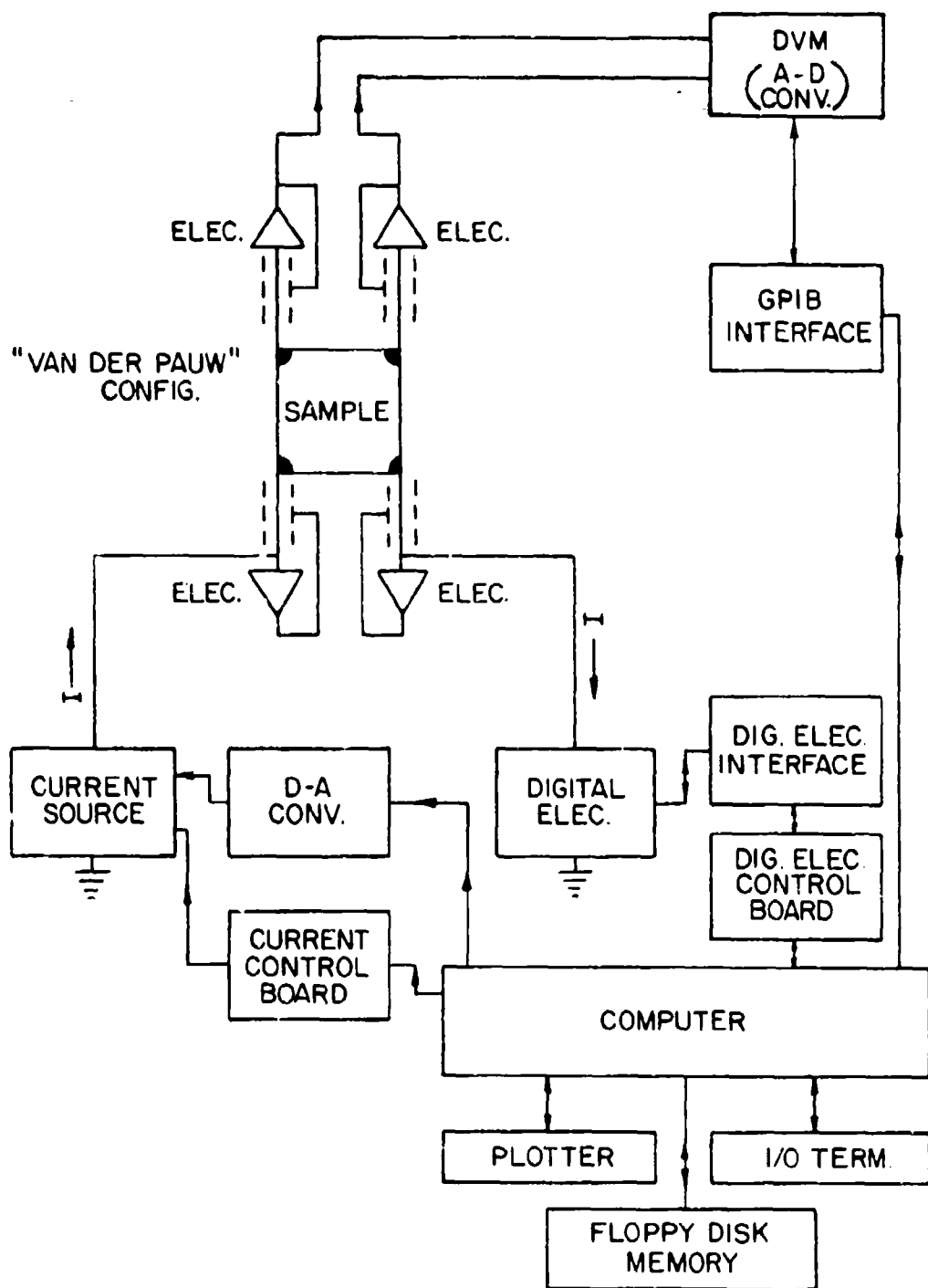


Figure 8. Block Diagram of Automated Hall-Effect/Sheet-Resistivity Measurement System.

TABLE 5

EQUIPMENT IDENTIFICATION OF AUTOMATED HALL-EFFECT/SHEET-RESISTIVITY MEASUREMENT SYSTEM. (ABBREVIATIONS: K = KEITHLEY; DEC = DIGITAL EQUIPMENT CORP.; H-P = HEWLET-PACKARD).

<u>Equipment Designation</u>	<u>Mfg. and Model No.</u>
ELEC. (Electrometer)	K610CR
DIGITAL ELEC.	K616
DIG. ELEC. INTERFACE	K6162
DIG. ELEC. CONTROL BOARD	K7901-6162 (in K790 mainframe)
CURRENT SOURCE	K725
CURRENT CONTROL BOARD	K7901-725 (in K790 mainframe)
D-A CONV. (D-A converter)	Keeco SNR 488-4
DVM (A-D CONV.)	K6900 Digital Multimeter
GPB INTERFACE	K55
COMPUTER	DEC PDP11-03 (with IEEE-488 I/O bus)
FLOPPY DISK MEMORY	DEC RXV11
I/O TERM. (I/O Terminal)	DEC LA-36
PLOTTER	H-P 9872A

For the van der Pauw configuration, four contacts are placed on the periphery of the sample. Current is passed between two of the contacts (the two electrometers are by-passed for this current mode), and the voltage difference between the other two is read. The current and voltage terminals are then switched between other pairs of contacts, and the process is repeated. Discussion of the van der Pauw method and relevant calculational equations are given in Section 3 of this report.

The central processing unit (computer) for the system is a PDP11-03 with software to control the IEEE-488 I/O bus. In general, programs have been written in the FORTRAN IV language because of its wide-spread use, and one of the programs is attached as an example (see Appendix D). The peripherals include a DEC LA36 terminal, a RXV11 dual floppy-disk system, and an HP9872A four-pen plotter. The results of measurements are calculated immediately after data are taken. An advantage of the computer is its calculational accuracy, which reduces the frequency of mistakes.

Section 3

ELECTRICAL PROPERTIES OF ION-IMPLANTED GaAs

3.1 SAMPLE PREPARATION

The substrate materials used, unless specified otherwise, were $\langle 100 \rangle$ -oriented semi-insulating Cr-doped GaAs single crystals obtained from Crystal Specialties, Inc. Prior to implantation, the samples were carefully cleaned with 10% aquasol, de-ionized water, trichloroethylene, acetone, and methanol and then dried with nitrogen gas. They were subsequently free-etched with an $\text{H}_2\text{SO}_4:30\% \text{H}_2\text{O}_2:\text{H}_2\text{O}$ solution in a 3:1:1 ratio by volume for 90 sec. Implantation was carried out at an energy of 120 keV to various ion doses at room temperature. The incident ion beam from a hot-cathode source was directed 7° off the $\langle 100 \rangle$ crystal axis to minimize ion-channeling effects. After implantation, the samples were carefully cleaned again and then encapsulated with Si_3N_4 caps either by a chemical-vapor-deposition (CVD) or an rf plasma-enhanced-deposition (PED) system. The samples were then annealed in flowing hydrogen gas for 15 min. at various annealing temperatures. After dissolution of the encapsulant in 48% hydrofluoric acid for about 3 min., an ultrasonic iron was used to make electrical indium contacts on the four corners of the square-shaped (typically 0.5 \times 0.5 cm) implanted surface. The contacts were then heated at 300°C for 3 min., unless specified otherwise, in flowing argon gas to produce ohmic behavior. Sheet resistivity of the unimplanted Cr-doped substrate capped with Si_3N_4 and annealed at 900°C varied from 10^7 to $10^5 \ \Omega/\square$.

3.2 ELECTRICAL MEASUREMENTS

Hall-effect/sheet-resistivity measurements are made using the standard van der Pauw technique³ and an apparatus which utilizes a guarded approach² with unity-gain electrometers to effectively reduce leakage currents and cable capacitance which in turn dramatically reduces the time constant of the system. A schematic diagram of the Hall-measurement system for the van der Pauw configuration is shown in Fig. 9. From measurements of a sample voltage V_c and a sample current I , the sheet resistivity r_s for a homogeneous sample is calculated using the equation

$$r_s = \frac{\pi}{\ln 2} \frac{V_c}{I}$$

From measurements of a sample current I , a Hall voltage V_H , and a magnetic field B , the sheet-Hall coefficient R_{HS} is found from the equation

$$R_{HS} = 10^8 \frac{V_H}{IB} \quad (\Omega\text{-cm}^3/\text{V}\cdot\text{sec})$$

Then the sheet-carrier concentration N_s and Hall mobility μ_H are calculated from the relations

$$N_s = \frac{r}{eR_{HS}}$$

and

$$\mu_H = \frac{R_{HS}}{r_s}$$

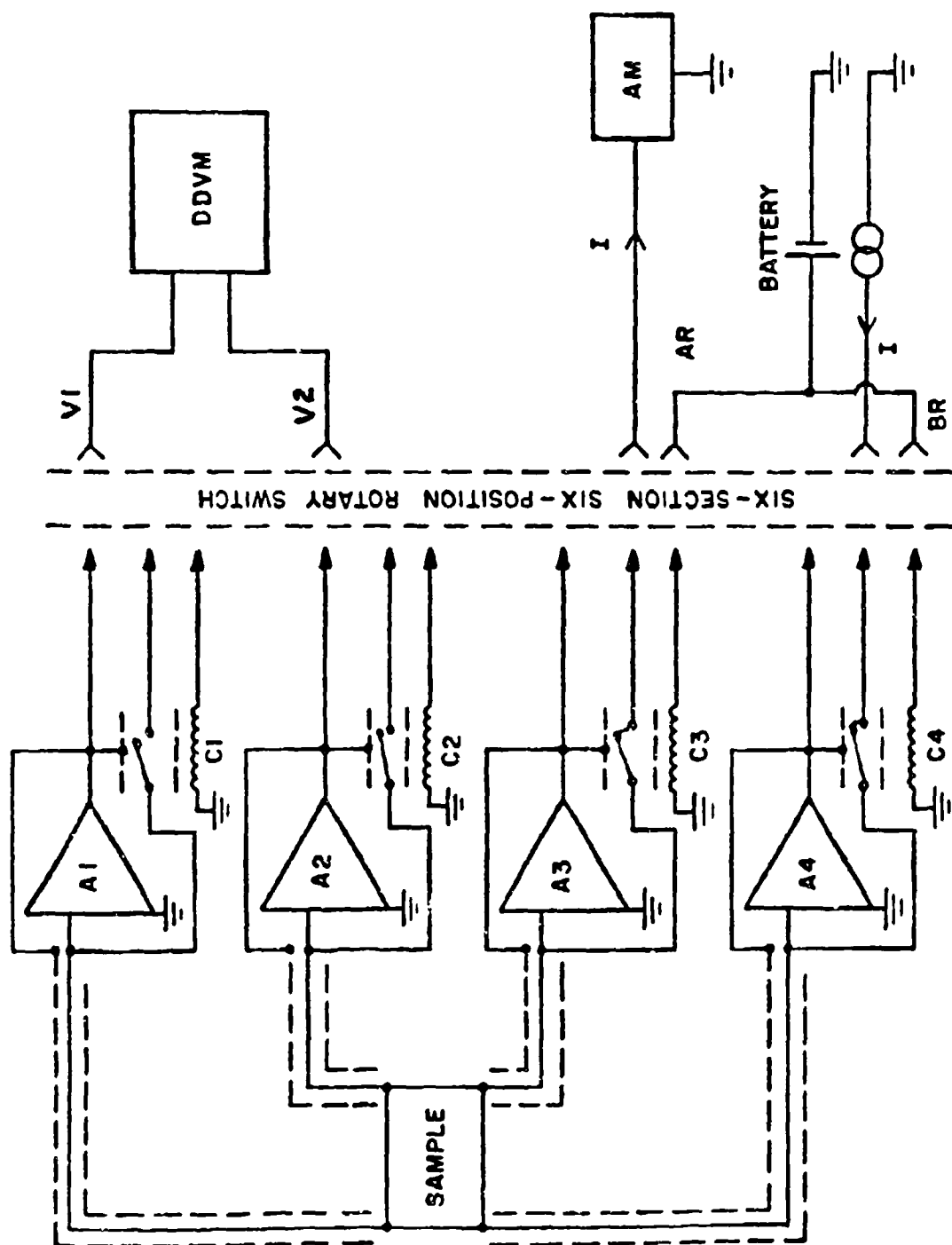


Figure 9. Schematic Diagram of the Hall-Measurement System for the van der Pauw Configuration.

where r is the Hall-to-drift mobility ratio, which is customarily taken to be unity.

Depth profiles of a carrier concentration N and a Hall mobility μ_H are accomplished by combining a layer-removal technique with the Hall and sheet-resistivity measurements. The number of carriers N_i in the i^{th} layer and their Hall mobility μ_{Hi} can be obtained from the relations^{4,5}

$$N_i = \frac{\Delta\left(\frac{1}{\rho_s}\right)_i}{e\mu_{Hi}d_i}$$

where

$$\Delta\left(\frac{1}{\rho_s}\right)_i = \frac{1}{(\rho_s)_i} - \frac{1}{(\rho_s)_{i+1}}$$

and

$$\mu_{Hi} = \frac{\Delta\left(\frac{R_{Hs}}{\rho_s}\right)_i}{\Delta\left(\frac{1}{\rho_s}\right)_i}$$

where

$$\Delta\left(\frac{R_{Hs}}{\rho_s}\right)_i = \frac{\left(\frac{R_{Hs}}{\rho_s}\right)_i}{(\rho_s)_i^2} - \frac{\left(\frac{R_{Hs}}{\rho_s}\right)_{i+1}}{(\rho_s)_{i+1}^2}.$$

In the above equations, $(R_{Hs})_i$ and $(\rho_s)_i$ are the sheet-Hall coefficient and

the sheet resistivity, respectively, which are measured after removal of the i^{th} layer with thickness d_i .

Successive thin layers of the implanted section were removed using a diluted solution of H_2SO_4 :30% H_2O_2 : H_2O in a 1:1:50 ratio by volume at 0°C . Such an etch produces uniform and damage-free surfaces. A typical etching rate is $\sim 200 \text{ \AA}/\text{min}$, as determined by a Sloan Dektak Surface Profile Measuring System.

3.3 ELECTRICAL PROPERTIES OF Mg-IMPLANTED GaAs

Measurements With CVD Si_3N_4 CAP

Be, Mg, Zn, and Cd are all known to be p-type dopants for GaAs. Many studies⁶ on the implantation of Be, Cd, and Zn into GaAs have been conducted. However, very few electrical studies have been reported for Mg-implanted GaAs; hence, details of the electrical properties are not well known. To the best of our knowledge, we presented⁷ the first published results of the measurement of carrier-concentration depth profiles on Mg-implanted GaAs. As in the case of Be, it is expected that the implanted Mg-ions penetrate more deeply into the substrate for a given ion energy than do other heavier p-type dopants for GaAs such as Zn and Cd. The dependence of surface carrier concentration and mobility upon Mg-ion dose and upon post-implantation annealing temperature has been reported^{8,9} previously. In the work of Hunsperger, *et al.*,⁸ a sputtered SiO_2 cap and n-type substrate were used, and it was found that in most cases maximum electrical activity was achieved at an annealing temperature of 800°C for the Mg-implanted sample.

and 600°C for the Be-implanted sample. In the work of Zblch, et al.,⁹ a pyrolytic SiO₂ and a sputtered Si₃N₄ cap and n-type and semi-insulating substrates have been used. As in the case of Be, reverse annealing was found at temperatures in the range 650 to 750°C for the Mg-implanted sample. Also higher electrical activation and smaller reverse annealing were found with the Si₃N₄ cap. In most investigations, SiO₂ has been widely used as an annealing cap on p-type implants in GaAs. However, pyrolytic Si₃N₄¹⁰ caps were used in the present experiment.

Implantation was carried out at an energy of 120 keV to doses ranging from 3×10^{12} to $1 \times 10^{15}/\text{cm}^2$ at room temperature. After implantation, the samples were encapsulated with an ~1500-Å layer of Si₃N₄ at ~700°C in a pyrolytic reactor for ~45 sec. After the indium contacts were made, the samples were heated at 300°C for 10 min.

The results of Hall measurements made on GaAs samples implanted with Mg to ion doses ranging from 3×10^{12} to $1 \times 10^{15}/\text{cm}^2$ and annealed at various temperatures are shown in Figs. 10 and 11. The results of sheet-carrier-concentration measurements for all doses annealed at 800°C or above agree in general with those reported by Hunsperger, et al.,⁸ except for samples having a dose of $5 \times 10^{13}/\text{cm}^2$ and annealed at 900°C, although the present results for samples annealed at 700°C show a much higher electrical activation (by a factor of ~4 for the two higher-dose samples) than those reported for annealing at 700°C. The electrical activity for the $5 \times 10^{13}/\text{cm}^2$ dose samples was reported to increase further after 900°C annealing than after 800°C annealing in the previously cited work, but the present results show a decrease in value.

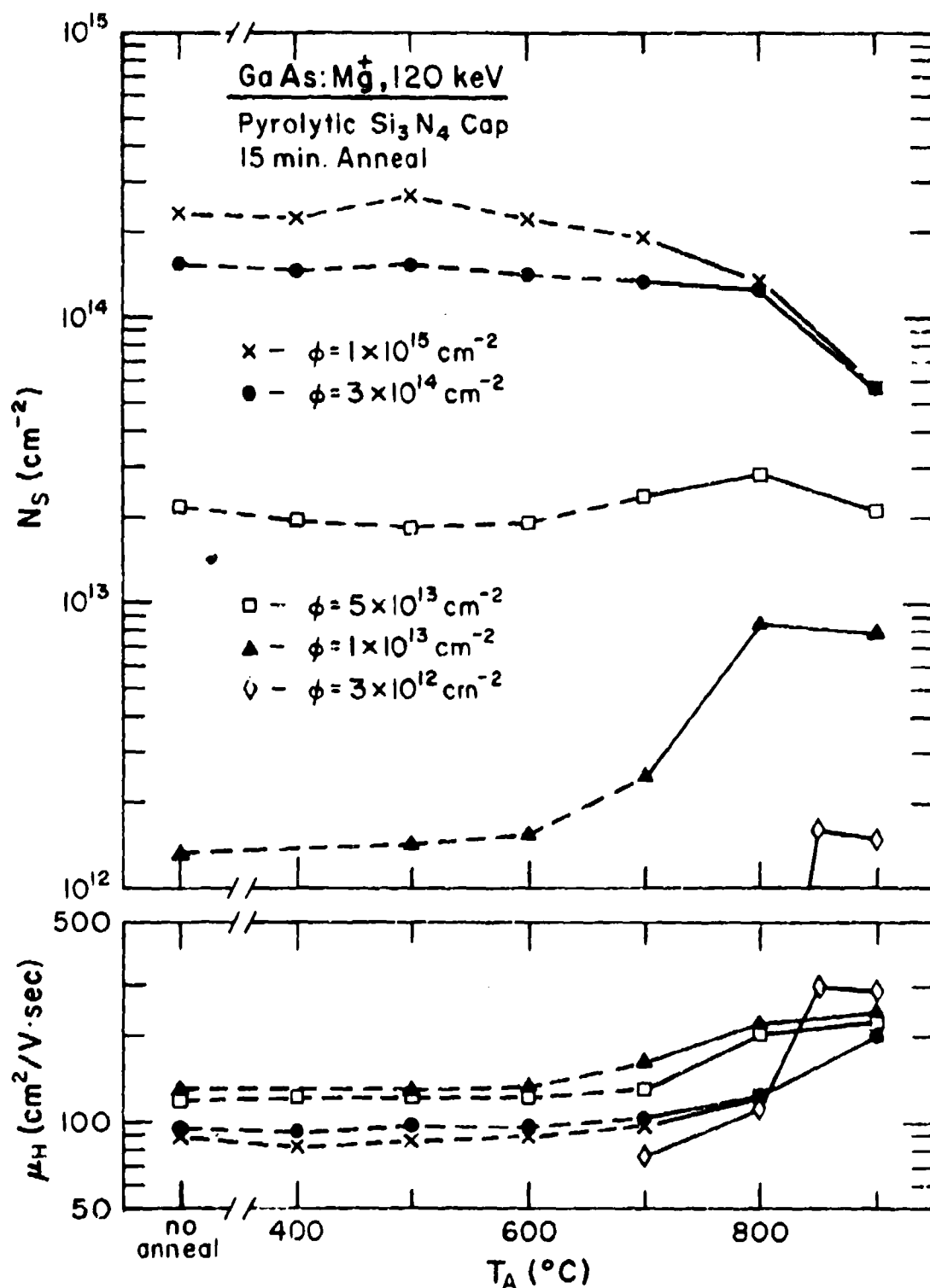


Figure 10. Dependence of Sheet-Carrier Concentration (N_S) and Hall Mobility (μ_H) upon Annealing Temperature (T_A) for GaAs:Mg Sample with CVD Si₃N₄ Cap.

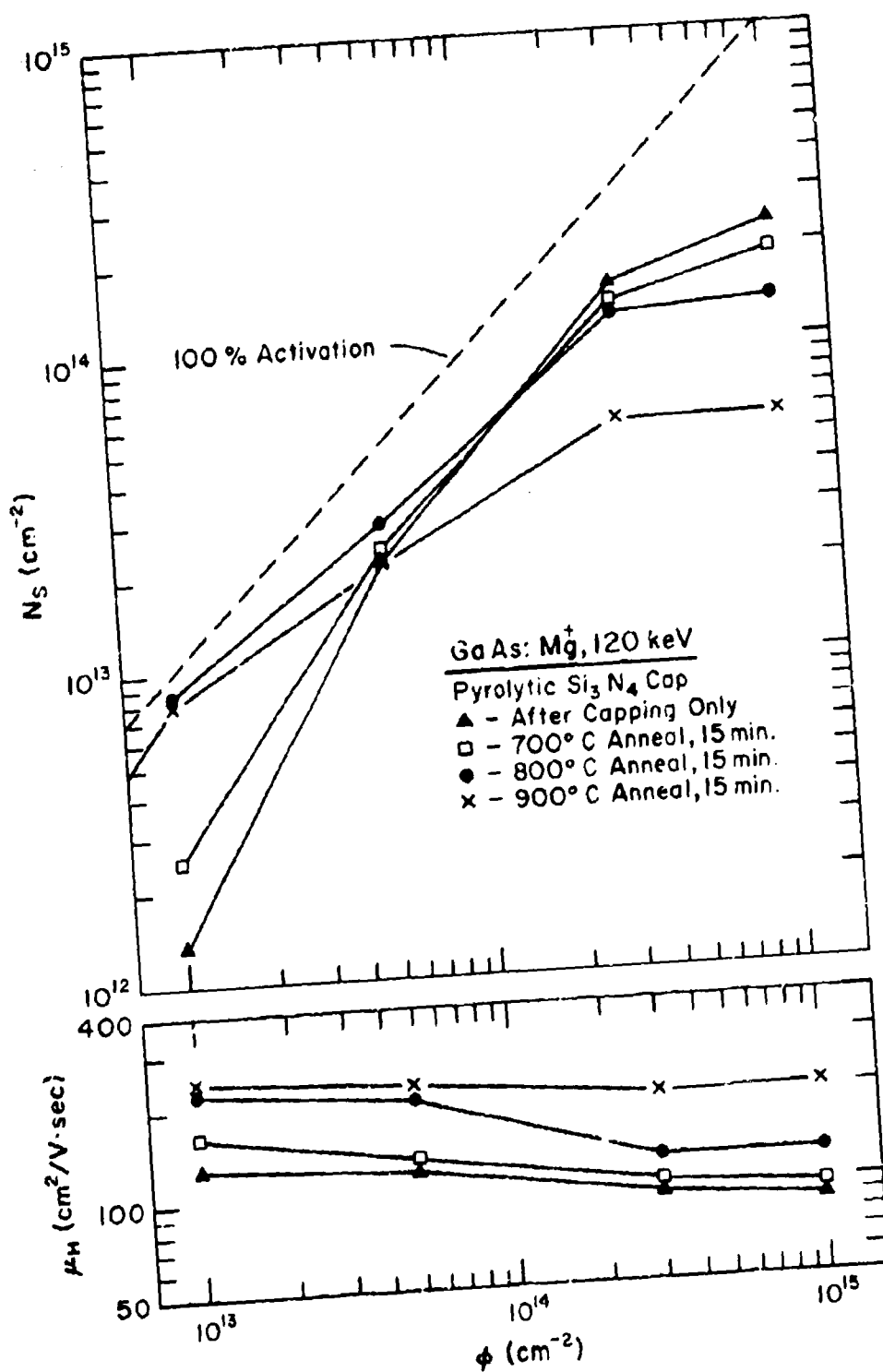


Figure 11. Dependence of Sheet-Carrier Concentration (N_S) and Hall Mobility (μ_H) upon Ion Dose (ϕ) for GaAs:Mg Samples with CVD Si_3N_4 Cap.

It has been found that for an ion dose of $\geq 5 \times 10^{13}/\text{cm}^2$, most of the electrical activation occurs during pyrolytic deposition of the Si_3N_4 cap which was accomplished at $\sim 700^\circ\text{C}$ for ~ 45 sec. The electrical-activation efficiency obtained was as high as 51% for samples having a dose of $3 \times 10^{14}/\text{cm}^2$ after capping only. This much activation in so short a capping time at 700°C is rather an unexpected result, even though the capping temperature is relatively high. No p-type layers have been observed for as-implanted samples. Neither the sheet-carrier concentration nor the mobility was altered during subsequent annealing up to 600°C , as indicated by the dashed lines in Fig. 10. For samples having an ion dose of $3 \times 10^{12}/\text{cm}^2$, the electrical activity is very poor up to 800°C , and no p-type was observed after capping only, but definite p-type conductivity became apparent at $\sim 700^\circ\text{C}$.

The annealing behavior of the sheet-carrier concentration is highly dependent upon ion dose. Also, annealing temperatures of the maximum electrical-activation efficiency increased with decreasing ion dose. For samples having an ion dose of $\leq 5 \times 10^{13}/\text{cm}^2$, the electrical activity increased with annealing temperature, yielding the highest activation at ~ 800 to 850°C , and then decreased at 900°C . The electrical-activation efficiencies obtained were as high as 85% for the sample having a dose of $1 \times 10^{13}/\text{cm}^2$ annealed at 800°C . For samples having an ion dose of $\geq 3 \times 10^{14}/\text{cm}^2$, the electrical activity decreased with increasing anneal temperature above 700°C , which is similar to the behavior reported by Zdenek, *et al.*⁹ The decrease in sheet-carrier concentration of all samples after annealing at 900°C and monotonic decrease in electrical activity with increasing annealing temperature for doses of $\geq 3 \times 10^{14}/\text{cm}^2$ can be considered to be caused by outdiffusion of Mg. The annealing temperature which produces maximum electrical activity for doses

of $\geq 3 \times 10^{14}/\text{cm}^2$ (with pyrolytic Si_3N_4 cap) could not be determined. The annealing behavior of the carrier mobility indicates that lattice damage caused by ion bombardment is reduced appreciably during capping and that the mobilities increase further with the annealing temperature for all samples. The Hall mobility, as expected, decreases with increasing fluence.

Depth profiles of hole concentrations, Hall mobilities, and compensation ratios for samples implanted to an ion dose of $3 \times 10^{14}/\text{cm}^2$ and annealed at various temperatures are shown in Fig. 12. These curves have been found to be reproducible through measurements on several samples. The Lindhard-Scharff-Schiott¹¹ (LSS) range-statistics theory predicts that peak concentrations occur at $\sim 0.124 \mu\text{m}$ for an ion energy of 120 keV. The LSS profile for a fluence of $3 \times 10^{14}/\text{cm}^2$ is also shown in Fig. 12 for comparison. The depth profiles of the hole-concentration data show the redistribution of implanted Mg impurities extending to roughly twice the projected range of the LSS theory. Furthermore, it clearly can be seen that the dopant profiles are highly dependent upon annealing temperature. The largest peak concentration of $1 \times 10^{19}/\text{cm}^2$ was found for the sample measured after capping only. However, after subsequent annealing, the peak concentration was found to decrease. Also, the position of the concentration peak shifts toward the inside of the sample. It is interesting to note that the dopant profile of the sample annealed at 600°C agrees very closely with that of the sample measured after capping only. This indicates that the 600°C anneal does not alter the electrical depth profile or the sheet-carrier concentration of the sample measured after capping only, as already pointed out.

The change in the peak-concentration magnitude and position is a complicated problem, but it can be explained by indiffusion and outdiffusion of the implanted Mg ions. For the case of the 700°C anneal, the dopant profile extends deep into the implantation damage-free region. Since the total number of hole concentrations with the 700°C anneal is about the same as that with capping only, it appears that there is very little, if any, outdiffusion of the implanted Mg after the 700°C anneal; mostly indiffusion is taking place. For the case of the 800°C anneal, it clearly can be seen from Fig. 12 that both indiffusion and outdiffusion take place in subsequent 800°C anneals. Therefore, the total number of hole concentrations has been reduced somewhat from the value with capping only. For the case of the 900°C anneal, both indiffusion and outdiffusion take place more dramatically; hence, the position of the peak concentration shifts toward the inside of the sample; also, the electrical-activation efficiency drops sharply as shown in Fig. 10.

Since the measured Hall mobility is in the range of 80 - 250 cm²/V·sec., ionized-impurity scattering must be an important effect. Therefore, the degree of electrical compensation has been analyzed using the Brooks-Herring¹² formula for ionized-impurity scattering,

$$\mu_I \text{ (cm}^2\text{/V·sec)} = 3.29 \times 10^{15} \frac{T^{3/2} \epsilon^2}{N_I} \left(\frac{m^*}{m_0}\right)^{-1/2} \left[\ln(1+Z) - \frac{Z}{1+Z} \right]$$

where $Z = 1.29 \times 10^{14} \frac{\epsilon T^2}{p} \left(\frac{m^*}{m_0}\right)$, μ_I is the ionized-impurity mobility in cm²/V·sec, N_I is the total ionized-impurity concentration in cm⁻³, T is the absolute temperature, ϵ is the relative dielectric constant ($\epsilon = 12.91$ for GaAs in static limit), m_0 is the rest electron mass in grams, m^* is the

effective mass in grams ($\frac{m^*}{m_0} = 0.5$ was taken for a hole in GaAs), and p is the measured carrier concentration. In this analysis, it is assumed that only lattice and ionized-impurity scattering are important. Then the ionized-impurity scattering mobility (μ_I), can be expressed as

$$\frac{1}{\mu_I} = \frac{1}{\mu} - \frac{1}{\mu_L},$$

where μ is the measured mobility in each stripped layer, the μ_L is the lattice-scattering mobility. The value of μ_L has been chosen as $450 \text{ cm}^2/\text{V}\cdot\text{sec}$ for the present analysis. From the computed value of μ_I , the value of N_I has been calculated in each stripped layer. Furthermore, the donor concentration (N_D) and acceptor concentration (N_A) have been determined from the relations

$$N_I = p + 2N_D \text{ and } P = N_A - N_D.$$

The ratio of donor-to-acceptor concentration is defined as $K = N_D/N_A$, which represents the degree of compensation.

Mobility profiles are also shown in Figs. 12 and 13. Except for the 900°C annealing case, the hole mobility is, in general, initially higher near the surface, gradually decreases to the region of the maximum hole concentration, and then increases with the decrease in hole concentration. The reduction of hole mobility near the peak hole concentration can be explained by hole scattering which is caused by the greater number of ionized impurities near the peak hole concentration. (An illustration of the ionized-impurity

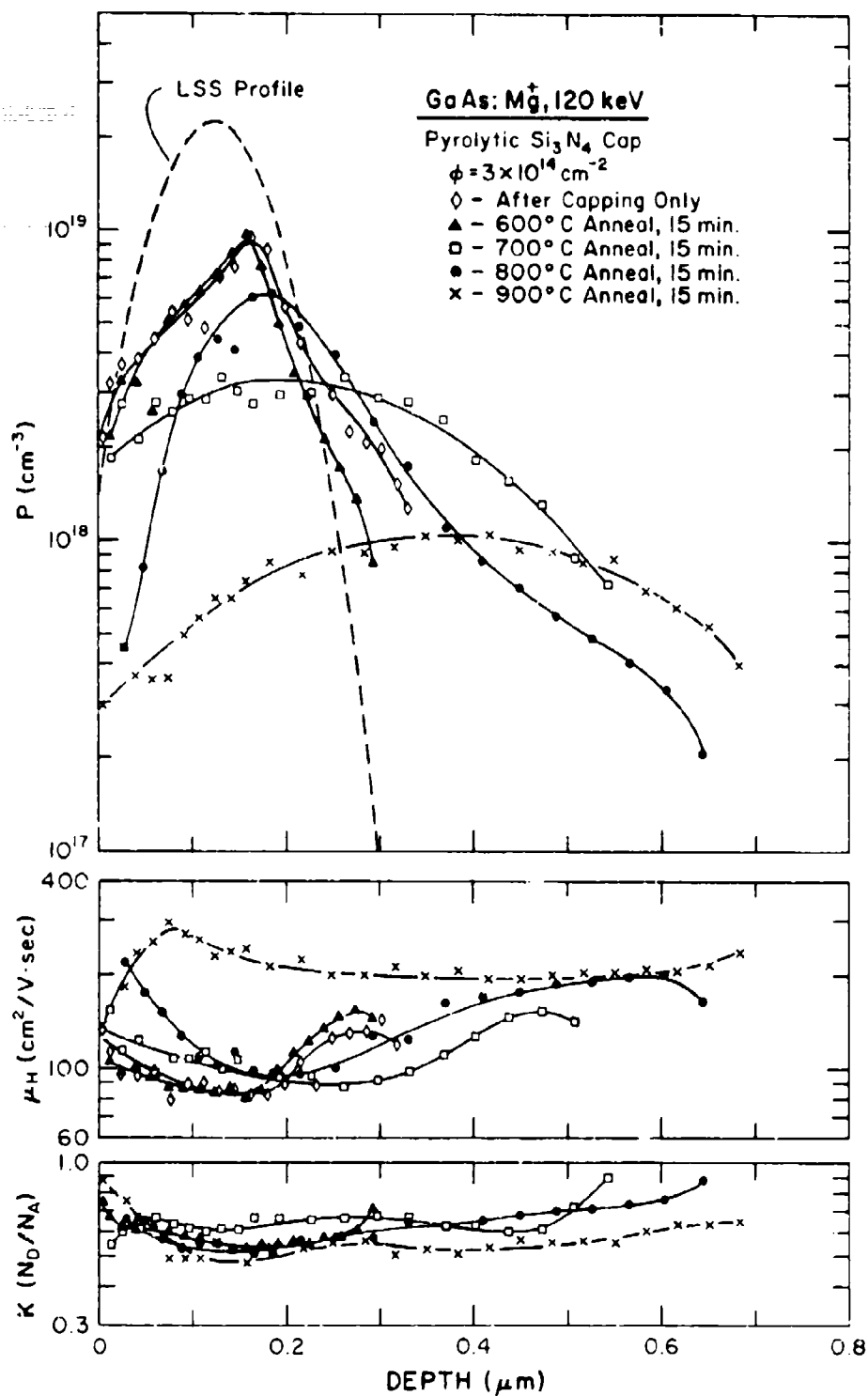


Figure 12. Dependence of Electrical Depth Profile upon Annealing Temperature for GaAs:Mg Samples with CVD Si₃N₄ Cap.

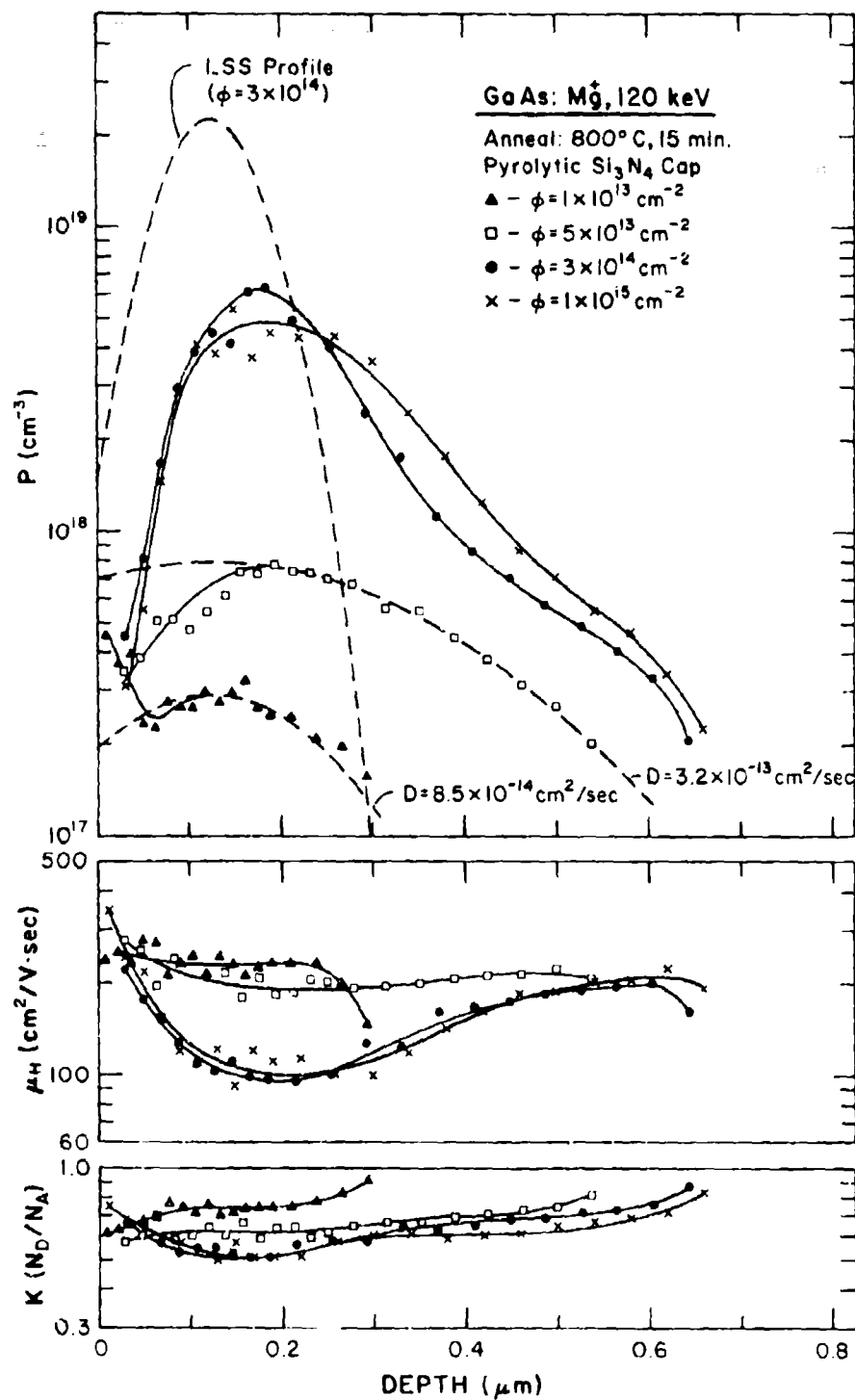


Figure 13. Dependence of Electrical Depth Profile upon Ion Dose for GaAs:Mg Samples with CVD Si₃N₄ Cap.

concentration is given in Fig. 14, and a detailed discussion will be given later). However, the mobility profile of the sample annealed at 900°C is quite different from the others. It can be seen that the hole mobility decreases sharply near the surface from the bulk value of mobility which is about $200 \text{ cm}^2/\text{V}\cdot\text{sec}$. This indicates that another scattering mechanism exists in this sample in addition to the two dominant scatterings, i.e., lattice and ionized-impurity scatterings. This scattering may be due to lattice defects such as dislocations and precipitates present at or near the surface region.

Figure 13 shows the depth profiles of hole concentrations, Hall mobilities, and compensation ratios for samples implanted to various ion doses and annealed at 800°C. Theoretical diffusion profile curves are also depicted in dashed lines for the two lower-dose samples. The LSS profile for a fluence of $3 \times 10^{14}/\text{cm}^2$ is shown for comparison purposes. The depth profiles of the hole-concentration data show that the implanted Mg impurities are redistributed from the original implant for all doses and also that the dopant profiles are highly dependent upon dose. The position of the peak hole concentration for a dose of $\geq 5 \times 10^{13}/\text{cm}^2$ occurs at a slightly different position from that predicted by the LSS theory, and this is not dependent upon dose. On the other hand, the peak position of a $1 \times 10^{13}/\text{cm}^2$ dose agrees with that of LSS theory. The shift in peak-concentration position is believed to be due to indiffusion and outdiffusion as explained earlier. Further diffusion analysis has been performed using the equation¹³

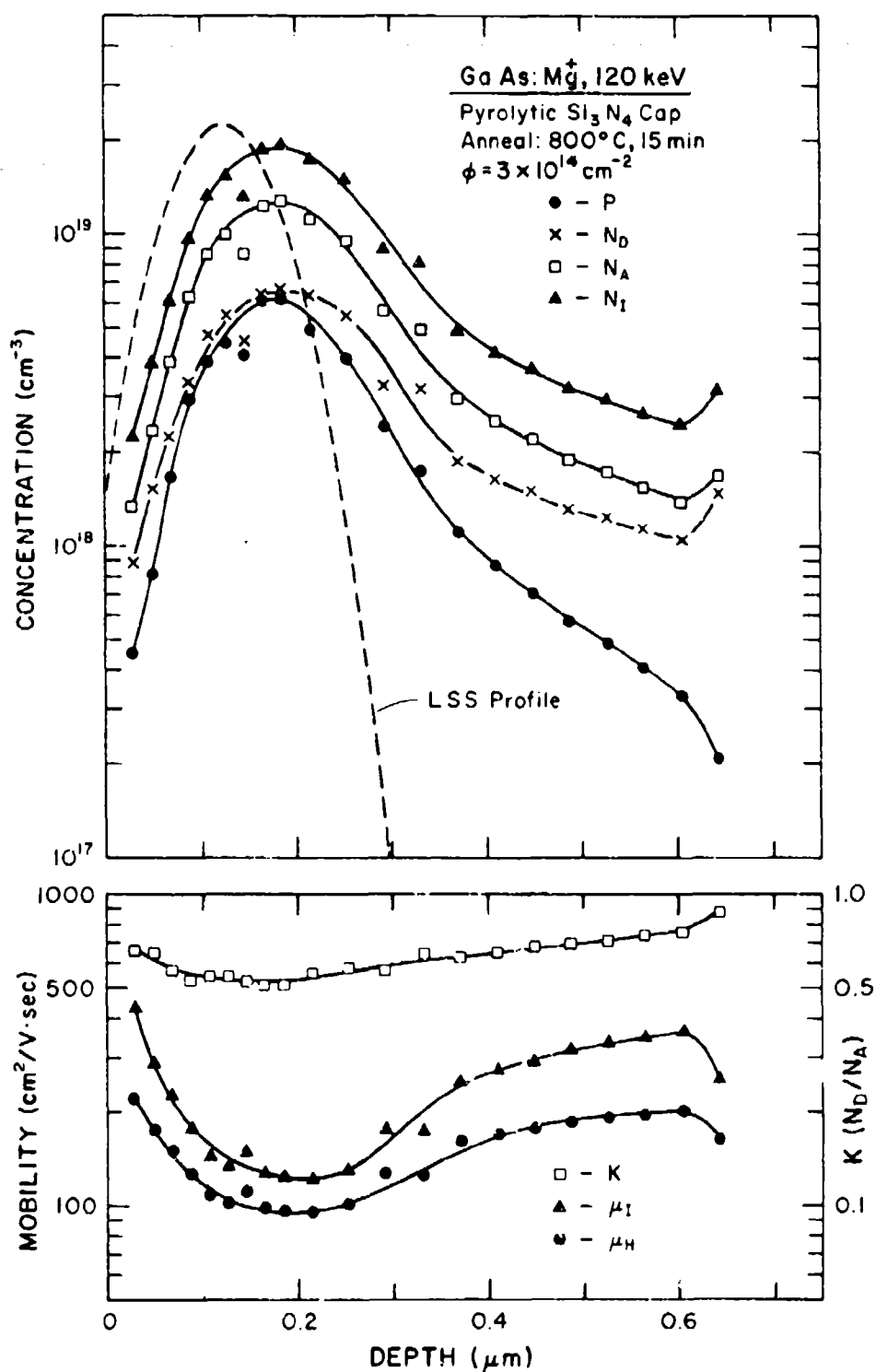


Figure 14. Depth Profiles of Hole, Acceptor, Donor, and Ionized-Impurity Concentrations for GaAs:Mg.

$$n(x_p, t) = \frac{\phi}{\sigma_p \sqrt{2\pi} \left(1 + \frac{4Dt}{\sigma_p^2}\right)^{1/2}} \exp \left[-\frac{(t_p - R_p)^2}{(2\sigma_p^2 + 4Dt)} \right], \quad (1)$$

where $n(x_p, t)$ is the carrier concentration ($1/\text{cm}^3$) at a given depth (x_p) and anneal time (t), ϕ is an implanted-ion dose ($1/\text{cm}^2$), σ_p is the standard deviation, R_p is the projected range, and D is the diffusion coefficient. As shown in Fig. 13, the depth profiles of the two lower-dose samples roughly follow the theoretical diffusion profiles with values of 3.2×10^{13} and $8.5 \times 10^{14} \text{ cm}^2/\text{sec}$ for doses of $5 \times 10^{13}/\text{cm}^2$ and $1 \times 10^{13}/\text{cm}^2$, respectively. These values are about the same order of magnitude as those found by Zölch, et al.⁹ For a dose of $5 \times 10^{13}/\text{cm}^2$, it appears that most Mg ions near the surface have disappeared by outdiffusion. However, for a dose of $1 \times 10^{13}/\text{cm}^2$, it appears that most Mg ions remain within the sample after diffusion, exhibiting some build-up of Mg near the surface. For a dose $\geq 3 \times 10^{14}/\text{cm}^2$, the complicated indiffusion and outdiffusion of Mg makes it difficult to analyze the depth profiles quantitatively by means of the simple Gaussian diffusion equations. However, it is interesting to note that the depth profile of a $1 \times 10^{15}/\text{cm}^2$ dose follows very closely that of a $3 \times 10^{14}/\text{cm}^2$ dose. The comparison of the two depth profiles indicates that the diffusion is more severe for higher doses.

Figure 14 shows the depth profiles of hole, acceptor, donor, and ionized-impurity concentrations for the sample having an ion dose of $3 \times 10^{14}/\text{cm}^2$ and annealed at 800°C . Also shown are the compensation ratio, impurity-mobility, and Hall-mobility depth profiles. Similar curves have been obtained for all

other profiled samples when two scattering (lattice and ionized-impurity scattering) mechanisms are assumed. In general, the compensation ratio ranges from 0.5 to 0.8 for all samples profiled as shown in Figs. 12 and 13, as expected from the implanted samples. Since (as shown in Figs. 10 and 11) the electrical activation is generally high (as much as 85% for the sample having a dose of $1 \times 10^{13}/\text{cm}^2$ and annealed at 800°C) and no other significant acceptors have been found in the substrates after annealing at 800 or 900°C , it is evident that the acceptors in the implanted layer are mainly due to implanted Mg ions.

The compensation level of 0.5 - 0.8 indicates that a considerable number of compensating donors are present in the implanted layer. Mass-spectroscopic analysis of the Cr-doped substrate showed the probable donor (mainly Si) concentration to be equal to or less than $3 \times 10^{16}/\text{cm}^3$. Even though all the silicon ions act as donors, it is difficult to explain the total number of donors observed in the implanted and annealed layers. Therefore, it is suspected that the compensating donors may be of two types, i.e., donors present originally in the substrate itself and additional donors formed during the annealing process. If these donors originate from the annealing process (for example, Si_3N_4 cap or heat treatment), the number of donors must be the same for all samples capped and annealed at the same time. However, this is not the case, and it has been found that the donor concentration varies significantly from sample to sample, depending upon the implanted ion dose. Therefore, it can be concluded that most additional donors are of an intrinsic nature. Since Mg can occupy Ga sites, an excess of arsenic vacancies can be expected to form. Therefore, As vacancies can be thought of as the main source of donors present in Mg-implanted layers.

Measurements With PED Cap

Electrical studies described above were carried out with a pyrolytic Si_3N_4 cap as a protective dielectric layer. It was pointed out that for ion doses of $2.5 \times 10^{13}/\text{cm}^2$, most of the electrical activation occurred during pyrolytic deposition of the Si_3N_4 cap, which was carried out at $\sim 700^\circ\text{C}$ for ~ 45 sec. Neither the sheet-carrier concentrations nor the mobilities were altered appreciably during subsequent annealing up to 700°C . Therefore, the annealing behavior of Mg-implants in GaAs at lower temperature (below $\sim 700^\circ\text{C}$) could not be observed. In the following work,¹⁴ a thorough study of the electrical properties of Mg implants in GaAs has been carried out with an rf plasma-deposited Si_3N_4 cap. Surface-carrier concentration has been measured at a temperature as low as 600°C for a wide range of implanted doses.

Implantation was carried out at an energy of 120 keV to doses ranging from 1×10^{13} to $3 \times 10^{15}/\text{cm}^2$ at room temperature. After implantation, the samples were encapsulated on both sides of the samples with an $\sim 700\text{-\AA}$ layer of Si_3N_4 , which was rf-plasma deposited at $\sim 220^\circ\text{C}$ for ~ 10 min. Unimplanted Cr-doped substrates capped with plasma-deposited Si_3N_4 and annealed at 850°C for 15 min. exhibited a sheet of resistivity of $\sim 10^7 \Omega/\square$.

The results of Hall-effect/sheet-resistivity measurements made on GaAs samples implanted with Mg ions to doses ranging from 1×10^{13} to $3 \times 10^{15}/\text{cm}^2$ and annealed at temperatures ranging from 600 to 750°C are shown in Fig. 15. Detailed annealing behavior of the sheet-carrier concentrations clearly revealed that the electrical activation increased monotonically with annealing temperature up to 750°C and the maximum electrical activation occurred at

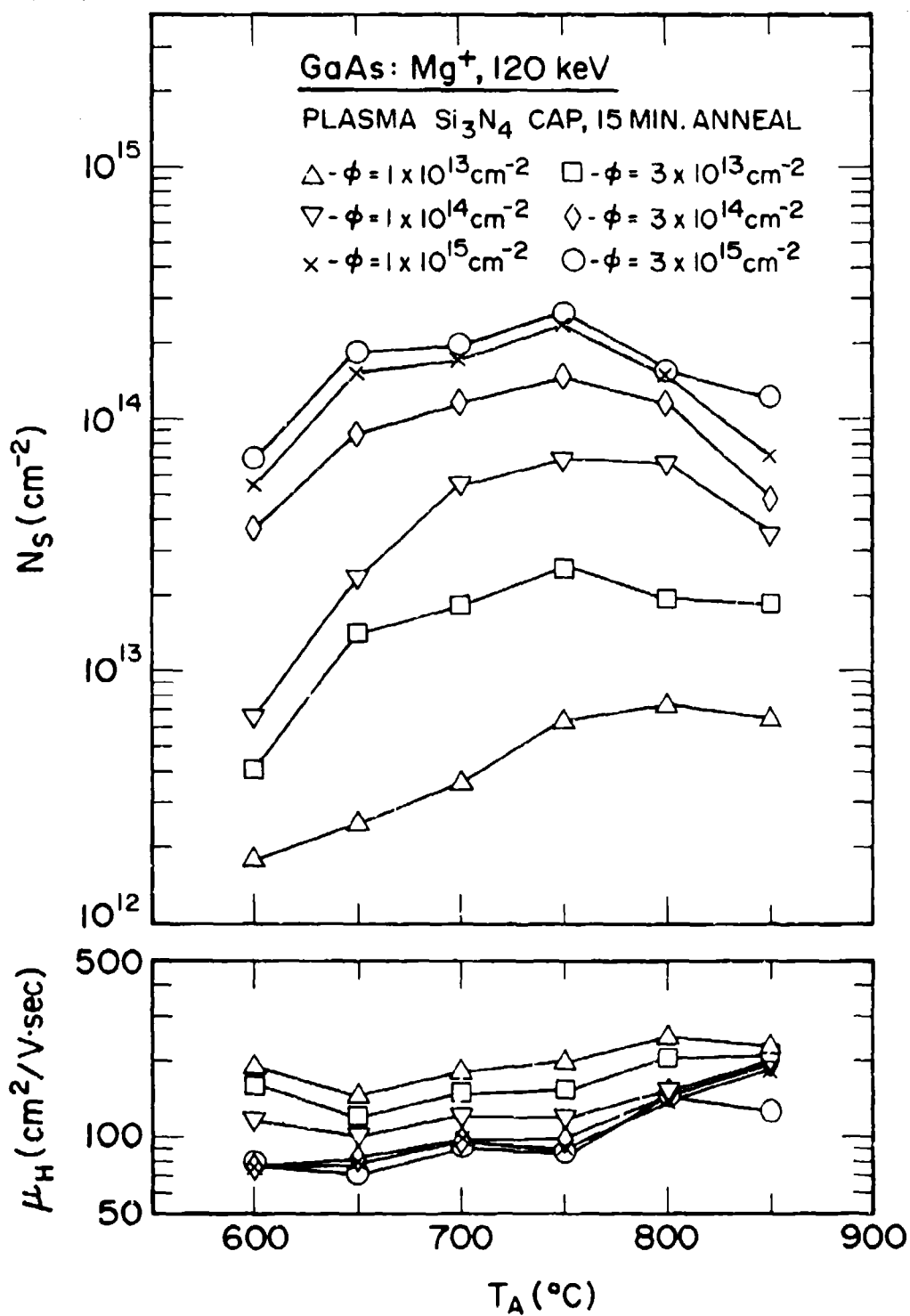


Figure 15. Dependence of Sheet-Carrier Concentration (N_s) and Hall Mobility (μ_H) upon Annealing Temperature (T_A) for GaAs:Mg Samples with PED Si₃N₄ Cap.

750°C for all except the lowest dose of $1 \times 10^{13}/\text{cm}^2$, for which the maximum activation occurred at 800°C. The maximum activation efficiency obtained was as high as 85% for the sample implanted to a dose of $3 \times 10^{13}/\text{cm}^2$ and annealed at 750°C. The electrical activation then decreased monotonically with increasing annealing temperature possibly due to outdiffusion of Mg, which will be discussed later. The annealing behavior of the sheet-carrier concentration generally agreed well with the above result obtained at an annealing temperature of 700°C or above. However, our results showed significantly higher electrical activation (as high as one order of magnitude) for the samples annealed at 700°C or below than that reported by Hunsperger, *et al.*,⁸ and also generally much higher activation (by a factor of ~ 2) for the samples annealed at all temperatures than that reported by Zölch, *et al.*⁹ In our work further study has been made of the annealing behavior of Mg implants in GaAs with different annealing times but at the same annealing temperature of 750°C. Significant electrical activation was achieved after annealing the samples for a short time. The electrical-activation efficiency obtained was as high as 53% for the sample implanted to a dose of $1 \times 10^{14}/\text{cm}^2$ after annealing for only 2 min. at 750°C. The activation increased further with annealing time and 82% activation was obtained after annealing for 30 min at 750°C.

The annealing behavior of carrier mobilities indicates that lattice damage caused by ion bombardment is reduced appreciably even at an annealing temperature of 600°C and that mobilities increase with annealing temperature. This damage recovery with increasing annealing temperature is more evident for the higher ion-dose samples.

Electrical depth profiles of hole concentrations and Hall mobilities for samples implanted to various ion doses and annealed at 750°C are shown in Fig. 16. In the profile measurements, an annealing temperature of 750°C was chosen specifically because the maximum electrical activation occurred at this temperature. The theoretical LSS profile for an ion dose of $1 \times 10^{14}/\text{cm}^2$ is also shown in this figure for comparison purposes. It clearly can be seen from the figure that the depth profiles of the hole concentrations are highly dependent upon dose. Furthermore, the dopant-profile data show a significant redistribution of Mg ions for the samples having an ion dose of $1 \times 10^{14}/\text{cm}^2$ or above.

The changes in the position of the peak concentration and magnitude represent complicated problems. In general, the profile peaks occur at three different positions--one at the LSS peak position, one near the surface, and the other at the inner side of the sample. For an ion dose of $3 \times 10^{13}/\text{cm}^2$ or below, the carrier concentration is high near the surface, with the peak position at $\sim 0.08 \mu\text{m}$. Most Mg ions remain in the implanted region for these lower doses. For a dose of $1 \times 10^{14}/\text{cm}^2$, the peak concentration occurs at the position predicted by LSS theory. The profile initially follows closely the theoretical curve near the surface, then becomes considerably flat in most of the implanted region, and shows a long tail indicating significant indiffusion at this dose.

For doses of $3 \times 10^{14}/\text{cm}^2$ or above, the dopant profile is much more complicated, and two distinct carrier-concentration peaks have been observed--one near the surface ($0.05 \mu\text{m}$) and the other at the deeper side of the sample ($\sim 0.18 \mu\text{m}$). The double peaks occurred nearly at the same position for the

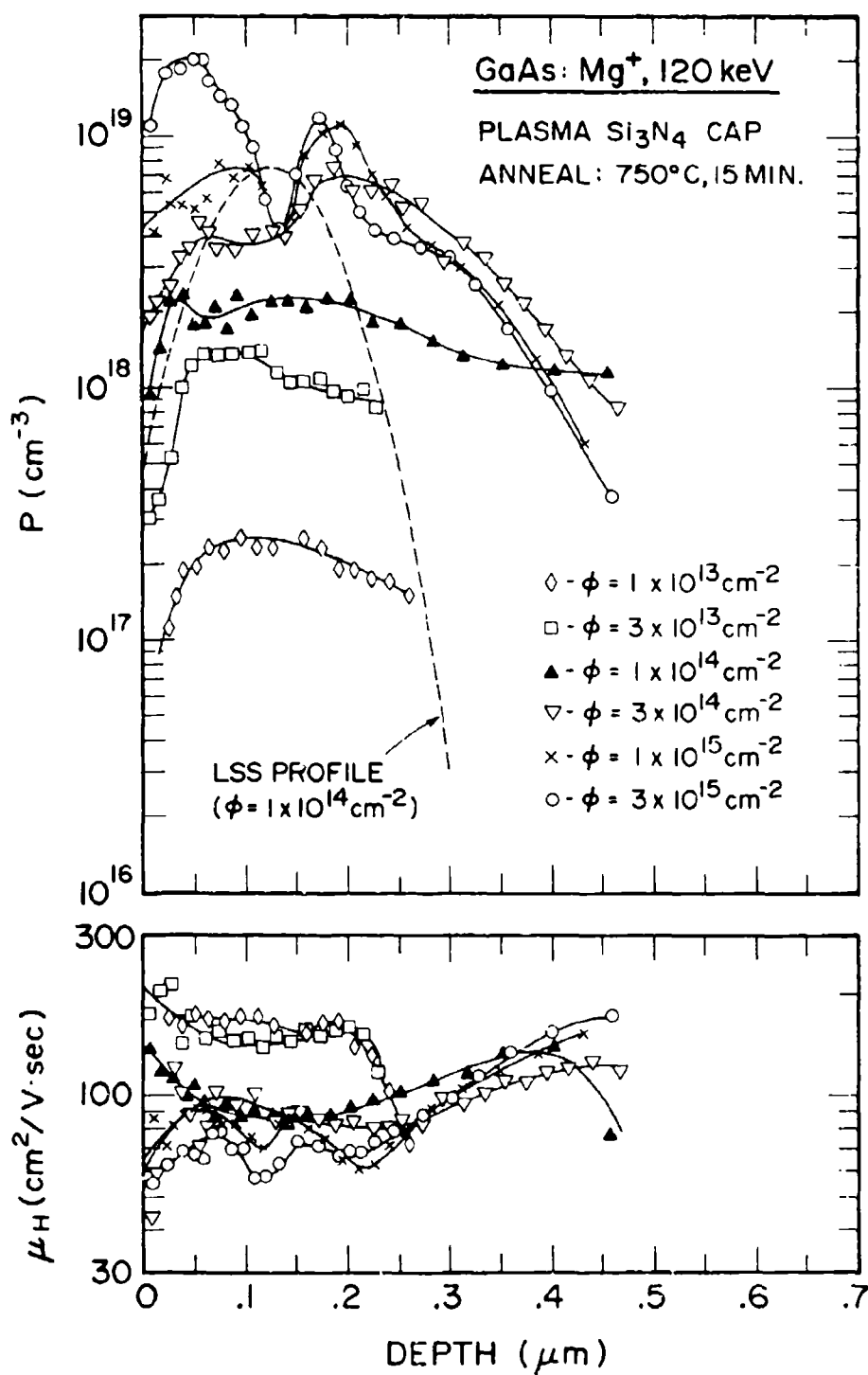


Figure 16. Dependence of Electrical Depth Profile upon Ion Dose for GaAs:Mg Samples with PED Si₃N₄ Cap.

three higher doses; also the profile tails are nearly independent of dose. These double peaks begin to appear at a dose of $1 \times 10^{14}/\text{cm}^2$, and the peaks are more pronounced as the dose level increases. The carrier concentration at the first peak position is smaller than that at the second peak position for a dose of $3 \times 10^{14}/\text{cm}^2$; the double peaks are much clearer for a dose of $1 \times 10^{15}/\text{cm}^2$; and finally the concentration at the first peak becomes much greater than that at the second peak for a dose of $3 \times 10^{15}/\text{cm}^2$. The maximum carrier concentration obtained was $2 \times 10^{19}/\text{cm}^3$ for a dose of $3 \times 10^{15}/\text{cm}^2$. Moreover, a local minimum rather than a maximum has been produced at the LSS peak position. It can be speculated that the local minimum observed near the LSS peak position for these higher doses may be due to the Cr redistribution and/or the implantation damage remaining at this relatively low annealing temperature. Preliminary data of SIMS analysis shows that a significant redistribution of Cr occurs in the implanted region after annealing at 750°C for Mg ion doses $\geq 1 \times 10^{14}/\text{cm}^2$.

The mobilities for the doses of $3 \times 10^{13}/\text{cm}^2$ or below are much higher throughout the implanted region than the mobilities for the higher doses, until they finally decrease near the substrate region. The mobilities for doses of $\geq 3 \times 10^{14}/\text{cm}^2$ also exhibit more complicated structures than those for the lower doses, which exhibit mobility peaks and valleys. The mobilities are generally lower ($<100 \text{ cm}^2/\text{V}\cdot\text{sec}$) throughout most of the implanted region, except well inside the sample, where they increase monotonically. These low values of mobility may be due to the remaining implantation damage as well as to the electrically inactivated Mg ions (activation efficiency is 46% for a dose of $3 \times 10^{14}/\text{cm}^2$) at an annealing temperature of 750°C , even though the activation is at a maximum at this temperature.

Depth profiles of the carrier concentrations and Hall mobilities for samples implanted to an ion dose of $1 \times 10^{14}/\text{cm}^2$ and annealed at various temperatures are shown in Fig. 17. The LSS profile for a fluence of $1 \times 10^{14}/\text{cm}^2$ is also shown for comparison purposes. It clearly can be seen that the dopant and mobility profiles are highly dependent upon annealing temperature. The redistribution of implanted Mg ions takes place well into the damage-free region at an annealing temperature of 750°C or above. However, the position of the maximum carrier concentration agrees well with that of the LSS peak for the samples annealed at 650, 750, and 850°C.

For the case of the 650°C anneal, it has been found that the dopant profile agrees well with the proportionally reduced LSS profile (by a factor of ~ 4) in most of the implanted region except for the deeper region near the substrate. This reduced factor of ~ 4 is equivalent to the electrical-activation efficiency of 24% for this sample. This may suggest that most of the implanted Mg ions remain as implanted but that only an equal fraction of the implanted ions become activated at 650°C; there seems to be no major loss of Mg due to outdiffusion. The profile also indicates that the implanted ions are activated considerably more in the deeper side of the sample at this annealing temperature. For the case of the 700°C anneal, the profile follows very closely the LSS profile near the surface region, and the concentration peak occurs close to the surface. Most activated Mg ions remain in the implanted region, and there is no evidence of indiffusion at this annealing temperature, which is in contrast to the results obtained using pyrolytic caps. It is interesting to note that the carrier concentrations in the peak region are higher than those of the samples annealed at 750°C. For the case of the 750°C anneal, the profile initially follows the theoretical curve

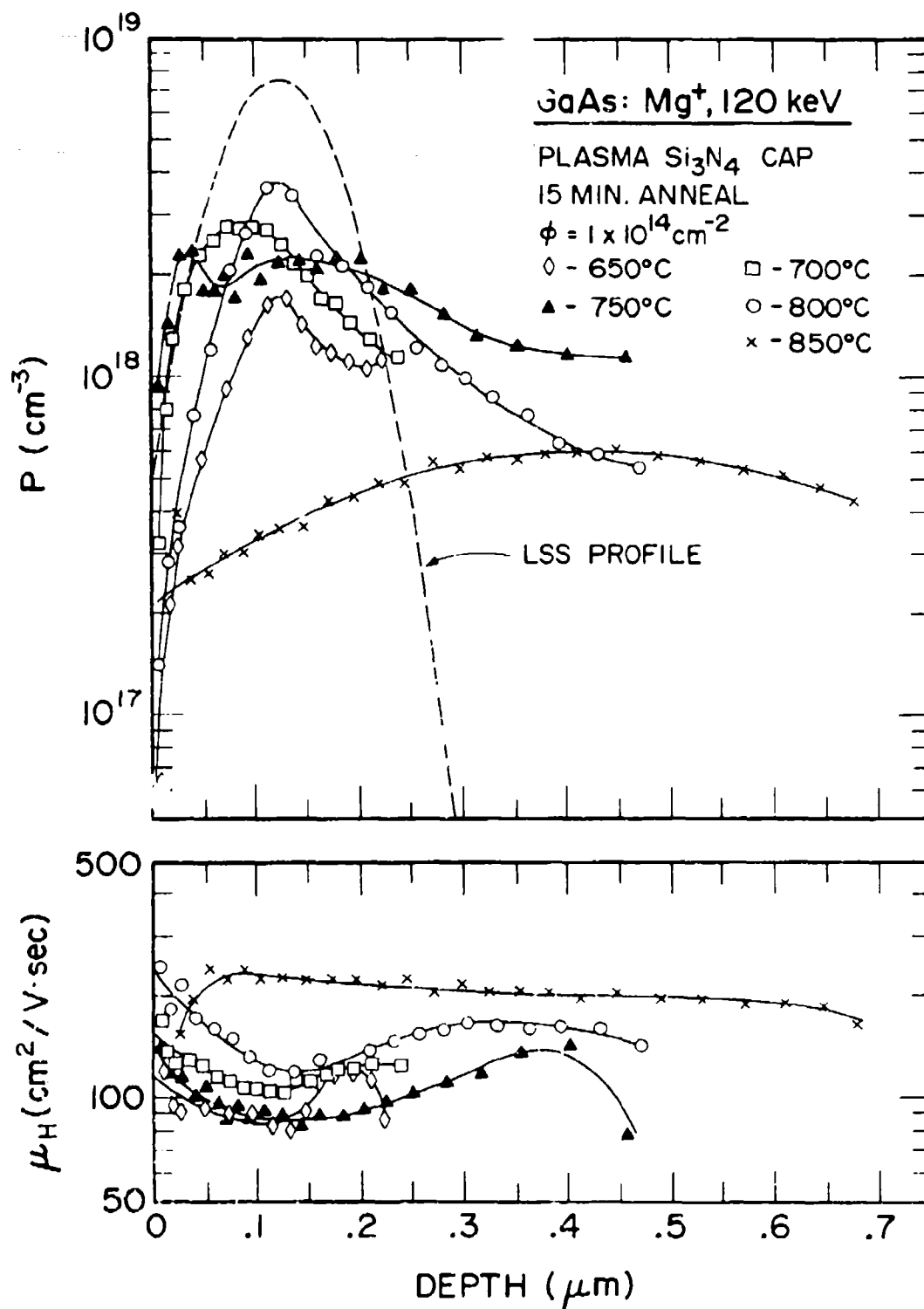


Figure 17. Dependence of Electrical Depth Profile upon Annealing Temperature for GaAs:Mg Samples with PED Si₃N₄ Cap.

closely; then it is nearly flat in the implanted region, and it exhibits significant indiffusion into the bulk of the sample. For the case of the 800°C anneal, a more pronounced peak has been observed along with a long indiffusion tail. Evidently both outdiffusion and indiffusion take place at this annealing temperature. The variations in profiles for the 700, 750, and 800°C anneals cannot be adequately explained at present. However, similar behavior was observed in the above measurement with CVD caps. For the case of the 850°C anneal, the profile is very flat, extending very deeply into the sample. This and the sharp drop in electrical activation efficiency indicate that both outdiffusion and indiffusion are very significant at this annealing temperature.

In general, the mobility values are higher near the surface, decrease gradually with increasing carrier concentration, and then increase gradually until they decrease again near the substrate region at all annealing temperatures except 850°C. For the case of the 850°C anneal, the mobility profile is quite different from the others. The Hall mobility is much lower near the surface than the bulk value of mobility ($200 \text{ cm}^2/\text{V}\cdot\text{sec}$) and this may be due to lattice defects such as dislocations and Mg precipitates which result from annealing at high temperature.

Depth profiles of hole concentrations and mobilities for samples implanted to an ion dose of $3 \times 10^{15}/\text{cm}^2$ and annealed at 750°C for different annealing times are shown in Fig. 18. The double-peak structures were observed for the three annealing times, and the profiles were found to be highly dependent upon annealing time. It is interesting to note that the profile of a 15-min. anneal is quite different than that of a 2-min. anneal throughout most

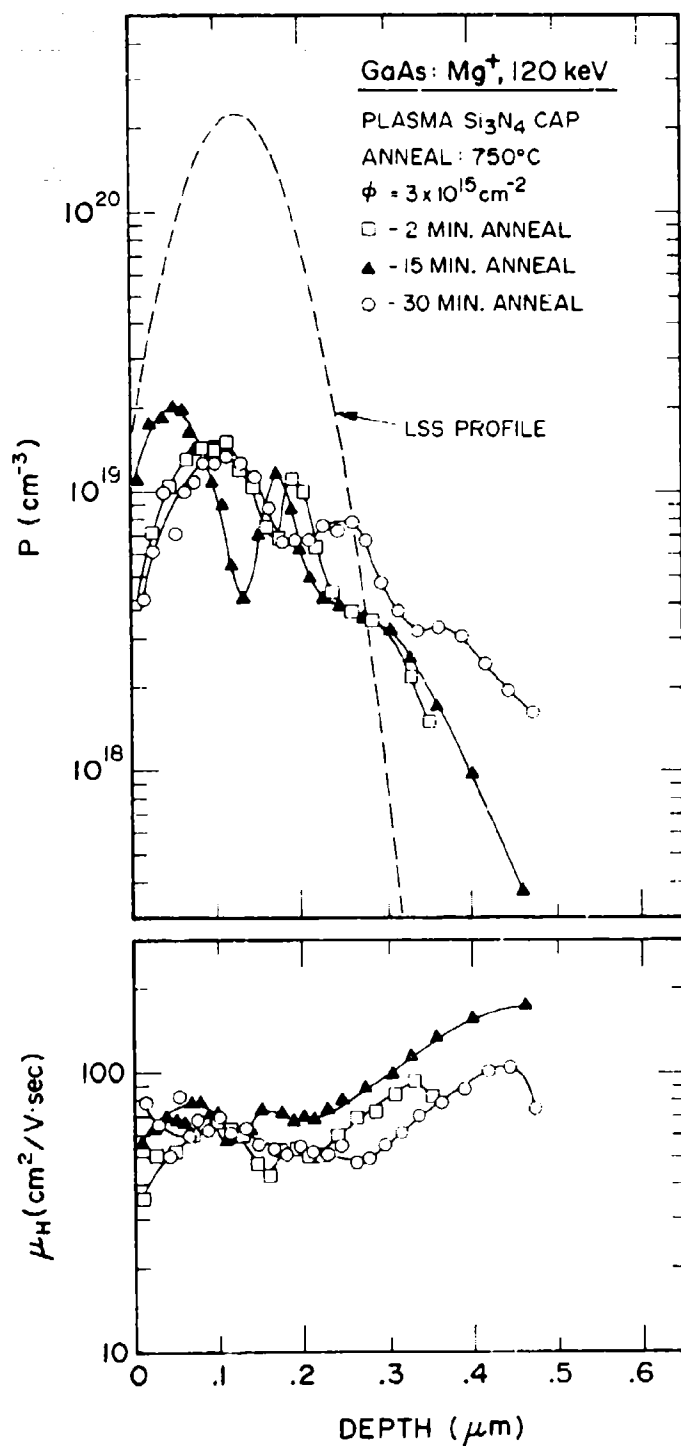


Figure 18. Dependence of Electrical Depth Profile upon Annealing Time for GaAs:Mg.

of the implanted region; however, the profiles closely resemble each other at the deeper side of the sample. On the other hand, the profile of a 30-min. anneal closely resembles that of a 2-min. anneal throughout most of the implanted region; however, the profile of a 30-min. anneal shows more indiffusion with a smaller secondary peak. It is also worthwhile to mention that the electrical-activation efficiency obtained was 9.2, 9.4, and 10.0% for 2-, 15- and 30-min. anneals, respectively. This indicates that most of the electrical activation occurs even after annealing for only 2 min. and that the activation does not increase significantly as the annealing time increases.

Measurements With Laser Annealing

Thus far, only thermal annealing has been discussed as a method to remove implantation damage and to activate the implants in GaAs. An alternative method, laser annealing, has recently received a great deal of attention in the study of ion-implanted materials. With this method, annealing can be achieved in a localized area without encapsulants within a very short time. Most of the work on laser annealing so far has been done on an elemental semiconductor such as Si, and many successful results have been reported.¹⁵⁻¹⁷ In contrast, the laser annealing method has not been very successful to date for ion-implanted GaAs, and only a few successful results have been recently reported.¹⁸⁻²⁰ Presumably, the crystal-growth dynamics are much different for the compound semiconductors than for the elemental semiconductors.

In our study,²¹ Mg ions were implanted at an ion energy of 120 keV to a dose of $1 \times 10^{15}/\text{cm}^2$ at room temperature. Laser annealing of the samples was

carried out using a Q-switched ruby laser of 24- μ sec pulse duration and energy densities ranging from 0.1 to 0.78 J/cm² per pulse. The irradiated area was ~4 mm in diam.

The results of sheet-resistivity measurements as a function of laser energy are given in Fig. 19 which shows clearly a threshold energy density of ~0.3 J/cm² above which the sheet resistivity decreases dramatically. The resistivity decreases further with increasing laser energy although the condition of the sample surface is gradually degrading. Even though the resistivity of Mg-implanted GaAs is reduced significantly above the threshold energy, mobilities of the samples are very low (~30 cm²/V·sec) compared to the values obtained from the thermally annealed samples (~150 cm²/V·sec). A typical activation efficiency obtained was about 30% for the laser energy densities above the threshold energy.

3.4 ELECTRICAL PROPERTIES OF Ge-IMPLANTED GaAs

Ge Single Implantation

Germanium, like Si and Sn, is known to be an amphoteric dopant in GaAs. It has been widely used as a dopant in epitaxial layers of GaAs, and the type of electrical conductivity seems to depend upon the crystal-growth mechanism. Vapor-phase epitaxially (VPE) grown Ge-doped GaAs yields an n-type²² conductivity, whereas liquid-phase epitaxially (LPE) grown Ge-doped GaAs yields a p-type.²³ Moreover, molecular-beam epitaxially grown Ge-doped GaAs yields both n- and p-type conducting layers²⁴ depending upon the substrate temperature and on the As₄ to Ga flux ratio in the molecular beams. Ge has been

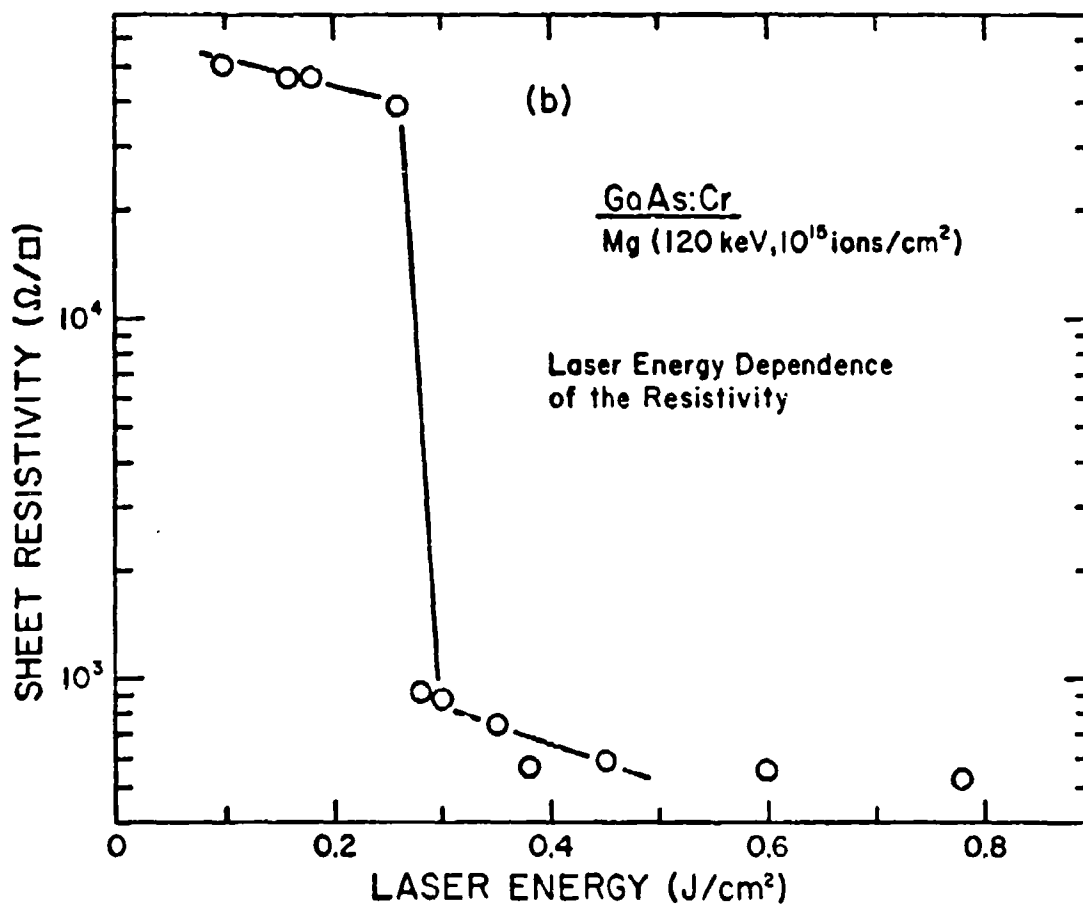


Figure 19. Dependence of Sheet Resistivity upon Laser Annealing Energy.

used in producing ohmic contacts²⁵ to n-type GaAs and has also been utilized in the fabrication of p/n junctions²⁶ by molecular beam epitaxy. However, very few studies on the electrical properties of Ge-implanted GaAs have been reported. To the best of our knowledge, we presented²⁷ the first published results concerning the amphoteric behavior in the electrical activity of Ge-implanted GaAs. Previously, Surridge and Sealy²⁸ reported n-type activity of Ge-implants for doses ranging from 1×10^{13} to $1 \times 10^{15}/\text{cm}^2$, using aluminum caps and semi-insulating epitaxial GaAs (n-type with $n = 10^{15}/\text{cm}^3$).

The implantation was carried out at an energy of 120 keV with doses ranging from 5×10^{12} to $3 \times 10^{15}/\text{cm}^2$ at room temperature in semi-insulating Cr-doped GaAs, LPE-grown undoped n-type ($n = 10^{10}/\text{cm}^3$) GaAs, and VPE-grown undoped n-type ($n = 10^{15}/\text{cm}^3$) GaAs. After implantation, the samples were encapsulated with a 1000-Å layer of Si_3N_4 deposited pyrolytically at 700°C. The Si_3N_4 films adhered well during annealing, except at 950°C, where a few pin holes appeared for the two highest doses.

The electrical behavior of Ge implants in semi-insulating Cr-doped GaAs is very complicated, producing both p- and n-type activity depending upon both the ion dose and the annealing temperature. For doses at or below $1 \times 10^{14}/\text{cm}^2$, the implanted layer is p-type at annealing temperatures up to 950°C. For doses at or above $1 \times 10^{15}/\text{cm}^2$, the implanted layer is n-type at all annealing temperatures. For an ion dose of $3 \times 10^{14}/\text{cm}^2$, type conversion occurs from p to n between 900 and 950°C. This behavior is in contrast to the n-type activity for all doses reported by Surridge and Sealy²⁸ and is unlike that of implanted silicon,²⁹ which produces only n-type activity. This dose-dependent amphoteric behavior has also been observed in two other

substrates (LPE and VPE grown) implanted with Ge ions to doses of 1×10^{13} , 1×10^{14} , and $1 \times 10^{15}/\text{cm}^2$.

The results of electrical measurements made on semi-insulating Cr-doped GaAs samples implanted with Ge to ion doses ranging from 5×10^{12} to $3 \times 10^{15}/\text{cm}^2$ and annealed at various temperatures are shown in Fig. 20. The anneal behavior of the sheet-carrier concentration indicates that for samples having an ion dose of $3 \times 10^{13}/\text{cm}^2$, the electrical activity increases monotonically with anneal temperature. The highest electrical activation efficiency obtained was 38% for an ion dose of $1 \times 10^{13}/\text{cm}^2$ and annealing at 950°C for 15 min. Below 850°C the electrical activity is very low for samples having an ion dose of $\leq 1 \times 10^{13}/\text{cm}^2$, although definite p-type conductivity becomes apparent at around 750°C . For samples implanted to an ion dose of $1 \times 10^{14}/\text{cm}^2$, the electrical activity increases gradually with anneal temperature, yielding the highest activation (~11%) at $\sim 850^\circ\text{C}$, and then decreases at higher anneal temperatures. The anneal behavior for an ion dose of $3 \times 10^{14}/\text{cm}^2$ is similar to that for $1 \times 10^{14}/\text{cm}^2$ up to 900°C . However, the electrical activation drops sharply (to 0.5%) at 950°C , accompanied by conductivity type conversion (indicated by dashed lines in the figure). For the two highest doses, the electrical activity increases with anneal temperature, but the activation efficiencies are low (only 5% and 2% for ion doses of 1×10^{15} and $3 \times 10^{15}/\text{cm}^2$, respectively) even after annealing at 950°C for 15 min. The activation may be somewhat affected by a few pin holes created during annealing at 950°C . P-type layers have been observed for doses of 3×10^{13} and $1 \times 10^{14}/\text{cm}^2$ after pyrolytic capping but without annealing, but no p-type layers have been observed for as-implanted samples. N-type layers have been observed not only for samples after capping only but also for as-implanted

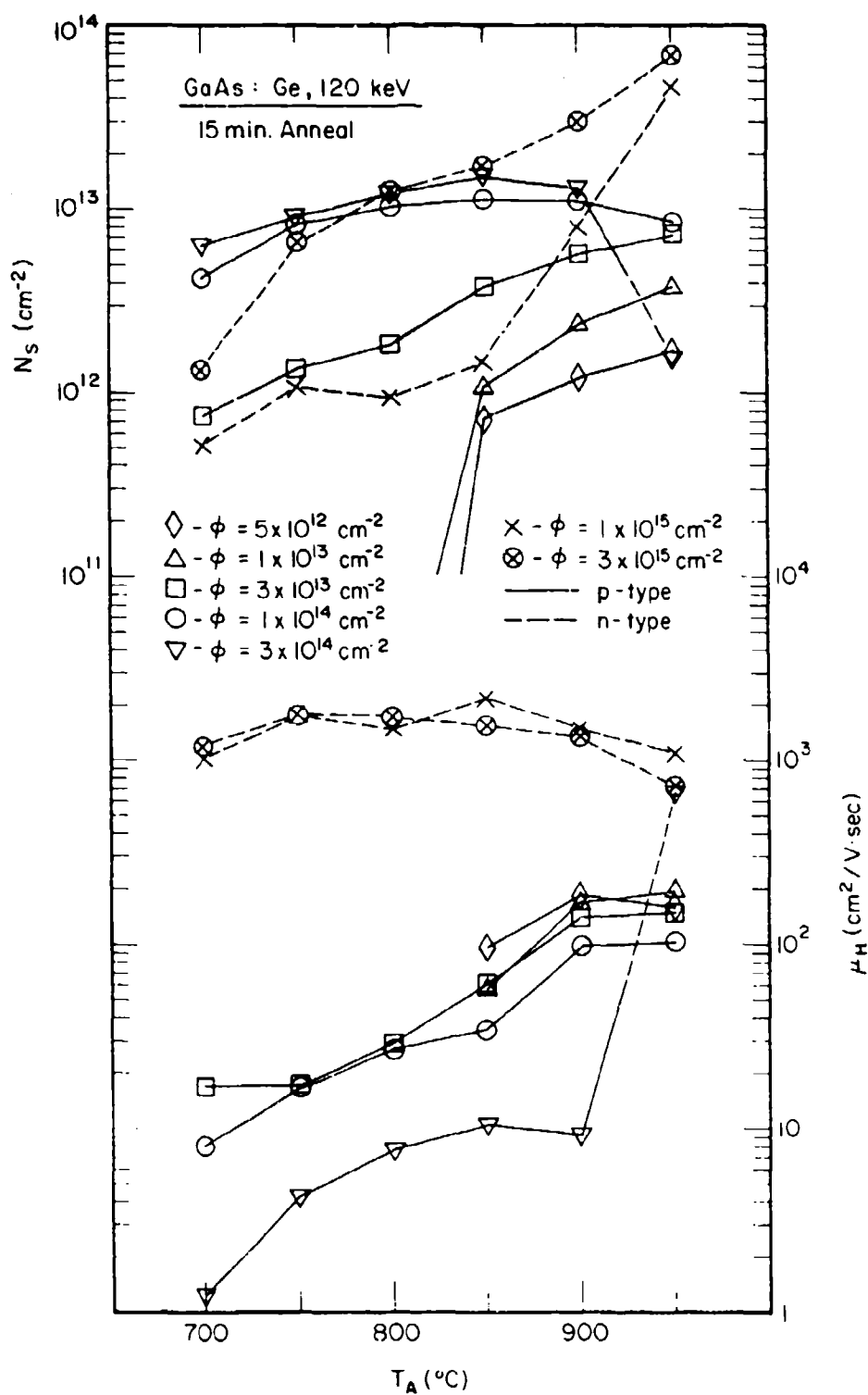


Figure 20. Dependence of Sheet-Carrier Concentration (N_S) and Hall Mobility (μ_H) upon Annealing Temperature (T_A) for GaAs:Ge.

samples having an ion dose of $1 \times 10^{15}/\text{cm}^2$, although the mobilities are very small ($\mu = 187 \text{ cm}^2/\text{V}\cdot\text{sec}$ for capping only and $0.15 \text{ cm}^2/\text{V}\cdot\text{sec}$ for as-implanted samples).

The anneal behavior of the carrier mobility indicates that the mobility increases with anneal temperature for samples having doses of $\leq 1 \times 10^{14}/\text{cm}^2$, which implies that the lattice damage caused by ion bombardment is appreciably reduced with increasing anneal temperatures. However, the mobilities of samples with an ion dose of $3 \times 10^{14}/\text{cm}^2$ remain low--below $10 \text{ cm}^2/\text{V}\cdot\text{sec}$ --with the sample remaining p-type. The mobility increases with anneal temperatures up to 850°C , levels off, then increases sharply at an anneal temperature of 950°C , becoming n-type as indicated by the dashed line. The low value of mobility at this dose may be caused by high electrical compensation. The mobility anneal behavior of n-type layers is different from that of p-type layers. The mobilities for the two highest doses remain essentially constant for all anneal temperatures. The slight decrease in mobility above 900°C , although accompanied by increasing activation, may be somewhat related to lattice defects created during the high-temperature anneal.

In Fig. 21 the sheet-carrier concentrations and Hall mobilities are again plotted as function of ion dose. The data for the 890°C anneal are very similar to those for the 750°C anneal and have been omitted for the sake of clarity. The amphoteric nature of Ge implants in GaAs as a function of ion dose can be clearly seen in this figure. The trend in activation efficiency η (sheet-carrier concentration divided by ion dose) as a function of fluence can be observed from this figure by comparing the slopes of the N_S lines with the slope of the 100%-activation line. Up to a dose of $1 \times 10^{14}/\text{cm}^2$,

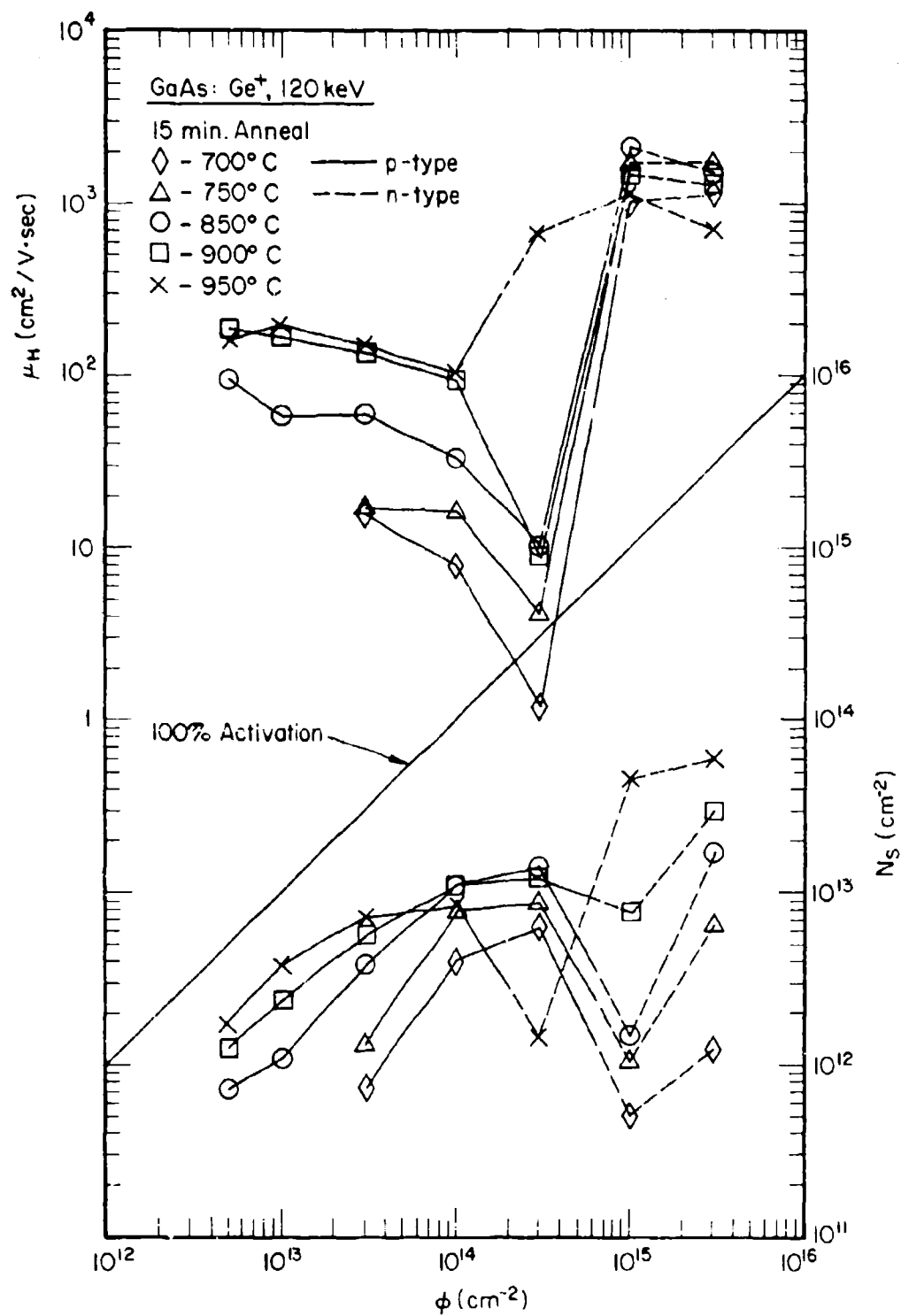


Figure 21. Dependence of Sheet-Carrier Concentration (N_S) and Hall Mobility (μ_H) upon Ion Dose (ϕ) for GaAs:Ge.

activation efficiencies remain relatively constant except for the 950°C anneal. Above $1 \times 10^{14}/\text{cm}^2$, η decreases appreciably and then drops sharply near the type-conversion dose level. It is interesting to note that for the 950°C anneal, η begins to decrease at lower doses and type conversion occurs sooner than at other anneal temperatures. Once the samples have become n-type, activation increases with ion dose at all anneal temperatures. It can also clearly be seen that the mobility decreases monotonically with ion dose at all anneal temperatures before the conversion to n-type occurs, and a mobility minimum is evident at a dose of $3 \times 10^{14}/\text{cm}^2$, except for the 950°C anneal.

Even though no adequate theory is available to explain our experimental results, the general electrical behavior suggests that in samples of lower dose and anneal temperature, the implanted Ge ions go into As sites preferentially, producing p-type activity. As the Ge-ion dose and anneal temperature increase, increasing numbers of Ge ions go into Ga sites, raising the compensation level. At even higher doses and anneal temperatures, more Ge ions go into Ga sites than into As sites, producing n-type activity; the compensation level still remains high. There is a possibility that defects such as As or Ga vacancies (both intrinsic and extrinsic due to high-temperature anneal) influence the electrical activity, especially in the case of compensation mechanisms. However, it is evident that the amphoteric electrical behavior is due mainly to the implanted Ge ions because: (1) no significant number of acceptors or donors has been found in the unimplanted substrates, even after annealing at 900 or 950°C; (2) not only p-type but also n-type activation continues to increase monotonically with anneal temperature as high as 950°C, except for the two intermediate doses which are nearing the type-conversion level.

Ge and Ga Dual Implantation

The influence of dual implantation of Ge and Ga on the activity of Ge in GaAs has been studied.³⁰ Heckingbottom and Ambridge³¹ proposed on the basis of solid state chemistry that if stoichiometry of GaAs is maintained by implanting quantitatively matched dual-ion combinations, an enhanced electrical activity compared with a single implant should be obtained. However, since amphoteric dopants will preferentially occupy a site associated with either of the sublattices, the effect of the dual implantation of the Ge is expected to be more complicated than that of the dual implantation with Group II and VI dopants of the periodic table, for which the dopants will almost exclusively locate on one of the sublattice sites. In spite of the complicated nature of the compensation, the addition of Ga to GaAs:Ge is expected to lower the probability of Ga-site occupancy by the Ge ions and to encourage As-site occupancy. In this way, the compensating effects produced by both type of carriers will be reduced and p-type activity will be greater.

The dual implantation was carried out sequentially at an energy of 120 keV with doses ranging from 1×10^{13} to 3×10^{15} ions/cm² at room temperature in semi-insulating Cr-doped GaAs. The doses of the dual implants were equal in each instance. After implantation, the samples were encapsulated with a 1000-Å layer of Si₃N₄ deposited pyrolytically at 700°C. During annealing, the samples rested cap-side down on bare GaAs substrate wafers in order to improve the performance of the caps. In this way, the caps held very successfully at temperatures as high as 1000°C.

Similar gallium arsenide control samples, implanted with the same doses of Ga alone, were also prepared, annealed at various temperatures, and otherwise prepared by the same procedures. The test samples did not show appreciable electrical activity, and in most cases no Hall effect could be determined. Figure 22 shows the variation of surface-carrier concentration and mobility for several doubly implanted doses as a function of the anneal temperature T_A . These results indicate that the implanted layer produces p-type activity (solid lines) for all ion doses and all anneal temperatures, except for the two highest doses at anneal temperatures above 900°C, where the implanted layer shows n-type activity. The two lowest doses of $1 \cdot 10^{13}$ and $3 \cdot 10^{13}/\text{cm}^2$ show electrical activity which increases monotonically with T_A and begins to level out at around 850°C. The dose of $1 \cdot 10^{14}/\text{cm}^2$ shows an annealing behavior which is nearly independent of T_A , while the electrical activity of the three highest doses actually decreases gradually with anneal temperature. We believe this general tendency toward decreasing activation with anneal temperature may be due to increasing compensation as the samples approach conditions for type conversion indicated by the dashed lines. It should be noted that the addition of Ga delays p- to n-type conversion to the two highest doses, compared with singly-implanted Ge which converts at the high T_A range of the $3 \cdot 10^{14}/\text{cm}^2$ dose.

The anneal behavior of the mobility shown in Fig. 22 is also determined largely by the amphoteric nature of Ge ions in GaAs. Due to damage annealing the mobilities of the three lowest doses increase with T_A to values which are smaller for higher doses, as expected, in the range of $100 - 200 \text{ cm}^2/\text{V}\cdot\text{sec}$. The three highest doses show much lower mobilities. In addition to increased implanted-ion scattering at higher doses, we believe the unusually low

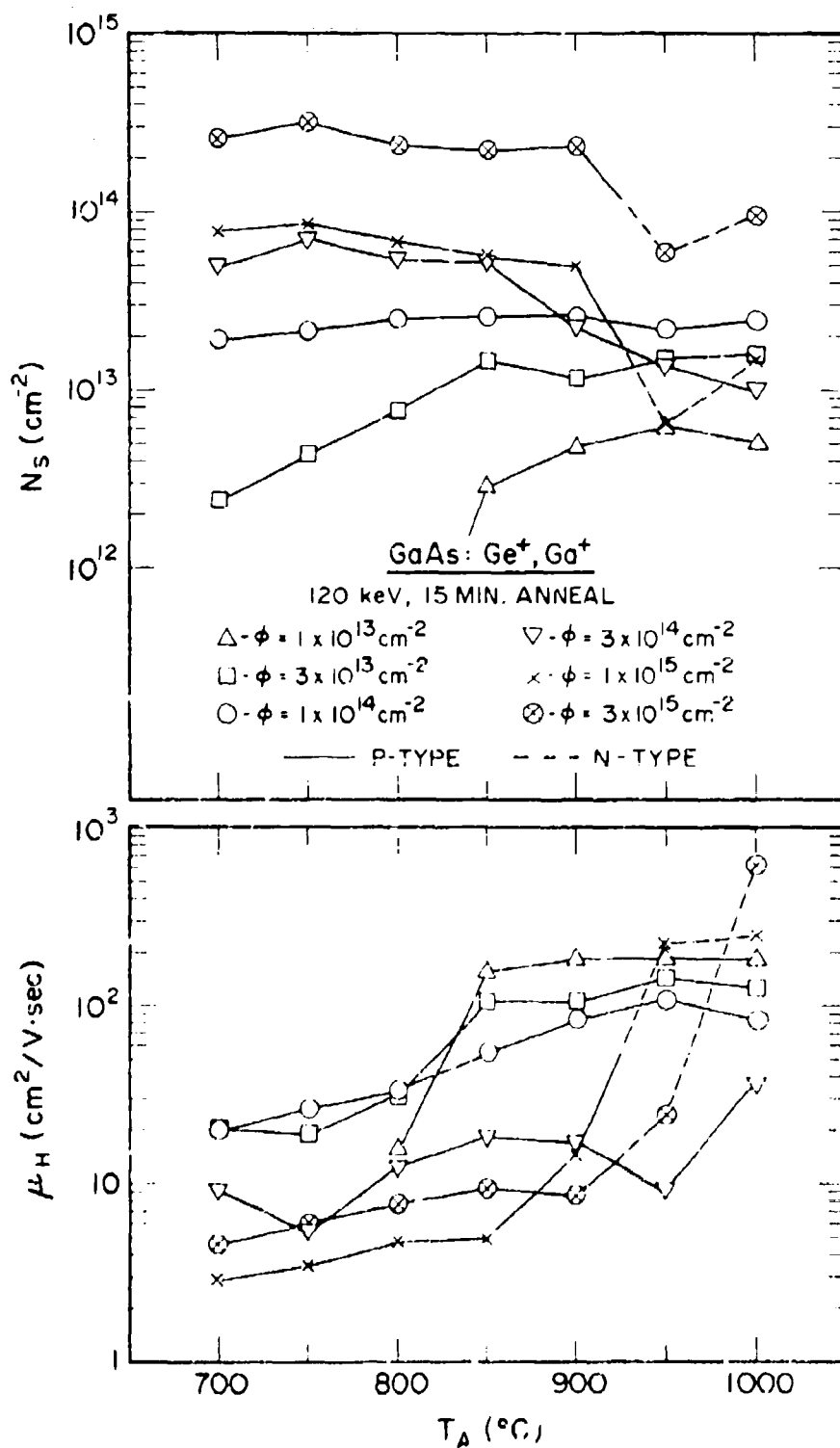


Figure 22. Dependence of Sheet-Carrier Concentration (N_s) and Hall Mobility (μ_H) upon Anneal Log Temperature (T_A) for GaAs:Ge⁺, Ga⁺.

mobilities can be attributed to a high degree of compensation which increases as the sample approaches the doses for which type conversion occurs. After type conversion, the mobility increases rapidly toward values representative of n-type mobilities, and then increases further with T_A as the carrier balance shifts increasingly to n-type carriers.

Figure 23 is a replot of the data, showing surface-carrier concentration as a function of implanted dose at different anneal temperatures, compared with a straight line which represents 100% activation efficiency. Activation efficiencies are highest for low doses annealed at high T_A , reaching 61% for a dose of $1 \times 10^{13}/\text{cm}^2$ and an anneal temperature of 950°C. Activation efficiencies are considerably lower at the higher doses and lowest at the higher anneal temperatures. Maximum efficiencies for the high doses reach 6×10^{-2} at T_A between 700 and 850°C. The amphoteric behavior of Ge in GaAs:Ge is again a function of ion dose can be seen clearly in Fig. 23. A sharp drop in activation efficiency for doses above $1 \times 10^{14}/\text{cm}^2$ at all T_A is very evident here. These decreases can be attributed to a high level of compensation in electrical activity.

Figures 24 and 25 display surface-carrier concentration and mobility as a function of anneal temperature T_A vs. dose on the dual-implant Ge 4 Ge, together with the comparable variation for the single-implant Ge. For the three lowest doses (Fig. 24), the anneal behavior of carrier concentration for single and dual implants of the same dose is strikingly similar, except that the dual implant shows reduced activity at all T_A . This fact indicates that dual implantation produces a significant concentration of compensating acceptor impurities at temperatures. In the lower T_A range, anneal activation is of 3-5

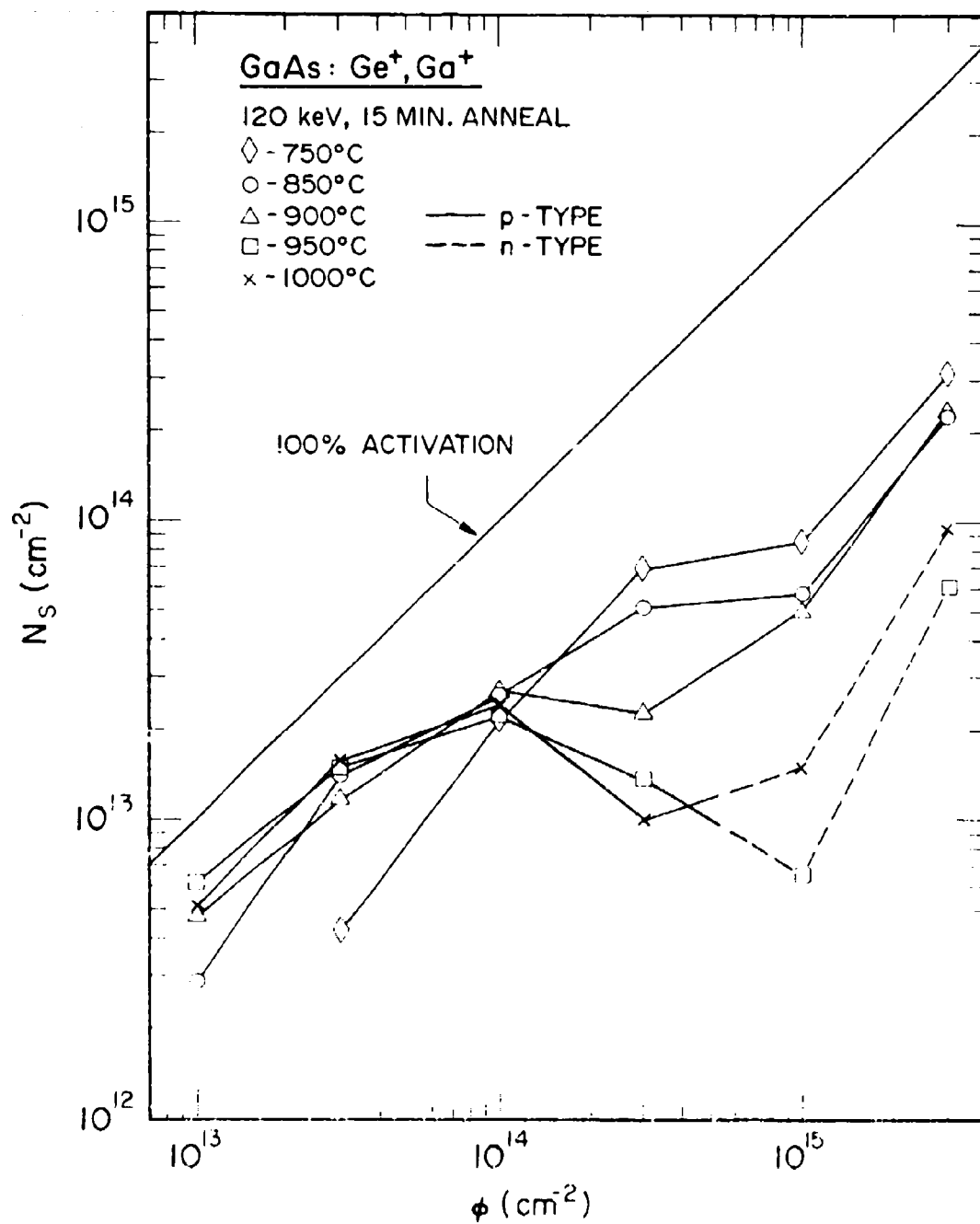


Figure 23. Dependence of sheet carrier concentration (N_s) upon Ion Dose (ϕ) for GaAs:Ge⁺, Ga⁺.

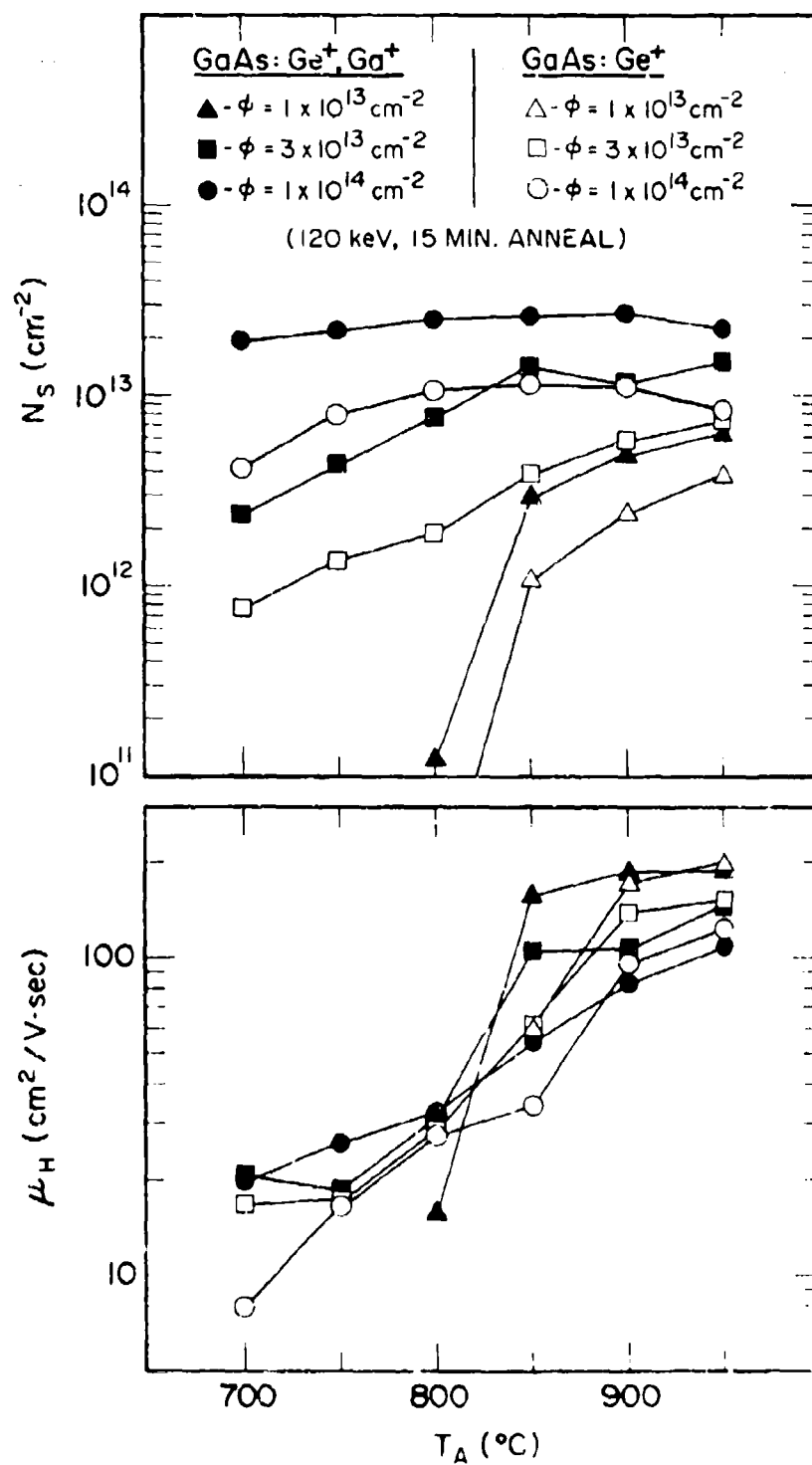


Figure 24. Dependence of Sheet-Carrier Concentration (N_s) and Hall Mobility (μ_H) upon Annealing Temperature (T_A) for Lower-Dose Samples of Both GaAs:Ge and GaAs:Ge+Ga.

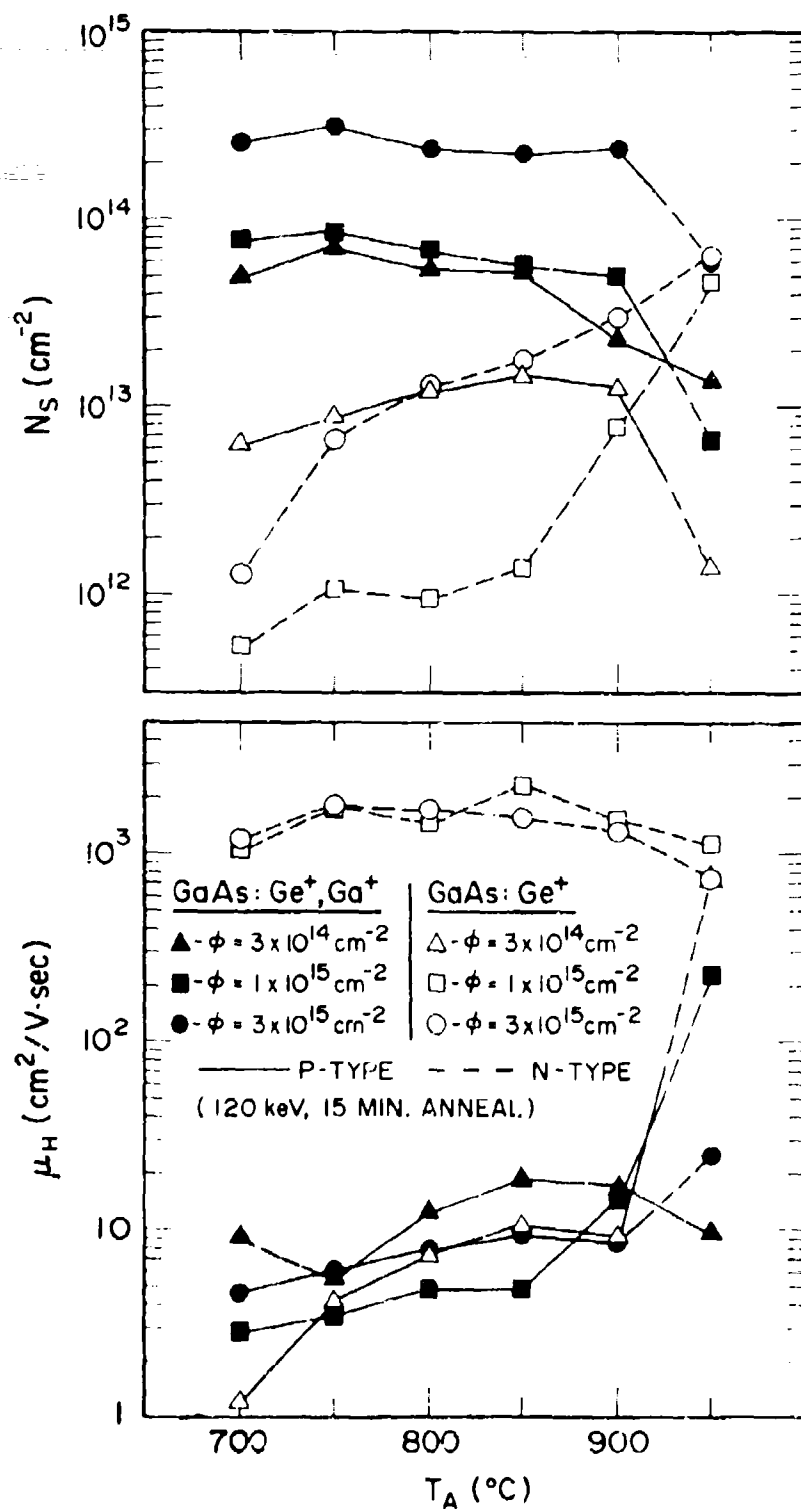


Figure 25. Dependence of Sheet-Carrier Concentration (N_S) and Hall Mobility (μ_H) upon Annealing Temperature (T_A) for Higher-Dose Samples of Both GaAs:Ge and GaAs:Ge + Ga.

give activation efficiencies up to 26%. At the higher anneal temperature of 950°C and dose $1 \times 10^{13}/\text{cm}^2$, where the single Ge implant has its highest activation of 38%, the dual implants yield a maximum efficiency of 51%. In Fig. 25, the dose of $3 \times 10^{14}/\text{cm}^2$ shows the greatest enhancement of p-type activity by a factor of 8 at anneal temperatures of 750°C or below. It is interesting to note that for the two highest doses, the n-type activity of the single Ge-implant is inhibited by the addition of Ga. The single Ge-implant converts to n-type at the higher T_A range of the $3 \times 10^{14}/\text{cm}^2$ dose and is n-type at all T_A for the two highest doses. The dual implantation does not yield n-type activity at the two highest dose levels until after high-temperature anneal at 950°C or above.

A comparison of mobilities for low doses in Fig. 24 shows generally similar behavior for the single and dual implants. At the lower anneal temperatures, mobilities of the dual implants are somewhat higher, but at the highest T_A they are comparable to the mobilities of the single Ge-implanted samples. In Fig. 25, mobilities are similarly compared for the three highest doses. P-type mobilities can be compared only for the dose $3 \times 10^{14}/\text{cm}^2$. Up to 900°C, the dual implantation shows some improvement of mobility over the single implantation, although mobilities are very low in this region due to compensation, as pointed out previously.

Ge and As Dual Implantation

In this work,³² the amphoteric characteristics of Ge ion implants in GaAs have been investigated by dual implantation of As and Ge into GaAs. Similar to the case of Ge and Ga dual implantation previously described, the addition

of As to GaAs:Ge is expected to lower the probability of As site occupancy by the Ge ions and to encourage Ga-site occupancy and hence n-type electrical activity.

The dual implantation was carried out sequentially at an energy of 120 keV with doses ranging from 1×10^{13} to $3 \times 10^{15}/\text{cm}^2$ at room temperature. In each case, equal doses of both Ge and As ions were implanted into GaAs. After implantation, the samples were encapsulated with $\sim 1000\text{-}\text{\AA}$ layer of Si_3N_4 at $\sim 700^\circ\text{C}$ in a pyrolytic reactor. During annealing, the samples rested cap-side down on bare GaAs substrates in order to improve the performance of the caps. In this way, the caps held very successfully at temperatures as high as 1000°C , and no sign of surface degradation could be observed. Without the additional protection provided by the bare GaAs substrate, the caps were found to deteriorate significantly due to As outdiffusion during annealing.

The results of electrical measurements made on semi-insulating Cr-doped GaAs samples implanted with both Ge and As to ion doses ranging from 1×10^{13} to $3 \times 10^{15}/\text{cm}^2$ and annealed at various temperatures are shown in Fig. 26. For ion doses $\geq 3 \times 10^{13}/\text{cm}^2$, p-type conductivity (solid lines) has been observed at all annealing temperatures, whereas for ion doses $\geq 1 \times 10^{14}/\text{cm}^2$, n-type conductivity (dashed lines) has been observed at all annealing temperatures. The annealing behavior of the sheet-carrier concentration indicates that electrical activities increase monotonically with annealing temperature for all but the lowest dose of $1 \times 10^{13}/\text{cm}^2$, where the electrical activation is found to decrease slightly between 950 and 1000°C anneals. For ion doses of 1×10^{13} and $1 \times 10^{14}/\text{cm}^2$, the electrical activation was too small to measure.

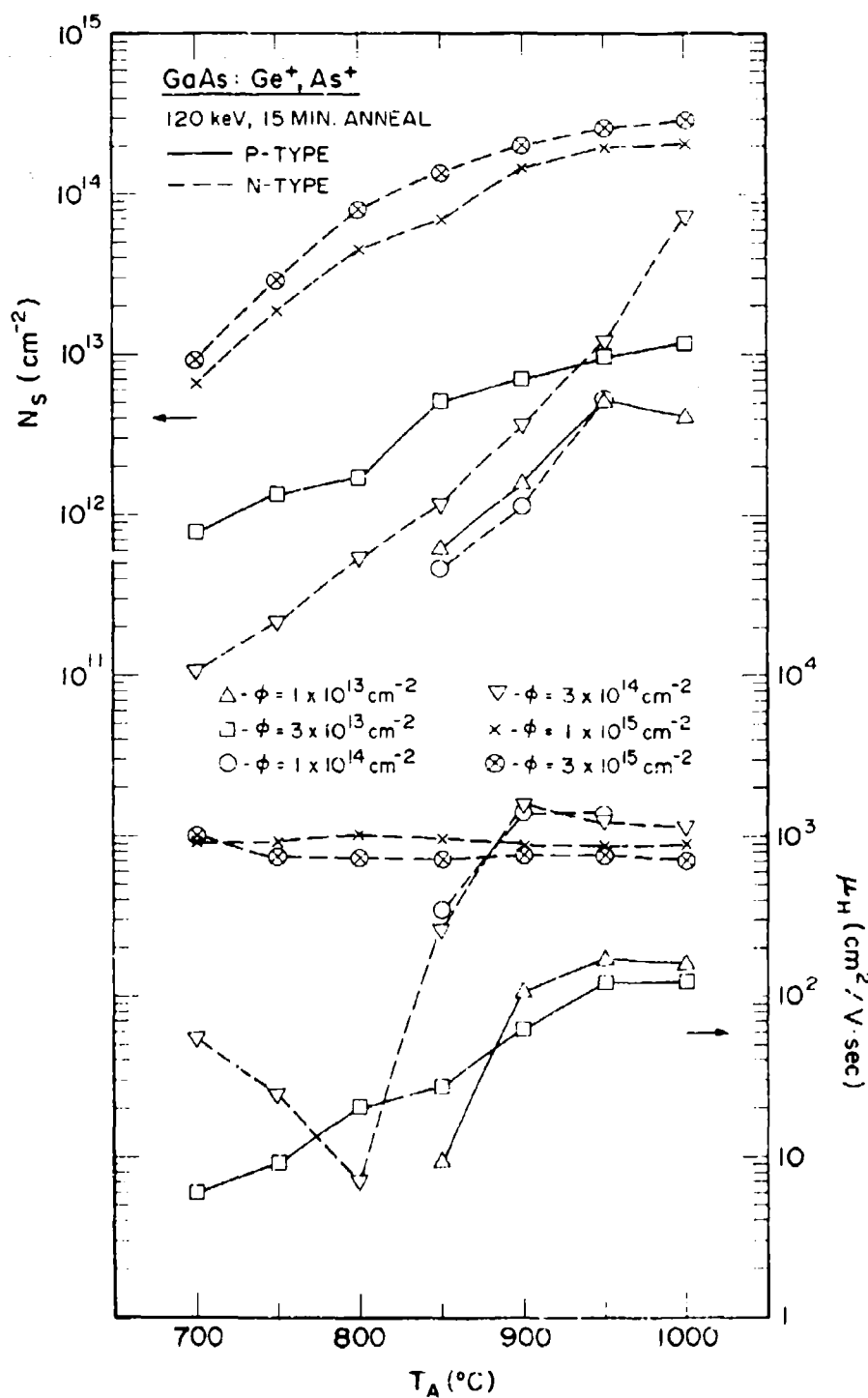


Figure 26. Dependence of Sheet-Carrier Concentration (N_s) and Hall Mobility (μ_H) upon Annealing Temperature (T_A) for GaAs:Ge + As.

for samples annealed at 800°C or below. The highest electrical-activation efficiency obtained from the p-type samples was 50% for a dose of $1 \times 10^{13}/\text{cm}^2$ at 950°C anneal; the highest obtained from the n-type samples was 24% for a dose of $3 \times 10^{14}/\text{cm}^2$ at 1000°C anneal.

Similar GaAs control samples, implanted with the same doses of As only, also have been measured. These test samples did not exhibit appreciable electrical activity, and in most cases no Hall effect could be determined. Several high-dose ($\geq 1 \times 10^{15}/\text{cm}^2$) samples exhibited some p-type electrical activity, at least one order of magnitude below that measured for the corresponding dual-implanted samples.

The annealing behavior of the Hall mobility indicates that the mobility increases with annealing temperature for p-type samples having doses $\leq 3 \times 10^{13}/\text{cm}^2$. However, the mobility of n-type samples having an ion dose of $3 \times 10^{14}/\text{cm}^2$ remains significantly low at annealing temperatures of 850°C or below, increases to 900°C, and then decreases slightly with annealing temperature. The low value of mobility below 850°C for this dose may be due to high electrical compensation under conditions where type conversion has taken place. The mobilities for the two highest doses remain essentially constant at all annealing temperatures.

The sheet-carrier concentrations are plotted next as a function of ion dose for samples annealed at three different temperatures in Fig. 27, and the electrical activations are compared with 100% activation indicated by the straight line. The data for other annealing temperatures show very similar variations and have been omitted for clarity. The solid and dashed lines,

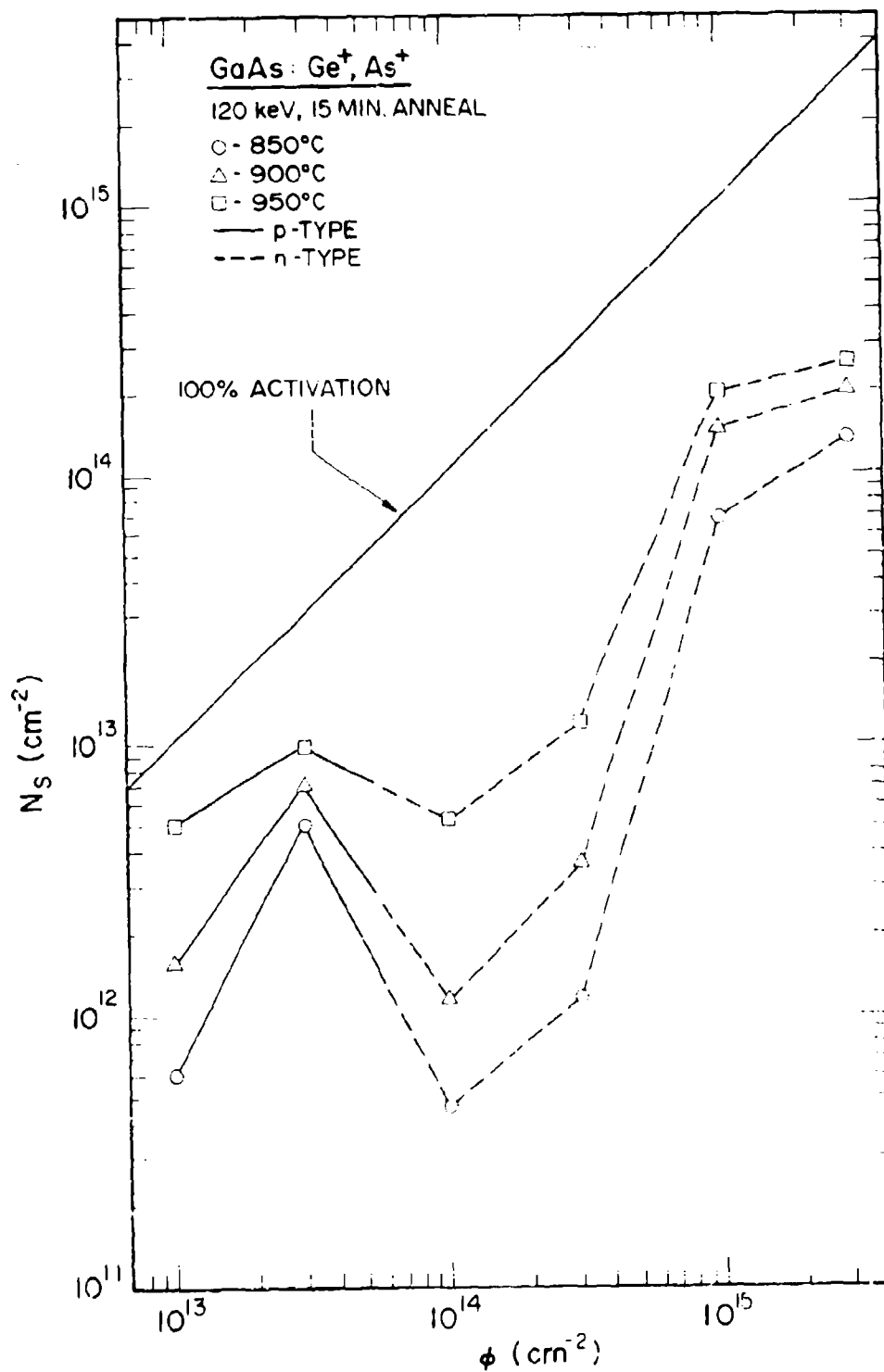


Figure 27. Dependence of Sheet-Carrier Concentration (N_s) upon Ion Dose (ϕ) for GaAs:Ge + As.

representing p- and n-type activity, respectively, clearly show the amphoteric nature of Ge in GaAs:Ge + As as a function of ion dose. In general, electrical-activation efficiencies are highest for most anneal temperatures at a dose of $3 \times 10^{13}/\text{cm}^2$, where the conductivity is p-type. At a dose of $1 \times 10^{14}/\text{cm}^2$, the conductivity type converts to n-type, and a sharp drop in activation efficiency occurs. The activation efficiencies for a dose of $3 \times 10^{14}/\text{cm}^2$ are about the same as that for a dose of $1 \times 10^{14}/\text{cm}^2$ at the annealing temperatures shown. These dramatic decreases in activation efficiencies in the intermediate dose range of 1×10^{14} to $3 \times 10^{14}/\text{cm}^2$ may be due to high electrical self-compensation. Beyond the type-conversion dose level, the activation efficiencies increase significantly with ion doses and are highest at a dose of $1 \times 10^{15}/\text{cm}^2$ for n-type activity at most annealing temperatures.

The sheet-carrier concentration and mobility are plotted as a function of annealing temperature in Figs. 28 and 29 for each dose of the dual implants of Ge and As, together with the comparable variation for singly implanted Ge. For doses $\geq 3 \times 10^{13}/\text{cm}^2$, the annealing behavior of sheet-carrier concentration and mobility for single and dual implants of the same dose shows similar trends. Although the additional implantation of As into GaAs:Ge in this dose range generally has little effect upon electrical activation, it leads to noticeably reduced mobilities. This result is somewhat surprising since dual implants of Ge + As are expected to result in a reduction of p-type activity. Such decrease in p-type activation by dual implantation has not been observed for samples having an ion dose of $1 \times 10^{13}/\text{cm}^2$ and annealed at 700° and 750°C. In all other cases, the activation after dual implantation is comparable to or even higher than that due to Ge implantation only. The reason for this result cannot be adequately explained at present.

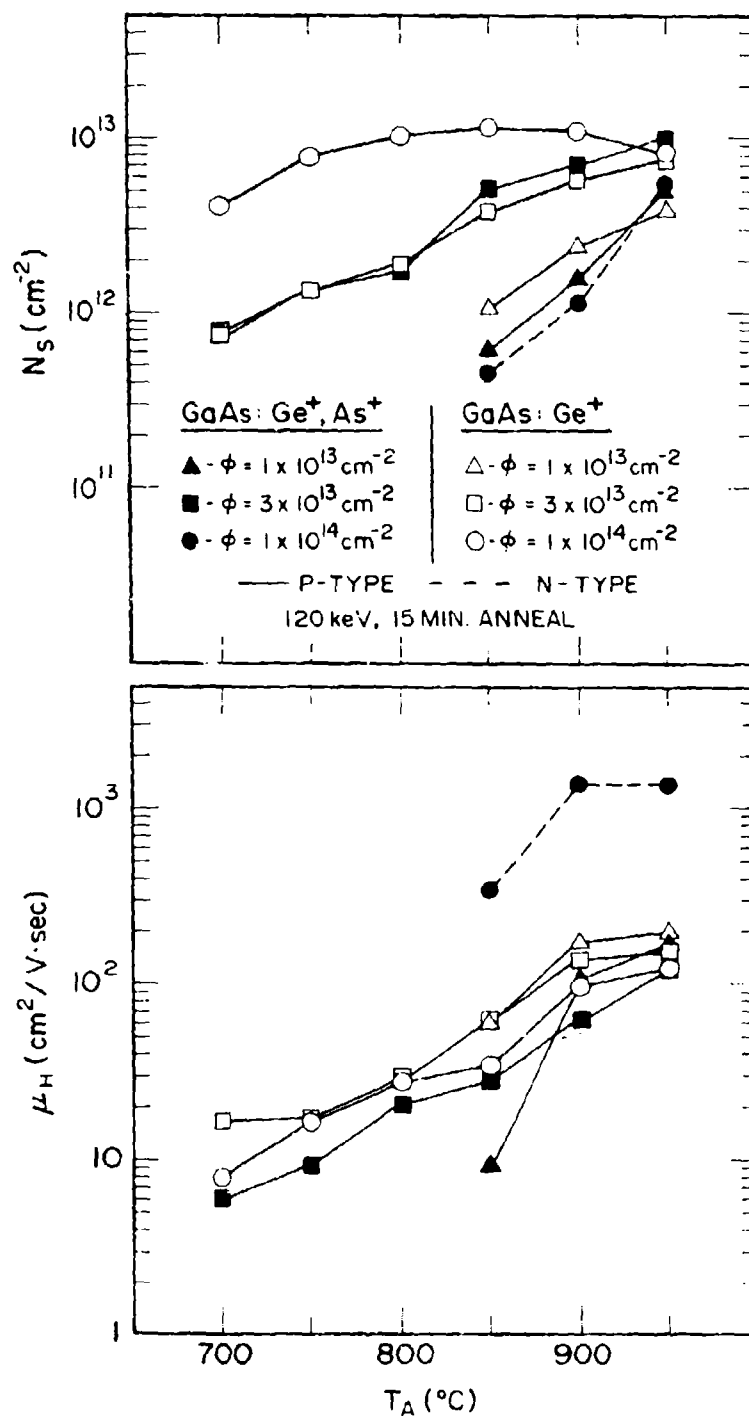


Figure 26. Dependence of Sheet-Carrier Concentration (N_s) and Hall Mobility (μ_H) upon Annealing Temperature (T_A) for Lower-Dose Samples of Both GaAs:Ge and GaAs:Ge + As .

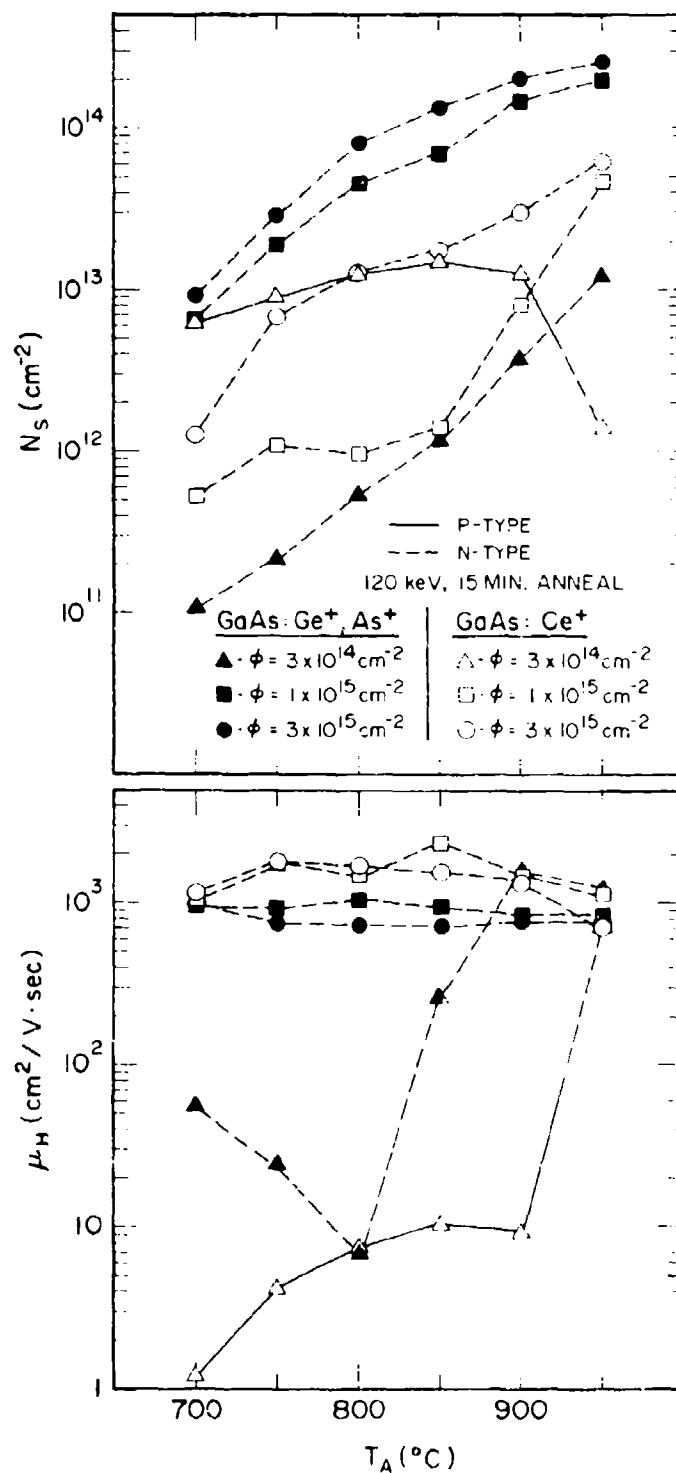


Figure 29. Dependence of Sheet-Carrier Concentration (N_s) and Hall Mobility (μ_H) upon Annealing Temperature (T_A) for Higher-Dose Samples of Both GaAs:Ge and GaAs:Ge + As.

It should be pointed out that the above results of dual implantation with Ge + Ga at these dose levels show comparable mobilities and p-type electrical activations significantly enhanced over those observed for single Ge implantation. For an ion dose of $1 \times 10^{14}/\text{cm}^2$, the effect of dual implantation is very dramatic. The p-type conductivity of Ge single implants is changed to n-type by the dual implantation of Ge + As, and electrical activation is reduced significantly due to self-compensation. Figure 29 shows that the conductivity type conversion persists due to dual implantation for an ion dose of $3 \times 10^{14}/\text{cm}^2$. For the two highest doses, dual implantation shows n-type electrical activation which is greatly enhanced over that of a Ge single implant at all annealing temperatures. In most cases, the activation is increased by about one order of magnitude. However, mobilities are generally reduced by a factor of ~ 2 for the dual implants at this dose level.

3.5 ELECTRICAL PROPERTIES OF CARBON DUAL-IMPLANTED GaAs

Although carbon is known to be an amphoteric dopant in GaAs, both ions-implanted³³⁻³⁵ and conventionally doped³⁶ Ga exhibit p-type conductivity. In a previous investigation,³⁵ it was demonstrated that efficient p-type doping can be achieved by C^+ -ion implantation in GaAs under appropriate annealing conditions. The interaction of implanted C atoms and residual damage centers during annealing were primarily attributed to the lowering of the free-carrier concentration. For example, a stable complex center can be formed between C atoms (C_{As}) and residual arsenic vacancies (V_{As}). The electrical CVA (free) can also be reduced with increased dose. The higher the dose creates more damage centers and therefore increases the tendency for C atoms to deviate from stoichiometry. Incomplete ionization of otherwise electrically

active centers with an increase in impurity concentration has been suggested as another possible source of reduction in "apparent" doping efficiency.³⁷

As stated earlier, Heckingbottom and Ambridge³¹ have proposed that the doping efficiency of ion-implanted binary semiconductors such as GaAs may be improved by dual implantation. In this study,³⁸ dual implantation was examined as a means of improving p-type conductivity in C^+ -ion-implanted GaAs.

The substrate wafers used were Cr-doped semi-insulating GaAs obtained from Laser Diode Lab., Inc. Samples were implanted with C^+ ions at an energy of 60 keV. In the case of dual implants, the Ga^+ ion was selected and implanted at 120 keV prior to the C^+ implantation. Samples were implanted to a dose of 10^{14} ions/cm² (for both C^+ and Ga^+) using ion current densities of ~ 20 nA/cm². Samples were encapsulated at 700°C with 1000-Å layers of Si_3N_4 using the CVD technique. For control samples, Ar-implanted (120 keV, 10^{14} /cm²) or unimplanted samples were encapsulated and annealed under the conditions described above.

Table 6 is a summary of electrical data obtained on various samples annealed at 700°C for 15 min. At this anneal temperature the sheet resistivity of both the C^+ single implant and the ($Ga^+ + C^+$) dual implants was two to three orders of magnitude lower than that of either Ar⁺-implanted or unimplanted samples. On these latter samples, it was not possible to obtain a Hall voltage. The significant result is that the sheet-hole concentration (p_s) of the dual implants was higher than the single implant by a factor of 3. The result of Sansbury³³ is also given in Table 6. At higher annealing temperatures, one might expect to obtain higher doping efficiency. For

TABLE 6

SHEET RESISTIVITY ρ_s , EFFECTIVE HALL MOBILITY μ_{eff} , AND THE SHEET-HOLE CONCENTRATION P_s FOR VARIOUS SAMPLES ANNEALED AT 700°C FOR 15 MIN. (IMPLANTS WERE PERFORMED AT ROOM TEMPERATURE TO A DOSE OF 10^{14} cm^{-2} . FOR Ga^+ AND Ar^+ IMPLANTS, $E = 120 \text{ keV}$; FOR C^+ IMPLANT, $E = 60 \text{ keV}$.)

Sample	ρ_s (Ω/\square)	μ_{eff} ($\text{cm}^2/\text{V}\cdot\text{sec}$)	P_s (cm^{-2})
Unimplanted	$1.08 \cdot 10^7$
GaAs:Ar ⁺	$5.01 \cdot 10^6$
GaAs:C ⁺	$1.17 \cdot 10^4$	150	$3.57 \cdot 10^{13}$
GaAs:Ga ⁺ +C ⁺	$4.56 \cdot 10^3$	114	$1.20 \cdot 10^{13}$
Sansbury (Ref. 33)	$2.72 \cdot 10^4$	242	$9.50 \cdot 10^{11}$

TABLE 7

COMPARISON OF ELECTRICAL PARAMETERS FOR SINGLE AND DUAL IMPLANTS ANNEALED AT 900°C FOR 15 MIN. (IMPLANTS WERE PERFORMED AT ROOM TEMPERATURE TO A DOSE OF 10^{14} cm^{-2} . FOR THE Ga^+ IMPLANT, $E = 120 \text{ keV}$; FOR THE C^+ IMPLANT, $E = 60 \text{ keV}$.)

Sample	GaAs:C ⁺	GaAs:Ga ⁺ , C ⁺
$P_s (\text{cm}^{-2})$	$9.5 \cdot 10^{12}$	$3.23 \cdot 10^{13}$
$N_A (\text{cm}^{-2})$	$1.8 \cdot 10^{13}$	$5.96 \cdot 10^{13}$
$N_I (\text{cm}^{-2})$	$2.74 \cdot 10^{13}$	$8.74 \cdot 10^{13}$
$K(N_D/N_A)$	0.52	0.47

additional samples annealed at 900°C for 15 min., the sheet-hole concentrations were $9.5 \times 10^{12} \text{ cm}^{-2}$ for the single implant and $3.23 \times 10^{13} \text{ cm}^{-2}$ for the dual implants.

In order to examine the 900°C annealed sample in more detail, the electrical profiles shown in Fig. 30 were obtained. The profile integrity of the dual implants is much better than that of the single implant, both being compared to the LSS C^+ profile. A peak concentration of $\sim 20 \times 10^{18} \text{ cm}^{-3}$ was obtained in the dual implants. The profile was further analyzed to obtain effective values of the sheet-acceptor concentration ($\bar{N}_A, \text{ cm}^{-2}$) and the sheet concentration of the total ionized impurity ($\bar{N}_I, \text{ cm}^{-2}$). The effective compensation ratio is defined as $\bar{K} \equiv (\bar{K}_I - \bar{N}_I)/\bar{N}_A$ (the basic analysis technique is described elsewhere³⁵). The results are summarized in Table 7. In view of the difficulties encountered with the use of other measurement techniques (such as Auger or even SIMS analysis) at these doping levels (i.e., $\leq 10^{14} \text{ cm}^{-2}$), the present analysis technique is believed to be useful in generating meaningful results in the GaAs ion-implantation studies. The results of the profiling analysis will be discussed.

The fact that the electrical efficiency of the dual implant is 12% higher by a factor of ~ 3 than that of the single implant when annealed at only 700°C--is quite encouraging. Furthermore, the electrical efficiency of the dual implants annealed at 700°C is comparable to that of the single implant annealed at 900°C. The dual implants are expected to yield a higher doping efficiency than the single implant, even at low annealing temperatures.³¹ At a higher annealing temperature (900°C), this trend continues. At 900°C the electrical efficiency of the dual implants is 32%.

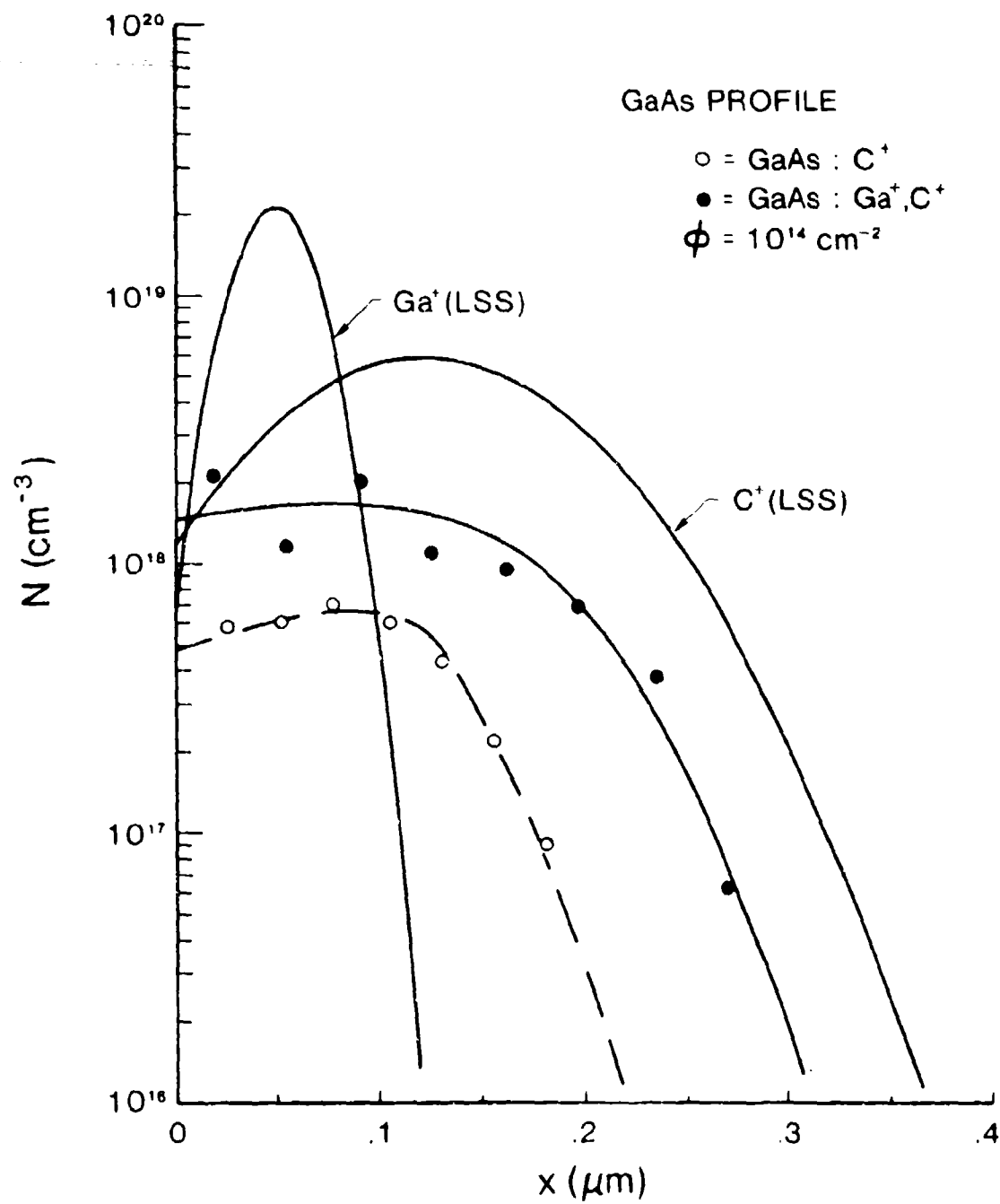


Figure 30. Profiles of Single and Dual C⁺-Implanted GaAs. For the Ga⁺ Implant, E = 120 keV; for the C⁺ Implant, E = 60 keV.

The profile analysis of both samples at 900°C indicates that the sheet-hole concentration P_g is lower than the calculated effective acceptor concentration \bar{N}_A (see Table 7). If \bar{N}_A is assumed to be the number of substitutional C atoms in As sites, then C atoms of only 18% for single implants and 60% for dual implants will be incorporated for the 900°C annealed samples and the remainder of the implanted C atoms cannot be accounted for. (Unlike this result, the $10^{13} \text{ C}^+/\text{cm}^2$ implantation in the previous study³⁵ indicated almost complete substitution of implanted C; the difference between 10^{13} cm^{-2} and 10^{14} cm^{-2} samples suggests strong dose-dependent annealing characteristics.) Annealing may induce outdiffusion of implanted C atoms in the implanted region, and encapsulation may play a significant role in this case. However, in Ref. 35, the lack of diffusion in the C^+ profiles was mentioned. This outdiffusion, if it is occurring, must be related to implant damage. Some of the implanted C atoms may occupy the Ga site (or, less probably, the interstitial site) and form electrically compensating (or inactive) centers. However, the value of the compensation ratio (K) is about the same for the single and the dual implants, while \bar{N}_A is higher for the dual implants than for the single implant. This suggests that "self-compensation" may be the predominant mechanism responsible for the lowering of electrical efficiency--not an uncommon process³⁹ in wide-band-gap binary semiconductors. The dual implants, therefore, appear to create a better annealing environment and minimize outdiffusion (and perhaps redistribution) of elements which contribute to the C doping process. In this way, the majority of the implanted C atoms may occupy a substitutional As site and become electrically active acceptor centers in GaAs.

Section 4

TRANSMISSION ELECTRON MICROSCOPY (TEM)

TEM studies of several implanted GaAs samples made during the last year resulted in the following important observations:

4.1 Si^+ -IMPLANTED Cr-DOPED GaAs

A Cr-doped GaAs single-crystal polished wafer having <100> orientation was implanted with Si^+ ions to a dose of $3 \times 10^{15}/\text{cm}^2$ at 120 keV at room temperature. Thin foils for TEM observations were prepared by jet polishing, using a bromine-methanol solution as described earlier [40]. A typical electron micrograph and the corresponding selected-area diffraction pattern obtained from an Si^+ ion-implanted specimen are shown in Fig. 31. The foils contained a high density of black spots with an average size of 60 Å. The majority of them exhibited black-white (B-W) contrast and a few exhibited double-arc contrast. The selected-area diffraction pattern revealed the presence of extra reflections (marked by * in the schematic diagram) resulting from precipitates. The d-spacings corresponding to the extra reflections A, B, and C can only be matched with (210), ($\bar{1}$ 21), and ($\bar{3}$ -12) planes, respectively, of SiAs_2 which has a cubic structure (Table 8). Good agreement between the measured and the calculated angles of different planes due to precipitates can be observed (Table 9).

Although the intensities of these extra reflections were weak, dark-field imaging techniques using these extra reflections could be attempted to reveal the SiAs_2 precipitates in the micrograph, which would aid in separating

the precipitates from the unresolved dislocation loops which appeared in the form of black spots in the micrograph. A few dislocation lines were also observed (shown by arrow).

4.2 ANNEALING STUDIES OF S^+ IMPLANTS

The microstructural changes in Cr-doped GaAs having $\langle 100 \rangle$ orientation implanted with S^+ ions at 120 keV to a dose of 10^{15} ions/cm² at room temperature were studied as a function of annealing temperature from room temperature to 860°C. The experiment was carried out inside an electron microscope equipped with a hot stage, and no capping of the implanted layer was used.

In the as-implanted condition, the image had a mottled appearance although a large number of small black spots could be seen (Fig. 32). The selected-area diffraction pattern showed the presence of diffuse rings characteristic of an amorphous material. Post-implantation in situ annealing at 330°C for 5 min. resulted in a complete elimination of the inner diffuse ring and the development of streaking along two mutually perpendicular directions around the (002) and (220) diffraction spots of GaAs (Fig. 33). However, the development of (002) spots had yet to take place. Observation of the elimination of the diffuse ring strongly suggests that recrystallization of the amorphous layer has taken place. Since no evidence of a polycrystalline material can be found in the diffraction pattern, it is speculated that single-crystal layers having identical orientation with respect to the substrate started to grow epitaxially on the substrate and consumed the amorphous layer during annealing at 330°C for 5 min. The streaking along two mutually perpendicular directions around the (002) spot on GaAs is due

TABLE 8

MEASURED d-SPACINGS FROM EXTRA REFLECTIONS AND THEIR ASSIGNMENT BASED UPON THE SiAs_2 STRUCTURE

	Measured d-Value of Precipitate	Calculated d-Value of SiAs_2 (Plane)
doA	2.679 Å	2.693 Å (210)
doB	2.418 Å	2.458 Å (211)
doC	1.617 Å	1.609 Å (321)

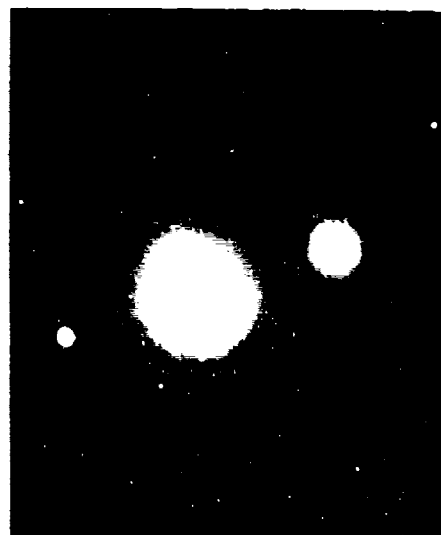
TABLE 9

COMPARISON OF MEASURED AND CALCULATED ANGLES (BASED UPON THE SiAs_2 STRUCTURE) OF DIFFERENT PLANES DUE TO PRECIPITATES

Plane	Measured Angle	Calculated Angle
(210) \wedge (121)	90°	90°
(210) \wedge (312)	133°	126.7°
(121) \wedge (312)	42°	40.2°



(a)



(b)

Figure 32. Bright-Field Electron Micrograph

- (a) Showing Mottled Microstructure Due to the Presence of Amorphous Layer as Evidenced by Diffuse Rings in the Diffraction Pattern
- (b) in Cr-Doped GaAs Implanted with S^+ Ions (120 keV) at Room Temperature to a Total Dose of 10^{15} ions/cm². A large number of black spots can also be seen in (a). $[111]$ orientation near (100) .

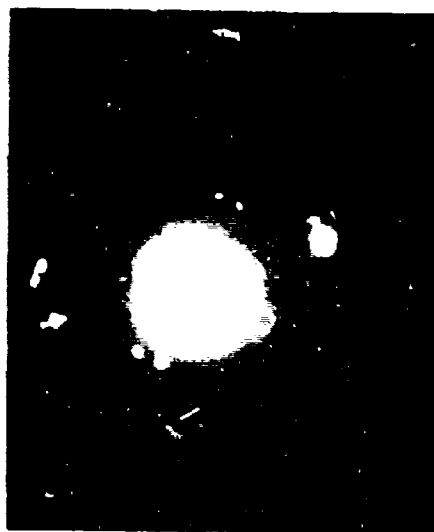


Figure 33. Elimination of Inner Diffuse Ring and Formation of Streaks along Two Mutually Perpendicular Directions around (002) and (220) Diffraction Spots of GaAs as a Result of In Situ Annealing at 540°C for 5 Min. Inside an Electron Microscope in etched GaAs irradiated with 2×10^{15} ions (120 keV) at Room Temperature to a Total Dose of 10^{15} ions/cm². Film orientation near (100).

to the formation of microtwins on the (111) plane of GaAs. Narayanan and Spitzer [41,42] have made similar observations in P^+ , N^+ , and Si^+ ion-implanted GaAs.

A new feature in the form of black spots began to appear during annealing around 600°C. In addition, the foil seemed to have a higher transparency with respect to the electron beam. This behavior may be attributed to a loss of As from the foil which effectively reduces the foil thickness. The black spots were found to grow in size at higher annealing temperatures and times. They could be easily resolved as dislocation loops at 790°C (Fig. 34). At 860°C, the dislocation loops grew by coalescence with a significant lowering of loop density, as shown in Fig. 35(a). Although streaking could be found after annealing at 730°C for 5 min, annealing at 860°C resulted in complete elimination of streaking around (002) and (220) spots and also resulted in development of (002) spots [see Fig. 35(b)]. No precipitates were found in the S^+ -implanted Cr-doped GaAs.

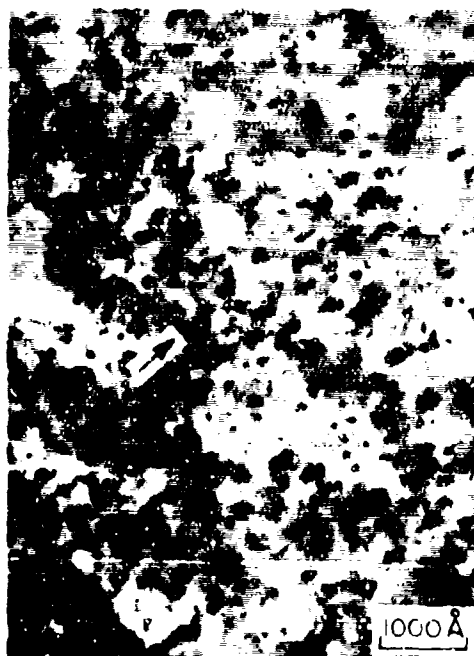
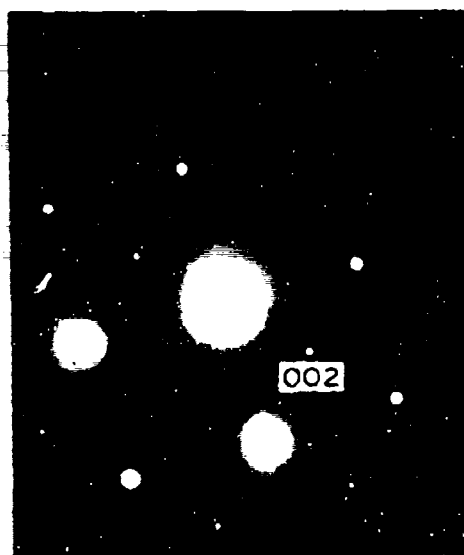


Figure 34. Observation of Dislocation Loop Formation during *In Situ* Annealing at 730°C for 5 min. Inside an Electron Microscope in Cr-doped GaAs. Incident electron beam (120 keV) at Room Temperature to a Total Dose of 10^{15} ions/cm². Film Orientation near (100).



(a)



(b)

- Figure 35. (a) Same Area as in Previous Figure. Annealing Temperature and Time are 860°C and 5 min., Respectively. Dislocation loop (marked by arrow) has grown larger but loop density is lower than that observed in previous figure.
- (b) Selected-Area Diffraction from Area (a). Note absence of streaking and development of (002) matrix spots. Foil orientation near (100).

Section 5

DEEP-LEVEL-TRANSIENT SPECTROSCOPY (DLTS)

5.1 INTRODUCTION AND EXPERIMENTAL TECHNIQUE

Deep-level-trap spectroscopy (DLTS) (also called fast capacitance) is a sophisticated technique for studying trapping states in the depletion region of a p-n junction or Schottky barrier. The technique can be applied to a wide variety of devices containing many types of traps and can yield considerable insight into material characterization, device performance and reliability, and evaluation of special processing technologies such as ion implantation and epitaxial growth.

A p-n junction held in reverse bias V_B will have a depletion region of width

$$W(V) = \left[2 \cdot (V_B + V_{bi}) / N^- q \right]^{1/2}$$

where V_{bi} is the junction built-in potential and N^- is the density of charge at the edge of the depletion region. The exact form of the relationship will depend upon the type and shape of the junction. Traps in this region will be generally empty, and the junction will have a defined capacitance. If the junction is brought into forward conduction by an electrical pulse, the injected charge will be trapped according to the particular kinetics of the traps and will also recombine after thermal emission from the metastable traps. The trap filling is described for each species of injected charge by

$$N(t) = N(\infty) (1 - e^{-t/\tau})$$

where $N(t)$ is the concentration of filled traps at time t and τ is a characteristic trap-filling time. The characteristic trap-filling time is further described by

$$\frac{1}{\tau} = \sigma(V)n + \frac{1}{T_1} + e_1$$

where σ is the capture cross-section of the trap, T_1 is the hole-recombination time of a filled trap, and e_1 is the thermal-emission rate of a trapped charge.

When the pulse is removed, no further charge is injected, the depletion width returns to $W(V)$, and the change in charge population produced during the pulse is reflected by a change in junction capacitance. The trapped charge recombines by means of thermal emission according to the kinetics of the trap and the spectrum of defect states. The spatial region in which this occurs is the depletion width. If the depletion region is ideal (i.e., there is zero free-carrier concentration), recombination will be by thermal emission only. The decay is not purely exponential because the change in hole concentration at the outer edge of the depletion region is not sharp but quadratic. The changing population of trapped charge in the depletion region is observed experimentally as a transient capacitance. It should be noted that the time required for decay may range from nanoseconds to many milliseconds, depending upon the nature of the trap.

If a second pulse is imposed on the junction shortly after the initial pulse, the effect of hole recombination can be evaluated. The second pulse

is of magnitude V_c which is less than V_B ; hence, the depletion width is reduced accordingly which permits that portion of the material no longer in the depletion region to act as neutral material, hole recombination being dominant. The second pulse is called the "clear" pulse which is reasonable since it serves to "clear" traps in a portion of the depletion region and injects no new charge into the traps. Hence, the quantity T_1 can be evaluated as a function of the clear-pulse width. The trap-concentration profile across the depletion region can be determined by variations of the clear-pulse height. Different clear-pulse heights "clear" different widths of the depletion region; therefore, an orderly series of measurements produces a profile of the entire region.

These pulse sequences and their effects upon the capacitance signal can be seen more clearly by reference to Fig. 36. The injection pulse brings the diode into forward conduction, resulting in an injection current. The clear pulse has a smaller magnitude than the injection pulse. The decay of capacitance signal after the injection pulse results from both hole recombination and thermal emission. The decrease in signal amplitude after the clear pulse is a measure of the hole recombination. It should be pointed out that the real experimental situation is not so clear cut as in this schematic. The pulses tend to overload the amplifier, and there is frequently "ringing" as a result of the fast pulses--two factors that tend to obscure the initial decay shapes. Also, in the schematic a positive capacitance change is shown, indicating the trapping and decay of a minority-carrier trap. If a majority-carrier trap had been shown, the capacitance change would be negative.

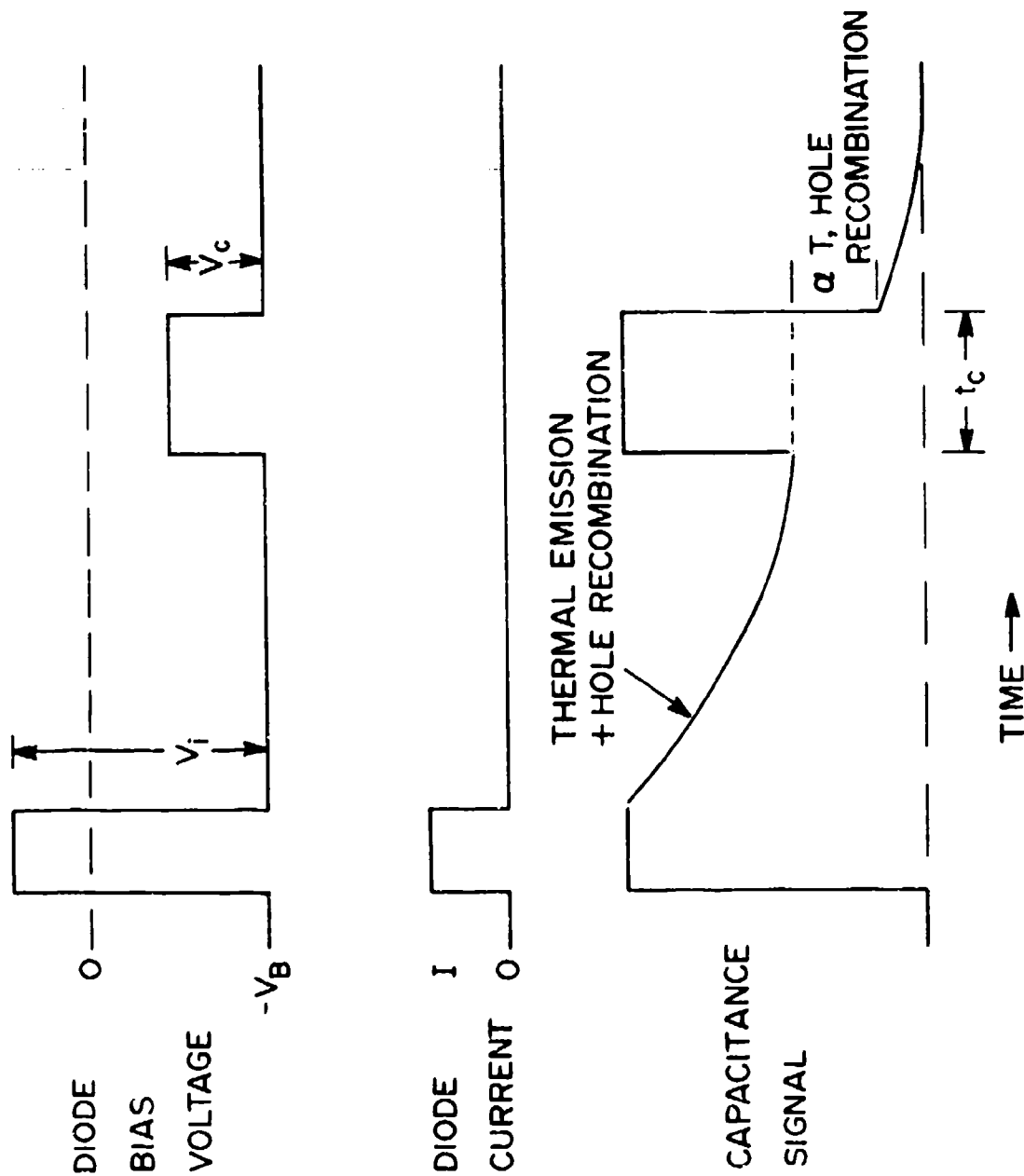


Figure 36. Schematic Diagram of Pulse Sequence, Charge Injection, and Capacitance Signal for Fast-Capacitance Experiment.

Thermal emission from the traps is a strong function of temperature. A simplified version of the temperature dependence of emission rates is

$$e_1 = \frac{\sigma N}{g} \exp(-\Delta E/kT)$$

where e_1 is the thermal-emission rate, σ is the capture cross section, N is the density of states in the band, g is the degeneracy of the trap level, ΔE is the thermal activation of the trap, and T is the temperature. The application of the expression depends upon such parameters as the type of material (n- or p-type) and the sign of the carrier (electron or hole), but the expression is handled in much the same way as the expression for thermoluminescence and thermally stimulated conductivity.

The temperature dependence of the transient capacitance is given in Fig. 37. On the left-hand side of the figure is a series of capacitance transients at various temperatures. The difference in capacitance during a time interval t_1 to t_2 is plotted on the right-hand side of the figure. At low temperature very little thermal emission takes place between t_1 and t_2 . At high temperatures the trapped charge recombines almost immediately, yielding no change in capacitance during the data-sampling time. A plot of the entire series yields the temperature dependence of the thermal emission from the trap--essentially a thermoluminescent glow curve. From this curve one can determine the thermal activation energy of the trap which is closely related to the energy separation between the trap and one of the bands. Since one is able to study traps having activation energies ranging from < 0.1 eV to > 1 eV, the temperatures to be scanned will range from liquid-He temperature to several hundred degrees above room temperature.

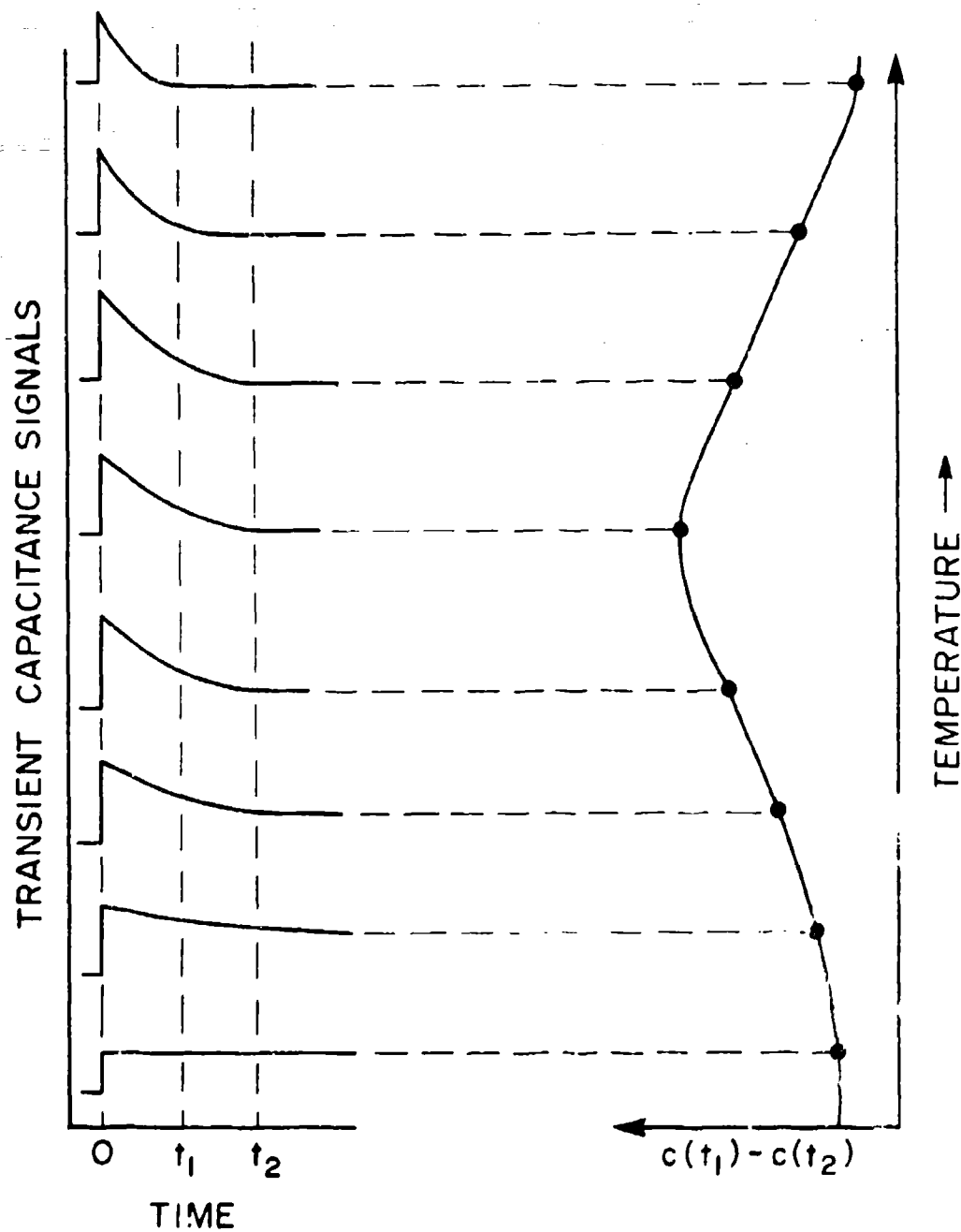


Figure 37. Temperature Dependence of Transient-Capacitance Signals.

For the transient-capacitance experiment, the diode is held in reverse bias in an ac capacitance bridge with the pulses superimposed on the diode under test. The choice of bridge depends upon the sample or junction being studied. For epitaxial GaAs, the sheet resistivity is very high, resulting in long transient decay times; hence, the frequency must be kept low and a bridge operated at 1 MHz is quite appropriate. For p-n junctions such as those used for light-emitting diodes where decay times are extremely short, a high-frequency bridge must be used to obtain clear resolution.

The basic electronics of the DLTS system are shown in Fig. 38. The basic instrument for making measurements was a Boonton 72BD 1-MHz capacitance bridge. The bias as well as the pulses are provided by the Systron-Donner 110B pulse generator. A very important piece of apparatus is the buffer/baseline restorer, developed and built by SRL. This unit not only eliminates noise but permits one to operate the Boonton on a more sensitive scale and prevents overload/memory problems with the double boxcar integrator.

The temperature of the sample was varied from 10 to 400°K using an Air Products Helitran. Thermometry, shielding, and electrical isolation were some of the problems that had to be solved in order to obtain meaningful measurements.

As an example of the energy determination, Fig. 39 shows three curves for a high-temperature trap, recorded using different emission-rate windows as defined by the boxcar settings. The temperatures at which the peak occurs are then plotted as a function of the emission rate on an Arrhenius plot as in Fig. 40 for a determination of thermal activation energy E .

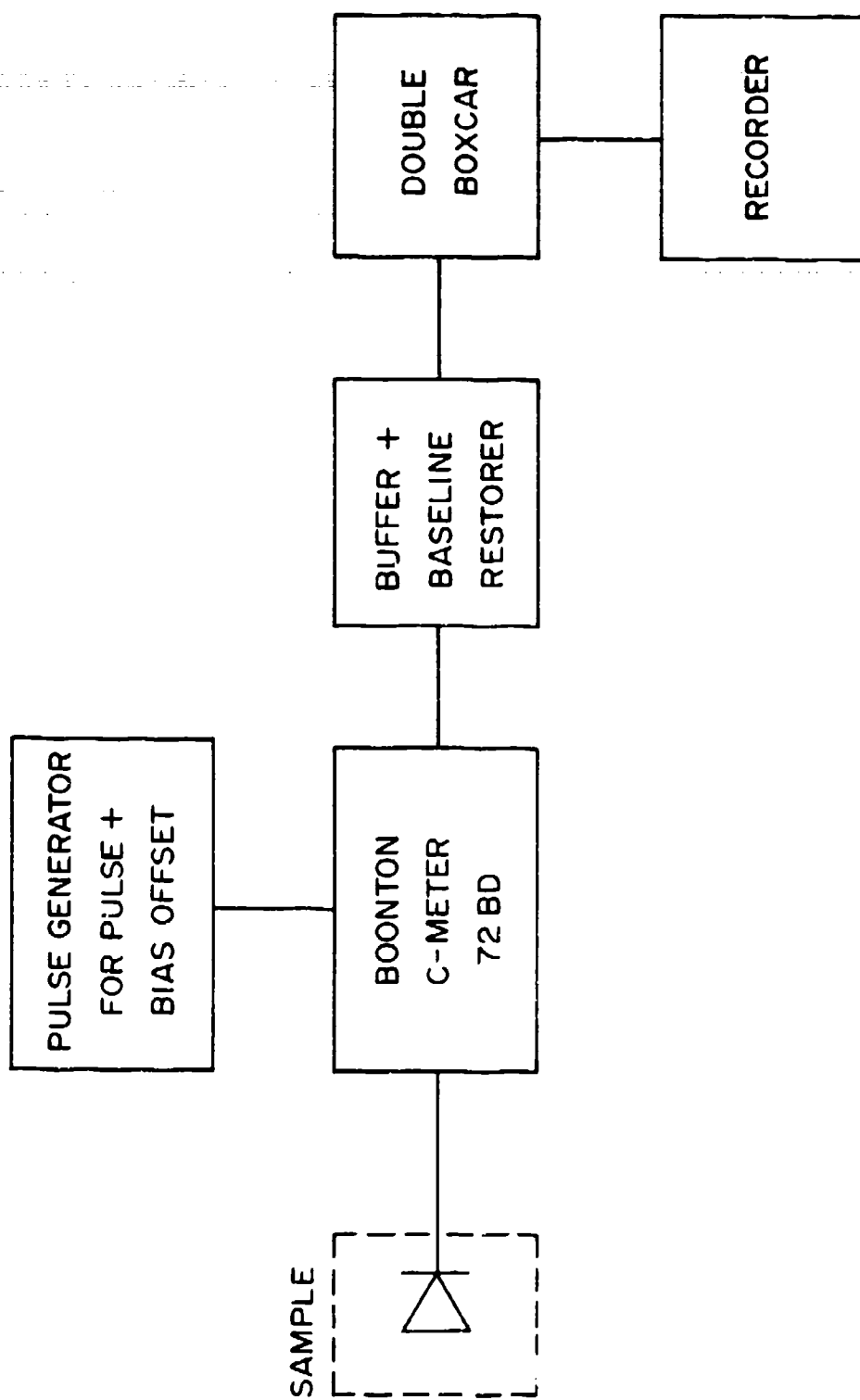


Figure 33. Simplified Schematic of DTS Experiment.

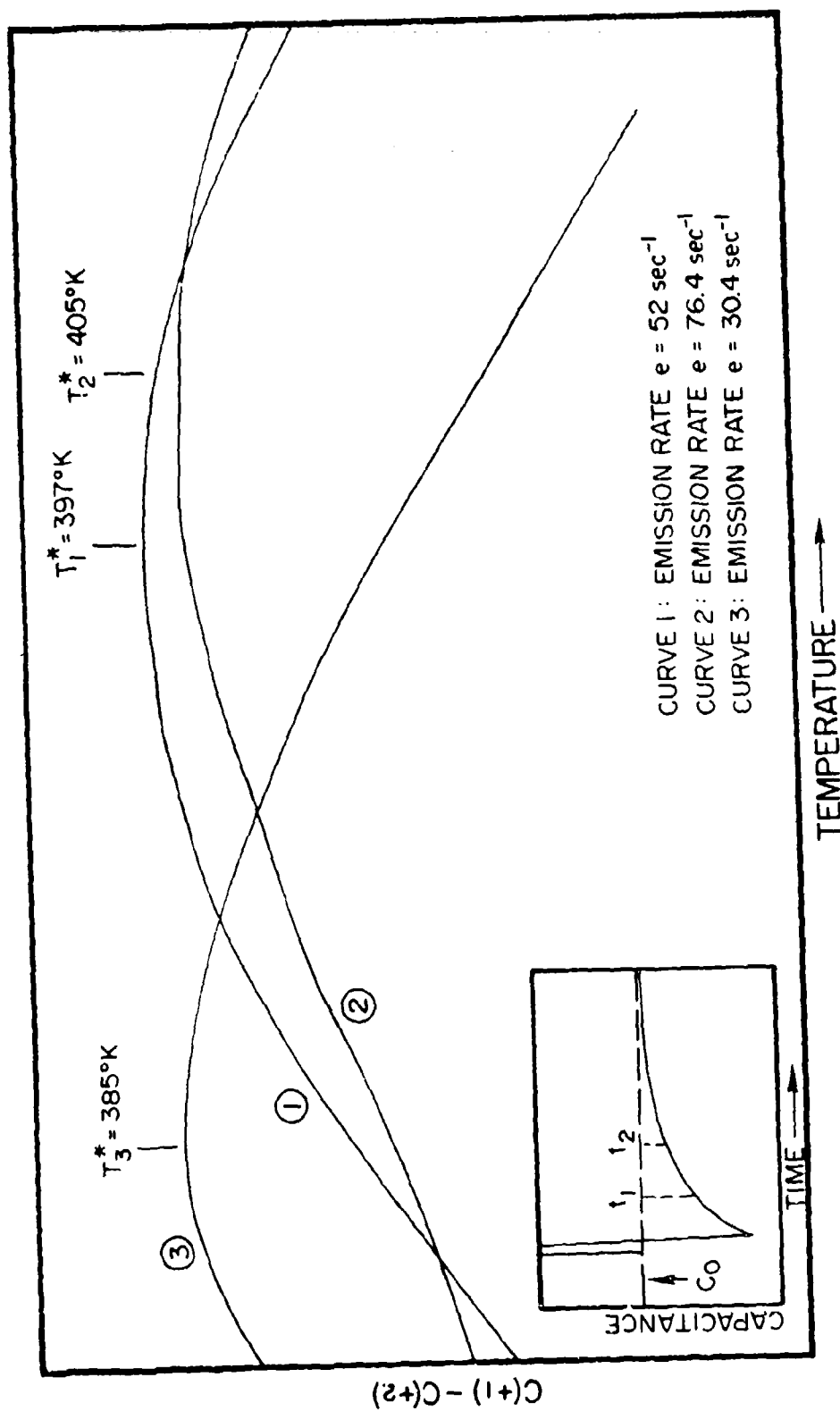


Figure 39. Example of Peak Shift with DLTS Emission-Rate Window.

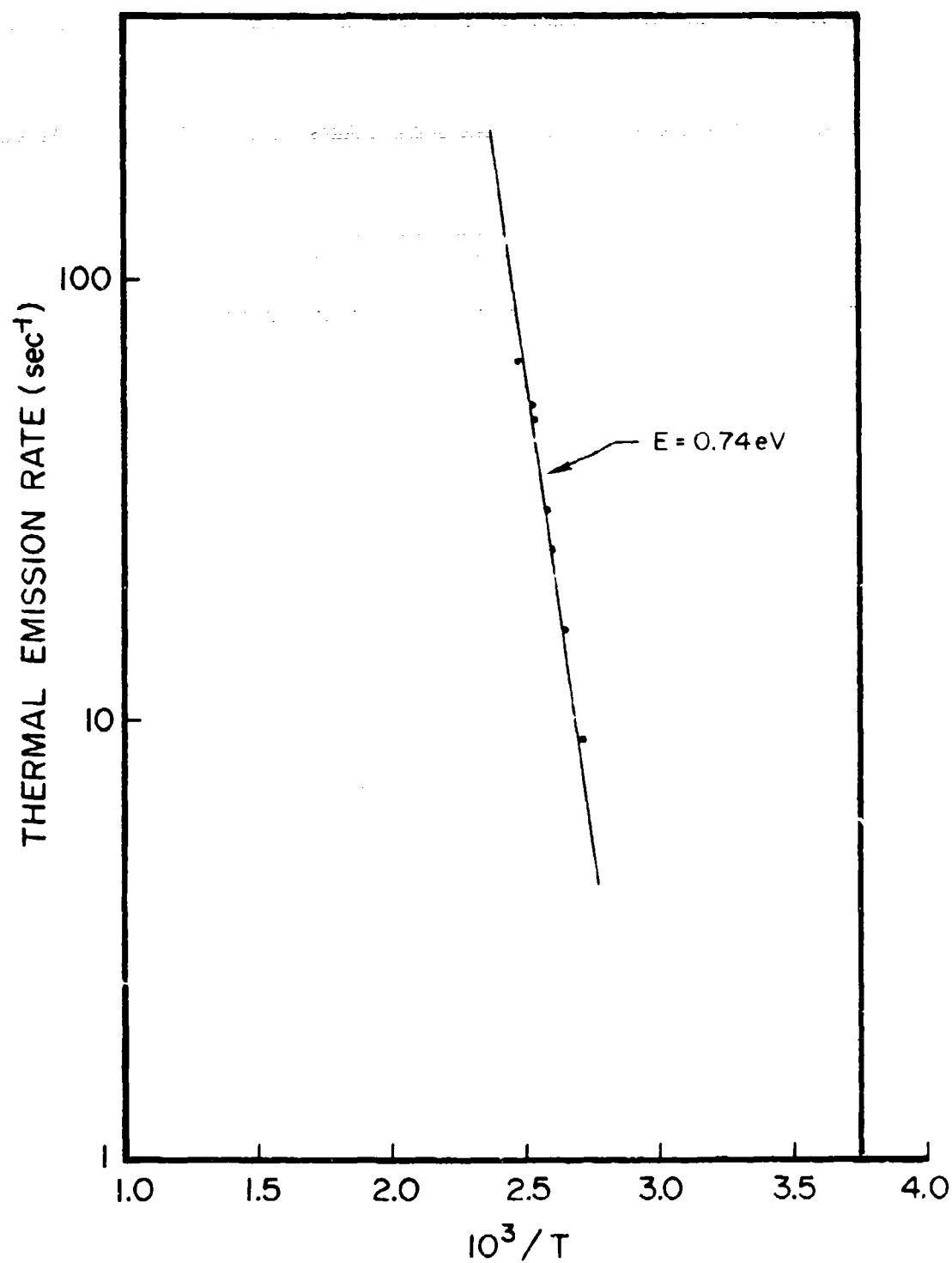


Figure 40. Typical Plot of Thermal-Emission Rate as a Function of Peak Temperature.

The DLTS experiment can be utilized for the following applications:

- Nearly any p-n junction or Schottky barrier having suitably low forward resistance to permit convenient charge injection by the pulses can be studied. Nominal values of 10 to 100 Ω have been found to be most reasonable.
- Junctions buried below the surface of the device can be analyzed readily because of the electrical nature of the measurements. This technique is particularly useful for studying traps at the interfaces of epi-layers and substrates or for studying material behavior under metal-electrode contacts.
- Epitaxial layers can be analyzed for trapping defects introduced in the epi-reactor or created at the interface with the substrate. The experiment can be either a routine analysis of epi-batches or a fundamental study of trapping states in devices.
- Concentrations of traps can be profiled as a function of distance from the junction which is particularly useful for ion-implanted layers and for devices such as READ diodes that depend upon accurate concentration changes.

The following information may be obtained from a study of traps by means of transient capacitance:

1. Sign of the trapped charge (electron or hole), which is revealed immediately by the sign of the capacitance change.
2. Concentration and population of the traps. The magnitude of the trap population is proportional to the magnitude of the capacitance change. The technique may be sufficiently sensitive for measuring capacitance changes from as few as 10^{12} centers/cm³.
3. Thermal-activation energy or depth of the traps. The temperature at which the most trapped charge is released per unit time is directly related to the thermal-activation energy of the trap. Activation energies from ~ 0.1 to ~ 1.0 eV in GaAs can be studied in the same sample.
4. Capture cross sections and kinetics of capture which are measured by the shape of the capacitance change during charge injection.
5. Emission and recombination kinetics of trapped charge. Measurement of the shape of transient decay curves yields the emission rates of the traps. The emission rates of different traps may vary by several orders of magnitude.
6. Profile as a function of depth of trapping centers. A plot of the clear-pulse height (which determines the depletion width) as a function of change in capacitance yields concentration of traps as a function of distance from the junction.

7. Minority carrier recombination. From the different widths of the clear pulses, the hole-recombination time for the material can be calculated.

8. Separation of types of defects and defect clusters. Individual defects or trap types have different thermal emission rates and different recombination times, in some cases varying by several orders of magnitude. Also, combinations of defects have unique emission rates, i.e., the properties of Zn, O, and Zn-O traps in GaP have different thermal-emission rates which can be clearly separated.

9. Radiative as well as non-radiative transitions can be studied.

5.2 SAMPLE PREPARATION, TEST PATTERNS, AND PRELIMINARY TESTING

Samples were prepared in basically two different geometries. In one case, the samples consisted of undoped bulk-grown GaAs or epitaxial GaAs grown on degenerate n^+ Te-doped substrate material, on which the Schottky barriers were formed by evaporating Au or Al dots on the active layer with ohmic contacts on the back. In the other case, epitaxial GaAs on semi-insulating GaAs was fabricated into FET-like test patterns by mesa-etching and metal evaporation using photolithographic techniques at AFWAL/AADR. One portion of the test pattern is shown in Fig. 41. This die consists of four FET-like structures (with 25- and 12.5- μ gates), a simple Schottky ohmic pair, and a set of three ohmic contacts with X and 2X spacings for distributed feedback analysis.

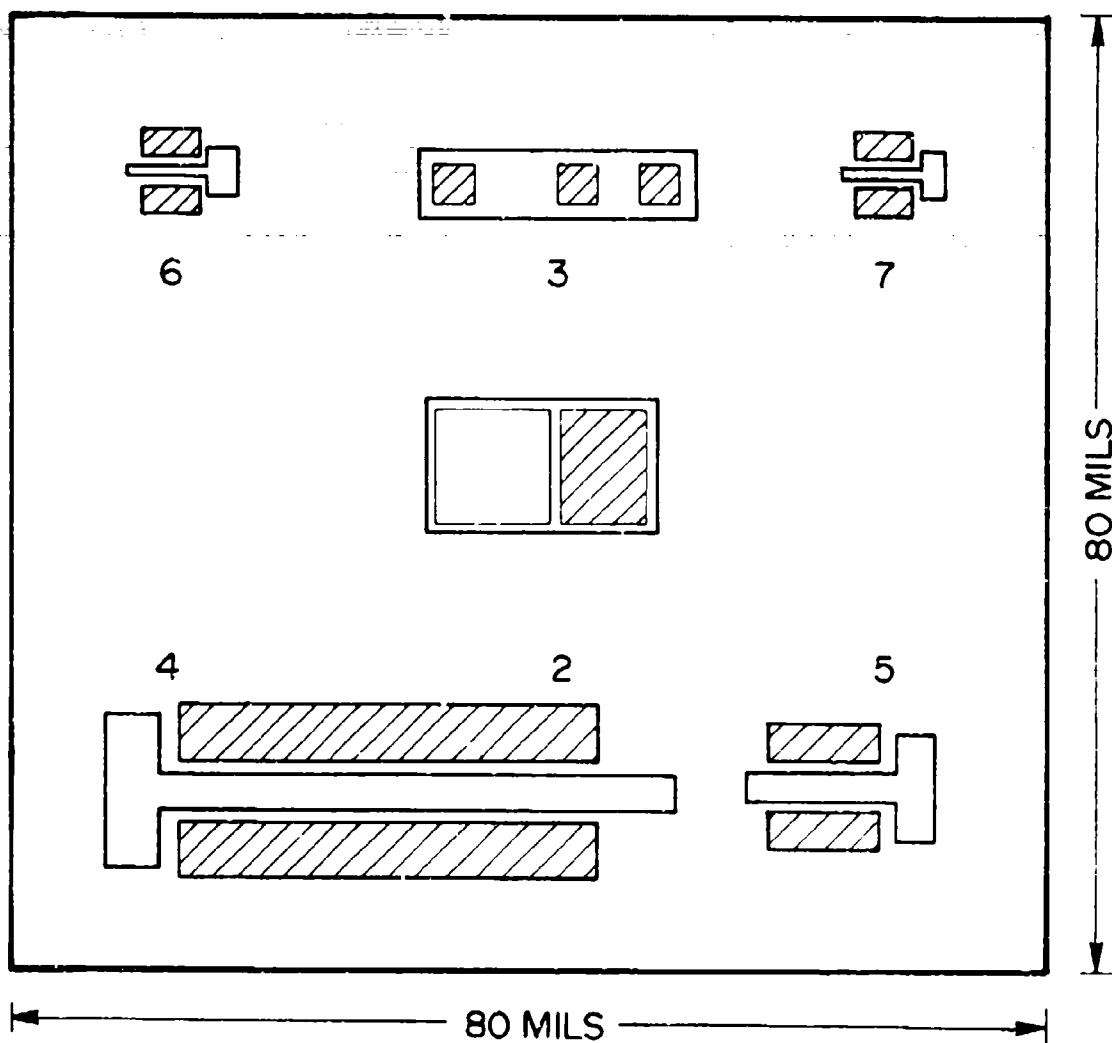


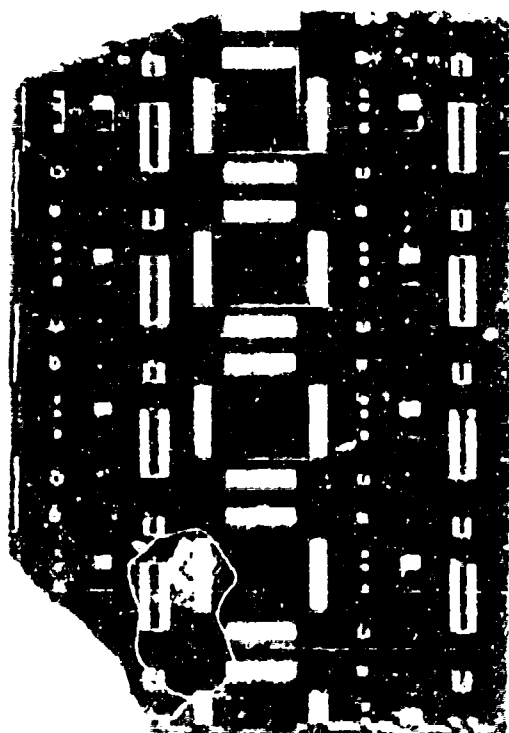
Figure 41. FET-Like Test Pattern for DLTS Measurements.

The wafers were characterized by C-V and I-V analysis, using probes in attempts to determine variations in basic properties across the wafer. Maps of these characteristics were generated to aid in the evaluation of the processing as well as the material, and these maps were used to select individual dies for further study. Individual dies were cut from the wafer and packaged on special all-metal T05 headers for use in the helitran. The individual devices were wire-bonded using an ultrasonic wire-bonder. The wafer and a bonded device are shown in Fig. 42 and typical I-V characteristics are shown in Fig. 43.

Figure 44 shows the results of C-V profiles, translated into N-W curves, for two devices on different dies of the same wafer. The wafer (R19) was an epitaxial GaAs wafer grown on a Cr-doped substrate. The dies (Nos. 6 and 30) exhibited dramatic differences in carrier profiles. Light chemical etching of the surface enhanced the apparent buried layer on Die 30. Sharp-line photoluminescence data taken by D. C. Reynolds indicated large differences in the shallow centers of the two dies.

5.3 RESULTS

The results of these studies are divided into three main categories: ion implantation, device-grade FET material, and miscellaneous studies which will include undoped substrate material and a study of electron damage in GaAs.



GaAs EPITAXIAL WAFER R9



BONDED DEVICE R9-3-5

Figure 12. Epitaxial wafer and bonded device for DTS Experiment.

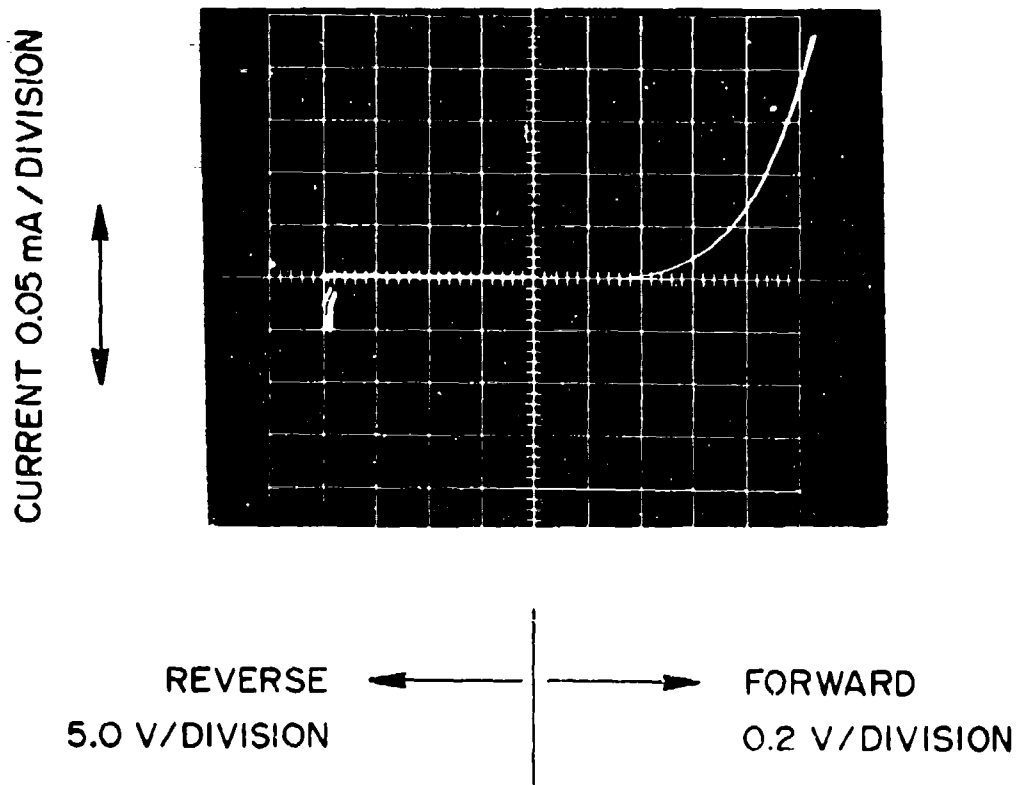


Figure 43. Typical I-V Characteristics of an Epitaxial DLTS Sample.

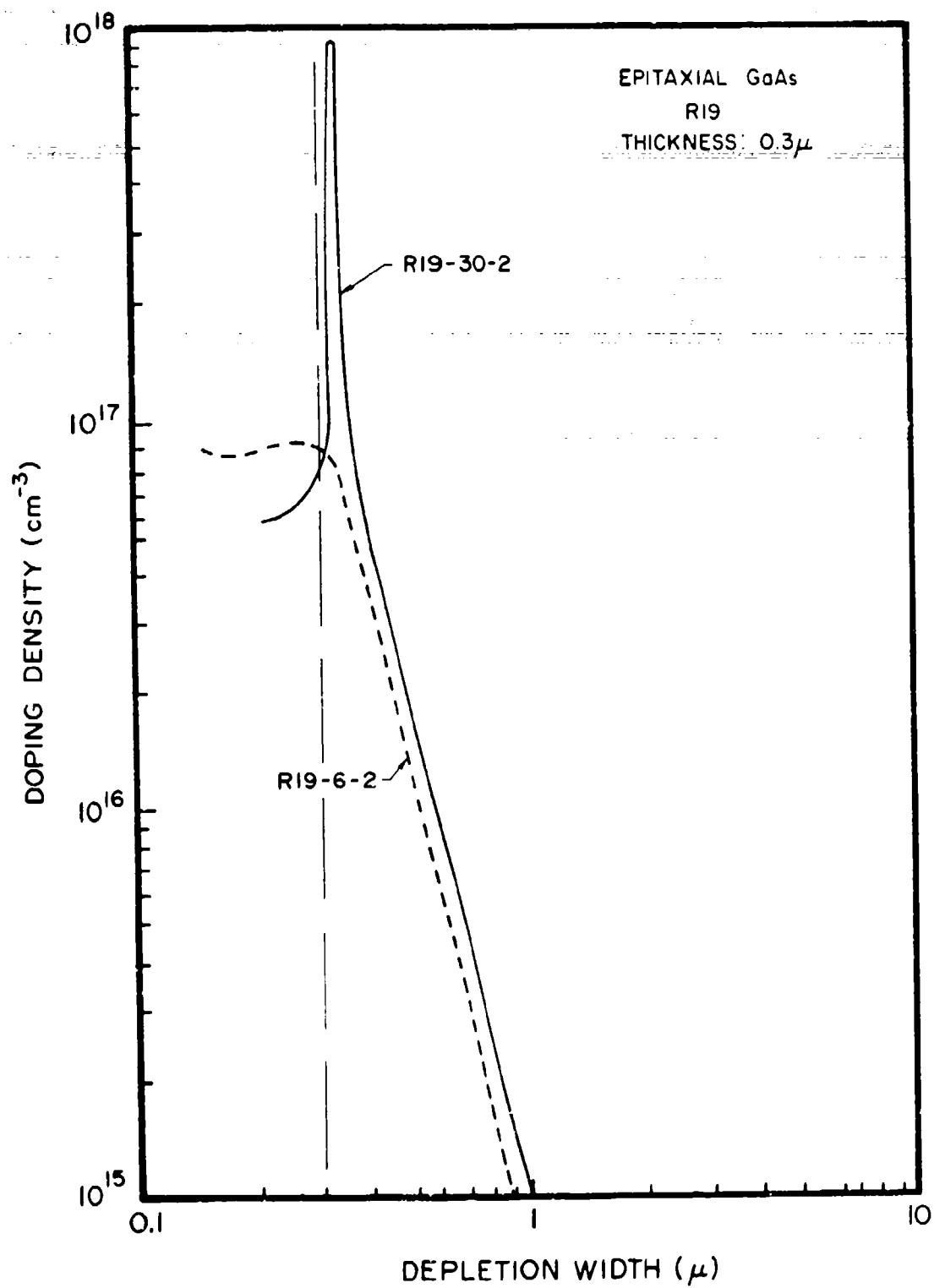


Figure 44. Example of N-W Variations on a Particular Wafer (R19) Between Different Dies (30 vs 6) as Determined by C-V Profiling.

Ion Implantation

DLTS is not currently a standard technique for the analysis of ion-implanted layers. Therefore, great care must be taken to assure that the equipment is performing adequately in more well-known sample systems. Figure 45 is a DLTS spectrum obtained from an "as-grown" piece of vapor-phase epitaxial GaAs on a conducting Te-doped substrate. Two DLTS peaks were observed which represent native defects in the material. In the literature, the peak at 200°K has been associated with a Ga vacancy through circumstantial evidence. The peak at 374°K has been associated with oxygen and chromium. These peaks were very well behaved under DLTS analysis and yielded uncorrected thermal activation energies of about 0.47 and 0.97 eV. The DLTS "figure of merit," $\Delta C/C$, was 10^{-4} with a sensitivity-above-noise of nearly 10^{-5} . This is about "state-of-the-art" for DLTS. Also, the heating rate employed was selected to yield nearly zero thermal hysteresis.

As a demonstration of the system, a rough profile of the trap density was generated using three different reverse-bias pulse combinations such that the trap signal originated from three different spatial regions below the surface of the sample. Data from these experiments are shown in Fig. 46. From these signals the trap densities were calculated; from the bias conditions, the depletion depths were calculated. The results are shown in Fig. 47 superimposed on the original N-W plots for the carrier concentrations. The trap-density curve is parallel to the carrier-concentration profile, but offset by three orders of magnitude.

As further demonstration of the system and technique, this epitaxial sample was subjected to 1-MeV electron bombardment at a dose of $2 \times 10^{13} \text{ cm}^{-2}$,

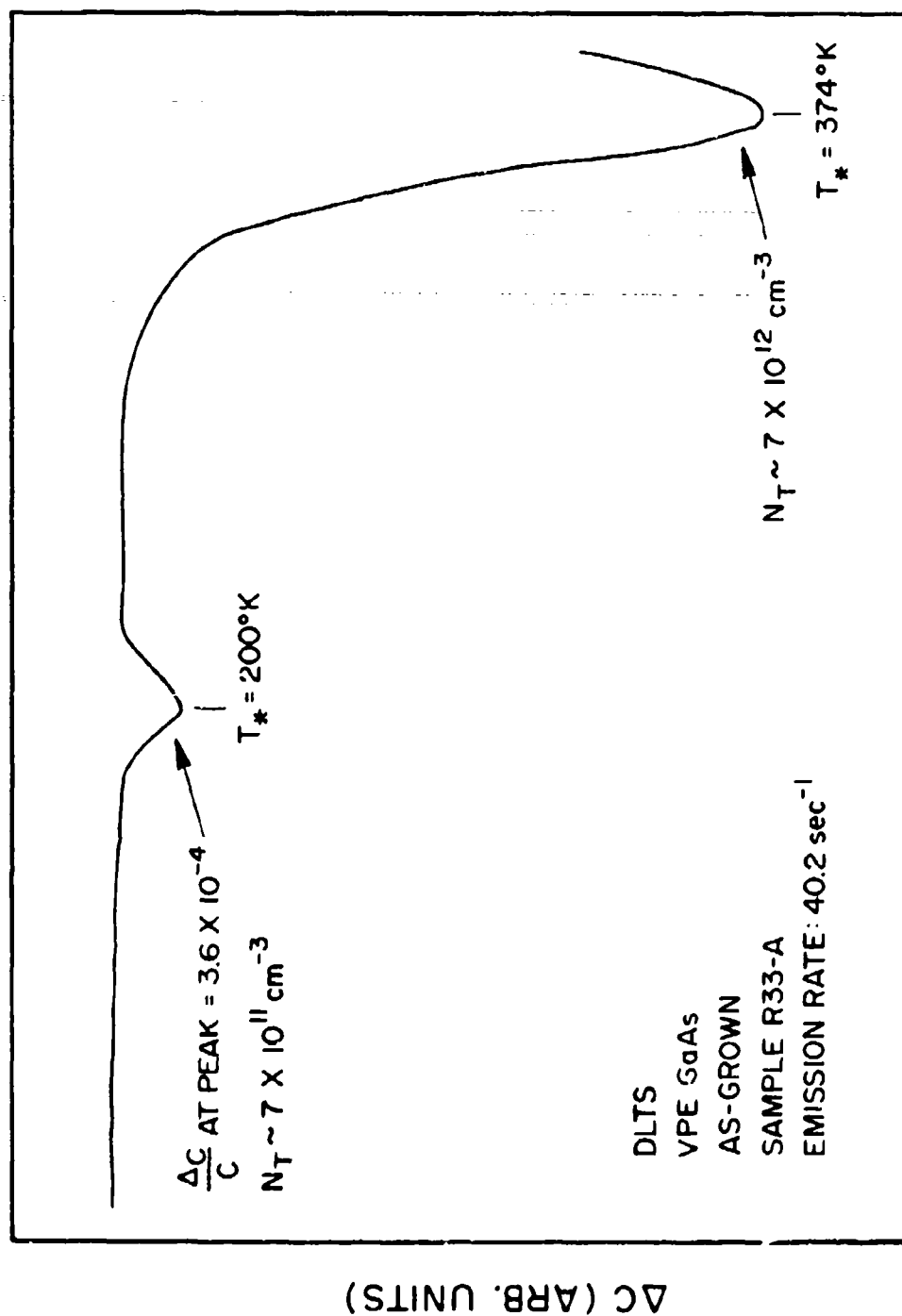


Figure -5. DLTS Spectrum of "As-Grown" VPE GaAs.

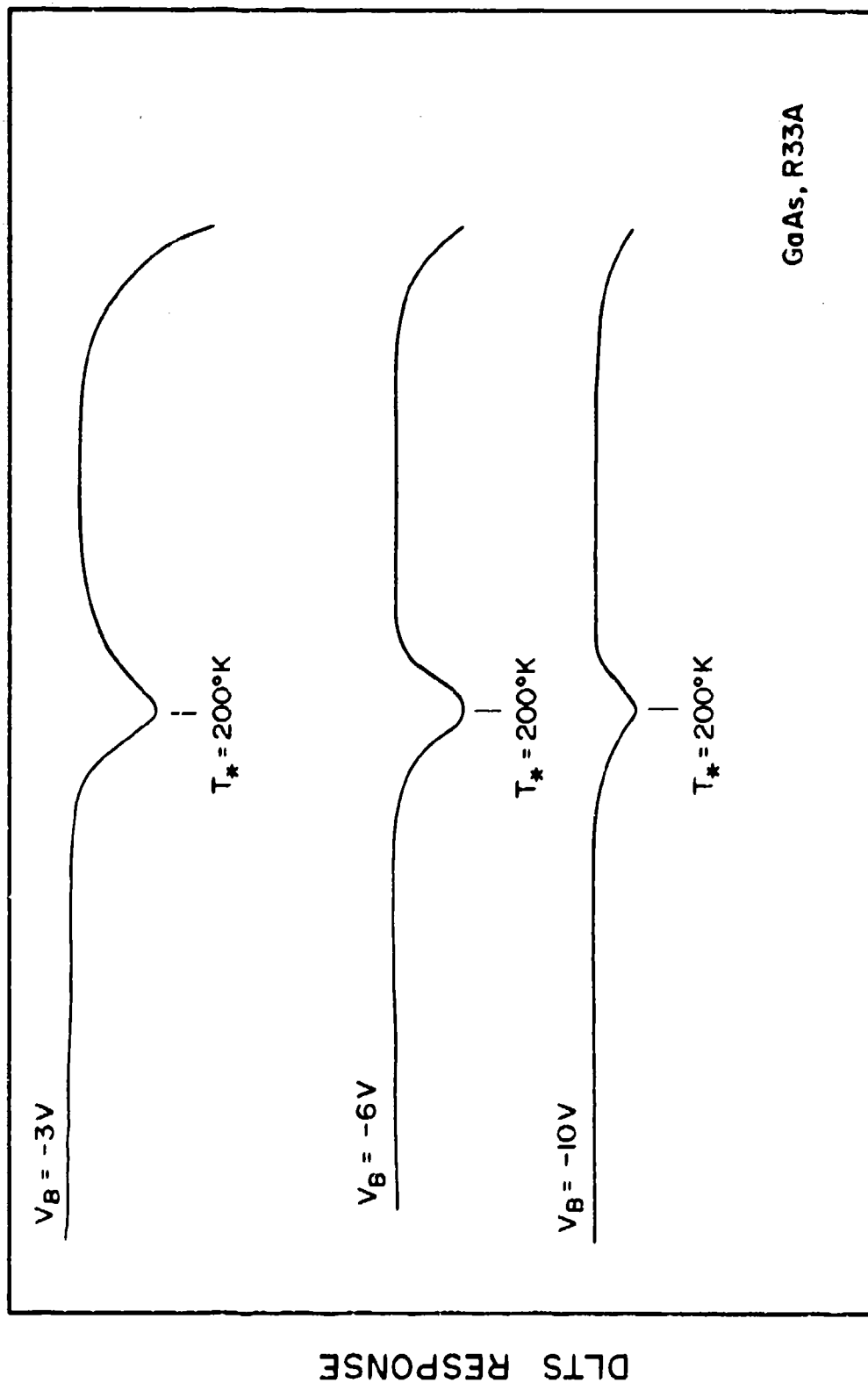


Figure 46. DLTS Data for Profile Measurements in As-Grown VPE GaAs.

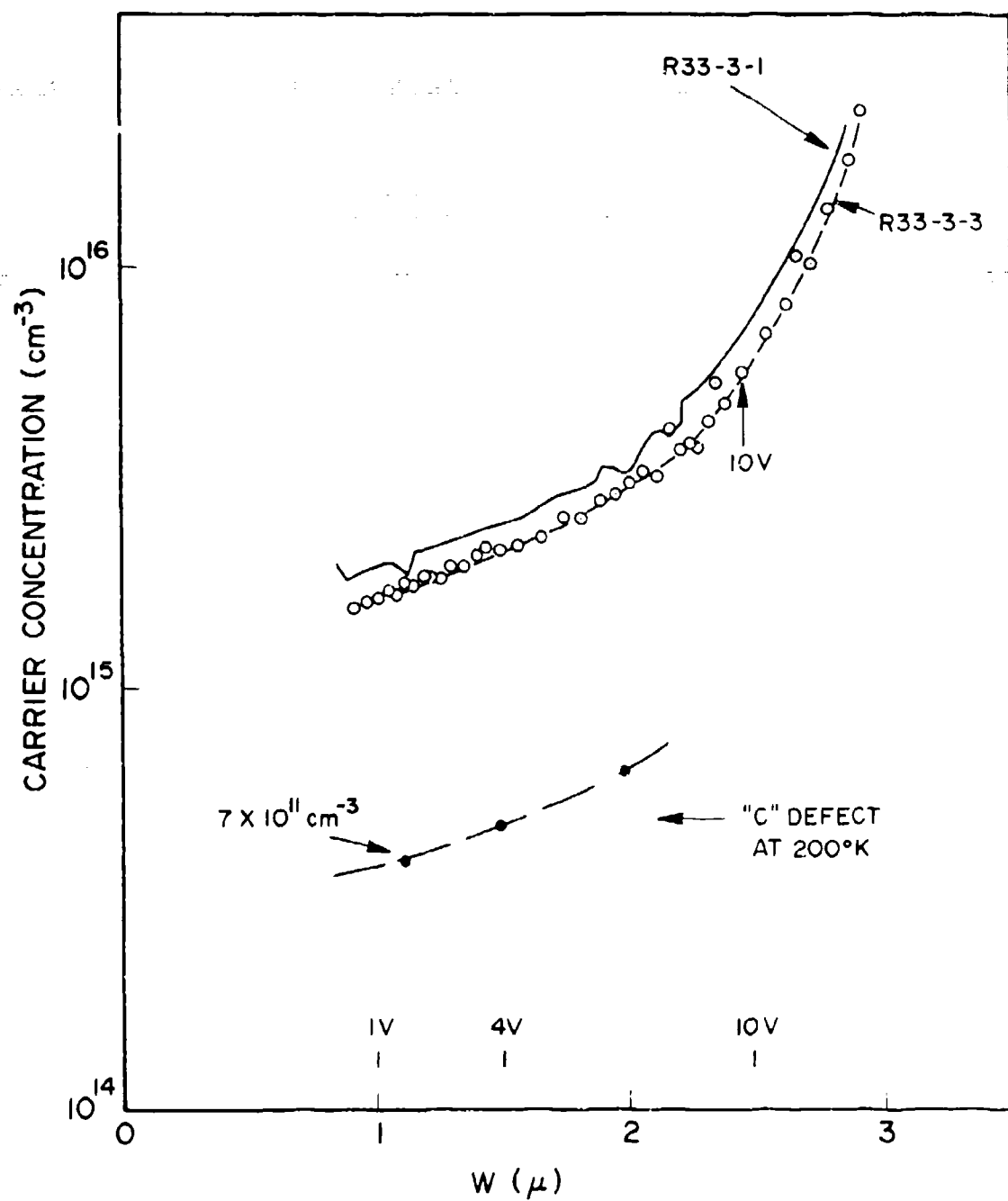


Figure 47. Carrier-Concentration Profiles from C-V Measurements and Trap-Concentration Profile from DLTS Measurements.

yielding a 1% carrier removal. Figure 48 shows that the native defect at 374°K was unaffected, and the native defect at 200°K grew according to the well-known production rate of the radiation-damage peak known as E3. The sharp low-temperature peaks at 35 and 75°K (known in the literature as E1 and E2) had been observed on numerous occasions. Figure 49 is a plot of the DLTS spectrum after 2% carrier removal by electrons. These figures indicate excellent DLTS behavior, excellent sensitivity to very modest electron irradiation, and excellent thermometry.

A large piece of the same VPE GaAs wafer from which the as-grown and electron-damage spectra were taken (Figs. 45 and 49) was implanted with Ar^+ at 150 keV. A series of samples with different annealing conditions was prepared from this slice. Figure 50 is the DLTS spectrum from an as-implanted piece that had been implanted to $10^{15}/\text{cm}^2$. The native defects which yielded peaks at 200 and 374°K in the as-grown and electron-irradiated samples were observed again. Peaks near 75°K may be complex versions of the E1 and E2 electron-damage peaks shown in Fig. 49. In addition, several new peaks were observed and a very large peak at about 260°K dominated the spectrum. Clearly, the ion implantation of Ar^+ has created considerable damage. Figure 51 is the DLTS spectrum obtained from an as-implanted sample that had been implanted to a smaller dose of $10^{13}/\text{cm}^2$. The structure and magnitude of the damage peaks are consistent with the other data and the different dose.

Figure 52, an Arrhenius plot of emission rate as a function of reciprocal peak temperature, is used to determine the thermal activation energies of the principal peaks. Plots for the two native defects at 200 and 374°K, plus the principal ion-implant peak at 260°K, are shown. The curves are very well

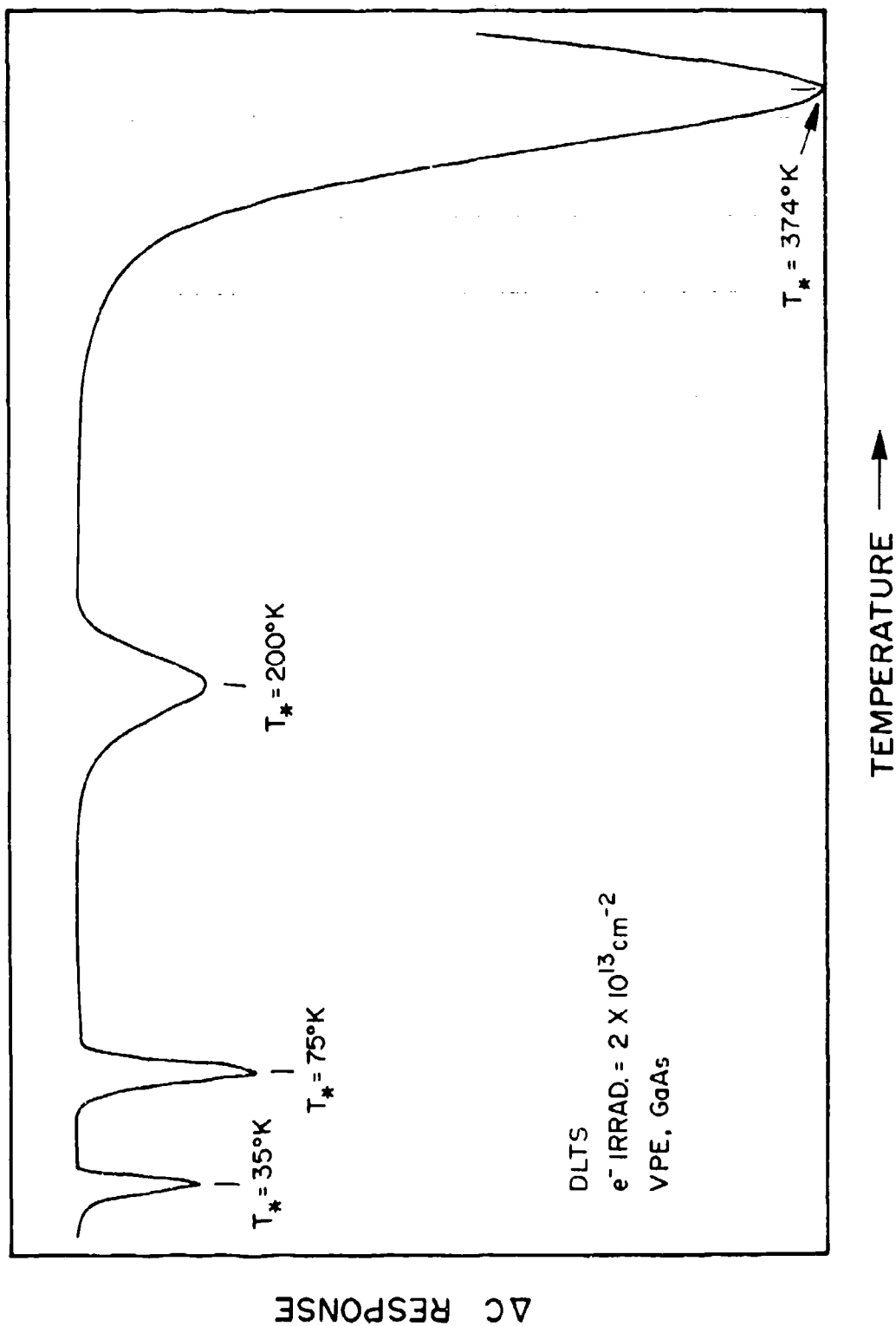


Figure 48. DLTS Spectrum after 1-MeV Electron Irradiate Yields 1% Carrier Removal.

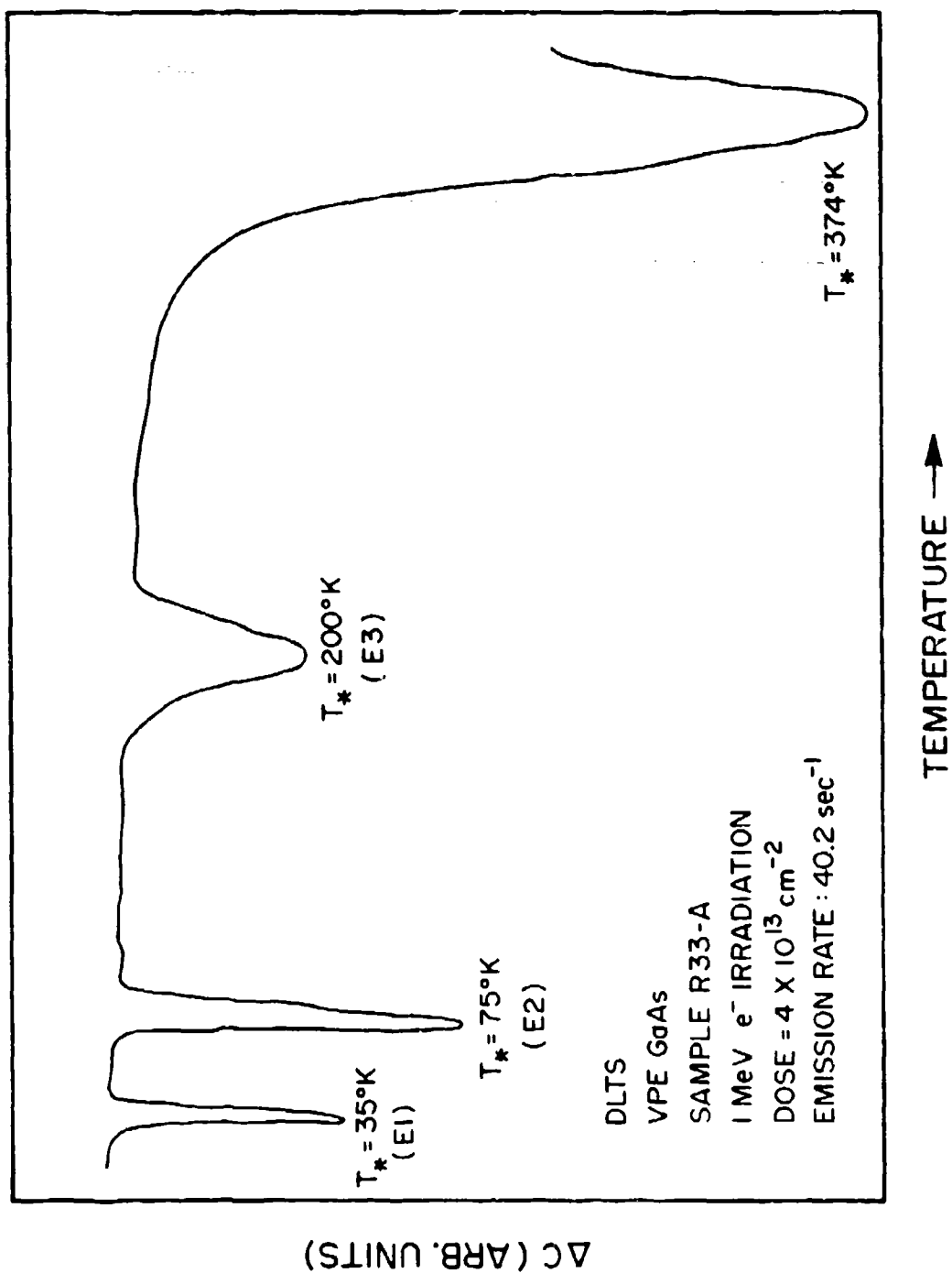


Figure 49. DLTS Spectrum after 1-MeV Electron Irradiate Corresponding to 2% Carrier Removal.

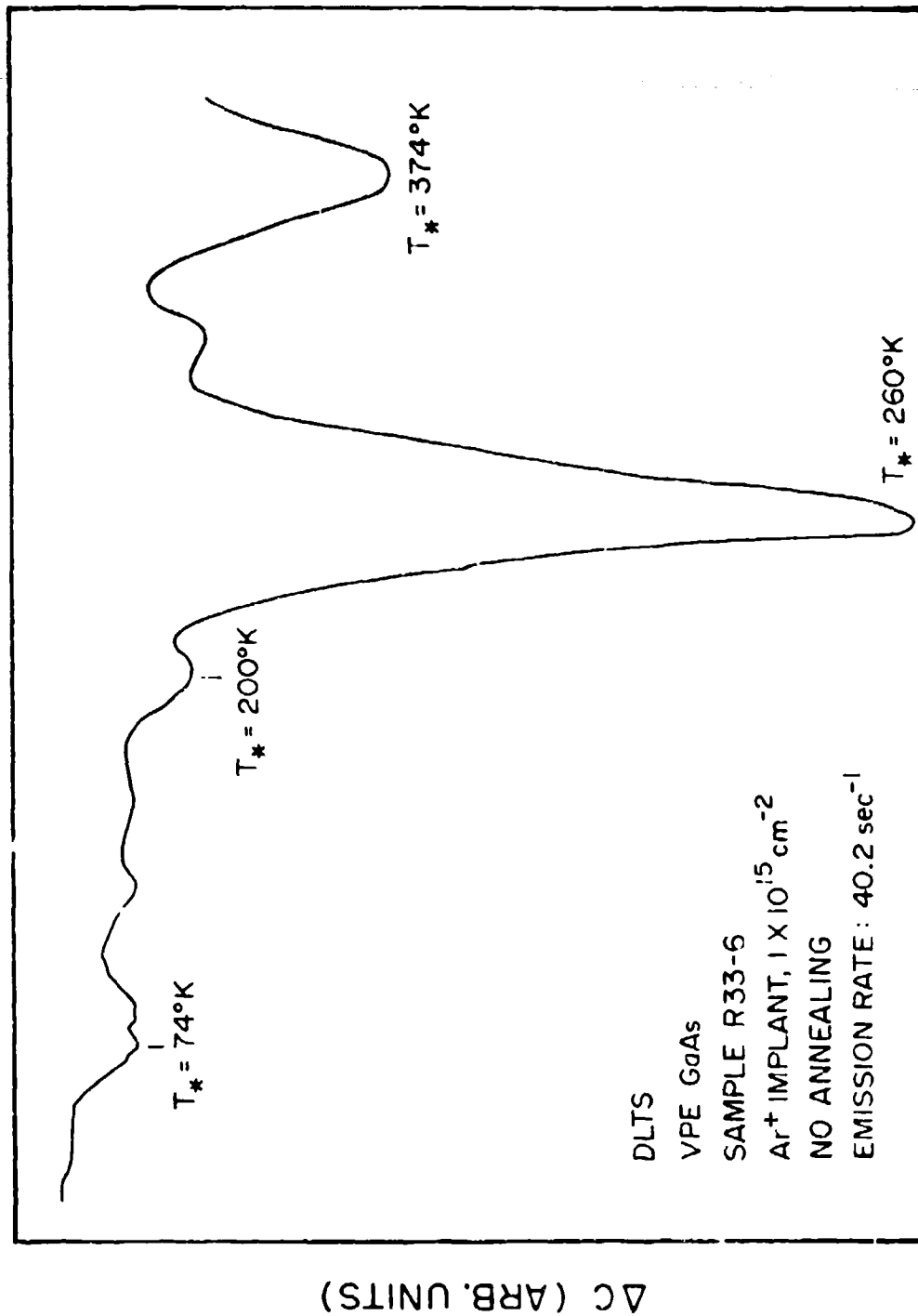


Figure 50. DLTS Spectrum of As-Implanted VPE GaAs:Ar.

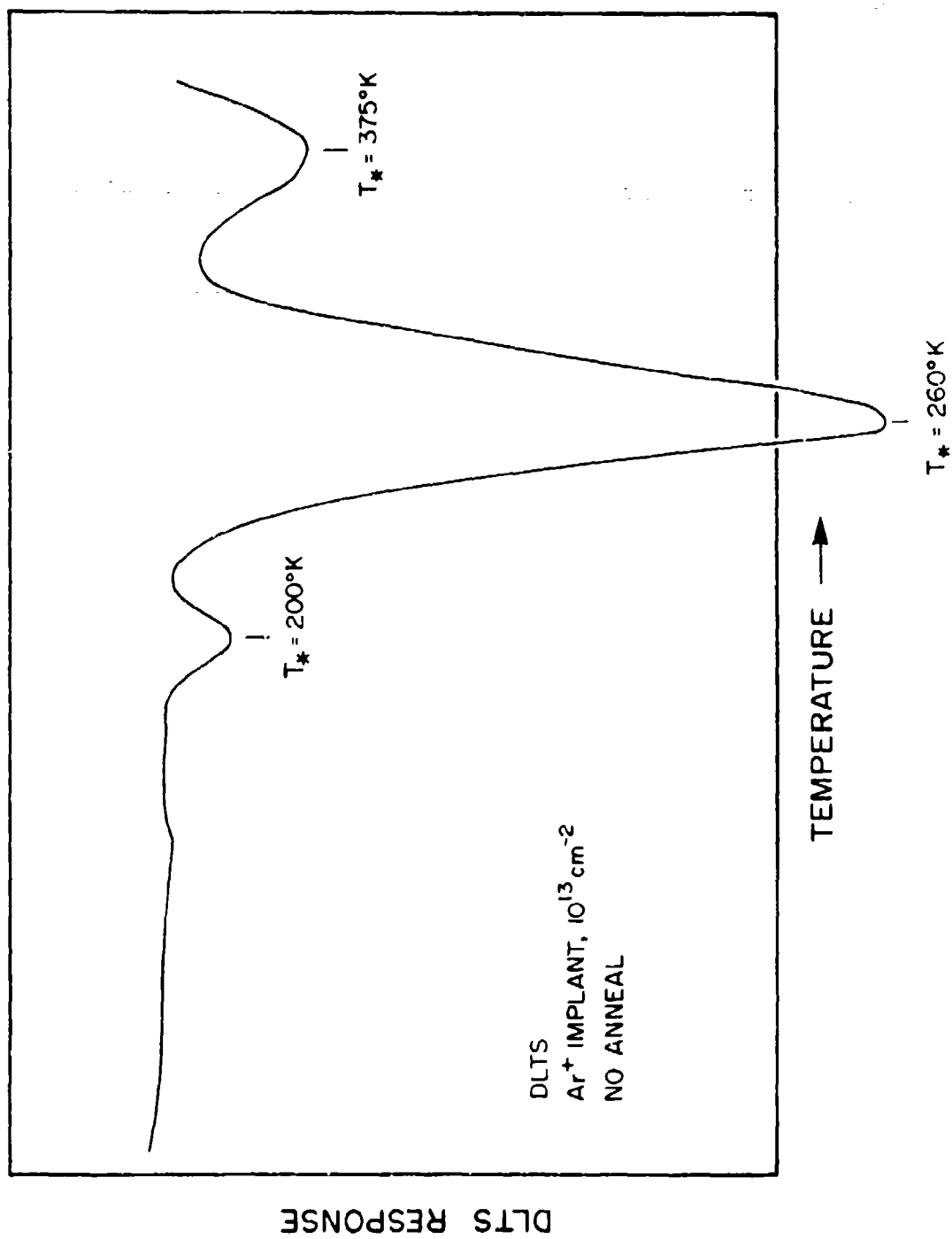


Figure 51. DLTS Spectrum of GaAs Implanted to 10^{13} cm^{-2} , No Annealing.

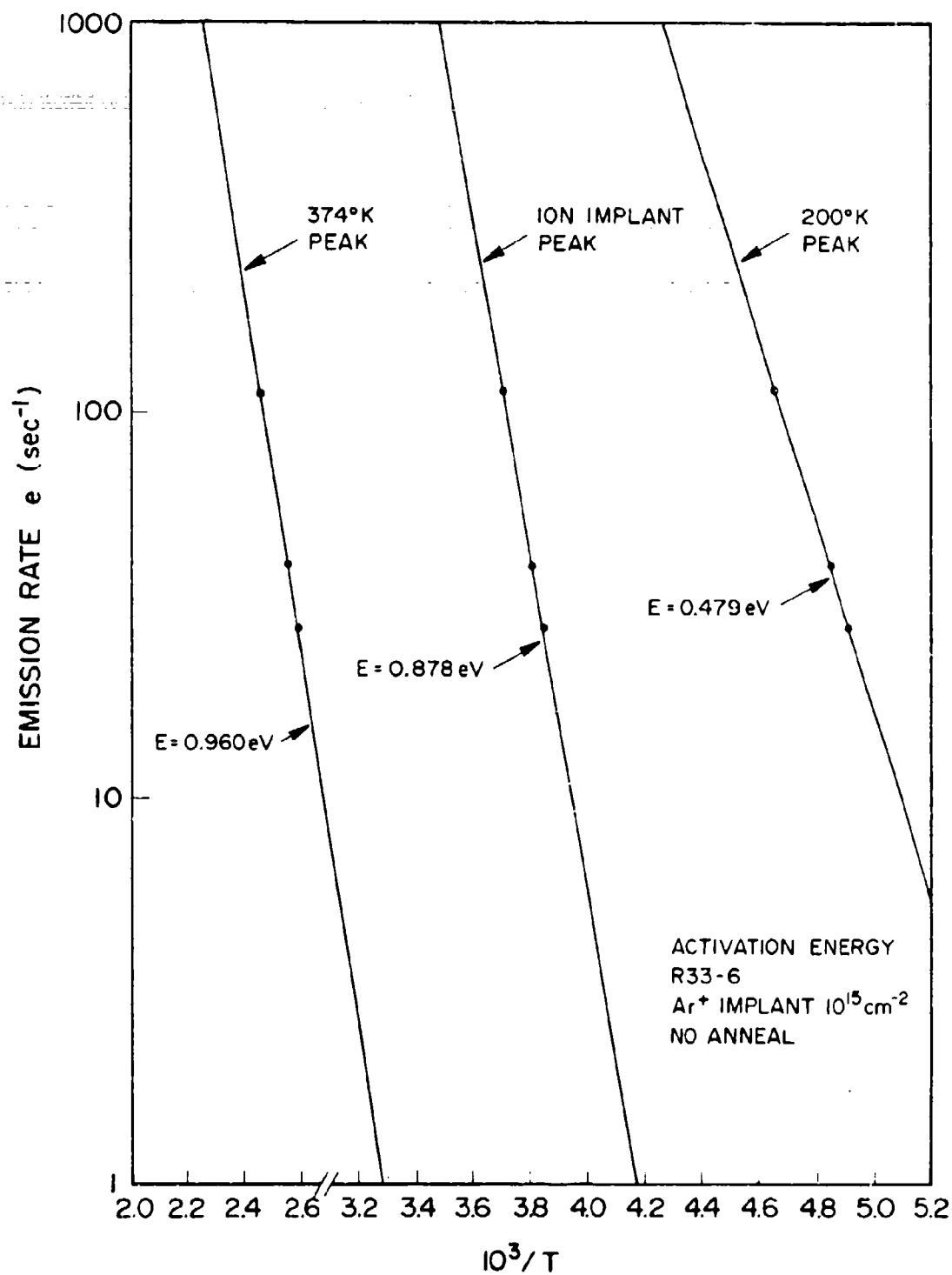


Figure 52. Thermal-Activation-Energy Plots of Native Defects and Ion-Implanted Peaks.

behaved and easily yield the activation energies. An identical sample was annealed to 300°C in an Ar atmosphere. In the DLTS spectrum shown in Fig. 53, most of the small damage peaks were annealed, and the native defect peaks and the principal ion-implant peak were unaffected.

Figures 54 and 55 are DLTS spectra from a sample that had been annealed to 700°C. The sample was implanted, capped, annealed, stripped, metallized, and then packaged. The spectra shown are for different emission rates; it is obvious that the large peak is quite complex, with numerous components that can be resolved by the emission-rate selection. The detailed nature of these peaks is unknown. It appears that the native defects as well as the damage peaks have shifted and complexed.

Figure 56 is the spectrum obtained from a sample from the same wafer, which was implanted at the same time, capped, and then annealed to 850°C. The spectrum is dramatically different from the previous runs. The majority-carrier emitter at about 200°K may be the native defect observed previously. The very large peak at 400°K is of opposite polarity to previous data and indicates the presence of a minority-carrier emitter. This situation should not occur in a Schottky device, and this may be evidence of thermal conversion to p-type material under the Si_3N_4 cap during high-temperature annealing.

Thermal conversion of GaAs during annealing has been discussed at length in previous sections of this report. The cap used for this set of samples appeared to be good visually and was electrically acceptable for substrate material. However, in this case the epitaxial layer is very heavily damaged, and the properties of the cap could be very different from those on a substrate.

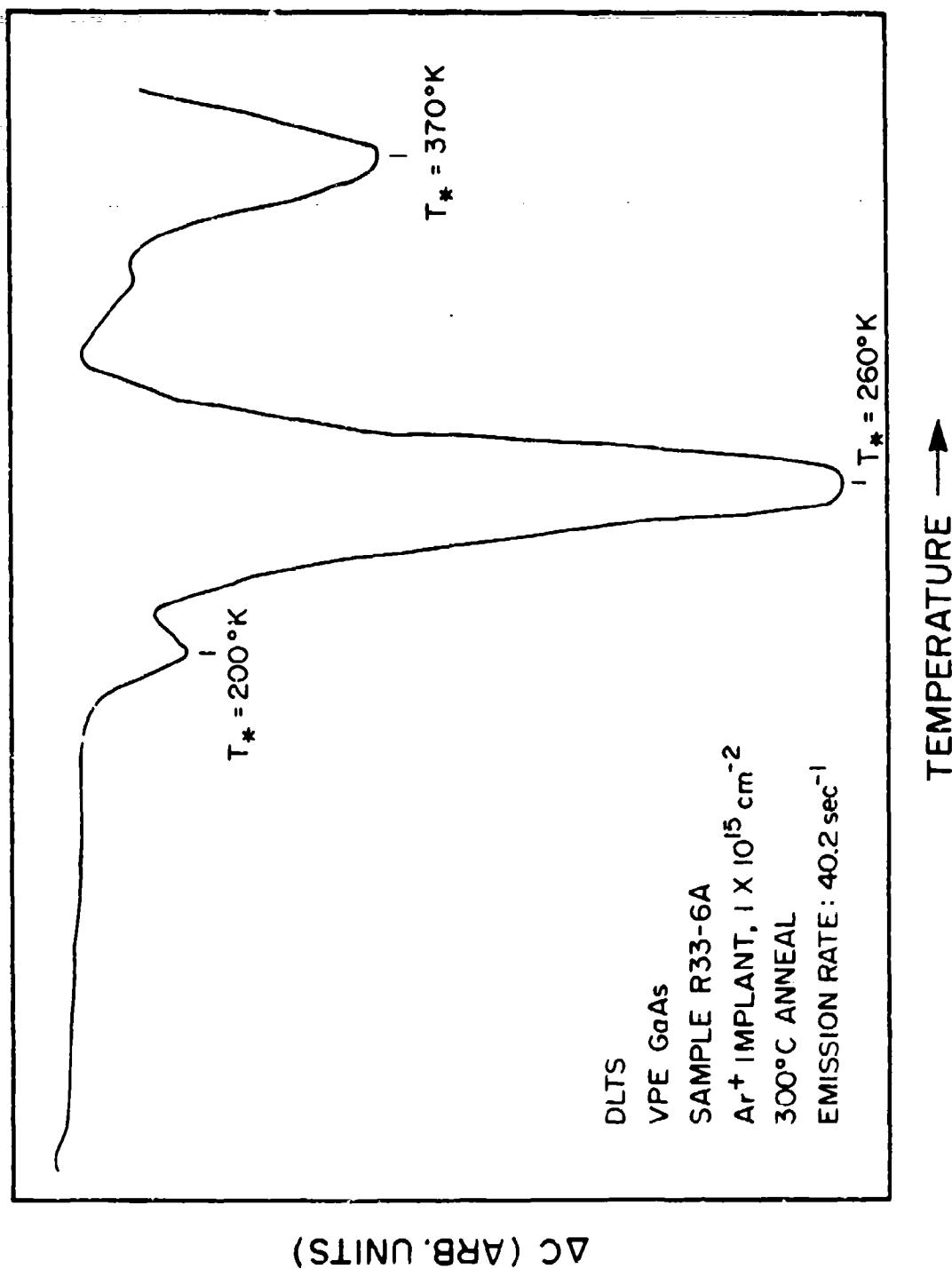


Figure 53. DLTS Spectrum of Ar-implanted GaAs Annealed at 300°C.

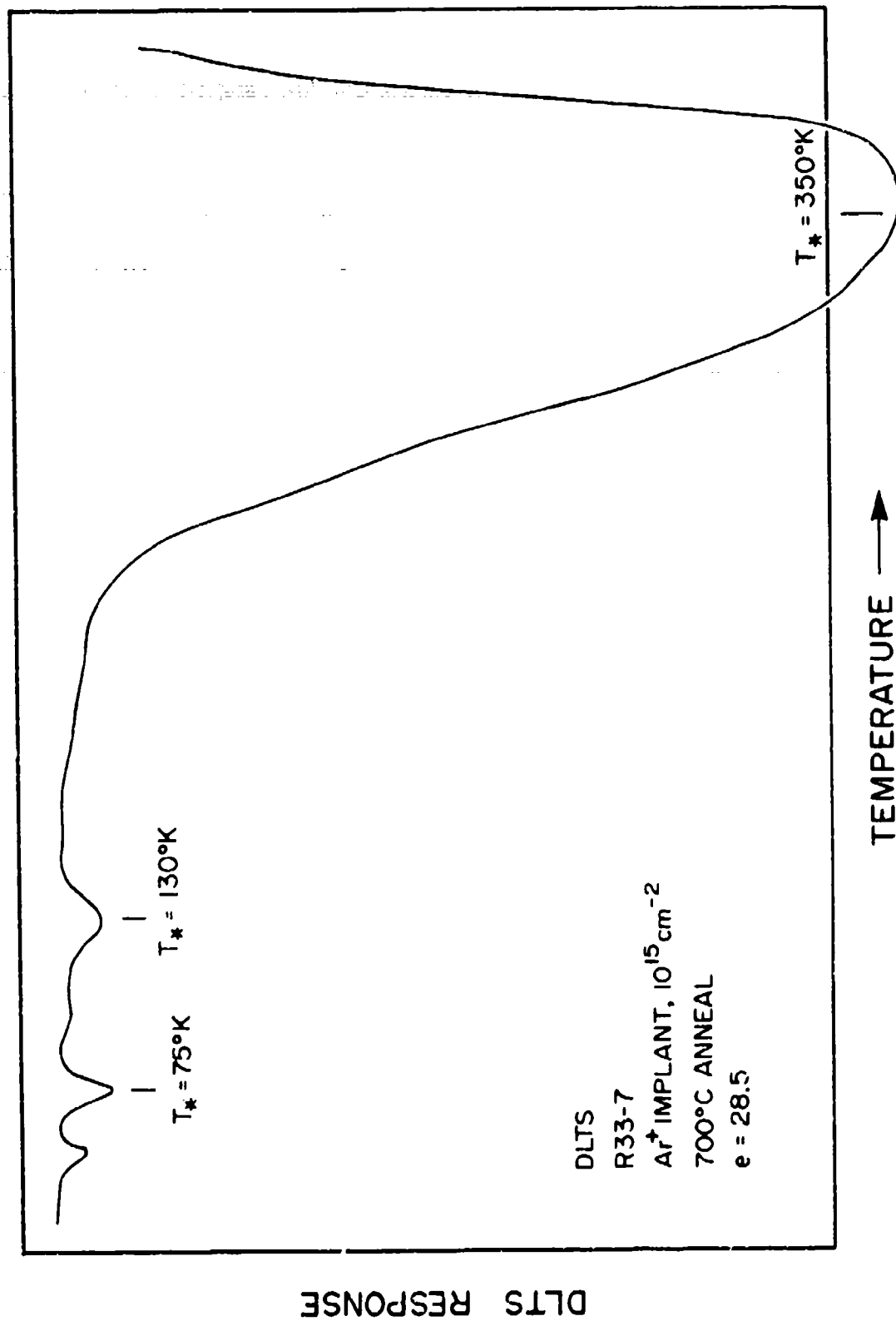


Figure 54. DLTS Spectra from Ar-Implanted GaAs Annealed to 700°C.

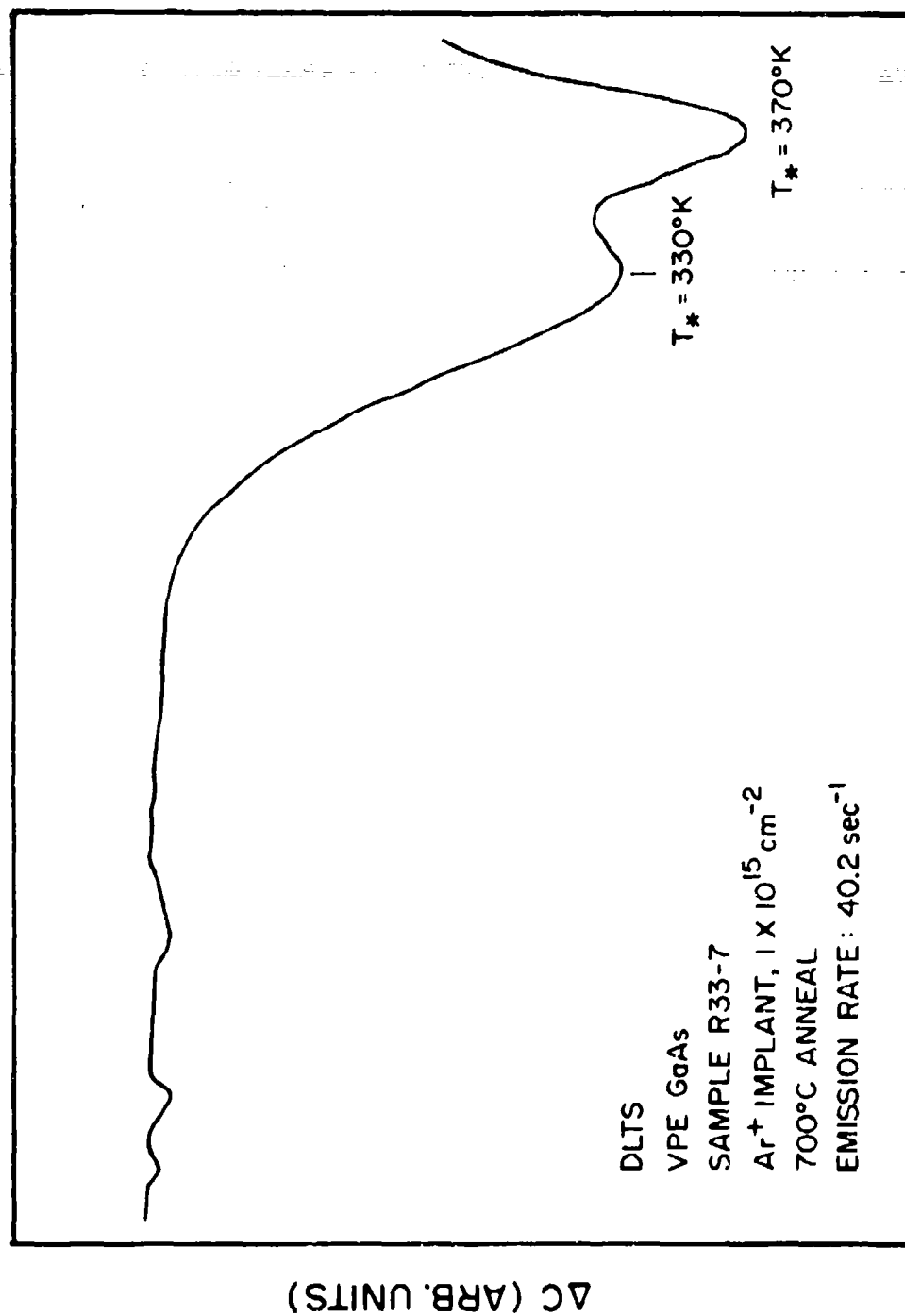


Figure 15. DLTS Spectrum for Ar-Implanted GaAs Annealed to 700°C.

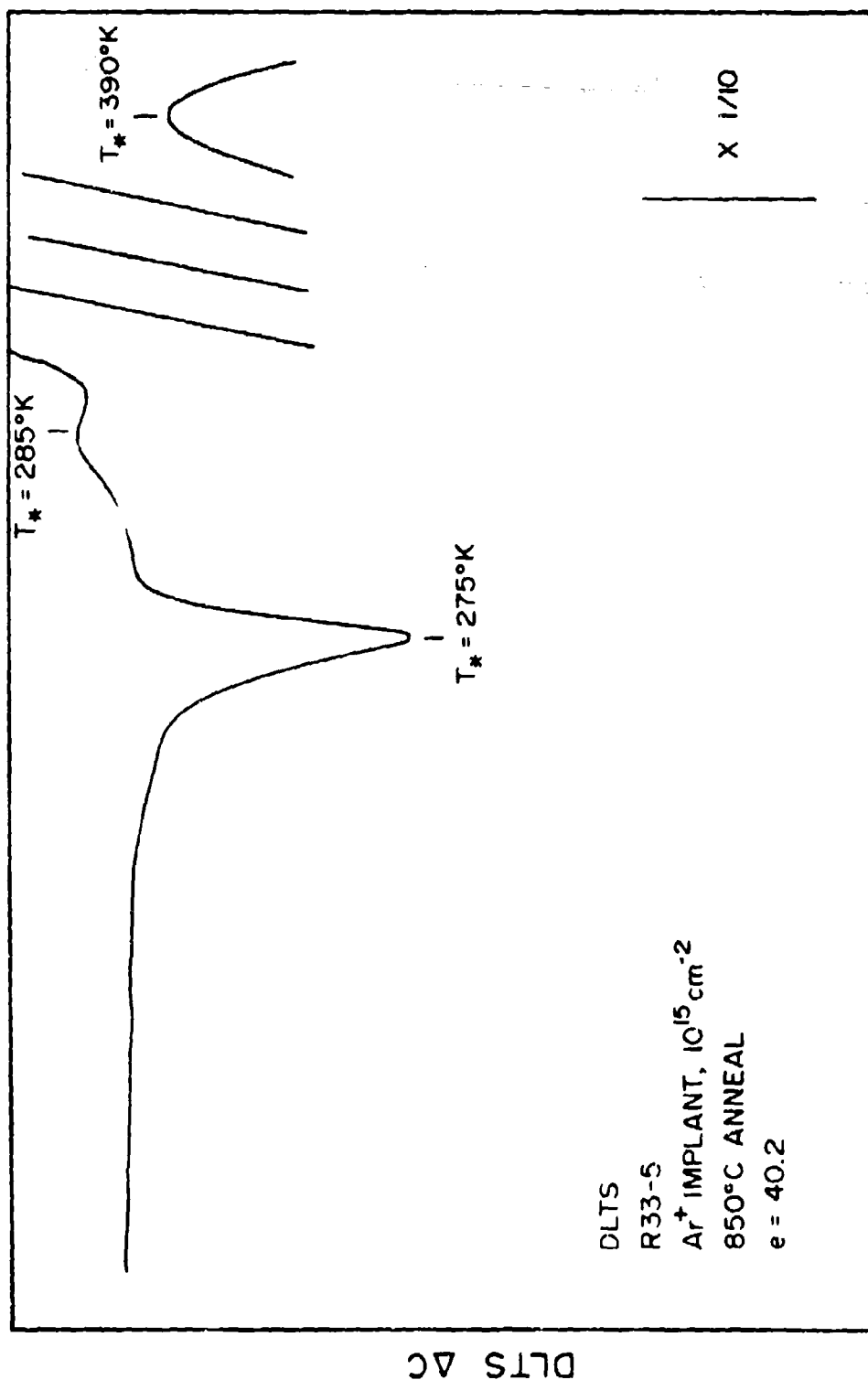


Figure 56. DLTS Spectrum of Ar-Implanted GaAs Annealed to 850°C.

A large piece of epitaxial GaAs was implanted to 10^{15} cm^{-2} with As^+ ions. A series of samples was generated with different annealing temperatures, as was done for the Ar implants. Again the dose was quite high. Considerable difficulty was encountered with the Schottky metallization after annealing. Many of the diodes were very leaky, especially for the samples that had been annealed at the highest temperatures. Figure 57 is a DLTS spectrum obtained from an As^+ implanted sample annealed to 700°C . In this case, the reverse bias was 2 V, and the sample was pulsed only to zero. The built-in potential of the Schottky barrier insured that the pulse would not affect the built-in depletion layer; hence, the region being studied did not include the implant layer (the built-in layer is larger than the implant range). In Fig. 57, a large native majority-carrier emitter at about 500°K dominates the spectrum. If the pulse is increased from the bias of - 2 V to + 2 V, the spectrum obtained is similar to that in Fig. 58. The nature of the DLTS signal changes completely from a majority-carrier emitter in n-type material to a majority-carrier emitter in p-type material.

At this time, it has not been established whether the material converts to p-type because of the As^+ implant or whether this is an effect of thermal conversion during annealing. In any case, considerable opportunity exists to study the deep centers created during ion implantation and its subsequent annealing.

Device-Grade FET Material

Initial attempts to measure the DLTS of device-grade GaAs on semi-insulating Cr-doped substrates resulted in very poor response that consisted entirely of

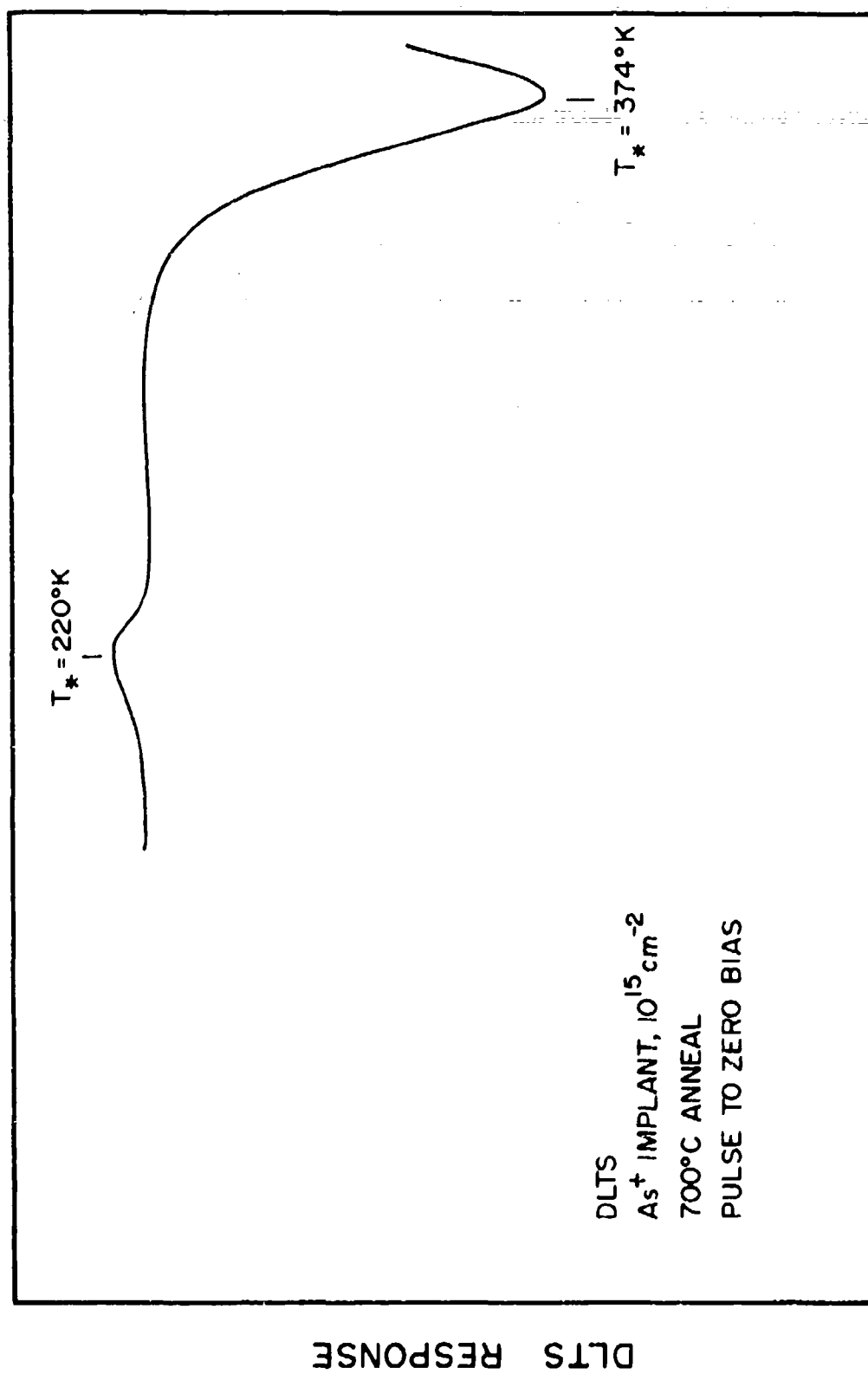


Figure 37. DLTS Spectrum of GaAs Implanted with As and Annealed to 700°C. Pulse to Zero Bias.

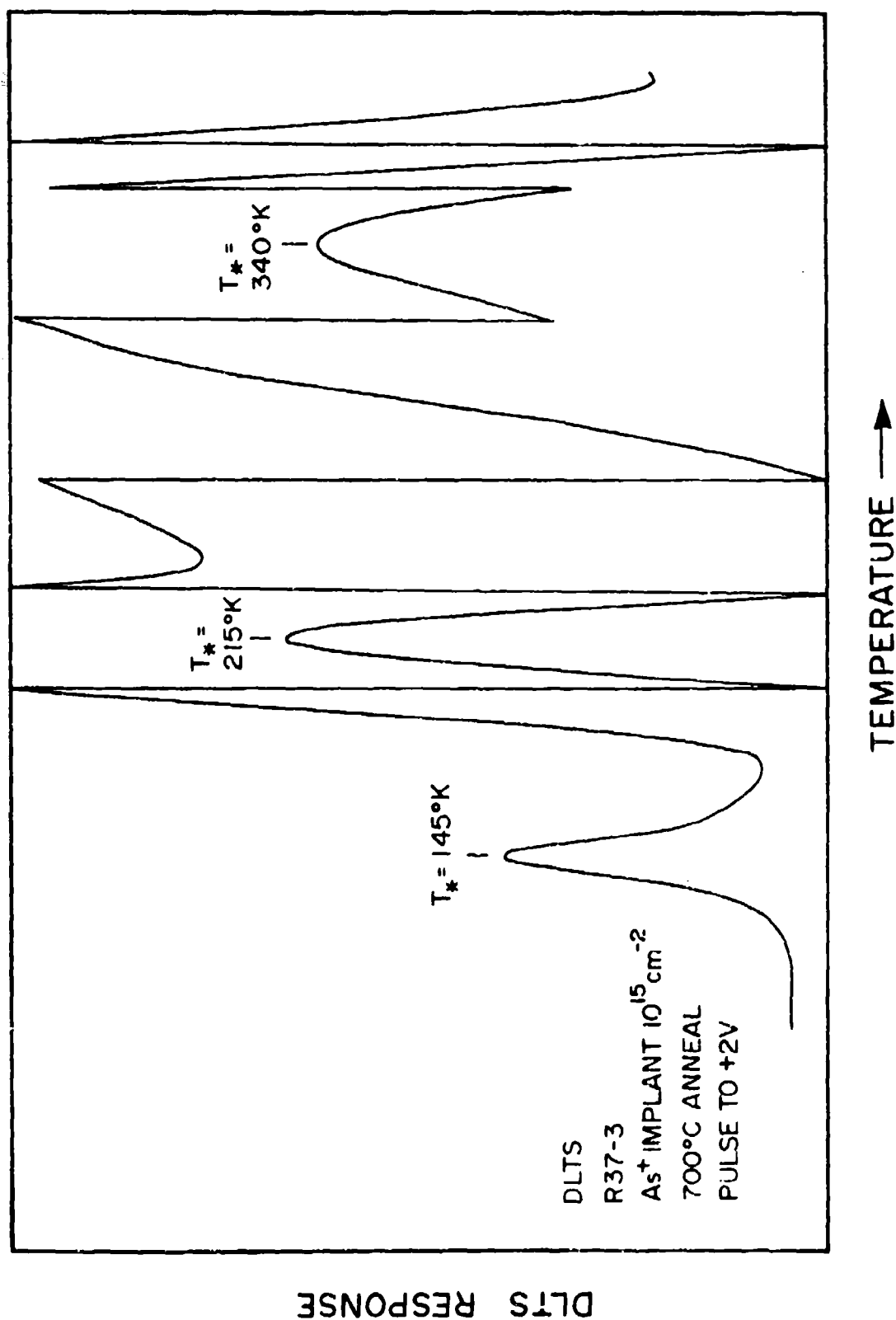


Figure 58. DLTS Spectrum of GaAs Implanted with As and Annealed to 700°C. Pulse to +2 V.

random, rather violent noise with some very broad (200°K-wide) peaks that could not be resolved. In the literature, references to the effects of high fields in an FET channel and the distortion of capacitance measurements in high-impedance situations indicated that it would be more prudent to look at very thick, lightly doped layers or epitaxial layers on conducting n^+ substrates. Further development of the electronics and the addition of the buffer/baseline restorer to the system changed the situation completely and, as a result, good, noise-free signals could easily be obtained from device-grade material on semi-insulating substrates.

An example of this effort is shown in Fig. 59. The DLTS data shown are from an FET-like device fabricated on an active layer of VPE GaAs which was 0.25- μ thick, with a carrier concentration of 10^{17} cm^{-3} . The active layer was on a buffer several microns thick and a Cr-doped substrate. The response is similar to DLTS spectra from other wafers, although the temperature dependence--especially for the 300°K peak--is quite puzzling. Figure 60 is a spectrum from a similar wafer, grown consecutively to the wafer which yielded the spectrum in Fig. 59. The peaks in Fig. 60 are somewhat more familiar, with the peak at 375°K probably being the one normally seen at 400°K. In both cases, some response was observed below 75°K and near 200°K. The primary peaks were very well behaved for energy analysis. The principal peaks were very large, in some cases driving the boxcar out of range. The peaks were very sensitive to pulse duration and seemed to grow at a linear rate with increasing pulse duration. An interesting feature of this growth was that the DLTS peak width was constant with increasing DLTS magnitude, indicating a relatively simple trap whose capture cross section could be determined.

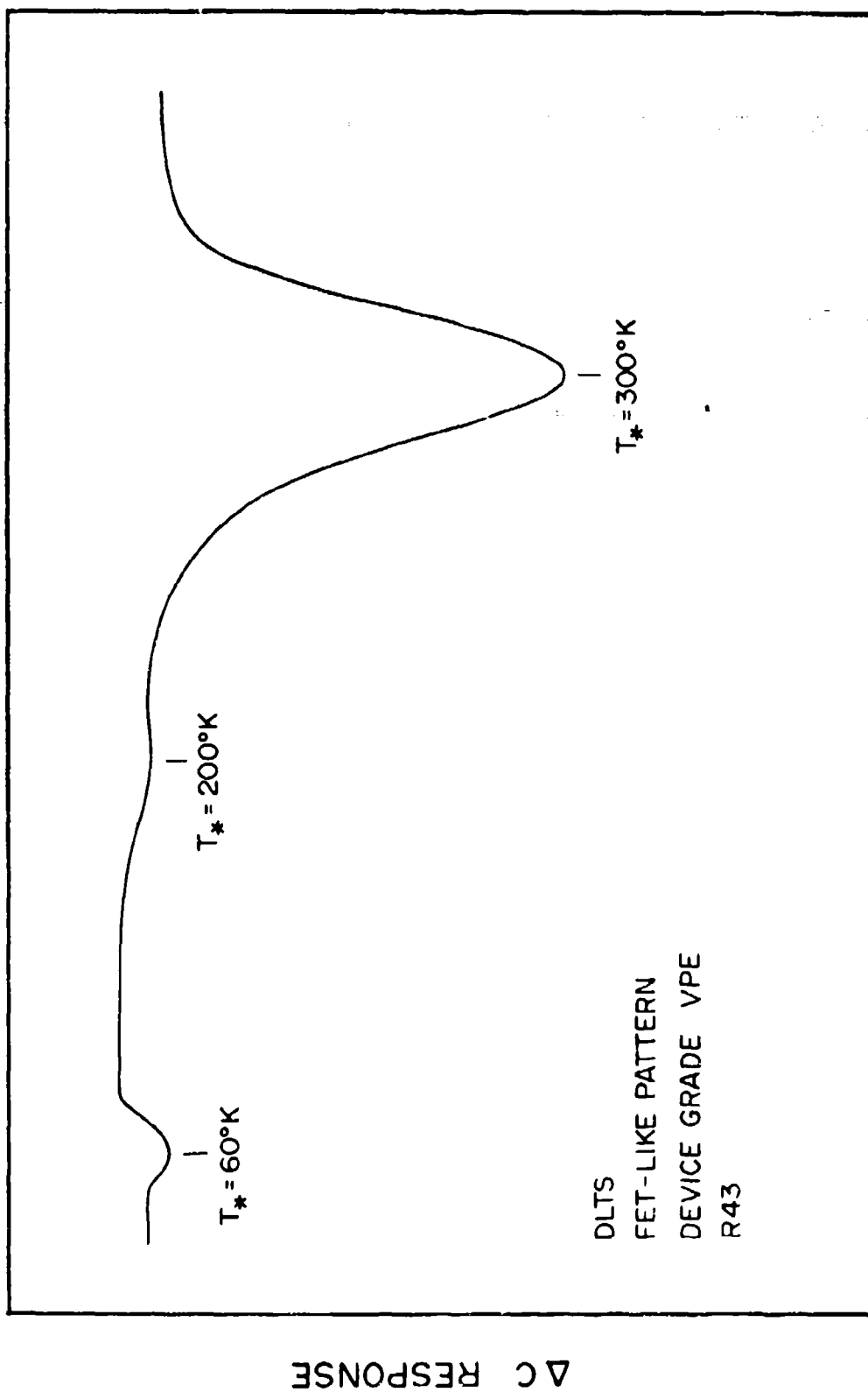


FIGURE 54. DLTS Spectrum from FET-Like Test Pattern on Device-Grade Material R43.

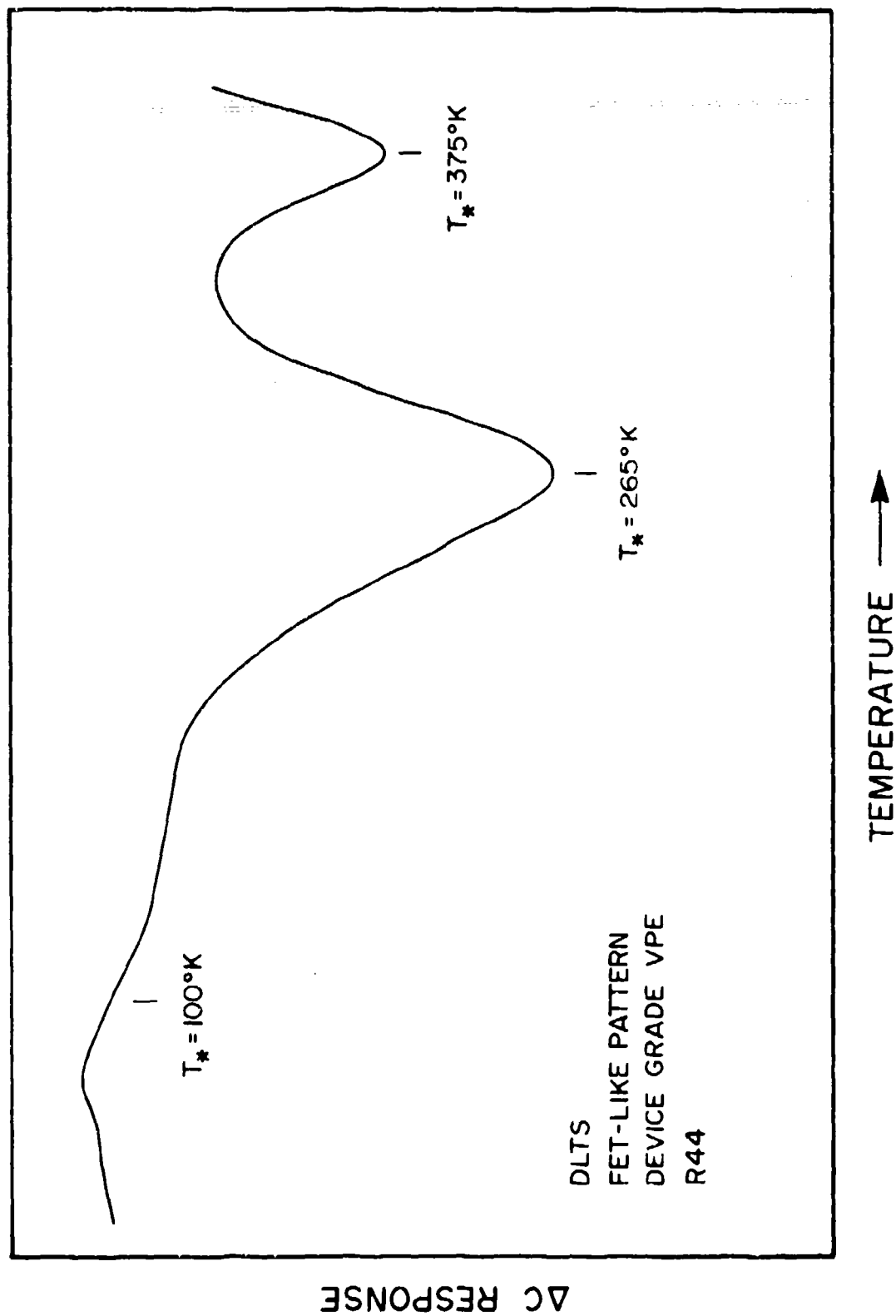


Figure 60. DLTS Spectrum from FET-Like Test Pattern on Device-Grade Material R44.

Figure 61 is a very different DLTS spectrum. The wafer, R19, was again an active layer of VPE GaAs, doped to 10^{17} cm^{-3} on a buffer and Cr-doped substrate. In this case the epi was grown by Teledyne Corporation on a Morgan, Inc., substrate. This sample was on a die adjacent to the one whose concentration profile is shown in Fig. 44 that had a buried donor layer near the active-layer-buffer interface. The sample had also been irradiated with 1-MeV electrons. It is entirely possible that the peaks shown in Fig. 61 are E1, E2, and E3, created by the electron damage plus a high-temperature native defect, that have been shifted to lower-than-normal temperatures by the high-field distortion in the high carrier concentration. Since the peaks are well shaped (not truncated), they may be defects at the interface of the epi and substrate, rather than distortions of the damage peaks. Furthermore, the I-V characteristics of the FET were measured at a very low temperature (12°K) with a curve tracer. The results are shown in the inset of Fig. 62. The forward resistance is shown to be a few thousand ohms--certainly insufficient to cause high-impedance problems with the capacitance measurement. Figure 62 also contains the N-W profiles of the sample as generated by C-V measurements taken at low temperatures. It is clear that the active layer is fully depleted at these temperatures, but sensible profiles of the substrate and interface are still obtained.

The thermal-activation energies of the principal peaks were determined in the usual manner. The Arrhenius plots are shown in Fig. 63. The first peak, shown in Fig. 61 as occurring at 21°K, had an activation energy of 4.6 meV. The second peak, at 57°K, had an activation energy of 36 meV. These energies are less than those normally observed for electron-damaged GaAs. Normally, the activation energies are several hundred meV. The energies obtained here

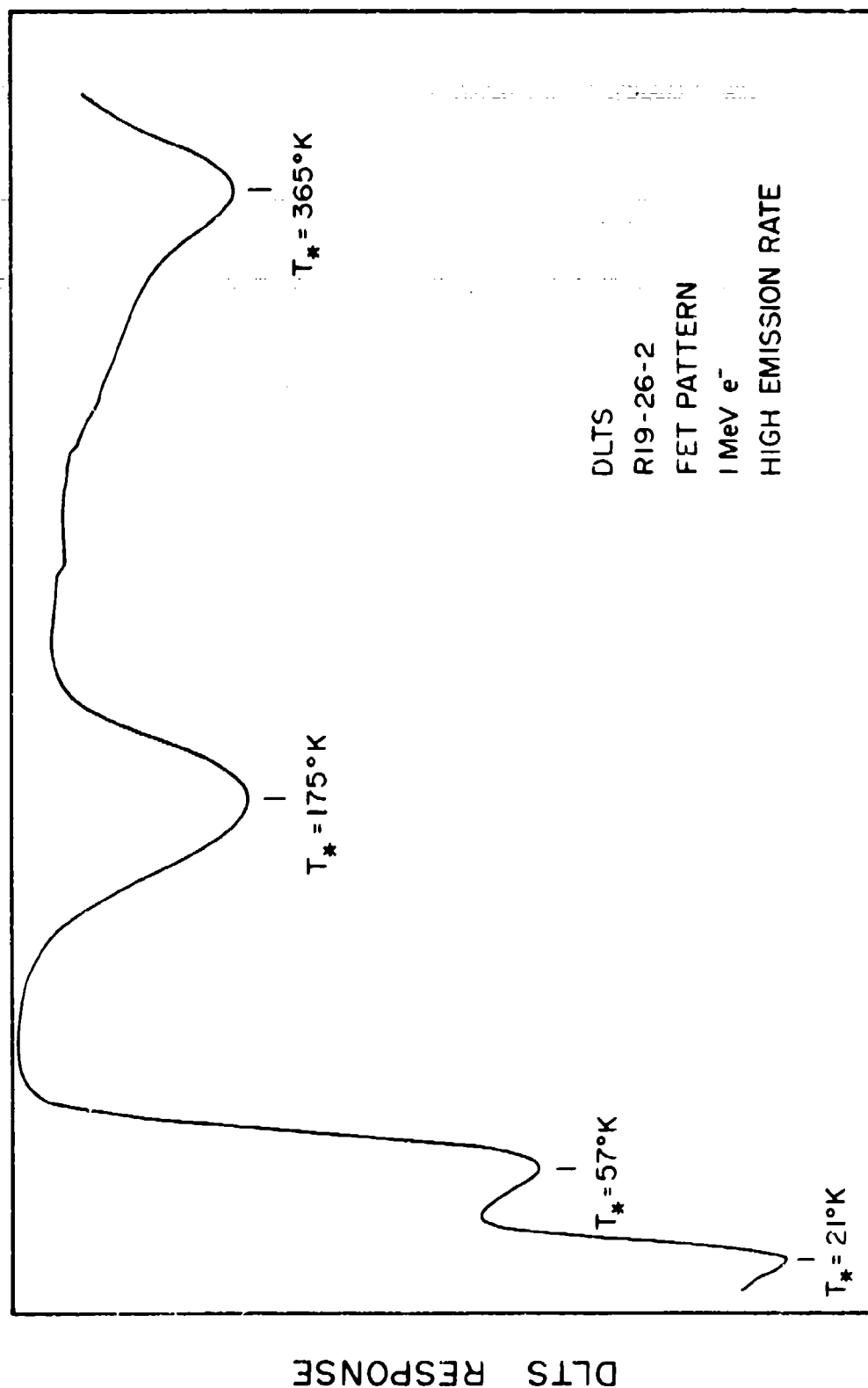


Figure 61. DLTS Spectrum from FET-Like Test Pattern on Device-Grade VPE GaAs Irradiated with 1-MeV Electrons.

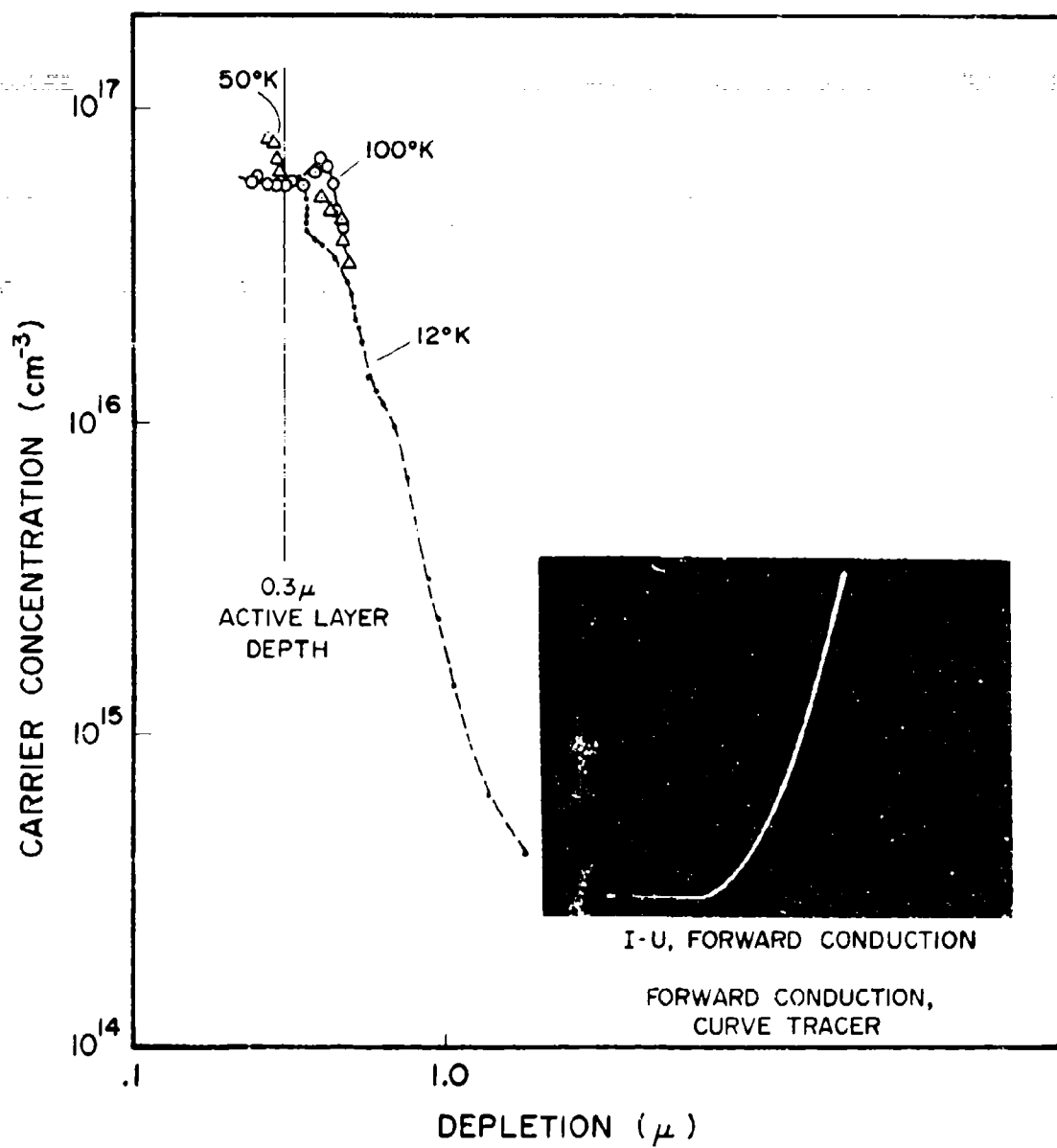
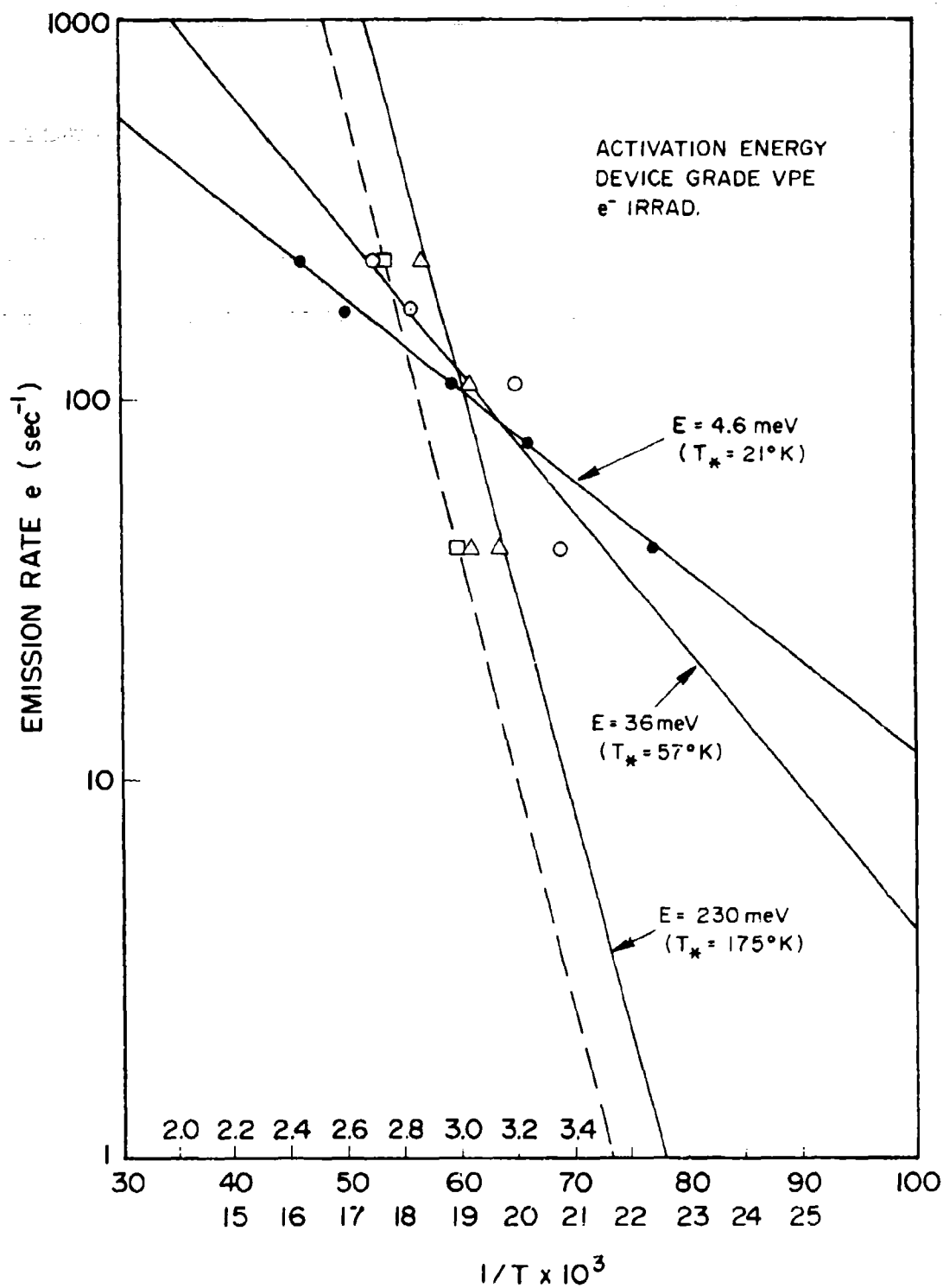


Figure 62. N-W Profiles of FET-like Test Pattern on Device-Grade VPE GaAs. Inset shows I-V characteristics from curve tracer at 12°K.



are more of the order of donor levels and are much lower than any reported to date for trap levels observed by DLTS.

It should also be noted that the thermal activation energy of the peak observed at 175°K was 0.23 eV (only a factor of two less than normally observed), and the peak at 375°K had an activation energy of 0.60 eV--about 50% less than previously observed.

Miscellaneous Studies

Numerous studies of the DLTS of GaAs were conducted for the purpose of building the system, checking the results with the literature, and surveying the presence of traps in various forms of the material. The first DLTS data in this laboratory were collected from a sample of bulk-grown, undoped GaAs with a nominal carrier concentration of 10^{15} cm^{-3} . Schottky dots were evaporated on one surface, ohmic contacts made to the back, and the transient capacitance measured.

Figure 64 is a typical DLTS spectrum from these samples. The sign of the DLTS is reversed in this figure (the traps were majority-carrier emitters). The traps observed are very similar to the native defects observed in other samples--especially the epitaxial samples run at a later date. The variations may be due largely to thermometry differences between the initial and final stages of the system development. It would be useful to re-run these studies with the new equipment and look for the subtle differences between material forms (bulk vs. epitaxial).

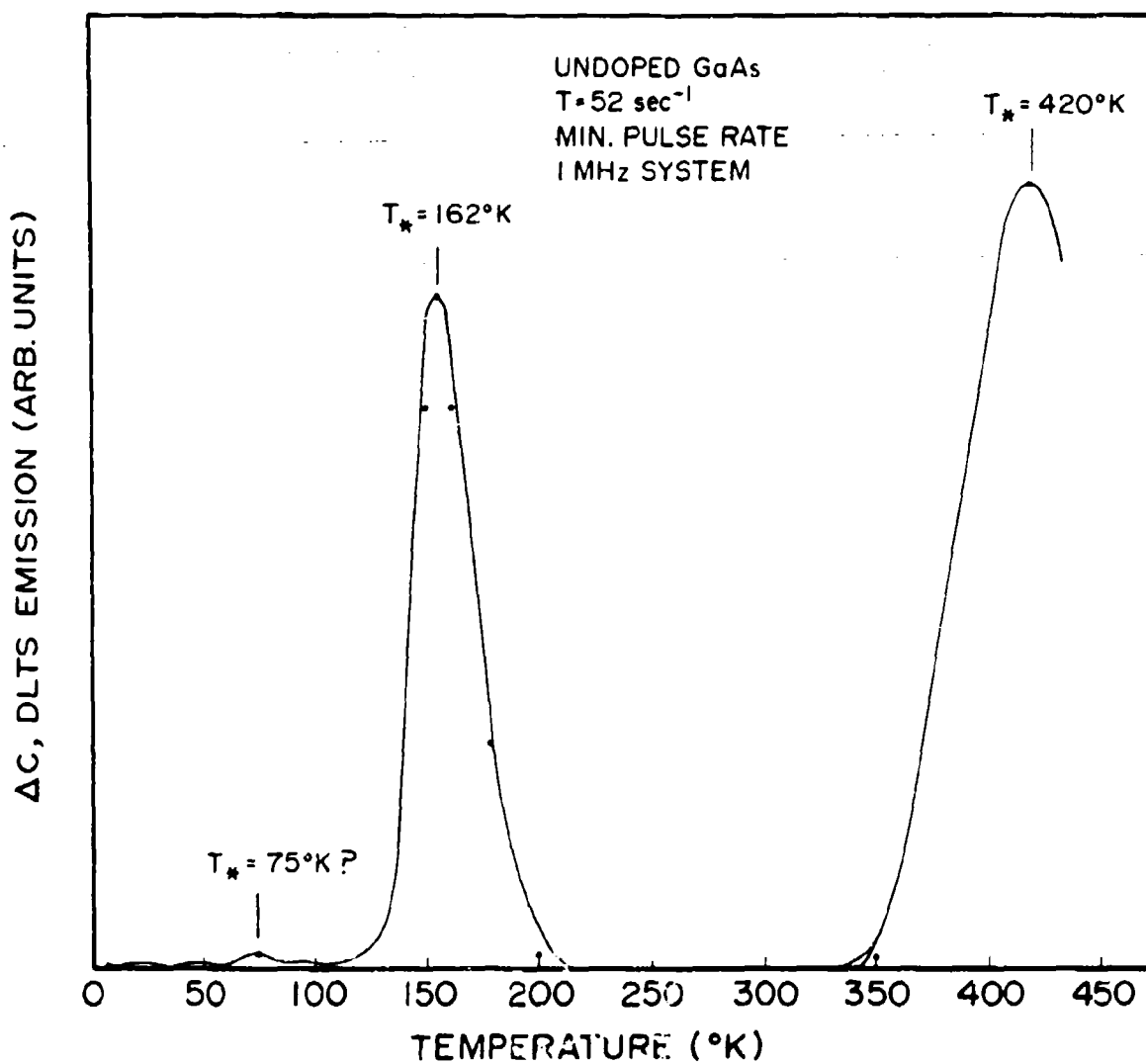


Figure 64. DLTS Spectrum for Undoped GaAs (initial data).

Extensive DLTS work was performed using epitaxial GaAs irradiated with 1-MeV electrons. The production rate of defects by 1-MeV electrons in GaAs is fairly well understood and provides a good set of marker defects in a range suitable for DLTS. During the course of these investigations, some anomalies were observed in connection with the FET-pattern geometry. A paper was published on this work and is included in Appendix E of this report. Figures 65 and 66 are typical DLTS spectra from the electron-irradiated samples. The differences in spectra were found to be highly dependent upon the emission rate set by the boxcar window and the reverse-bias conditions on the active buffer-layer combination. These studies were quite useful in developing the DLTS system.

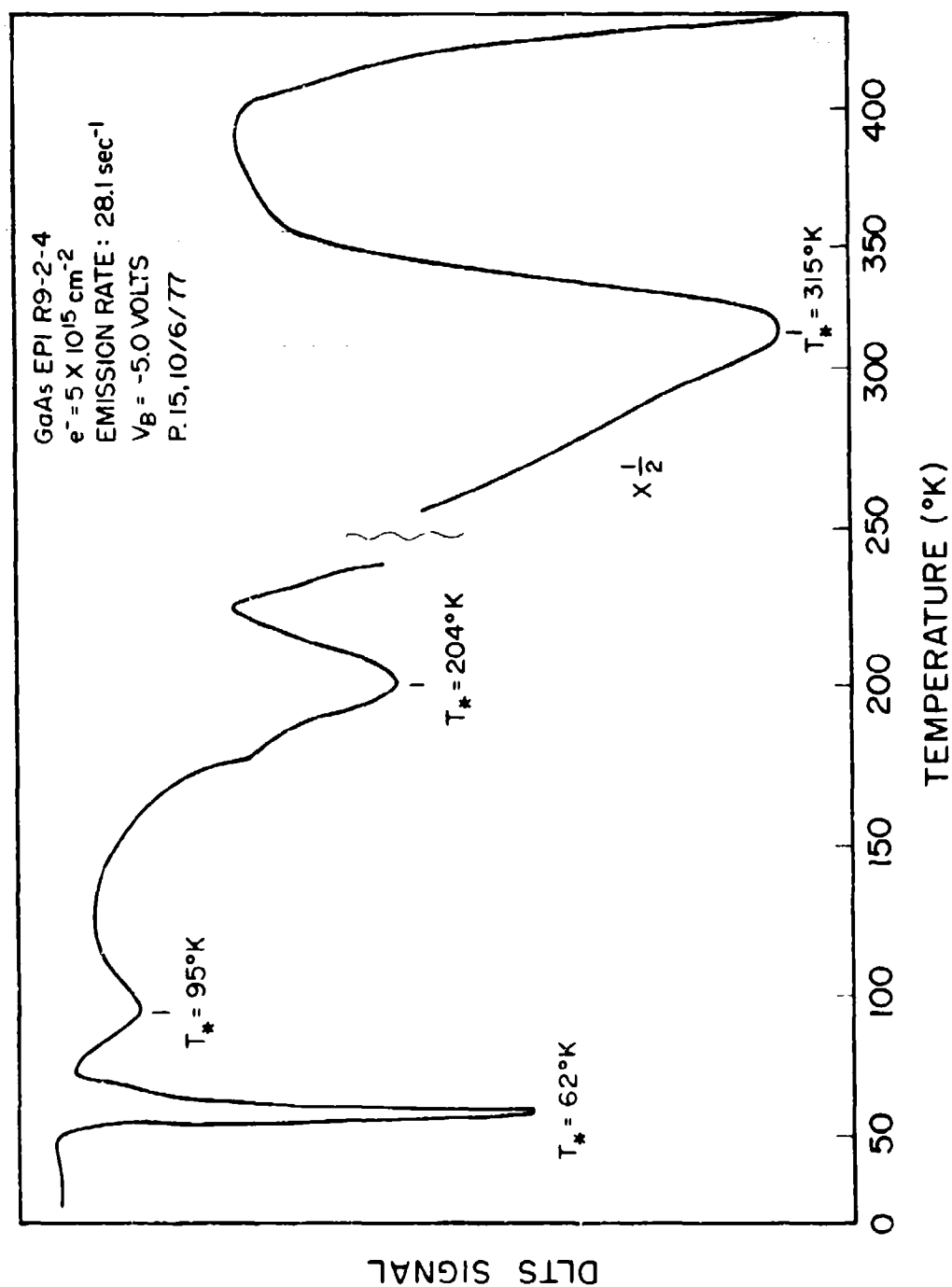


Figure 65. DLTS Spectrum from Electron-Irradiated VPE GaAs (slow emission rate, moderate reverse bias).

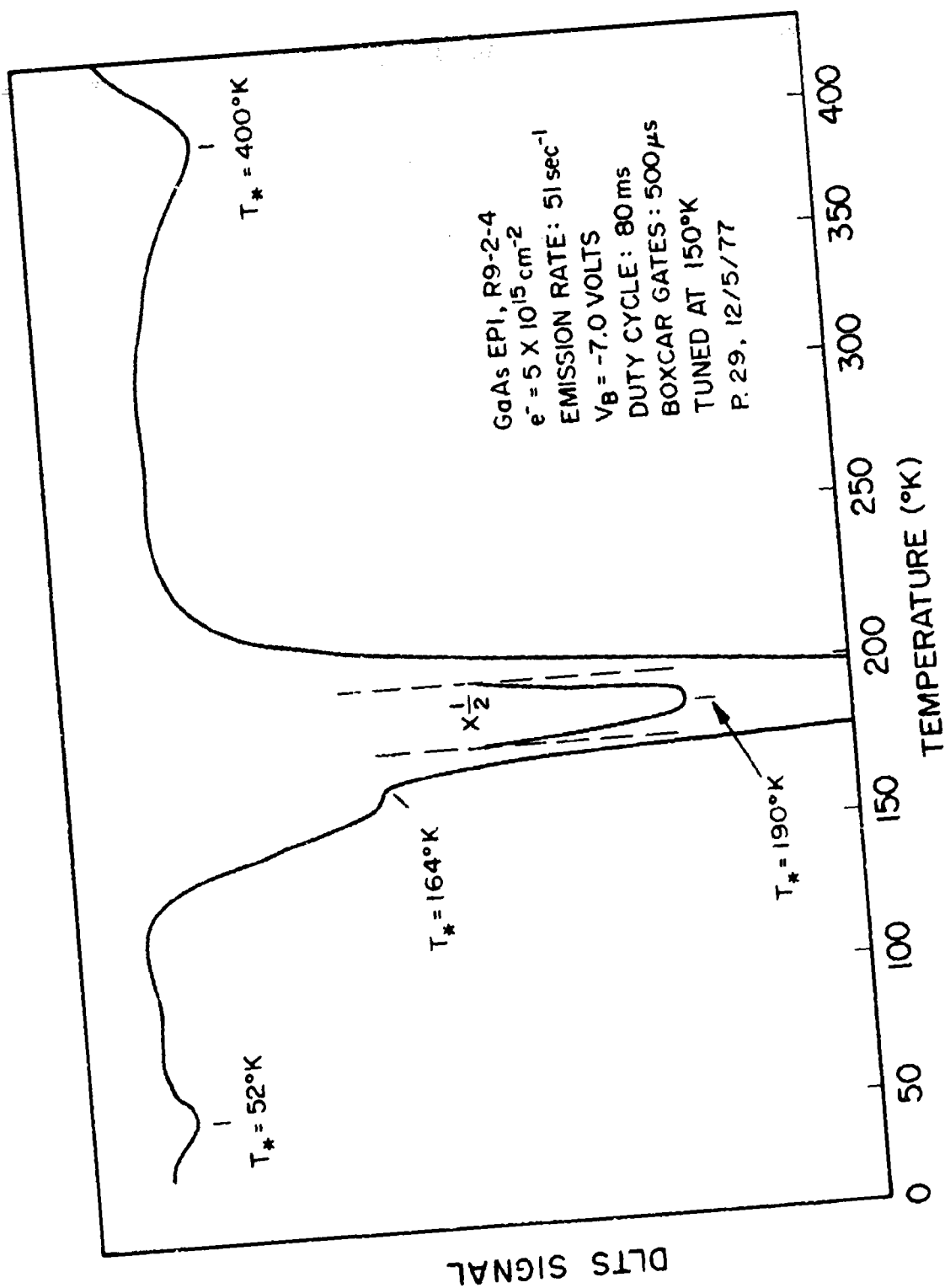


Figure 66. DLTS Spectrum from Electron-Irradiated VPE GaAs (moderate emission rate, high reverse bias).

Section 6

OPTICAL STUDIES

6.1 MAGNETO-OPTICS OF FREE EXCITONS IN GaAs AND InP

In this chapter the optical studies that have been carried out on GaAs and InP are described.

INTRODUCTION

During the past twenty years, a great deal of interest has existed in both experimental and theoretical investigations of the behavior of Wannier excitons in semiconductors in the presence of a magnetic field. A wealth of data in both elemental and compound semiconductors has been obtained. Several features of these data, such as the dependence of the energy spectrum upon polarization, could not be explained in terms of a model involving simple parabolic valence bands. It soon became obvious that any successful attempt to explain this behavior should include the degenerate and anisotropic nature of the valence bands. Altarelli and Lipari,⁴³ Swierkowski,⁴⁴ and Cho, et al.,⁴⁵ calculated the energies of the ground state of an exciton in low magnetic fields using a perturbation approach and including the effects of anisotropy and degeneracy of the valence bands. Altarelli and Lipari⁴⁶ later extended their calculations to high magnetic fields using an adiabatic approximation. An interesting region from the experimental viewpoint, however, is the intermediate one (say, 20 to 200 kG in GaAs), where most of the measurements have been made.

The following work describes a calculation of the energies of the six lowest optically allowed states of a direct exciton in a cubic semiconductor in the presence of an arbitrary magnetic field, taking into account the effects of degeneracy and anisotropy of the valence bands. The exciton-effective mass Hamiltonian used was first proposed by Kohn and Luttinger.⁴⁷ This Hamiltonian function is solved following a variational approach in which the exciton wave functions are expressed as linear combinations of the eigenfunctions of an anisotropic hydrogen-like system in a magnetic field. Using the experimentally suggested values of the various Kohn-Luttinger valence-band parameters in GaAs, the energies of these six states in GaAs are calculated. The results thus obtained are compared with those derived from magneto-reflection measurements of high-purity epitaxial layers of GaAs, and good agreement is found.

Theory

Within the effective mass approximation, the Hamiltonian of a direct exciton in a cubic semiconductor, in relative coordinates, can be written as⁴⁸

$$H_{ex} = H_e \left[-i\vec{\nabla} + \frac{e}{2\hbar c} (\vec{B} \times \vec{r}) \right] + H_h \left[i\vec{\nabla} + \frac{e}{2\hbar c} (\vec{B} \times \vec{r}) \right] - \frac{e^2}{\epsilon_0 r} \quad (2)$$

where \vec{B} is the applied magnetic field and ϵ_0 is the static dielectric constant of the medium. The corresponding Schrödinger equation is

$$H_{ex} \psi = E \psi \quad (3)$$

where the wave function ψ , because of the four-fold degeneracy of the upper

valence band (the split-off valence band being assumed to be quite far away in energy) and two-fold spin degeneracy of the conduction band, is an eight component function. Equation (3) is actually an 8×8 system of equations which reduces the two 4×4 systems of equations for negligible electron-hole exchange, as is assumed in the present case. The electron and the hole Hamiltonians, H_e and H_h , respectively, can be written explicitly as^{43,44}

$$H_e(\vec{k}) = \frac{\hbar^2 k^2}{2m_e} + g_e \mu_B B \quad (4)$$

and

$$\begin{aligned} -H_h(\vec{k}) = & \frac{\hbar^2}{m_0} \left[\left(\gamma_1 + \frac{5}{2} \gamma_2 \right) \frac{k^2}{2} - \gamma_2 (k_x^2 J_x^2 + k_y^2 J_y^2 + k_z^2 J_z^2) \right. \\ & - 2\gamma_3 (\{k_x, k_y\} \{J_x, J_y\} + \{k_y, k_z\} \{J_y, J_z\} + \{k_z, k_x\} \{J_z, J_x\}) \\ & \left. - \frac{e}{c} \kappa \vec{J} \cdot \vec{B} - \frac{e}{c} q (J_x^3 B_x + J_y^3 B_y + J_z^3 B_z) \right] \quad (5) \end{aligned}$$

where γ_1 , γ_2 , γ_3 , κ , and q are the five Kohn-Luttinger parameters;⁴⁷ J_x , J_y , and J_z are the 4×4 angular momentum matrices corresponding to the $J = 3/2$ state; μ_B is the Bohr magneton; $\{A, B\} = 1/2(AB + BA)$; m_0 is the free electron mass; and m_e and g_e are the effective mass and g-value of the conduction electron, respectively. Assuming that \vec{B} is along one of the cubic axes--say the z-axis--and using the standard expressions for the angular-momentum matrices J_x , J_y , and J_z ⁴⁴ for this case, the exciton Hamiltonian can be cast in a 4×4 matrix:

$$H_{\text{ex}} = \begin{bmatrix} H_{11} & \frac{\sqrt{3}\mu_0}{\mu_-} K_-^2 & -\frac{i\mu_0}{\mu_2} K_- P_z & 0 \\ \frac{\sqrt{3}\mu_0}{\mu_+} K_+^2 & H_{22} & 0 & \frac{i\mu_0}{\mu_2} K_- P_z \\ \frac{i\mu_0}{\mu_2} K_+ P_z & 0 & H_{33} & \frac{\sqrt{3}\mu_0}{\mu_-} K_-^2 \\ 0 & \frac{i\mu_0}{\mu_2} K_+ P_z & \frac{\sqrt{3}\mu_0}{\mu_+} K_+^2 & H_{44} \end{bmatrix} \quad (6)$$

where

$$\vec{K} = i\vec{\nabla} + \frac{e}{2\hbar c} (\vec{B} \times \vec{r}), \quad (7)$$

$$K_{\pm} = K_x \pm i K_y \quad (8)$$

and where energies are expressed in units of $R_0 = \mu_0 e^4 / 2\epsilon_0^2 \hbar^2$ and lengths in units of $a_0 = \epsilon_0 \hbar^2 / \mu_0 e^2$ and the reduced-magnetic-field parameter

$$\gamma = \frac{e\hbar B}{2\mu_0 c R_0} \quad (9)$$

is introduced and

$$\frac{1}{\mu_0} = \frac{\gamma_1}{m_0} + \frac{1}{m_e} \quad (10)$$

defined. In addition, the new mass parameters, such as μ 's and m_h , are defined in terms of γ 's as in Ref. 46 and terms involving $(\gamma_3 - \gamma_2)$ have dropped since these are small⁴⁶ in most semiconductors. Each diagonal term in Eq. (6) essentially describes the Hamiltonian of an anisotropic hydrogen-like system in a magnetic field. For instance, H_{11} has the form

$$H_{11} = \frac{\mu_0}{\mu} (p_x^2 + p_y^2) + \left(1 - \frac{2\mu_0}{\mu_1}\right) p_z^2 + r \left[\left(\frac{\mu_0}{\mu} - \frac{2\mu_0}{m_h} \right) (x p_y - y p_x) - \frac{\mu_0}{m_0} \left(3\kappa + \frac{27}{4} q \right) \right] + \frac{1}{4} \frac{\mu_0}{\mu} \gamma^2 (x^2 + y^2) \pm \frac{\hbar}{4r} - 2/r \quad (11)$$

The other terms have expressions very similar to that of H_{11} .⁴⁶

It is obvious that an exact solution of the Schrödinger equation corresponding to the exciton Hamiltonian cannot be obtained. As pointed out earlier, low-field ($\gamma \ll 1$) solutions⁴³⁻⁴⁵ using perturbation theory and high-field ($\gamma \gg 1$) solutions⁴⁶ using an adiabatic approach have been obtained.

To briefly outline a calculation of the energies of the six lowest optically allowed states of the system in the presence of an arbitrary magnetic field, a variational approach is followed, similar to that of Altarelli and Lipari.⁴⁶ The basis functions, however, are more general than those used in Ref. 46 and are more appropriate to the arbitrary

values of the magnetic field. The use of these basis functions reproduces both the low-field and the high-field results quite well.

The first step toward establishing a basis set is to consider the diagonal terms of the Hamiltonian described by Eq. (6). Each of the four diagonal terms describes essentially an anisotropic hydrogenic system, which cannot be exactly solved analytically. However, a straightforward numerical method which has been used to calculate the excitation spectra of an isotropic hydrogenic system⁴⁸ is easily adapted to this problem. The method essentially involves expressing the wave functions of the anisotropic hydrogenic system in terms of a basis set which reflects the symmetry of the system and is easy to use. Since the system is invariant under rotations about the z-axis (magnetic-field axis), the z-component (m) of the total angular momentum is a good quantum number. In addition, the Hamiltonian is invariant under reflections through the origin and, therefore, the system wave functions have definite parity which is specified by a factor of the form z^q , where q is a conserved quantum number, $q = 0, 1$. The remainder of the wave function is chosen for its simplicity for use in numerical calculations and for its ability to reproduce hydrogenic and Landau wave functions. Thus, the wave functions of an anisotropic hydrogen-like system can be expressed as

$$\psi_{n\pm m} = \sum_{i,j} A_{ij} z^q \phi_{qm}(x_i, y_j) \quad (12)$$

where

$$\chi_{qm}(\alpha_1, \beta_j) = e^{im\phi} \rho^{|m|} z^q e^{-(\alpha_1 \rho^2 + \beta_j z^2)} \quad (13)$$

n is used to label different states with each set of quantum numbers and α_1 and β_j are the variational parameters. Thus,

$$H_{ss} \psi_{nqm}^s = E_n^s \psi_{nqm}^s \quad (14)$$

where $s = 1, 2, 3$, and 4 . Then to solve for the eigenfunctions and the eigenvalues of H_{ss} , a standard variational approach is used. To minimize the computer time, even-tempered Gaussians are used where needed only to determine the smallest and the largest exponents from a and b sets; the other exponents are given by the geometric progression between the extreme values. In the presence of the off-diagonal terms, the solutions of Eq. (6) will be some mixture of the solutions of the diagonal terms. Thus, one can write the eigenfunctions of Eq. (6) as

$$\psi_{nml} = \begin{pmatrix} \psi_1(0, m) \\ \psi_2(0, m+2) \\ \psi_3(1, m+1) \\ \psi_4(1, m+3) \end{pmatrix} \quad (15)$$

where

$$\psi_i(q, m) = \sum_n a_n^i \psi_{nqm}. \quad (16)$$

To solve for Eq. (6), the Hamiltonians must be evaluated for the exciton states with the values of m ranging from -3 to 0. Obviously, these are not the only states of the system, but they are the only ones which can be created by one quantum absorption.⁴⁶ In addition, the symmetry of the exciton Hamiltonian requires that all components of the envelop wave function have even parity. Therefore, the Hamiltonian [Eq. (6)] is evaluated say for $m = 0$ and the various elements of the column matrix ψ_{nmi} are chosen, also for $m = 0$. Each of these elements is further expanded in terms of eigenfunctions of H_{ss} , the diagonal elements of the Hamiltonian. These eigenfunctions of H_{ss} are further expressed as linear combinations of $\chi_{mq}(\alpha, \beta)$ as explained earlier. The number of ψ_{nqm} 's used in our calculations is 42, and the number of $\chi_{mq}(\alpha, \beta)$'s in each ψ_{nqm} is 120. These numbers of the basis functions seem to be adequate for the present purpose. Using this basis set, the lowest energy level is calculated by diagonalizing the Hamiltonian numerically. The procedure is repeated for $m = -1, -2$, and -3 and thus all of the four lowest energy levels are calculated, corresponding to $m_j = 3/2, 1/2, -1/2$, and $-3/2$. By incorporating the two possible values of the electron spin, eight distinct energy levels are obtained. The various optical transitions are then defined as

$$\begin{aligned} \Delta M &= +1 & \pi^+ \\ \Delta M &= -1 & \pi^- \\ \Delta M &= 0 & \pi \end{aligned}$$

where M is the z component of the total angular momentum to the hole and the electron. The selection rules for optical transitions depend upon the experimental configuration and upon the polarization of the electromagnetic wave. In particular in the Voigt configuration (i.e., when the direction of propagation is perpendicular to the magnetic field), all of the four σ lines and the two π lines are allowed. In the Faraday configuration (i.e., for propagation parallel to \vec{B}), only four transitions are allowed--two for σ^+ polarization and two for σ^- polarization.

Comparison With Experiments

The energies of the transitions calculated are compared with those determined from magneto-reflection measurements on high-purity epitaxial layers of GaAs and InP at liquid-helium temperature. First consider the case of GaAs. Recently, Nam, et al.,⁴⁹ measured the energies of the σ lines in the Voigt configuration in GaAs in magnetic fields up to 45 kG, whereas Hess, et al.,⁵⁰ have studied both σ and π lines in fields up to 200 kG using the Voigt and Faraday configurations. Due to the very high resolution of their spectrometer, Nam, et al.,⁴⁹ were able to resolve all four σ lines at fields as low as about 25 kG. Using experimentally known values of the conduction electron band mass (m_c), the static dielectric constant (ϵ_0), and theoretically suggested values of the various Kohn-Luttinger parameters of Lawetz⁵¹ (see Table 10), the energies of the six optically allowed transitions were calculated as a function of the magnetic field. The theory does not compare well with the experiment.^{49,50}

TABLE 10

VALUES OF THE BAND-STRUCTURE PARAMETERS OF GaAs. MASS PARAMETERS m_e , γ_1 , γ_2 , AND γ_3 ARE ALL EXPRESSED IN TERMS OF FREE ELECTRON MASS.

m_e	g_e	γ_1	γ_2	γ_3	γ	q	Ref.
0.0665	-0.44	6.85	2.1	2.90	1.2	0.04	50
0.067	-0.06	7.65	2.41	3.28	1.72	0.04	9

TABLE 11

VALUES OF THE BAND-STRUCTURE PARAMETERS OF InP. MASS PARAMETERS m_e , γ_1 , γ_2 , AND γ_3 ARE EXPRESSED IN TERMS OF FREE ELECTRON MASS.

m_e	g_e	γ_1	γ_2	γ_3	γ	q	Ref.
0.0803	1.31	4.95	1.65	2.35	0.97	0.0	51
0.0803	1.2	6.28	2.08	2.76	1.47	0.01	53

Hess, et al.,⁵⁰ have fitted their high-field ($\gamma > 2.5$) data with the adiabatic theory of Altarelli and Lipari⁴⁶ and have suggested a different set of Kohn-Luttinger parameters (see Table 10). The energies of the σ lines are now calculated using these parameters and are compared with their experimental values as measured by Nam, et al.,⁴⁹ in Fig. 67, and good agreement is found. In Fig. 68 the energies of the σ lines thus calculated are also compared with their experimental values measured by Hess, et al.,⁵⁰ at high magnetic fields. In Fig. 69 a similar comparison is displayed between theory and experiment for π lines for high magnetic fields.⁵⁰ The theoretical values of both σ and π lines calculated agree very well with the experimental values in GaAs at all fields.

Recently, Nam, et al.,⁵² have measured the energies of the σ lines in the Voigt configuration in InP in magnetic fields up to about 40 kG, whereas Bimberg, et al.,⁵³ have investigated the behavior of the σ and the π lines in fields up to 200 kG using both Voigt and Faraday configurations. Using the experimentally known values of the static dielectric constant (ϵ_0) and the conduction electron band mass (m_c) and theoretically proposed values of the various Kohn-Luttinger parameters of Lavaetz⁵³ (see Table 11), the energies of the six optically allowed states have again been calculated as a function of the magnetic field. The agreement between the theoretical and experimental values is not good. Bimberg, et al.,⁵³ have fitted their high field ($\gamma > 2.5$) data with the adiabatic theory of Ref. 46 and have proposed a different set of Kohn-Luttinger parameters (see Table 11). Using these parameters the energies of the σ lines are calculated and compared with their experimental values as measured by Nam, et al.,⁵² in Fig. 70. In Fig. 71 similar calculated values of the σ lines are compared with their experimental

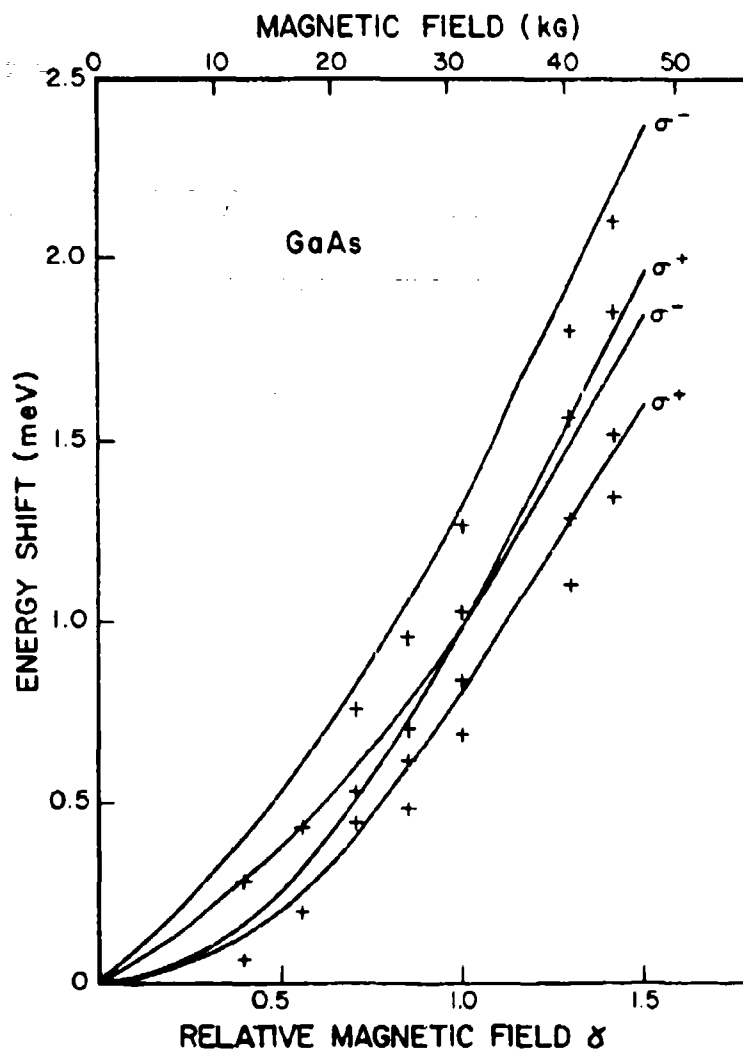


Figure 67. Variations of Energy Shifts of σ^+ and σ^- lines in GaAs as a Function of Reduced Magnetic Field δ . Solid Lines are present calculations and crosses are experimental points from Ref. 49.

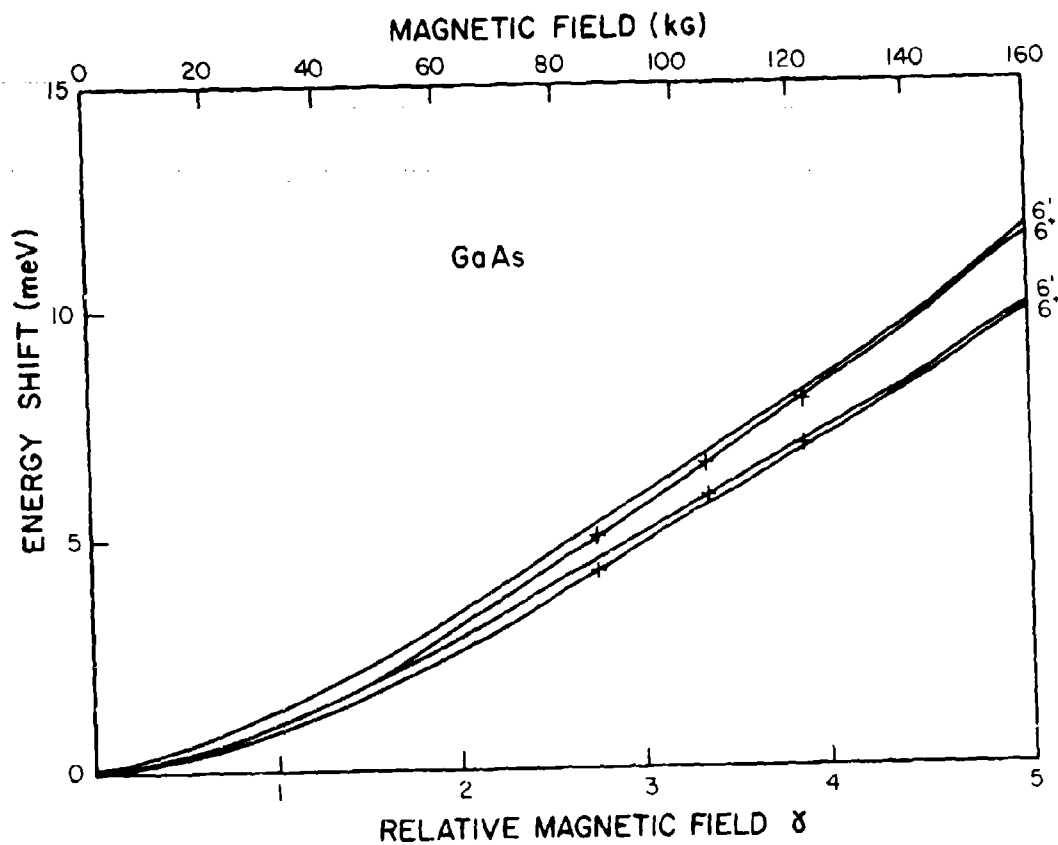


Figure 68. Variations of Energy Shifts of δ^+ and δ^- Lines in GaAs as a Function of Reduced Magnetic Field δ . Solid lines are present calculations, and crosses are experimental points from Ref. 50.

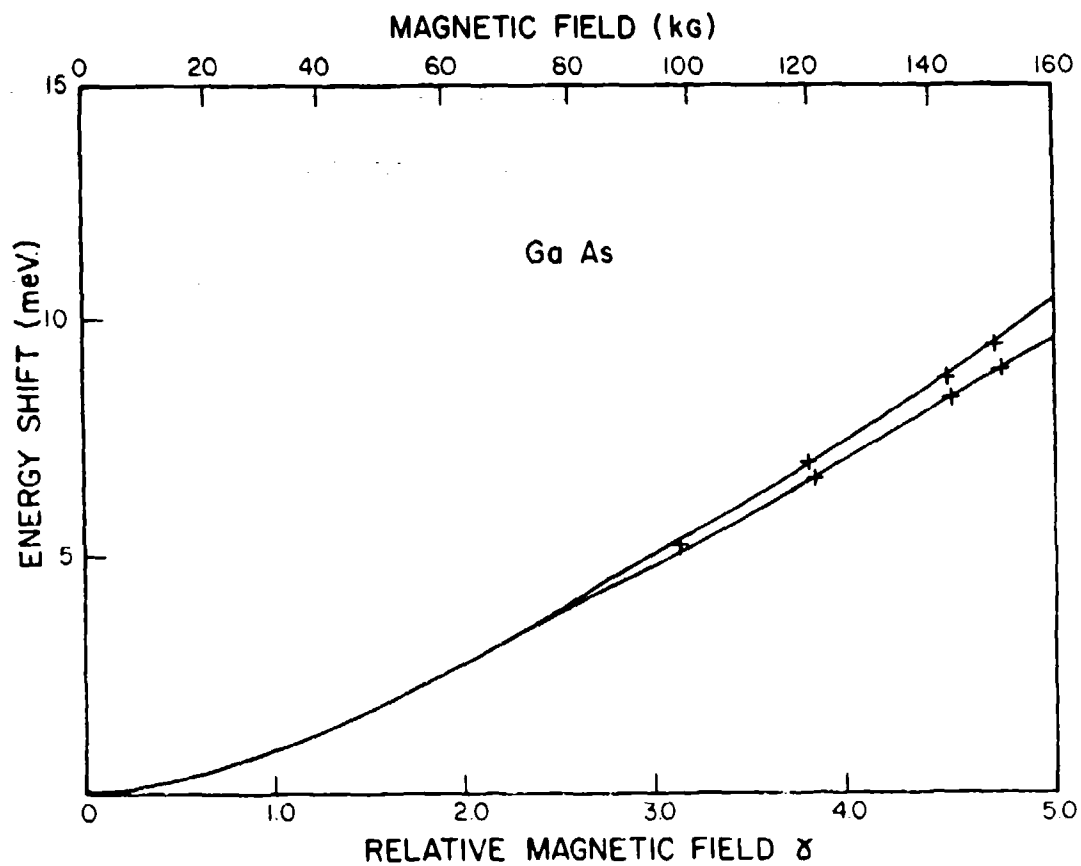


Figure 69. Variations of Energy Shifts of $+$ and $-$ Lines in GaAs as a Function of Reduced Magnetic Field δ . Solid lines are present calculations, and crosses are experimental points from Ref. 50.

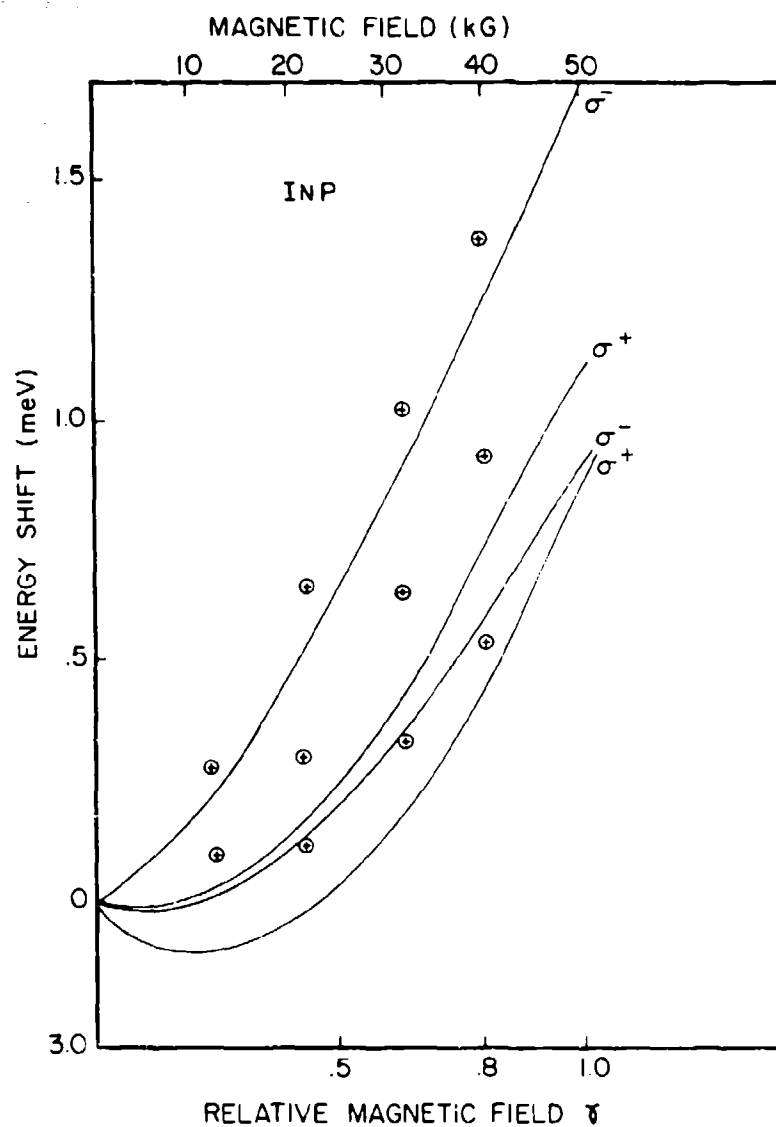


Figure 70. Variations of Energy Shifts of σ^+ and σ^- Lines in InP as a Function of Reduced Magnetic Field γ . Solid lines are present calculations, and crosses are experimental points from Ref. 52.

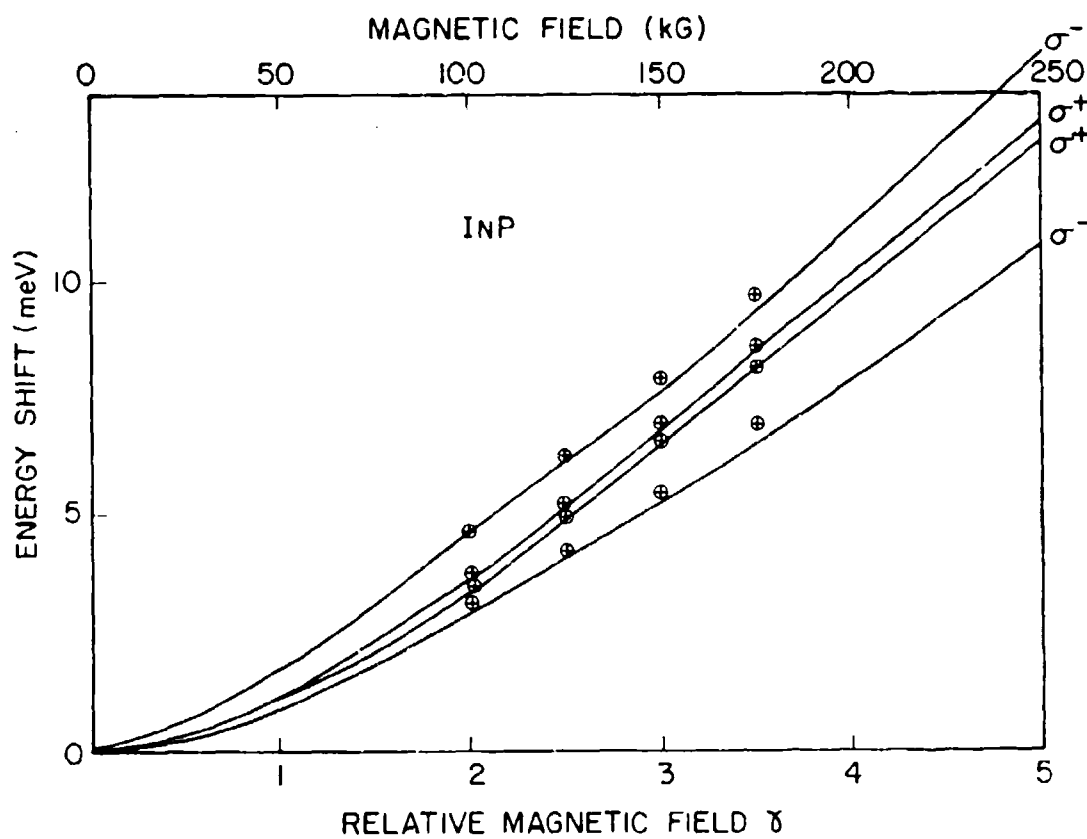


Figure 71. Variations of Energy Shifts of σ^+ and σ^- Lines in InP as a Function of Reduced Magnetic Field γ . Solid lines are present calculations, and crosses are experimental points of Ref. 53.

values as measured by Bimberg, et al.,⁵³ at high fields. In both cases a good overall agreement between theory and experiment is found. Similar agreement has also been found for the case of π lines.

The magneto-optical measurements on the exciton states of semiconductors along with the use of the appropriate theoretical calculations, therefore, lead to the reliable determination of broad structure parameters of these materials.

6.2 BOUND MULTIEXCITON COMPLEXES IN GaAs

Several groups recently have reported observations of relatively sharp photoluminescence lines of energies less than the energy of the line associated with an exciton bound to a neutral donor in silicon,⁵⁴ germanium⁵⁵ and silicon carbide.⁵⁶ Similar lines⁵⁷ have also been reported for acceptors in silicon, although the study in this case is not so detailed for the donors. The energies and the widths of these lines were such that they could not be explained in terms of any recombination mechanism involving simply a single exciton bound to a neutral shallow impurity center. A model involving a multiexciton complex bound to a donor (acceptor) was invoked in which each line was associated with radiative recombinations of an exciton in the bound multiexciton complex. The behavior of these lines in the presence of magnetic⁵⁸ and stress⁵⁴ fields has been studied, and some doubt⁵⁴ has been cast on the donor-bound multiexciton complex model in silicon. Recently, however, Herbert, et al.,⁵⁹ Thewalt,⁶⁰ and Lyon, et al.,⁶¹ have investigated this problem in greater detail and have been able to answer successfully the objections raised in Ref. 54, thus establishing the viability of the bound multiexciton complex model.

The following describes the first observation of at least six sharp photoluminescence lines with energies less than the energies of the lines associated with a radiative recombination of a single exciton bound to a neutral acceptor in high-purity epilayers of GaAs at liquid-helium temperature. This, as far as we know, is the first observation of such lines in a direct gap semiconductor. It is proposed that these lines arise as a result of radiative recombination of an exciton in a multiexciton complex bound to a neutral acceptor. It will now be shown that this model can explain the data satisfactorily.

Experimental Details

The samples used in this investigation were high-quality epitaxial layers grown on semi-insulating GaAs:Cr substrates using the $H_2:AsCl_3:Ga$ vapor-deposition technique. The samples were not intentionally doped, but the spectra generally indicated the presence of zinc (strong), and sometimes carbon (less strong), acceptors and at least one unidentified donor (perhaps silicon). More than twenty such samples were investigated with similar results in all cases.

The samples were mounted in a strain-free manner on one end of a sample holder which was, in turn, placed in the tip of a glass helium Dewar. The mounting was arranged so that the samples were immersed in liquid He with provision for over-vacuums to lower the bath temperature to the range 1.2 - 2.1°K. A krypton laser (6471 Å) with pump-power density of the order of 35mW/mm^2 was used to pump the luminescence. Spectral analysis of the photoluminescence spectra was made with a modified Bausch and Lomb 4-m

grating spectrograph employing a large high-resolution diffraction grating. Reciprocal dispersion at the wavelengths of interest was approximately 0.54 \AA mm^{-1} in the first order. All of the spectra were photographically recorded on Kodak type 1-N spectroscopic plates.

Wavelength calibration of the plates was performed by fitting well-known, interferometrically determined neon spectral lines to the grating equation using a non-linear least-squares technique. A wavelength-to-energy conversion factor of 12395.13 \AA-eV was used.

Results and Discussion

Typical photoluminescence spectra are displayed in Fig. 72. The lines marked A_1 , A_2 , and A_3 are due to radiative recombination of a single exciton bound to a neutral acceptor, which in this case is zinc.⁶² The line marked A'_2 results from an exciton similarly bound to a carbon acceptor. The initial system consists of two holes and a single electron bound to a negative ion. Within the framework of the j-j coupling scheme, the two holes--usually considered equivalent,⁵⁶ each having a j-value of $3/2$ --lead to two different states with total J values of 2 and 0 which are split in energy due to electrostatic interactions. The $J = 2$ state is further split into $J = 5/2$ and $J = 3/2$ states due to its interaction with the electron spin of $1/2$. The $J = 0$ state couples with the electron spin and gives rise to a $J = 1/2$ state. Thus, the initial system consists of three distinct states with J values of $5/2$, $3/2$, and $1/2$. The final system, after the exciton has recombined, consists of a hole in a singlet $J = 3/2$ state. The three lines A_1 , A_2 , and A_3 arise as a result of transitions between these systems. The separation

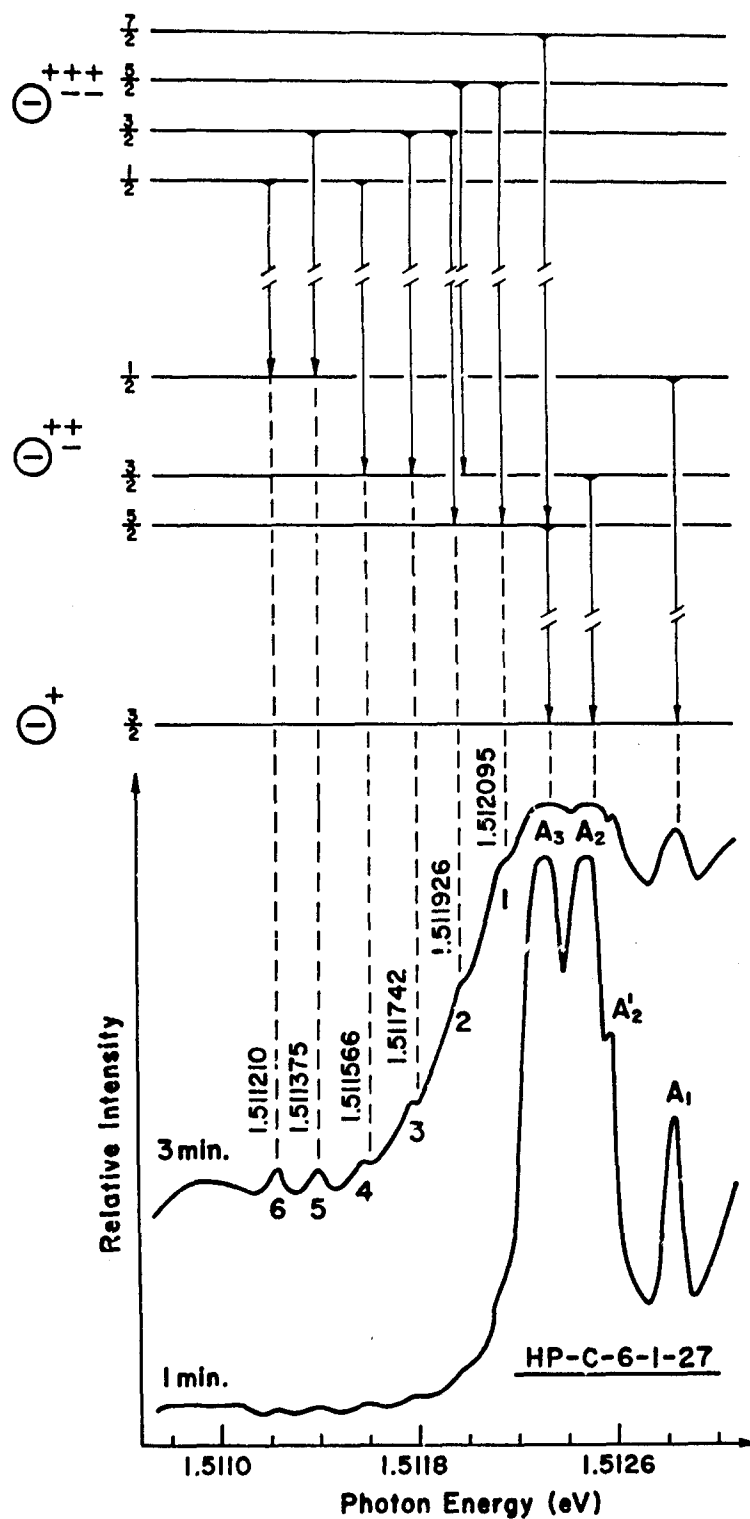


Figure 72. Photoluminescence Spectra for GaAs High-Purity Epitaxial Specimen Taken at 2°K with 1-min. and 3-min. Exposures. The proposed electronic transition scheme for complexes composed of one and two excitons bound to the neutral zinc acceptor is illustrated and is discussed further in the text.

between A_1 and A_2 lines is about 0.35 meV, which is about twice the separation between A_2 and A_3 . The localization energy of an exciton bound to a neutral acceptor is about 2.75 meV, whereas the binding energy of the zinc acceptor is 30.7 meV.⁶²

On the lower-energy side of the principal-bound-exciton (PBE) lines is observed, for the first time, a series of six sharp lines with a constant energy separation of about 0.17 meV. These lines are observed only in those samples in which strong PBE lines are also observed. In the following several possible models are discussed to explain the origin of these lines. It is proposed that only the model involving an exciton recombination in a multi-exciton complex bound to a neutral acceptor can explain the observed spectra satisfactorily.

The first possibility suggested by these six lines is that they may result from two different sets of PBE transitions associated with two different chemical acceptors which have different binding energies (larger if Haynes' rule is obeyed) from the one which gives rise to A_1 , A_2 , and A_3 . The energies of these lines, however, do not agree with the energies of PBE lines associated with different known chemical acceptors in GaAs.⁶² It is extremely unlikely that these lines are associated with two shallow acceptors which have not been detected previously in epilayers of GaAs and which appear only in those samples in which Zn-related PBE lines are strong.

A second possible explanation is that these lines arise as a result of radiative recombination of an electron and a hole belonging to different donor-acceptor pairs or arise due to a radiative recombination of an exciton

bound to a donor-acceptor pair. It is easy to show that the positions and the separations of these lines rule out such a possibility.

A remaining possibility for explaining the origin of these lines is the multiple-bound-exciton (MBE) complex. It is suggested that these lines arise as a result of radiative recombination of an exciton in a two-exciton complex bound to a neutral acceptor. In the discussion which follows, it will be shown that such a model can readily explain the data presented.

To determine the number of states of this system, the j-j coupling scheme is used. Assume, along with Dean, et al.,⁵⁶ that in the ground state of this system, the three holes are equivalent and thus have the same orbital quantum number. This leads to a value of the total angular momentum, J, for these holes equal to 3/2. The two electrons are assumed to have their spins paired, giving rise to a total angular momentum of 3/2 for the whole system.

If we consider only this state of the multiexciton complex, complexes bound to a neutral acceptor containing as many as five excitons are needed to explain the data--the usual assumption made by previous investigators.⁵⁶ This seems rather unlikely in the present case because transitions are observed even at low excitation intensities, where the probability--solely from kinematic considerations--of having such large complexes is very small. Also, the intensities of the lines are almost the same (within a factor of three), and this tends to rule out the possibility of large multiexciton complexes.

If the possibility is considered that such a system might have low-lying excited states (which can be obtained in at least two different ways), sufficient multiplicity can be achieved with the two-exciton model being proposed.

As a first possibility, consider the case in which the holes remain equivalent, but the two electrons are assumed to be in different orbital states and are treated, therefore, as nonequivalent. The maximum value of the angular momentum of the two electrons is 1, which when coupled to the J -value of the holes leads to three different total angular momentum states: $5/2$, $3/2$, and $1/2$. It is also assumed that the ground-state energy ($J = 3/2$ electron spins paired) differs little from that of the excited $J = 3/2$ state. The positions of these states are schematically shown in Fig. 72 where it is assumed that the separation between the states is approximately the same as that between the $J = 5/2$ and $J = 3/2$ levels of the PBE. The state corresponding to $J = 7/2$ shown in Fig. 72 arises from the second model discussed below. The final states for these transitions are the states of a single exciton bound to an acceptor, assumed to be those observed experimentally, and have been discussed already. It is suggested that the six sharp lines observed may arise as a result of transitions between the three states of the PBE as shown in Fig. 72.

A second possible way to obtain the excited states of the initial system is to treat the two electrons as equivalent but assume that one of the three holes is in a different orbital state and is, therefore, nonequivalent to the other two. Within the framework of the j - j coupling scheme, the two electron spins are paired and the two equivalent holes give rise to $J = 2$ and $J = 0$ states. The coupling between the $J = 2$ state and the $j = 3/2$ state of the

nonequivalent hole then leads to four possible different J states: $7/2$, $5/2$, $3/2$, and $1/2$. The coupling between the $J = 0$ state and the $j = 3/2$ state of the nonequivalent hole leads to a $J = 3/2$ state whose energy is again assumed to differ little from the other $J = 3/2$ states. The transitions between these four initial states and the three final states of the PBE will give rise to the observed lines as shown in Fig. 72. The transition corresponding to $J = 7/2$ to $J = 5/2$ is assumed to coincide with the A_3 line.

To explain the observed spectra using either of these models, it has been assumed that there is a reasonably good probability of finding the present system in low-lying excited states. This assumption permits explanation of the observed data without requiring extremely large and unwieldy multiexciton complexes. Two different ways have been mentioned of arriving at the low-lying excited states proposed; but in such a preliminary model, it is not possible to decide in favor of one or the other. In both cases, it was assumed for simplicity that all $J = 3/2$ states have equal energies; in the absence of this simplifying assumption, other acceptable schemes could also be proposed.

Following is the process responsible for the formation of multiexciton complexes bound to neutral acceptors in GaAs. The neutral acceptor sequentially captures a free hole and a free electron, which have been created by the exciting radiation, to form a bound-exciton complex. This complex further captures, successively, free excitons to form two, three, etc., exciton complexes with varying probabilities. In this model it was assumed that the localization energy of the second exciton is somewhat larger than that of the first exciton. This assumption is consistent with the recent measurements of the work functions of excitons in bound multiexciton complexes in Si^{61} and

with the theoretical work of Herbert.⁶³ The detailed mechanism of binding of multiexciton complexes to neutral impurity centers is, however, still far from clear.

6.3 LOCALIZED VIBRATIONAL-MODE ABSORPTION OF CARBON-IMPLANTED GaAs

Introduction

When an impurity atom of mass smaller than the mass of Ga and As atoms is substituted in a GaAs lattice, it gives rise to a vibrational mode whose frequency is usually higher than that of the higher eigenmode of the lattices. As the introduction of the impurity atom breaks the translational symmetry, the vibrations of the impurity atom are highly localized. These localized vibrational modes are characteristic of the type of impurity and the strengths with which this impurity is coupled with the surrounding lattice.

The following describes the first observation of a localized vibrational mode (LVM) due to carbon implanted in GaAs and its behavior as a function of annealing temperature. Similar studies for the case of aluminum,⁶⁴ phosphorous,⁶⁴ silicon,⁶⁵ and nitrogen⁶⁶ implanted in GaAs have already been reported in the literature. In Ref. 66, the behavior of the LVM due to nitrogen implantation as a function of annealing temperature was found to be quite different from the behavior of the other three impurities. The strength of the absorption peak due to the LVM of nitrogen decreased slightly with increasing annealing temperature up to ~600°C, after which it dropped rapidly, disappearing completely at 800°C. However, the strengths of the LVM absorption peaks due to Si, Al, and P implants increased as a function of annealing

temperature up to about 600°C and then remained relatively constant. Different speculations were invoked⁶⁶ to explain this difference in behavior between nitrogen and the other three impurities.

This study of the behavior of the LVM of carbon implanted in GaAs was partial motivated by the desire to determine the behavior of carbon in comparison with the other four impurities. As a substitutional impurity in GaAs, ^{12}C was first shown to produce an LVM at 582.4 cm^{-1} at liquid-nitrogen temperature by Newman, *et al.*,⁶⁷ who compared observation of the LVM of ^{12}C with ^{13}C at 561.2 cm^{-1} .

Experimental

The samples used in this study included both undoped and Cr-doped substrates. The undoped samples were n-type with a free carrier concentration of $3.7 \times 10^{16}\text{ cm}^{-3}$, whereas the Cr-doped substrates were semi-insulating. All samples were polished on one side prior to carbon-ion implantation. C^{++} ions were implanted with fluences ranging from 0.6 to $4.7 \times 10^{16}\text{ C}^{++}\text{ ions/cm}^2$ at an energy of 6 MeV. An extrapolation of a standard LSS range table⁶⁸ to 6 MeV gives an approximate range of $6.4\text{ }\mu\text{m}$ for the implanted carbon ions in GaAs. The standard deviation is approximately $0.4\text{ }\mu\text{m}$.

It was decided, on the basis of the results of some preliminary absorption studies, to polish the crystals on the unimplanted sides also and to wedge them in order to avoid interference fringes in the absorption measurements. This wedging and mechanical polishing was accomplished without any visible harm to the implanted area. The mean thickness of the sample varied from 165

to 343 μm . The implanted areas were 4.7-mm-diam. circles. The samples were mounted for measurement such that the implant areas were centered over a circular aperture of 4.0 mm in diam. in a copper plate. Cellulose tridecanoate was used to bond the samples to the plate, which was then mounted onto a cold finger of a Dewar system having ZnSe windows.

Prior to the measurements, the samples were cleaned with trichlorethylene and rinsed with acetone. Unimplanted reference samples from the same wafers were treated in an identical manner. In this experiment annealing was not done in situ. All anneals were carried out in a vacuum for a duration of 1 hr., after which the crystals were remounted for measurement.

The measurements were carried out in a specially designed vacuum grating monochromator, using Czerny-Turner optics having a focal length of 1.5 m. The light source was provided by a silicon-carbide glowbar which was chopped at a frequency of 5.93 Hz. To eliminate high-energy radiation, the light was reflected twice by MgO reststrahlen filter plates before entering the slit. The slit width used in this study yielded an inverse linear dispersion of energy and wavelength of $3.2 \text{ cm}^{-1}/\text{mm}$ and $10.0 \mu\text{m}/\text{mm}$, respectively. The radiation passing through the slit traveled a distance of 1.5 m to the front-surface spherical collimator-mirror where it was reflected to a $23 \times 17 \text{ cm}$ reflection grating. The diffracted light from the grating was collected by a telescope-mirror and passed through an exit slit of the same size as the entrance slit. The two slits, collimator-mirror, grating, and telescope-mirror comprise the Czerny-Turner optical system which is advantageous in that it helps to cancel out coma.⁶⁹ In these measurements the grating drive was controlled externally by an automatic scan control typically set at $2.3 \text{ cm}^{-1}/\text{min}$.

Results

Some typical results are shown in Fig. 73, which contains a collection of recorder traces from a number of different measurements on three separate crystals, showing the relative transmission as a function of energy (cm^{-1}). The results for the carbon-implanted undoped sample show that annealing to 300°C increases the strength of the carbon peak. However, further annealing reduces the total absorption of the carbon LVM. This decrease is also observed in the chromium-doped sample. The undoped crystal was implanted with a dose of $2.8 \times 10^{16} \text{ C}^{++} \text{ ions/cm}^2$, whereas the chromium-doped sample received an implant dose of $3.0 \times 10^{16} \text{ C}^{++} \text{ ions/cm}^2$. For comparison, the affects of annealing on an unimplanted, undoped sister sample have been included. From these traces one can calculate a value of the integrated LVM absorption, $I = \alpha\Delta$, where α is the absorption coefficient and Δ is the width of the absorption peak at half maximum. It was found for the undoped crystal that the value of I first increases from 1.0 to 5.1 cm^{-2} as the annealing temperature is raised to 300°C . As the annealing temperature is further increased to 500 and 650°C , the value of I decreases approximately to 1.6 and 0.2 cm^{-2} , respectively. For the chromium-doped crystal, I decreases from 1.0 cm^{-2} to approximately 0 as the annealing temperature is raised from 500 to 650°C .

In a recent paper on a study of carbon, oxygen, and silicon impurities in GaAs, Brozel, et al.,⁷⁰ provided a calibration for the strength of the LVM absorption as a function of C^{++} concentration, namely, 1 cm^{-2} corresponds to $2.4 \times 10^{16} \text{ C}^{++} \text{ ions/cm}^3$. According to this calibration the largest LVM absorption value at 300°C (annealing temperature) for the

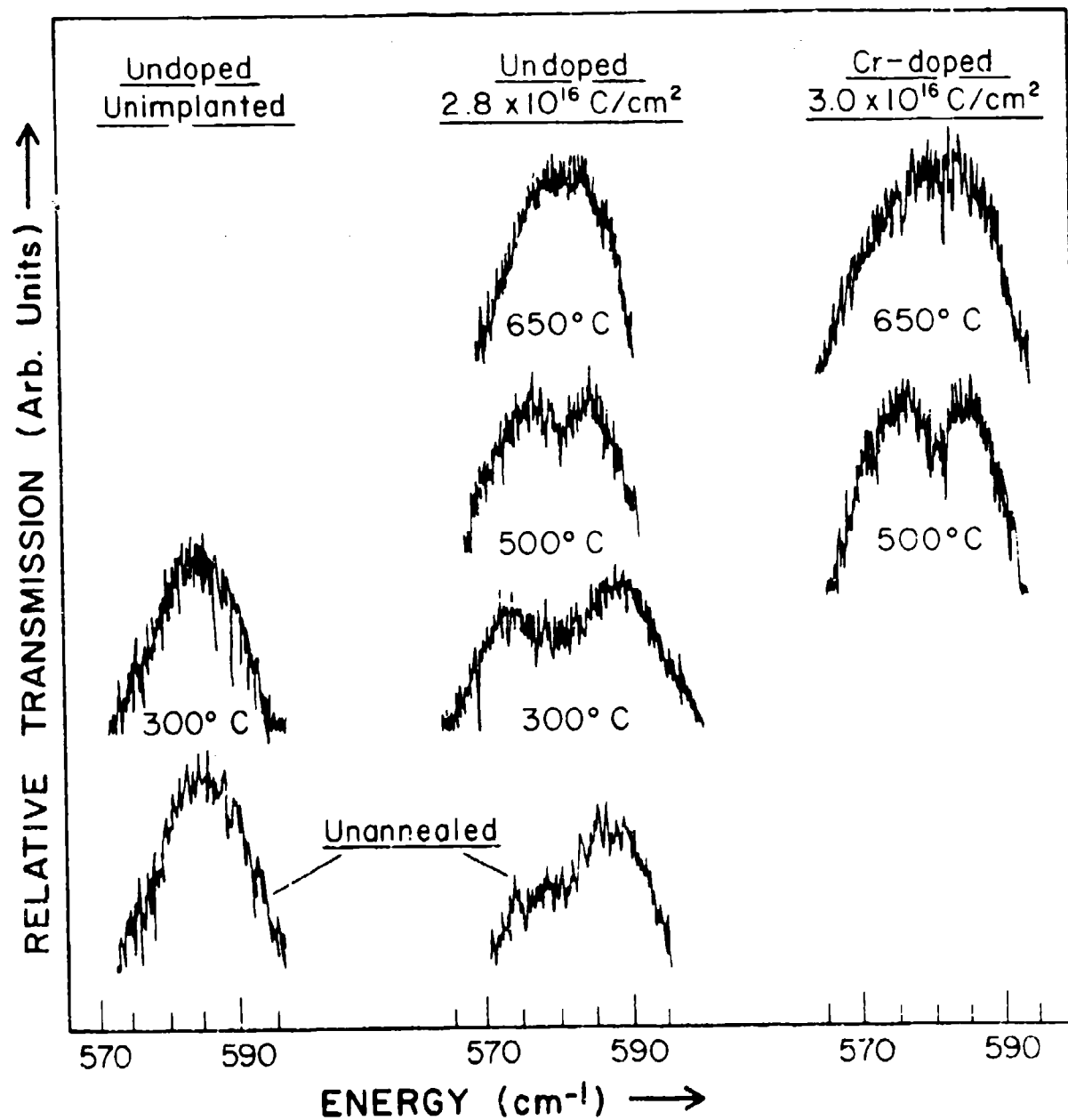


Figure 73. Relative Transmission and Annealing Temperature as a Function of Energy for Three Different Crystals. All data shown here were taken with the samples at $\sim 67^\circ\text{K}$.

undoped sample corresponds to $0.20 \times 10^{16} \text{ C}^{++} \text{ ions/cm}^2$. This calculated value should be compared with the value of the implant dose, $4.7 \times 10^{16} \text{ C}^{++} \text{ ions/cm}^2$ for that sample, which implies that less than 5% of the carbon atoms have moved into isolated substitutional sites during the 300°C anneal.

Discussion

The results on carbon implants show them to share features with both the N and the Si, Al, and P implants. For annealing temperatures below 300°C, the carbon LVM absorption increases--a result similar to the cases of Si, Al, and P. However, in contrast to the latter three species, the carbon LVM absorption decreases rapidly at temperatures above 500°C (similar to the case for N).

In summary, it is concluded that the LVM for ion-implanted C^{++} in GaAs has been observed and that it occurs at the same frequency reported⁶⁷ for carbon-doped GaAs. Furthermore, the measurements imply that even under favorable annealing temperatures, only about 5% of the implanted carbon atoms (for the implant dose of the experiment) are to be found in isolated substitutional sites. Therefore, it is suggested that either appreciable clustering is taking place and/or a large number of the carbon atoms occupy interstitial positions in the GaAs lattice. Another explanation could involve extensive outdiffusion of carbon through the damaged regions. In addition to the 528 cm^{-1} carbon LVM, another weak absorption at slightly higher energies has been observed. Further study is required to understand both the decrease in substitutional carbon absorption and the higher energy absorption.

6.4 EMISSION SPECTRA FROM GaAs FET-LIKE STRUCTURES

Introduction

The development of GaAs FET's has created great interest in the investigation of techniques to isolate the moderately doped active epitaxially deposited films from the less controlled bulk-grown substrates on which they are placed. Many manufacturers are using a high-purity epitaxial layer (buffer) deposited between the active region and the substrates to provide such isolation. The following describes the use of laser-pumped photoluminescence as a non-destructive probe technique to investigate sharp transition lines originating from the technologically important interface region between the active and buffer epi-layers.

Experimental Procedure

Samples investigated in this study (Fig. 74a) consisted of moderately sulfur-doped ($4 \times 10^{16} - 5 \times 10^{17} \text{ cm}^{-3}$) active layers, 0.5 to 5.0 μm thick, deposited in the vapor phase on doped or undoped VPE buffer layers, 1.0 to 26.0 μm thick. The doped buffers were oxygen-doped by the addition of water vapor to the halogen transport gas, while the undoped buffers were grown to high resistivity using a technique developed by Kozaki, et al.,⁷¹ in which excess AsCl_3 is added to the growth region. In both types of buffers, the majority carriers determined by Hall measurements were holes (except Sample 4377), and concentration of carriers and of impurities were in the 10^{14} cm^{-3} range at most. The substrates were high resistivity ($10^9 \text{ } \Omega\text{-cm}$) chromium-doped GaAs. The sample characterizations are summarized

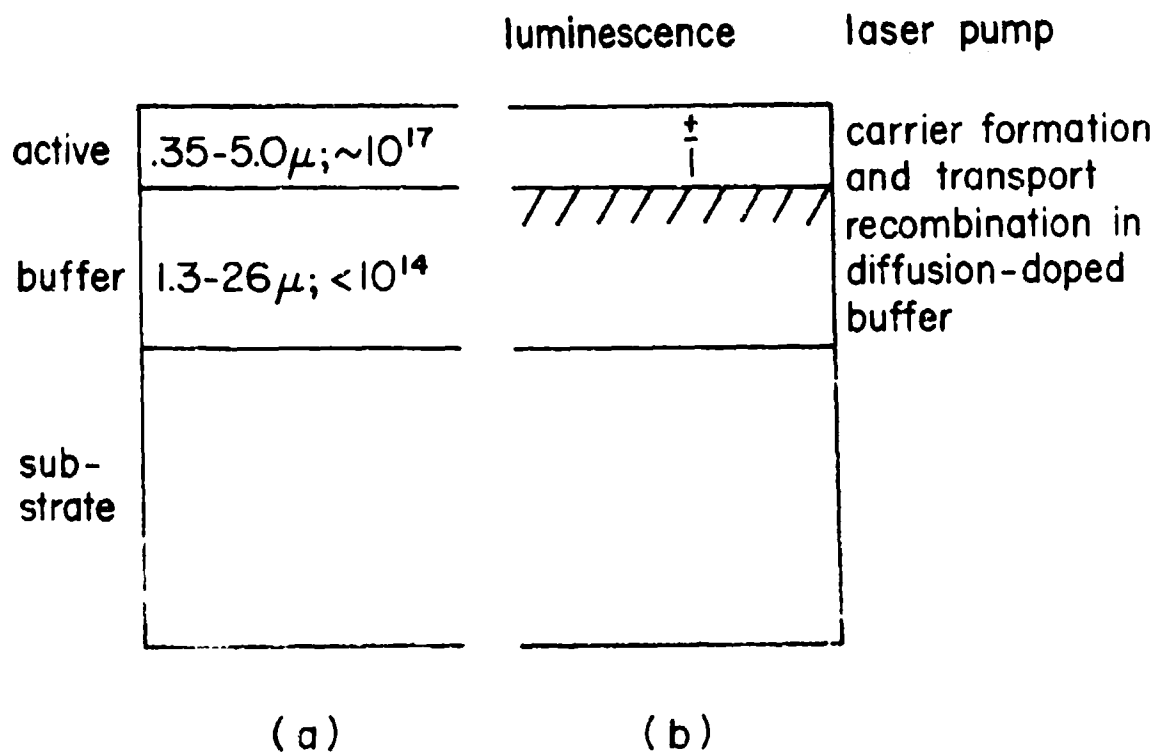


Figure 74. (a) Typical GaAs Structures Investigated.

(b) Photoluminescence Mechanisms; Photoelectron Absorption ($\sim 10^3 \text{ \AA}$ Deep), Carrier Formation and Diffusion ($\sim 1 \text{ cm}$ Diffusion Length for Holes), Pair Recombination in a Diffusion Doped Region Parity Interface Region beneath the Active Layer.

in Table 12. Samples 13/77 and 43/77 were grown especially for this investigation and consisted of active layers thicker than could be used for FETs; the remainder were produced during FET development research.

Photoluminescence measurements were made using a krypton-ion laser as a pump source at wavelengths of 6471, 5208, or 4762 Å. Pump power could be varied from about 15 to 350 mW and focused to a spot-size of about 1.5 mm diam. Pumping radiation was nearly normally incident on the sample surface (15° from normal). Samples were cooled by immersion in liquid helium to less than 2°K and could be subjected to an external magnetic field of up to 45 kG supplied by a conventional iron-core electromagnet.

Luminescence was collected in a cone with half-angle of about 12° and focused on the entrance slit on a modified 4-m-techl-length Bausch and Lomb grating spectrometer.

Data were collected on Kodak Type 1-N spectrographic plates with linear dispersion of less than 0.54 Å/mm . The experimental arrangement is indicated schematically in Fig. 75.

The mechanisms leading to the creation of the photoluminescence in the interface region were discussed previously⁷² and are shown schematically in Fig. 74. Pump photons at the frequencies of the krypton source are absorbed near one surface of the active layer ($\alpha \approx 10^{11} \text{ cm}^{-1}$) and form electron-hole pairs. The carriers tend to diffuse into the material due to the concentration gradient created by the surface pumping. Those which recombine radiatively in the highly-doped active region produce only a broad, generally

TABLE 12

SAMPLE CHARACTERISTICS

Sample Number	Structural Features			Spectral Features						
	Active Thickness (μm)	Active Concentration (n cm^{-3})	Buffer Thickness (μm)	Donor BE Doublet ¹	A	B	C	D	E	F Deeper Structure
132/76	<1	10^{17}	3	Yes				X		
133/76	<1	10^{17}	4	Yes	X	X	X	X	X	
134/76	<1	10^{17}	6	Yes				X		
135/76	1.8	1.9×10^{17}	1.5	Yes	X	X				
136/76	1.7	1.5×10^{17}	4.7	Yes	X	X				
137/76	2.4	1.4×10^{17}	6.3	Yes	X	X	X	X	X	
138/76	2.0	6×10^{16}	4.0	Yes	X	X	X	X	X	
155/76	0.35	7×10^{16}	12.8	Yes	Weak					$0^2, 2n, 1.5118^3$
8/77	1.6-2.5	6×10^{16}	1.5-3	Yes	Very Weak					
9/77	2.2-2.7	4×10^{16}	2.7-3.1	Yes	Very Weak					
11/77	1.6-2.2	6×10^{16}	1.7-2.1	Yes	Very Weak					
12/77	1.3-1.8	6×10^{16}	1.3-1.8	Yes	Very Weak					
13/77	3.5-5	3×10^{16}	2.5-3	Yes				X		
29/77	0.7	5×10^{17}	4	Yes	Very Weak					0, 1.5118
33/77	4	10^{17}	26	Yes ⁴	X	X	X	X	X	Zn, Ge(?), 1.5118

Notes: 1. 1.5112 and 1.5117 eV; A, 1.51346; B, 1.51458; C, 1.51469; D, 1.51483; E, 1.51490; F, 1.51501

2. 1.4884 eV

3. Compton line previously noted in high-quality epi (10)

4. 1.5112 and 1.5117 eV. In addition

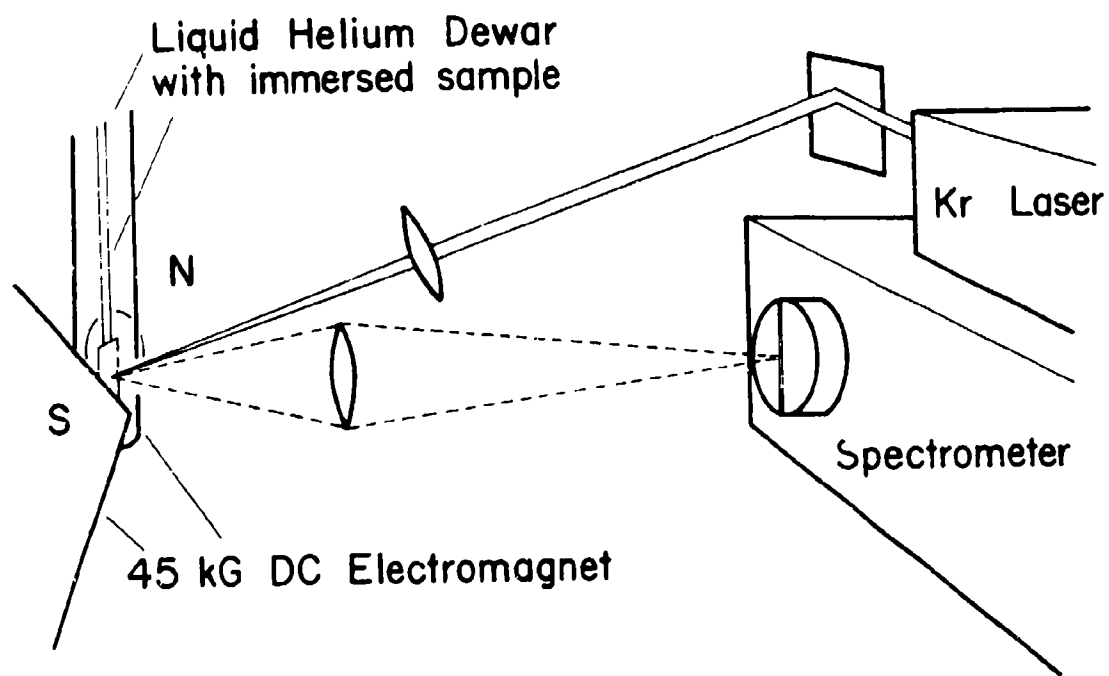


Figure 75. Equipment Schematic.

structureless, luminescence in the near gap region, while those which combine non-radiatively are not detected using the present technique. The observation of sharp-line structure reported here supports the contention that a significant number of the carriers diffuse through the highly doped layer and enter the less-doped buffer region before they recombine. Our observation of dominant sharp-line structure, even in samples with 4 to 5 μm of highly-doped active region, tends to support the existence of large minority-carrier diffusion lengths (2 μm or greater) reported previously in GaAs doped at the 10^{17} level,⁷³⁻⁷⁵ although in the referenced works the samples were not equivalent to those used in this study. All employed room-temperature measurements in which scattering mechanisms and surface recombination might be quite different than at 2°K. Further, only Ettenberg⁷⁵ used epitaxial layers in which peak mobilities are considerably enhanced compared to bulk-grown material; but, in that study, the minority carriers were electrons. Direct laser pumping of the interface as a viable explanation for our observations has been eliminated because of well-documented absorption coefficients $> 10^4 \text{ cm}^{-1}$ at the wavelength employed in this study (see Ref. 76).

Ettenberg's convincing experimental observation⁷⁵ argues strongly against recombination radiation as a viable source of pumping energy for interface transitions. This mechanism is further rejected in the present study because of the low probability that recombination photons created in the highly doped region near the surface would have sufficient energy to pump the exciton states at the interface. For the impurity densities considered in the active regions of our samples, the position of the Fermi level will be at or above the low-concentration conduction-band minimum.⁷⁷ The impurity band will extend below the Fermi level from 6 to 20 meV, depending upon the dopant

concentration. The highest probability for recombination radiation from this region will involve electrons near the impurity-band minimum and holes near the $k \approx 0$ valence-band maximum (since the hole densities will generally be very small). Such photons will have energies from 6 to 20 meV less than the low-concentration-gap energy and hence will fall in the range of 1.500 to 1.513 eV at liquid-helium temperatures. The probability of reabsorption of these low-energy photons in the interface or buffer-layer regions is exceedingly small since they are incapable of exciting transitions across the fundamental gap.

The existence of an interface zone lightly doped by indiffusion of the active layer dopant (sulfur) as well as inherent impurities (silicon, zinc, etc.) is supported by the observation of a clearly defined doublet due to exciton binding to two donor species (1.51412- and 1.51417-eV peaks, Fig. 76). Sequential chemical etching of the surface (using $\text{H}_2\text{O}_2:\text{H}_2\text{SO}_4:\text{H}_2\text{O}$) resulted in the disappearance of the lower-energy peak (sulfur) as one would expect when the diffusion distance of the dopant is exceeded. A residual shallow donor (tentatively identified as silicon) remained through the buffer layer. Although a direct Hall measurement of the interface diffusion region is difficult, the nature of photoluminescence suggests that the layer is n-type, unlike the buffer, but with an impurity concentration of $< 10^{16} \text{ cm}^{-3}$.

Spectra

As indicated in Table 12, spectra from these samples had many structural characteristics in common. While photoluminescence intensity and quality (line widths, number of lines produced, etc.) varied in a somewhat

unpredictable manner from sample to sample, all spectra did contain the same recognizable donor-bound exciton doublet and one or more of the lines marked A through F in Fig. 76. Sample 43/77, which was coincidentally the thickest buffer layer, indicated two additional, much weaker, donor-bound exciton peaks at 1.51414 and 1.51422 eV. Several of the samples produced spectral structure identifiable as shallow acceptor-bound excitons, but in all cases this structure was very weak and can probably be traced to the residual zinc impurity nearly always found in VPE GaAs.⁷⁸ Sample 43/77 also contained a second acceptor with slightly less exciton binding energy (0.4 meV less than Zn-bound exciton) which might tentatively be identified as Ge,⁷⁸ but no confirmation for such an identification exists.

It is interesting to note that all of the spectra (except 136/76) were dominated by the strong donor-bound exciton lines, with the lines A through F being considerably weaker by comparison. Sample 136/76 (Fig. 77) produced a significantly different spectrum, obviously dominated by the line B and, to a lesser extent, A, rather than the donor-bound excitons (seen at ~ 1.514 eV). As the active layers were removed, by etching, from samples 137/76 and 13/77, their spectral characteristics became more similar to those of 136/76 in that some or all of lines A through F tended to dominate the shallow structure. It is concluded, therefore, that lines A through F rise from mechanisms different from the shallow hydrogenic donor-bound excitons and are probably more characteristic of the buffer material than the lightly doped n-type interlayer region.

The two samples grown on oxygen-doped buffers also produced the deep bound exciton line at 1.4889 eV associated with oxygen,⁷⁸ and this line was not seen in any of the samples not intentionally doped.

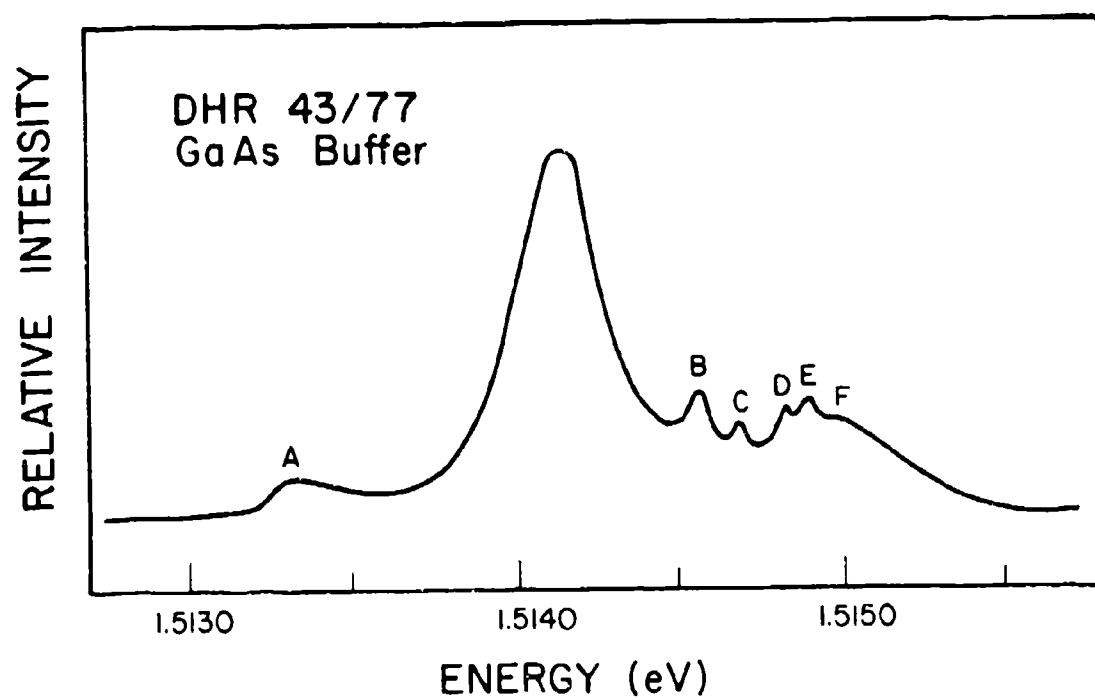


Figure 76. Photoluminescence Spectra of Typical Donor-Bound Exciton-Dominated Shallow Structure. Peaks at 1.51412 and 1.51417 eV are associated with sulfur and silicon, respectively. Spectral features A through F are associated with other mechanisms.

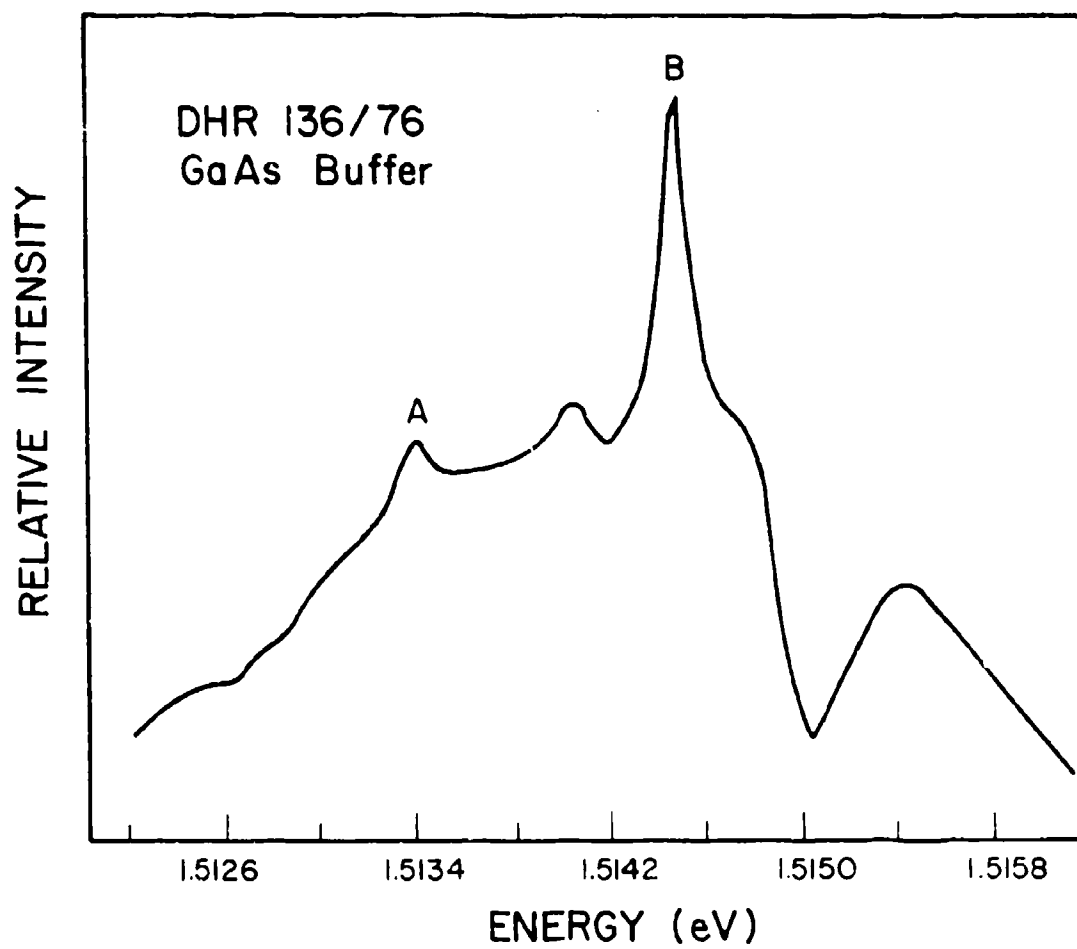


Figure 77. Photoluminescence Dominated by Complex Lines.

Discussion

The behavior of the donor-bound exciton doublet in an applied magnetic field is shown in Fig. 78, and the linear Zeeman fan construction for these data is shown in Fig. 79. It is clear from Fig. 79 that unambiguous line assignments for these transitions have not been accomplished due to the complexity of the data, although the general linear splitting of the lines is clear. While the data did not permit determination of electron and hole g-factors for this exciton complex, it was sufficiently well defined that a determination of the quadratic (diamagnetic) shift coefficients, plotted in Fig. 82, could be performed.

Since several of the samples produced spectra in which lines A and B were well isolated and intense, magnetic characteristics of these lines were more easily obtained. The behavior of the lines is shown in Fig. 80. Both lines produced well-defined linear Zeeman splittings. The multiplicity of line B suggests a transition involving $j = 3/2$ (hole) and $j = 1/2$ (electron) states leading to calculation of the hole and electron g-factor as 0.41 and 0.36, respectively. Figure 81 illustrates the fit to such a model for the peaks measured at 41.3-kG applied field. The direction of this transition is not directly defined by the data, but the simplest model available would be with the initial state having two paired electrons and a hole (similar to the donor-bound exciton) and the final state--a single electron. A simple donor-bound exciton is eliminated as a possibility because of a clearly different diamagnetic shift for complex B compared to the (S°, X) and (Si°, X) complexes (Fig. 82). The next simplest model is the double-donor-acceptor complex previously suggested.⁷⁹

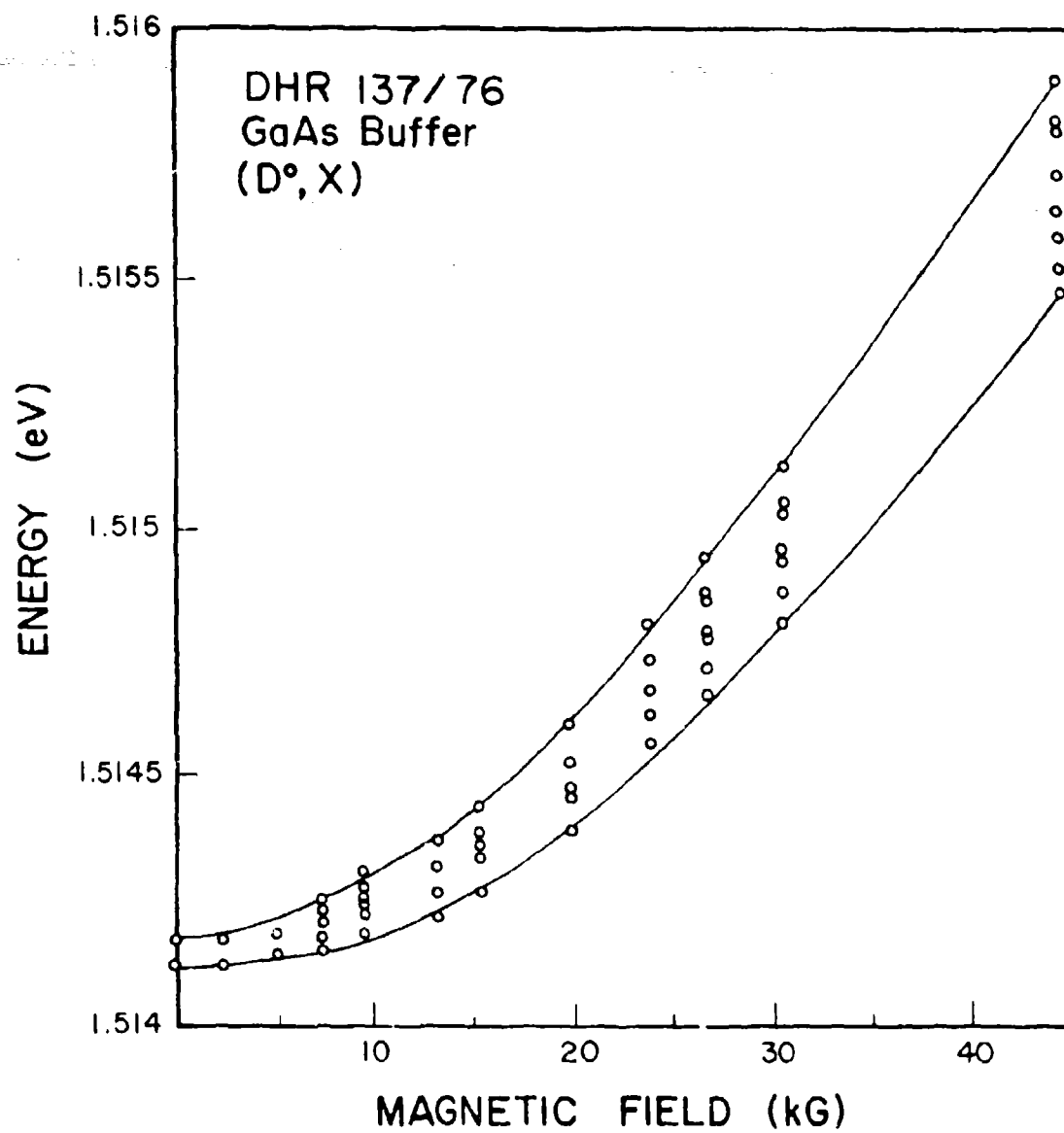


Figure 78. Magnetic-Field Behavior of Sulfur and Silicon-Bound Exciton Lines.

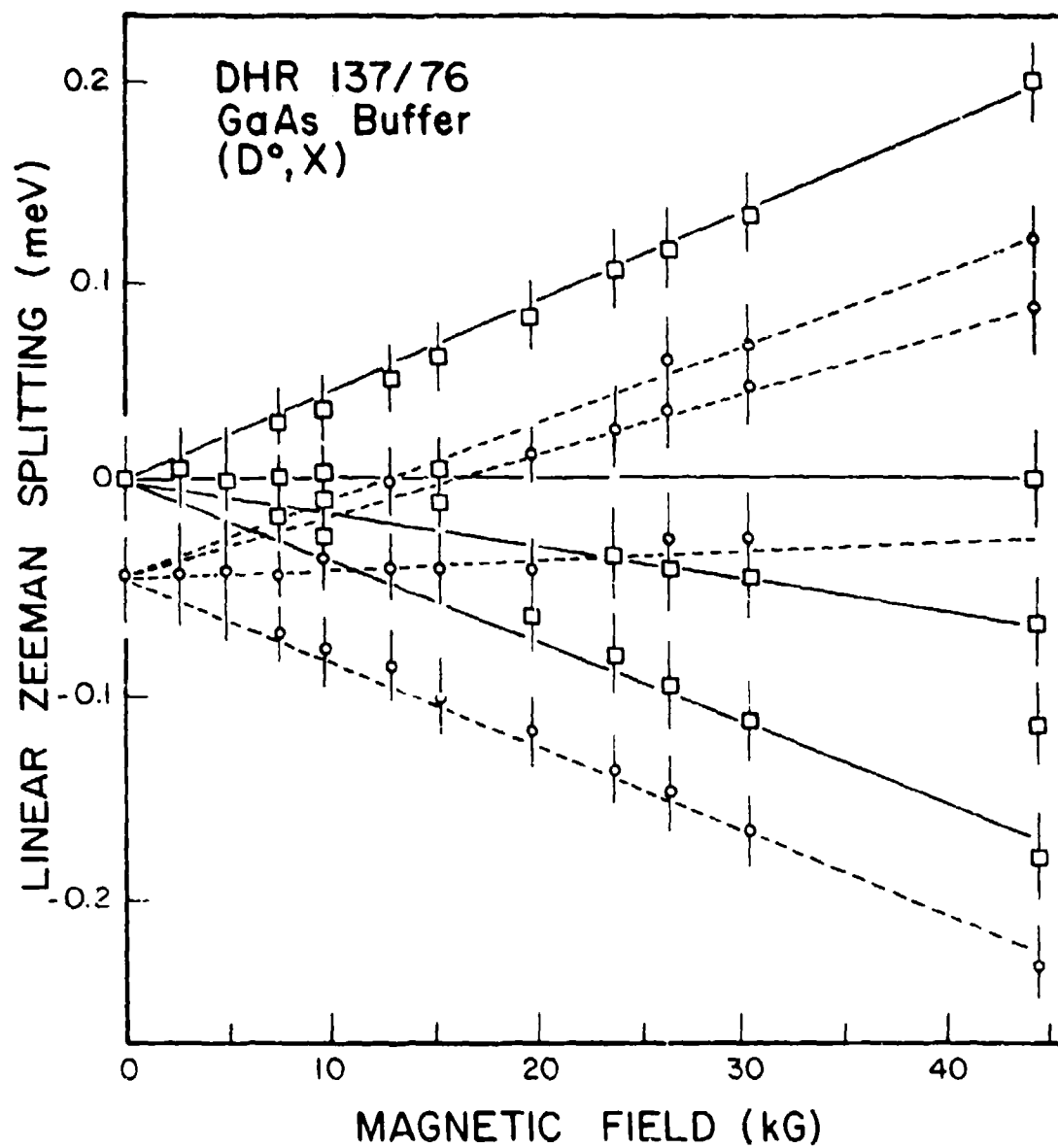


Figure 29. Linear Zeeman Splitting of Sulfur and Silicon-Bound Exciton Lines.

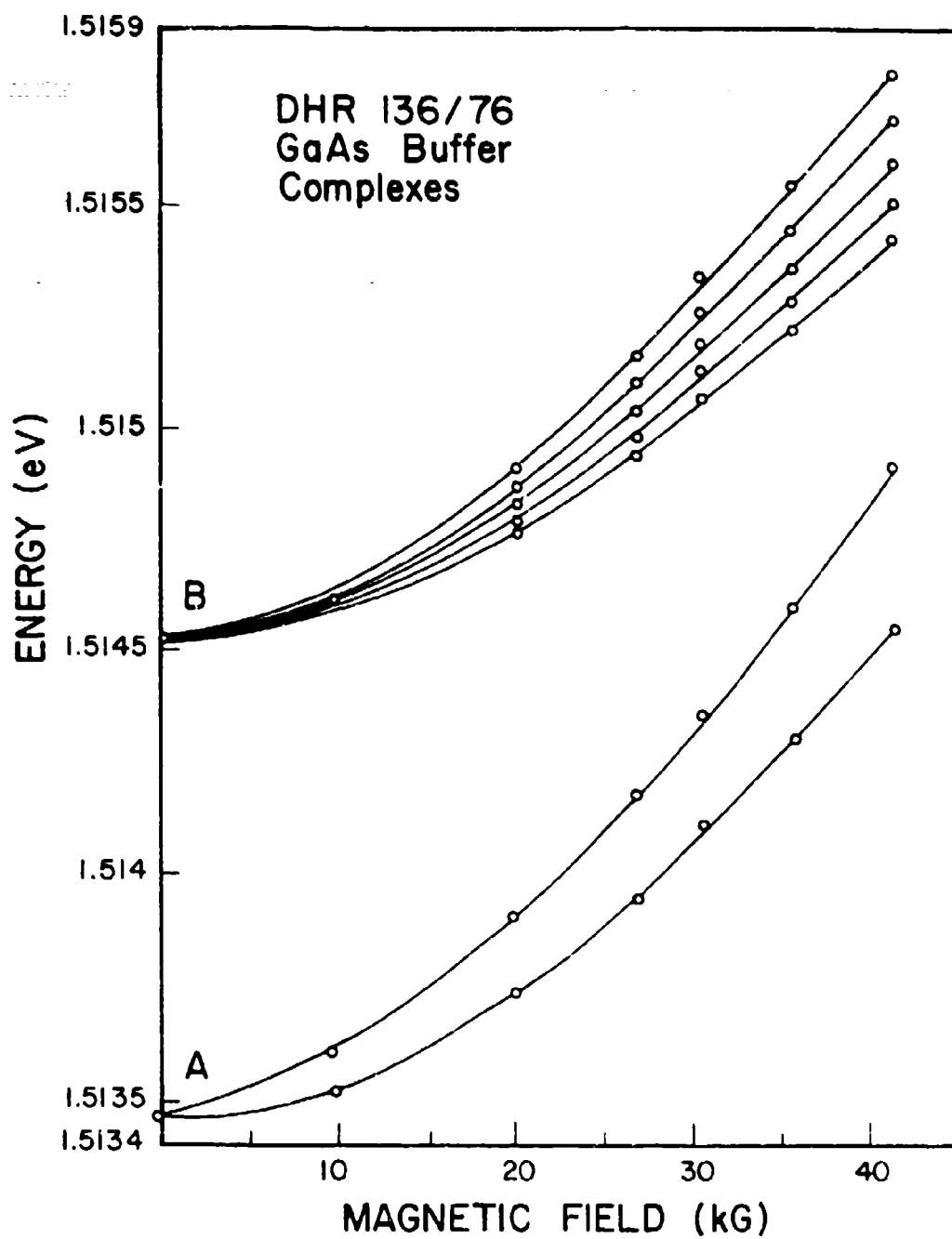


Figure 80. Magnetic-Field Behavior of Complex Lines A and B.

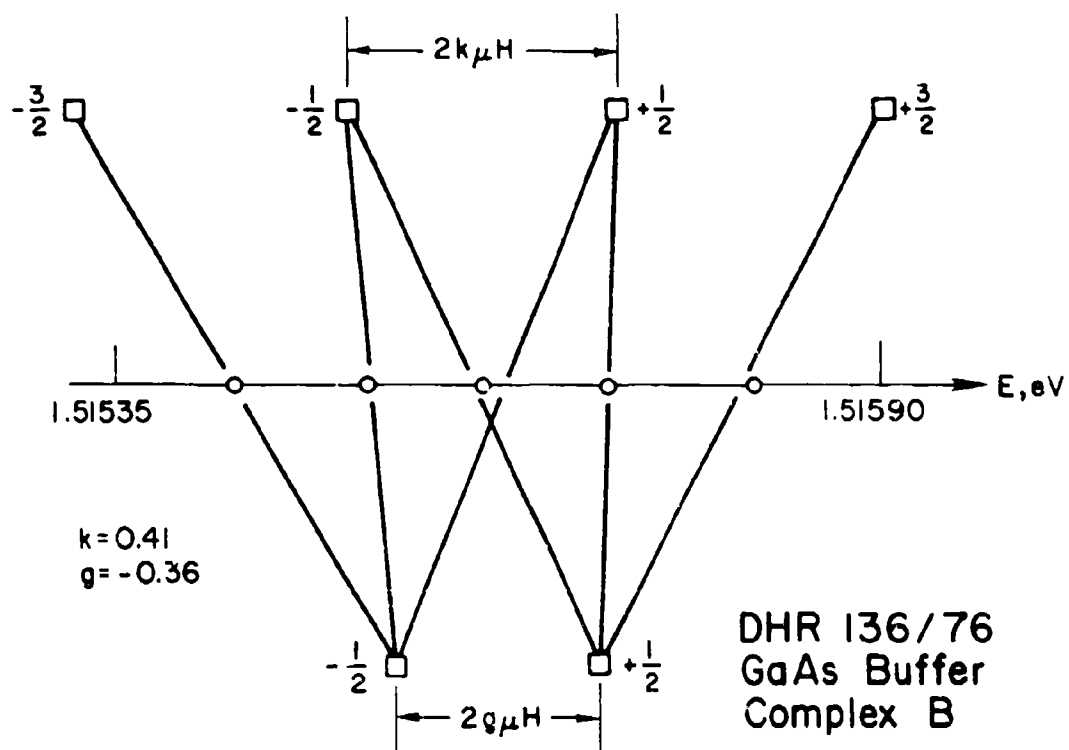


Figure 81. Linear Zeeman Splitting of the Line B (1.514538 eV) at 41.3-kG Applied Field.

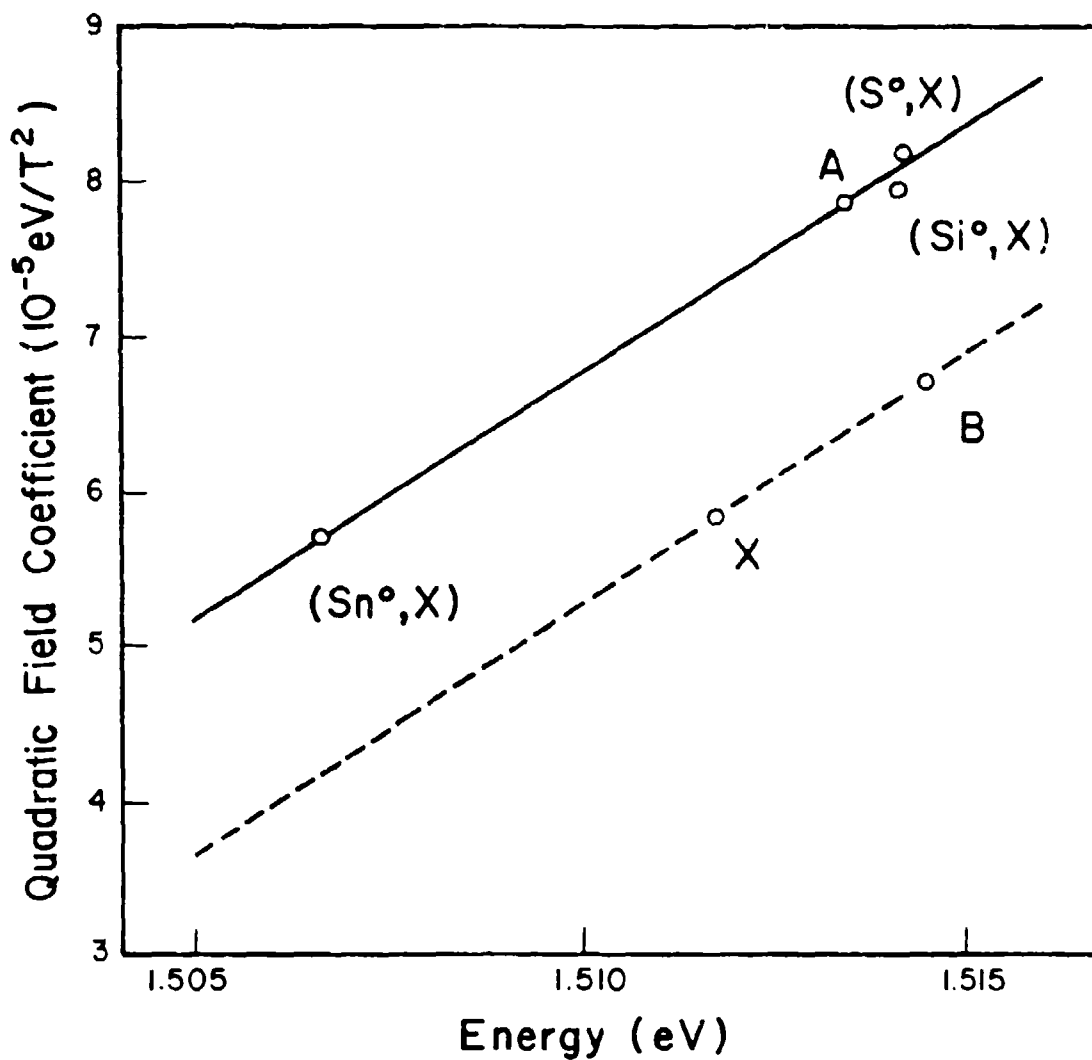


Figure 82. Diamagnetic Shift of Various Sharp Lines as a Function of Transition Energy. Straight lines indicated are suggested by the data but are not related to a theoretical model. Tin-bound exciton line after Schairer, *et al.*⁸¹

Line A showed no additional structure in any sample except the doublet plotted in Fig. 80. We note that the linear splitting of this line is markedly greater than that observed for other lines in this region, although without additional structural features, neither a model or a meaningful measure of g-factors can result. The diamagnetic shift for line A is comparable to the donor-bound excitons as seen in Figs. 78, 80, and 82.

Finally, certain similarities are noted in the diamagnetic behavior of various sharp lines reported here and elsewhere and shown in Fig. 82. One would expect that the quadratic shift for similar centers should increase with transition energy as shown qualitatively, since such an increase in transition energy represents a decrease in the binding energy of the associated carriers. Analysis of the simple hydrogenic system suggests that the diamagnetic coefficient should vary inversely as the cube of the binding energy. Note that many unsettling simplifications are required to evolve a similar theoretical expectation for the behavior of the complex systems described here, and success has not been achieved in this regard. It is interesting to note nevertheless that the behavior of complexes B and X⁸⁰ appears unusual with regard to that of the simple center bound exciton complexes associated with tin, sulfur, and silicon.

Continuing investigations will provide correlation of the behavior of buffer-layer FET devices with the presence of impurities and impurity complexes in the interface region as reported here. The development of photoluminescence as a sensitive and non-destructive technique which can be employed during device processing should greatly enhance this effort.

REFERENCES

1. J. P. Donnelly, C. O. Bozler, and W. T. Lindley, "Low-Dose n-Type Ion Implantation into Cr-Doped GaAs Substrate," *Solid State Electron.* 20, 273 (1977).
2. P. M. Hemenger, *Rev. Sci. Instrum.* 44, 698 (1973).
3. L. J. van der Pauw, *Philips Res. Repts.* 13, 1 (1958).
4. J. W. Mayer, O. J. Marsh, G. A. Shifrin, and R. Baron, *Can. J. Phys.* 45, 4073 (1967).
5. N. G. E. Johansson, J. W. Mayer, and O. J. Marsh, *Solid State Electron.* 13, 317 (1970).
6. See, for example, J. A. Hutchby and K. V. Vaidyanathan, *J. Appl. Phys.* 48, 2559 (1977); Y. Yuba, K. Game, K. Masuda, and S. Namba, *Jap. J. Appl. Phys.* 13, 641 (1974); and B. K. Shin, D. C. Look, Y. S. Park, and J. E. Ehret, *J. Appl. Phys.* 47, 1574 (1976).
7. Y. K. Yeo, Y. S. Park, and P. W. Yu, *J. Appl. Phys.* 50, 3274 (1979).
8. R. G. Hunsperger, R. G. Wilson, and D. M. Jamba, *J. Appl. Phys.* 43, 1318 (1972).
9. R. Zölch, H. Ryssel, H. Kranz, H. Reichl, and I. Ruge, in *Ion Implantation in Semiconductors*, (F. Chernow, J. A. Borders, and D. K. Brice, Eds.) (Plenum, New York and London, 1976), p. 593.
10. J. P. Donnelly, W. T. Lindley, and C. E. Hurwitz, *Appl. Phys. Lett.* 27, 41 (1975).
11. J. Lindhard, M. Scharff, and H. Schott, *Mat. Fys. Medd. Dan. Vid. Selsk.* 33, 1 (1963).
12. H. Brooks, in *Advances in Electronics and Electron Physics*, Vol. VII, (L. Marton, Ed.) (Academic, NY, 1955), p. 87.
13. T. E. Seidel and A. U. MacRae, *Trans. Met. Soc. A.I.M.E.* 245, 491 (1969).
14. B. D. Choe, Y. K. Yeo, Y. S. Park, published in September 1980 issue of *J. Appl. Phys.*
15. R. T. Young, C. W. White, G. J. Ch. J. Narayan, W. B. Christie, M. Murakami, P. W. King, and S. D. Kramer, *Appl. Phys. Lett.* 32, 139 (1978).
16. A. Gat, J. F. Gibbons, T. J. Magee, J. Peng, V. R. Deline, P. Williams, and C. A. Evans, *Appl. Phys. Lett.* 32, 296 (1978).

17. Laser-Solid Interactions and Laser Processing (S. D. Ferris, H. J. Leamy, and J. M. Poate, Eds.) (American Institute of Physics, NY, 1979).
18. J. C. C. Fan, J. P. Donnelly, C. O. Bozler, and R. L. Chapman, in Proceedings 7th International Symposium on GaAs and Related Compounds, St. Louis, 1979 (Institute of Physics, Ondon, 1979), p. 472.
19. S. U. Campisano, G. Foti, E. Rimini, F. H. Eisen, W. F. Tseng, M. A. Nicolet, and J. L. Tandon, J. Appl. Phys. 51, 295 (1980).
20. T. Inada, S. Kato, Y. Maeda, and K. Tolunaga, J. Appl. Phys. 50, 6000 (1979).
21. Q. Kim, Y. S. Park, R. S. Mason, T. E. Luke, R. L. Hengehold and Y. K. Yeo, in AIP Conference Proceedings on Laser-Solid Interactions and Laser Processing, Vol. 50 (American Institute of Physics, NY, 1979), p. 597.
22. W. Schairer and W. Graman, J. Phys. Chem. Solids 30, 2225 (1969).
23. F. E. Roszlooczky, F. Ermanis, I. Hayashi, and B. Schwartz, J. Appl. Phys. 41, 264 (1970).
24. A. Y. Cho and I. Hayashi, J. Appl. Phys. 42, 4422 (1971).
25. W. T. Andersen, Jr., A. Christou, and J. E. Davey, J. Appl. Phys. 49, 2998 (1978).
26. K. Ploog, A. Fischer, and H. Künzel, Appl. Phys. 18, 353 (1979).
27. Y. K. Yeo, J. E. Ehret, F. L. Pedrotti, Y. S. Park, W. M. Theis, Appl. Phys. Lett. 35, 197 (1979).
28. R. K. Surridge and B. J. Sealey, J. Phys. D10, 911 (1977).
29. J. L. Tandon, M-A. Nicolet, and F. H. Eisen, Appl. Phys. Lett. 34, 165 (1979).
30. F. L. Pedrotti, Y. K. Yeo, J. E. Ehret, and Y. S. Park, to be published in November 1980 issue of J. Appl. Phys.
31. R. Beekingbottom and T. Ambridge, Rad. Effects 17, 31 (1973).
32. Y. K. Yeo, F. L. Pedrotti, and Y. S. Park, to be published in November 1980 issue of J. Appl. Phys.
33. J. D. Samsbury and J. F. Gibbons, Radiat. Eff. 6, 269 (1970).
34. J. S. Harris, in Ion Implantation in Semiconductors (I. Ruge and J. Graul, Eds.) (Springer-Verlag, Berlin, 1971), p. 157.
35. B. K. Shin, Appl. Phys. Lett. 29, 438 (1976).

36. D. J. Ashen, P. J. Dean, D. T. J. Hurle, J. B. Mullin, and A. M. White, *J. Phys. Chem. Solids* 36, 1041 (1975).
37. J. F. Gibbons and R. E. Tremain, Jr., *Appl. Phys. Lett.* 26, 199 (1975).
38. B. K. Shin, J. E. Ehret, Y. S. Park, M. Stefiniw, *J. Appl. Phys.* 49, 2988 (1978).
39. See, for example, C. M. Wolfe and G. E. Stillman, *Appl. Phys. Lett.* 27, 564 (1975).
40. SRL Monthly R&D Status Report 6913-42 covering period 1 Jan - 31 Jan 1980 under contract F33615-76-C-1166 (Systems Research Laboratories, Inc., Dayton, OH, 12 Feb 1980).
41. G. H. Narayanan and W. G. Spitzer, *J. of Mat. Sci.* 13, 2418 (1978).
42. G. H. Narayanan and W. G. Spitzer, to be published.
43. M. Altarelli and N. O. Lipari, *Phys. Rev.* B7, 3798 (1973); B8, 4046 (E) (1973).
44. L. Swierkowski, *Phys. Rev.* B10, 3311 (1973); 111 Nuovo Cimento, 29B, 340 (1975).
45. K. Cho, S. Suga, W. Dreybrodt, and F. Willman, *Phys. Rev.* B11, 1512 (1975); B12, 1608 (E) (1975).
46. M. Altarelli and N. O. Lipari, *Phys. Rev.* B9, 1733 (1974). This paper contains extensive references to earlier work.
47. W. Kohn and J. M. Luttinger, *Phys. Rev.* 96, 529 (1954); J. M. Luttinger, *Phys. Rev.* 102, 1030 (1956).
48. C. Aldrich and R. L. Greene, *Phys. Stat. Sol. (b)* 93, 343 (1979).
49. S. B. Nam, D. C. Reynolds, C. W. Litton, R. J. Almassy, T. C. Collins, and C. M. Wolfe, *Phys. Rev.* B13, 761 (1976).
50. K. Hess, D. Bimberg, N. Lipari, J. V. Fischbach, and M. Altarelli, in Proceedings of the 13th International Conference on the Physics of Semiconductors, Rome, Italy, (F. G. Fumi, Ed.) (Tipografia Marver, Rome, 1977), p. 142.
51. P. Lawaetz, *Phys. Rev.* B4, 3400 (1972).
52. S. B. Nam, D. C. Reynolds, C. W. Litton, T. C. Collins, P. J. Dean, and R. C. Clarke, *Phys. Rev.* B13, 1643 (1976).
53. D. Bimberg, K. Hess, N. O. Lipari, J. V. Fischbach, and M. Altarelli, *Physica* 89B, 139 (1977).

54. R. Sauer and J. Weber, Phys. Rev. Lett. 39, 770 (1977). This paper contains references to earlier work.
55. R. W. Martin, Solid State Commun. 14, 369 (1974).
56. P. J. Dean, D. C. Herbert, D. Bimberg, and W. J. Choyke, Phys. Rev. Lett. 37, 1635 (1976).
57. See, for example, M. L. W. Thewalt, Phys. Rev. Lett. 38, 521 (1977) and references cited therein.
58. R. Sauer and J. Weber, Phys. Rev. Lett. 36, 48 (1976).
59. D. C. Herbert, P. J. Dean, and W. J. Choyke, Solid State Commun. 24, 383 (1977).
60. M. L. W. Thewalt, Solid State Commun. 25, 513 (1978).
61. S. A. Lyon, D. L. Smith, and T. C. McGill, Phys. Rev. Lett. 41, 56 (1978).
62. D. J. Ashen, P. J. Dean, D. T. J. Hurle, J. B. Mullin, A. M. White, and P. D. Greene, J. Phys. Chem. Solids 36, 1041 (1975).
63. D. C. Herbert, J. Phys. C: Solid State Phys. 10, 3324 (1977).
64. L. H. Skolnik, W. G. Spitzer, A. Kahan, and R. G. Hunsperger, J. Appl. Phys. 42, 5223 (1971).
65. L. H. Skolnik, W. G. Spitzer, A. Kahan, F. Euler, and R. G. Hunsperger, J. Appl. Phys. 43, 2146 (1972).
66. A. H. Kachare, W. G. Spitzer, A. Kahan, F. K. Euler, and T. A. Whatley, J. Appl. Phys. 44, 4393 (1973).
67. R. C. Newman, F. Thompson, M. Hyllands, and R. F. Peart, Solid State Commun. 10, 505 (1972).
68. J. T. Gibbons, W. S. Johnson, and S. W. Mylroie, Projected Range Statistics, (John Wiley and Sons, Inc., NY, 1975).
69. M. Czerny and A. Turner, Z. Physik 61, 792 (1930).
70. M. R. Brozel, J. B. Clegg, and R. C. Newman, J. Phys. D: Appl. Phys. 11, 1331 (1978).
71. T. Nozaki, M. Ogama, H. Terao, and H. Watanabe, In GaAs and Related Compounds, Inst. of Phys. Conf. Series 24 (Institute of Physics, B.F., 1974), pp. 46-54.
72. B. C. Reynolds, R. Almasy, C. Litton, E. E. Bajaj, and D. L. Look, Bull. Am. Phys. Soc. 22, 435 (1977).
73. B. C. Casey, Jr., and T. Stern, J. Appl. Phys. 47, 631 (1976).

74. C. J. Hwang, Phys. Rev. B6, 1355 (1972).
75. M. Ettengerg, Appl. Phys. Lett. 30, 207 (1977).
76. M. Cardona, in Semiconductors and Semimetals (R. K. Willardson and A. C. Beer, Eds.), Vol. 3 (Academic Press, NY, 1967), p. 134.
77. N. F. Mott, Metal-Insulator Transitions (Barnes and Noble Books, NY, 1974), p. 211.
78. D. Ashen, P. J. Dean, D. T. J. Hurle, J. B. Mullin, A. M. White, and P. D. Greene, J. Phys. Chem. Solids 36, 1041 (1975).
79. D. C. Reynolds, R. J. Almassy, C. W. Litton, S. B. Nam, and G. L. McCoy, in GaAs and Related Compounds (St. Louis) 1976, Inst. of Phys. Conf. Series 33b (Institute of Physics, U. K., 1977), pp. 129-135.
80. R. J. Almassy, S. B. Nam, C. W. Litton, and D. C. Reynolds, Bull. Am. Phys. Soc. 22, 437 (1977).
81. W. Schairer, D. Bimberg, W. Kottler, K. Cho, and Martin Schmidt, Phys. Rev. B13, 3452 (1976).

APPENDIX A

AUTOMATED LUMINESCENT TOPOGRAPHIC SYSTEM

Automated luminescent topographic system

Michael J. Luciano

Systems Research Laboratories, Inc., 2800 Indian Ripple Road, Dayton, Ohio 45416

D. L. Kingston

Air Force Avionics Laboratory, Wright Patterson AFB, Ohio 45433

(Received 9 June 1977; in final form 21 July 1977)

A new optical-scanning technique with a spatial resolution of $10\text{ }\mu\text{m}$ has been developed for the observation of surface luminescence. The photoluminescence topographic technique is a fully automated system capable of measuring luminescence intensity from a surface area as large as 25.8 cm^2 as well as the actual luminescence spectra from a spot as small as $10\text{ }\mu\text{m}$ in diameter. The system consists of an Ar-ion laser for excitation, a bidirectional scanner with focusing lens, a spectrometer for high spectral resolution, and a photomultiplier for photon counting. Experimental control and data acquisition and display are performed by a Hewlett-Packard 9820A calculator and interface package. Applications of the technique in the analysis of impurity segregation in semiconductor wafers are illustrated.

INTRODUCTION

The optical technique of photoluminescence is highly sensitive and has long been applied to the analysis of trace impurities. In addition to its quantitative applications, photoluminescence also yields important information concerning the energy levels of impurities in the bandgap of semiconductors.¹

The technique of photoluminescence topography as developed here not only takes advantage of these two applications of photoluminescence but also permits measurements to be made on any spot ranging in size from 10 to $500\text{ }\mu\text{m}$ in diameter within an area as large as 25.8 cm^2 . The depth to which the measurement is made is determined by the absorption coefficient of the material under investigation for the photon energy of the excitation source.

The purpose of this paper is to describe in detail the components of this instrument and to show its application in the analysis of semiconductor-device material.

I. INSTRUMENTATION

The system consists of six basic components: (1) excitation source, (2) optical scanner and focusing lens, (3) sample holder and helium Dewar for low-temperature analysis, (4) spectrometer for high spectral resolution, (5) photomultiplier and electronics for photon counting, and (6) programmable calculator and interface for experimental control and data processing. The system is shown schematically in Fig. 1.

A. Excitation source

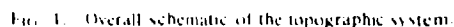
A Spectra Physics Ar-ion laser was used as the excitation source to provide coherent high-intensity light. The maximum output power at 514.5 nm was 1 W . A Spectra Physics beam expander was used to produce a 2.54-cm coherent beam. The beam expander distributes

the intensity of the beam over a large area, thus preventing excessive heating of the front-surface mirrors and neutral density filters and reducing problems that may arise due to material inhomogeneity. The large diameter beam also increases the ease and accuracy with which the beam may be focused to a small-diameter spot. Finally, neutral-density filters are placed in the light path to vary the power of the laser beam.

B. Optics and scanner

The optical scanner is the heart of the system. Its purpose is twofold—first, it scans the focused laser beam in two orthogonal directions perpendicular to the surface plane of the sample and, secondly, it collects luminescent emission from the sample and focuses it into the spectrometer.

The scanning system as shown in Fig. 2 consists of an Ortel achromatic dielectric beamsplitter which reflects 40% of the laser power onto a reference photomultiplier for monitoring the output power of the laser. The transmitted light falls onto the first front-surfaced mirror and is directed upwards at a 90° angle in the plane of the laser beam where the second mirror deflects the beam 90° perpendicular to the laser plane. The beam then passes through the focusing lens. The first mirror in its mount is attached to a translational stage which moves along the axis of the laser beam, producing a horizontal translation across the sample. The second mirror in its mount moves along the plane normal to the laser beam, producing the vertical scan of the sample. In addition, the second mirror is rigidly attached to the first translational stage and as a result the beam during the horizontal translation always strikes the same spot on the second mirror. To insure that the center of the beam always passes through the center of the lens, the lens mount is rigidly attached to the second translational stage. The lens itself is used both



C. Sample holder and helium Dewar

size will be uniform over the sample surface. The Dewar is rigidly held in position within a steel framework mounted to a base plate. The base plate is connected, through a system of ball bushings, to a high-precision lead screw. This allows the translation of the Dewar assembly along the axis of the focused beam. Adjustments of the lead screw produce the desired spot size on the sample, and the movement of the lead screw is accurate to $\pm 12.7 \mu\text{m}$. A translation of $25.4 \mu\text{m}$ is equivalent to a $10\text{-}\mu\text{m}$ increase in spot diameter.

The spectrometer used for wavelength selection and spectral scanning was a Spex 1401 Czerny-Turner with 0.85-m focal length and $f/7.8$ optical aperture. Since the second pass of the instrument can separate any laser excitation reflected from the sample into the spectrometer, a suitable filter is needed to accomplish this separation when only one pass of the spectrometer is used and the wavelength of the reflected light is sufficiently separated from the wavelength of the luminescence. A CdSe filter is presently being used for this purpose. To increase the optical throughput, only one-half of the double-pass instrument was used. This instrument provides the spectral resolution needed for the present investigations. The dispersion at 632.8 nm is 11 cm⁻¹/mm and the resolution at 579.1 nm, Order 1 is 0.006 nm.

The photomultiplier is mounted at the exit slit of the spectrometer and is contained in a thermo-electrically cooled housing to decrease the dark current. The signal generated at the output of the photomultiplier is connected to an SSR photon-counting system. When used in conjunction with a chopper, the instrument can display signal-plus-background count, background count,



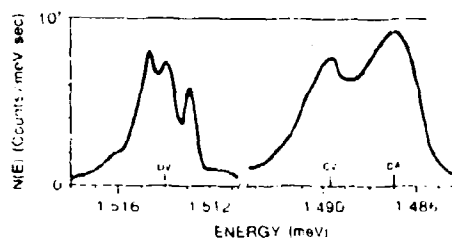


Fig. 3. Typical spectral scan of a high-purity GaAs epitaxial layer showing luminescence peaks corresponding to labeled transitions.

and the sum and difference of the former and latter quantities. The photon-counting system digitizes the signal and collects the data as counts per unit time and is remotely controlled by the calculator system.

F. Experimental control and data acquisition

An HP-9820A calculator, when interfaced to an HP-2570A coupler controller, is capable of controlling the scanner, SSR photon counter, and multichannel analyzer. Data are stored permanently on cassette tapes and displayed on an X-Y plotter.

The HP-2570A coupler controller is a programmable bidirectional link capable of controlling various interface boards through the ASCII code. Commands generated by the calculator are sent to a specific board in the coupler controller which converts the commands to 8-bit ASCII code. The commands are placed on the ASCII bus backplane and sent to the desired board, which interfaces to the final instrument for control and data acquisition.

Signals are sent to the SSR photon counter for automatic programming through a binary-coded-decimal (BCD) output board in the coupler controller. Using the proper set of commands, one can select the time of measurement, the particular mode of data acquisition, and also the type of data to be displayed, i.e., signal plus-background, background, and their sum and difference. The measurement is initiated and the data collected by using the proper interface between the SSR and the BCD input card of the coupler controller.

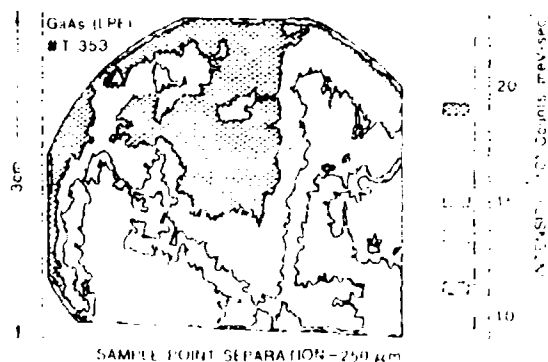


Fig. 4. Representation of a full topograph of a GaAs wafer showing the spatial distribution of UV luminescence.

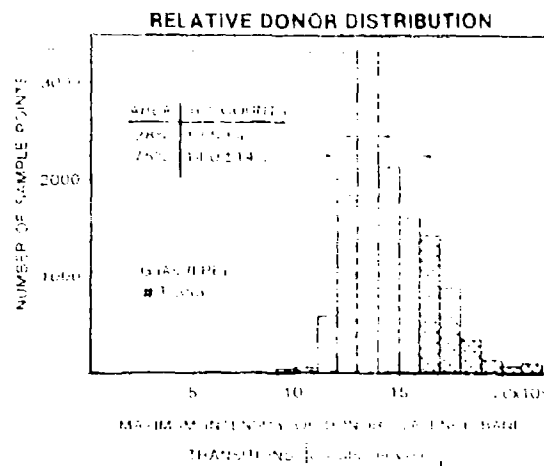


Fig. 5. Histogram of the data obtained from the topographs in Fig. 4 showing the relative donor distribution.

A Unidex Acrotech drive system controls the stepping motors of the scanner translational stages; this system is programmed through a BCD output card in the coupler controller. A preset number of steps can be selected for both the X and Y directions. Twenty-five steps is equivalent to a translation of 10 μm .

The multichannel analyzer (MCA) is used for temporary storage and display of a spectral scan or a line of the topograph. It is also interfaced to the coupler controller and controlled by the calculator. The data are permanently stored on a cassette tape and can be displayed on an X-Y plotter.

II. APPLICATIONS

Donor and acceptor impurities in a semiconductor contribute to the electrical characteristics of the semiconductor device.⁷ Knowledge concerning both concentration and type of the impurity is essential to the characterization of semiconductor materials. Solid state devices are fabricated on wafers which have been sliced from large boules of semiconductor device material. Since each wafer may contain hundreds of similar devices, it is important that the electrical properties of the material be consistent over the entire wafer. Analysis used to characterize the material should be nondestructive to permit fabrication of the final devices from the tested material. Present day techniques such as Hall and mobility measurements lack both the necessary spatial resolution and nondestructive quality. Recently, Nam *et al.*⁸ showed that donor-acceptor concentrations can be determined from initially interpreted measurements of luminescence. Luminescence topography, as it has been developed here, not only provides this information on the impurity centers but also is capable of doing so nondestructively with a spatial resolution of 10 μm .

Because of the automation and storage capabilities of the system, a number of different types of measurements can be made to characterize the material.

(1) Varying λ , constant ω —spectrum scan

(2) constant λ , constant $x(y)$, varying $y(x)$ —one-line topograph;

(3) constant λ , varying x, y —full topograph.

The first type of measurement provides a spectral scan at one specific spot on the wafer. Of course, the spot may be positioned at any x, y coordinate on the wafer before the scan is begun. The second measurement can be made at any selected wavelength and displayed on the scope of the MCA. This provides an analog output of the luminescence variation along one of the translation axes. The third measurement can be made at a selected wavelength to provide a full topograph of the luminescence emitted from the sample.

Figure 3 shows a typical luminescence spectrum for a high-purity GaAs epilayer. The spectrum was taken at 8 K. The peaks corresponding to the transitions from donor to valence band, conduction band to acceptor, and donor to acceptor are labeled DV, CA, and DA, respectively. The wavelengths corresponding to these are determined, and for each wavelength the spatial distribution of luminescence intensity over the surface of the sample is measured.

Figure 4 is a topograph obtained from monitoring the maximum of the DV luminescence intensity. Segments of the intensity scale are represented by different colors. The spatial resolution of the DV luminescence intensity is thus represented by a matrix of points having corresponding colors. The single-crystal wafer measured $\sim 3 \times 3$ cm. The laser beam was focused to $500 \mu\text{m}$, and each measurement was made after stepping $250 \mu\text{m}$. The different grid patterns correspond to various intensities of luminescence as shown at the right of the figure. The topograph indicates considerable variation in the luminescence over the surface of the crystal. The actual variation would be useful information for the crystal grower who is interested in the correlation between the

crystal orientation in the furnace and the uniformity of the grown epilayer. The luminescence distribution may also be correlated with final device efficiency. Furthermore, the availability of the data on magnetic tape also facilitates its representation as a histogram (see Fig. 5) which can be used as a guide for overall quality assurance. In the present example it can be seen that 75% of the wafer would qualify as a device if the tolerance limit were set at $\pm 14\%$ of the mean value; however, only 28% would qualify for a hypothetical tolerance limit of $\pm 4\%$ of the mean value. Numerous other statistical analyses can be performed with the stored data to facilitate the characterization of the material. In addition similar topographs can be made for the other optical transitions in GaAs.

This type of analysis should be useful in predicting which areas of a wafer should produce efficient solid-state devices. Using a novel theoretical analysis of luminescence data,³ the topographic data can be used to calculate various electrical parameters such as donor and acceptor concentrations and carrier mobilities. The distribution of these parameters can then be mapped with the same spatial resolution as the luminescence measurements.

ACKNOWLEDGMENT

This work was supported in part by AF Contract F33615-76-C-1166.

¹ J. I. Pankove, *Optical Processes in Semiconductors* (Prentice Hall, Englewood Cliffs, NJ, 1971).

² C. Kittel, *Introduction to Solid State Physics* (Wiley, New York, 1957).

³ S. B. Nam, D. W. Tager, M. J. Luciano, and D. L. Kingston, in *Bull. Am. Phys. Soc.* 11 22, 377 (1977), and *Appl. Phys. Lett.* 31, 652 (1977).

APPENDIX L

DETERMINATION OF CONCENTRATIONS OF DONORS AND ACCEPTORS IN GAS BY AN OPTICAL METHOD

Determination of concentrations of donors and acceptors in GaAs by an optical method

Sang Boo Nam^{a)}

Department of Physics, University of Dayton, Dayton, Ohio 45460

D. W. Langer and D. L. Kingston

Air Force Avionics Laboratory, Wright Patterson Air Force Base, Ohio 45433

M. J. Luciano^{b)}

Systems Research Laboratories, Dayton, Ohio 45440

(Received 18 May 1977; accepted for publication 7 September 1977)

The concentrations of donors (N_D) and acceptors (N_A) in a high-quality GaAs epitaxial layer sample are determined by the optical method. The numerical values of N_D and N_A are deduced from the limiting values of combinations of the excitation-dependent integrated emission intensities due to the conduction-band-to-neutral-acceptor, neutral-donor-to-valence-band, and neutral-donor-to-neutral-acceptor transitions.

PACS numbers: 61.70.Wp, 78.55.Ds

The concentrations of donors (N_D) and acceptors (N_A) in a semiconductor are determined conventionally by electrical ways, such as Hall and mobility measurements. These measurements require electrical contacts and homogeneity of the sample. Even when these problems are solved, the results rely on the theoretical treatments of various scattering processes of carriers.^{1,2} Therefore, an entirely different method for the determination of N_D and N_A is desirable. There have been several attempts to obtain the compensation ratio N_A/N_D from the photoluminescence data by analyzing the shapes of emission bands due to the conduction-band-to-neutral-acceptor and the neutral-donor-to-neutral-acceptor transitions at a low excitation level.³⁻⁵

Recently, a theoretical scheme was proposed⁶ by which N_D and N_A are determined from the excitation-dependent integrated photoluminescence emission intensities due to the conduction-band-to-neutral-acceptor (I_{D-A}), neutral-donor-to-valence-band (I_{D-V}), and neutral-donor-to-neutral-acceptor (I_{D-N}) transitions. The purpose of this letter is to demonstrate this scheme by presenting its application to a high-quality GaAs epitaxial sample. To make our discussion clearer, we first recapitulate this scheme⁶ and discuss the photoluminescence data.

When an excitation is introduced in a semiconductor, say optically, the electrons and holes are created. They may form excitons or be trapped and distributed such that the charge neutrality be preserved,

$$n + N_A = p + N_D + n_0, \quad (1)$$

where n , p , n_0 , and p_0 are the concentrations of the neutral donors, neutral acceptors, electrons in the conduction band, and holes in the valence band, respectively. For simplicity, we hereafter discuss a semiconductor with shallow donor and shallow acceptor centers. It is easy to incorporate other centers in the theory

and recombination centers do not affect the final results. The emissions due to decays of free excitons and excitons bound to impurity centers are not of interest. The emissions associated with impurities are needed for our purpose. The integrated emission intensities associated with impurity centers are easily calculated by a standard golden rule⁷ and can be written as

$$I_{D-A} = \int dE N_A \langle I_{D-A} \rangle = m^2 n_0 \langle I_{D-A} \rangle, \quad (2)$$

$$I_{D-V} = \int dE N_D \langle I_{D-V} \rangle = m^2 p_0 \langle I_{D-V} \rangle, \quad (3)$$

$$I_{D-N} = \int dE N_D \langle I_{D-N} \rangle = m^2 n_0 \langle I_{D-N} \rangle, \quad (4)$$

where N 's are the emission intensities per spectral width and m^2 is the mean value of the square of the transition matrix element times the appropriate kinematic factor,

$$m^2 = 0.35k^2 / (m^* E_g + m^* E_g^2 + m^* E_g^3 + 1), \quad (5)$$

where E_g , m^* , and k are the band-gap energy, the effective masses of the electron in the conduction band in the unit of the free electron mass m_0 , and the elementary constant, respectively. We hereafter use the units of $E_g = 1$ eV. The I_{D-V} and I_{D-N} are the mean values of the squares of the amplitudes of the impurity wave functions in the k space, and I_{D-A} is the summation of the square of the overlapping integral of the donor and acceptor wave functions. Using the hydrogenic envelope wave functions, appropriate for shallow donor and shallow acceptor, the I 's are given by

$$I_{D-A} = 64\pi^2 / (2\pi)^3 \times (E_g^2 / E_g^3 + E_g^2 + 1) \times (N_A / N_D), \quad (6)$$

with

$$E_g = E_g / (E_g + 1), \quad (7)$$

$$E_g = [2\pi^2 \times (E_g^2 + 1) \times (2\pi^2 + 1) \times 1.26]$$

where E_g and E_g are the donor and acceptor binding energies in eV, respectively.

Now the principal idea is to obtain N_D and N_A from Eqs. (1)–(4). Observe the fact that the experimental values of I 's depend upon the excitation intensity, that

^{a)} Supported by the AF Contract F49620-76-C-0001.

^{b)} Supported by the AF Contract F49620-76-C-0001.

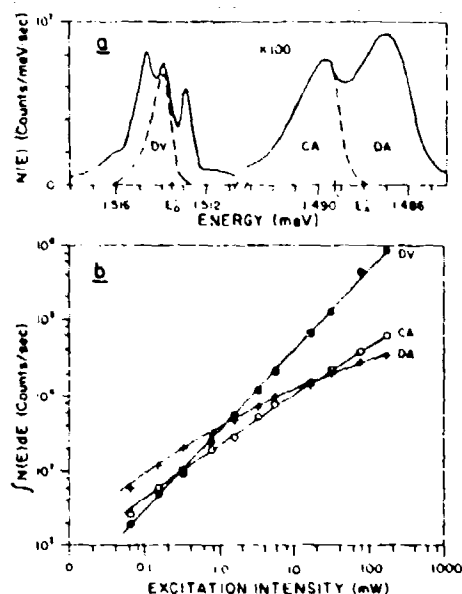


FIG. 1. (a) A typical photoluminescence spectrum from a high-quality GaAs epitaxial layer sample at about 8 K. $E_D = E_F - E_B$ and $E_A = E_F - E_A$. (b) Integrated emission intensities due to the conduction-band-to-neutral-acceptor (CA), neutral-donor-to-valence-band (DV), and neutral-donor-to-neutral-acceptor (DA) transitions versus the excitation intensity.

can be done as follows. In the high excitation limit, we expect that $n_D = N_D$ and $n_A = N_A$, and the charge neutrality condition yields $p = n$. On the other hand, in the low excitation limit, $n_D = N_D - N_A$ and $n_A = 0$ for the n -type or $n_D = 0$ and $n_A = N_A - N_D$ for the p -type materials, respectively, since at low temperature the numbers of thermally excited electrons and holes are negligibly small, $|p - n| \ll |N_D - N_A|$. Thus, getting the expressions for n_D , n_A , n , and p in terms of N_D and N_A , and taking the limiting values of them, one obtains the following results for p -type material⁶:

$$\lim_{G \rightarrow 0} F_1 = (N_A - N_D)mf_{DA} = \lim_{G \rightarrow 0} F_2, \quad (7)$$

$$\lim_{G \rightarrow \infty} F_3 = N_A/N_D = \lim_{G \rightarrow \infty} F_4, \quad (8)$$

with

$$F_1 = [I_{DA}(1+C)/V]^{1/2},$$

$$F_2 = (I_{DA}C/V)^{1/2} - (I_{DA}V/C)^{1/2},$$

$$F_3 = [(b^2 + \gamma)^{1/2} - b]^2,$$

$$F_4 = C/V,$$

$$\gamma = (1+V)(1+C)^{-1} = 2\beta(1+V),$$

$$b = \beta(N_A - N_D)mf_{DA}(I_{DA})^{-1/2},$$

$$C = (I_{CA}/I_{DA})(f_{DA}/f_A)^2, \quad V = (I_{DV}/I_{DA})(f_{DA}/f_D)^2,$$

where G denotes the excitation intensity. For n -type material, the equivalent formulas are obtained by simply interchanging donor and acceptor variables. The value of $N_A - N_D$ can be determined by the limiting value of F_1 or F_2 in two distinctive different cases involving opposite limits of the excitation dependence. The result

from F_1 or F_2 is needed for F_3 ; on the other hand, for F_4 it is not.

This scheme can be applied to the indirect-gap as well as direct-gap semiconductors with the appropriate f 's and β 's, providing the integrated emission intensities F_i can be written in the forms of Eqs. (2)–(4). One can also obtain the value of C/V in the low excitation limit, which can be easily shown to correspond to the ratio of the lifetimes of holes and electrons.⁷ Further by measuring the absolute value of C , one may obtain the values of lifetimes and mobilities of electron and hole.⁸

Figure 1(a) shows a typical photoluminescence spectrum in a high-quality GaAs epitaxial layer sample⁹ at about 8 K. For the excitation, an argon laser of $\lambda = 514.5$ nm was used with 4.4×10^{-4} W/cm² and focused to a spot of 10 μ m diameter. The integrated emission intensities F_i are measured as functions of the excitation intensity and are shown in Fig. 1(b). Using these data, we plot in Fig. 2 the functions F_i 's to obtain the self-consistent values for N_D and N_A of

$$N_D = 1.1 \times 10^{17} \text{ cm}^{-3} \quad \text{and} \quad N_A = 6.5 \times 10^{14} \text{ cm}^{-3}.$$

The numerical values used are $E_D = 1519.5$ meV, $E_B = 5.7$ meV, $E_A = 30.5$ meV, and $m_D^* = 0.065$ with $\beta = 12.5$ and $R_D = 13.60$ eV. Note that N_D and N_A are the concentrations of radiative donors and radiative acceptors only.

The limiting values of F_1 and F_2 agree remarkably well, considering the fact that they are deduced from the extrapolations to two opposite extremes of the excitation dependences. The difference between the limiting values of F_1 and F_2 may be due to the presence of nonradiative centers and also thermal effects. The present measurement convinced us that the above effects are not significant in the sample tested. The agreement between the limiting values of F_1 and F_2 should be also noted. Since the result of F_1 or F_2 is used for F_3 , while for F_4 it is not. Actually, we used the mean value of those from F_1 and F_2 for plotting F_3 . Furthermore, since $F_1 = m_D f_{DA} F_4$, this agreement indicates that Eq. (1) is sufficient for our analysis. In other words, the inclusion of additional terms associated with nonradiative centers in Eq. (1) is irrelevant for our purpose. Depth profiling the concentration by the optical and electrical methods are in progress, and the details will be reported elsewhere.

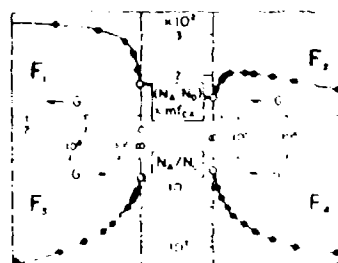


Fig. 2. The functions F_1 , F_2 , F_3 , and F_4 versus the excitation intensity G .

One of us (S.B.N) thanks E. Wagner for Refs. 3 and 4 before publication.

- ¹D. L. Rode, *Semiconductors and Semimetals*, edited by R.K. Willardson and A.C. Beer (Academic, New York, 1975), Vol. 10, p. 1.
- ²C.M. Wolfe and G.E. Stilman, Ref. 1, p. 175.
- ³T. Kamiya and E. Wagner, *J. Appl. Phys.* **48**, 1928 (1977).
- ⁴E. Wagner, W. Bludau, and T. Kamiya (unpublished).

⁵S. B. Nam (unpublished).

⁶See, for example, L.I. Schiff, *Quantum Mechanics* (McGraw-Hill, New York, 1966), Chap. 10. H.B. Hebb and E.W. Williams, Ref. 1, Vol. 8, p. 191.

⁷See, for example, C. Kittel, *Quantum Theory of Solids* (Wiley, New York, 1964), p. 283.

⁸The mobilities of electron and hole in the same sample turned out to be $\mu_e = 18000 \text{ cm}^2/\text{V sec}$ and $\mu_h = 180 \text{ cm}^2/\text{V sec}$, respectively.

⁹M.J. Luciano and D.L. Kingston, *Rev. Sci. Instrum.* **48**, 30 (1977).

APPENDIX C

GLOW-DISCHARGE OPTICAL SPECTROSCOPY MEASUREMENT OF B-, Ge-, AND Mg- IMPLANTED GaAs

Glow-discharge optical spectroscopy measurement of B-, Ge-, and Mg-implanted GaAs

Kenneth R. Williamson

Air Force Institute of Technology, Wright-Patterson Air Force Base, Ohio 45433

W. M. Theis, S. S. Yun,^{a)} and Y. S. Park

Air Force Avionics Laboratory, Wright-Patterson Air Force Base, Ohio 45433

J. E. Ehret^{b)}

Systems Research Laboratories, Inc. 2800 Indian Ripple Road, Dayton, Ohio 45440

(Received 21 May 1979; accepted for publication 25 July 1979)

Glow-discharge optical spectroscopy (GDOS) was used as a technique for obtaining impurity-concentration profiles of annealed and unannealed GaAs implanted with Ge, B, and Mg. Calibration to obtain the absolute concentration was accomplished by comparison to pure elemental standards. For implantation fluences of $1 \times 10^{17}/\text{cm}^2$ and energies of 60 and 120 keV, the range and magnitude are compared with the theoretical predictions of LSS. Large surface pileup and out diffusion have been observed for Mg implants annealed at temperatures between 700 and 900 °C. As-implanted Mg samples exhibited different profiles for pyrolytic and plasma Si_3N_4 encapsulation due to differences in deposition temperatures.

PACS numbers: 61.70.Tm, 61.70.Wp, 66.30.Jt

I. INTRODUCTION

Glow-discharge optical spectroscopy (GDOS) has been used in determining the distributions of certain implanted species in semiconductors and has proven to be quite an attractive method because of its simplicity and versatility. The methods generally used for measuring the concentration profile of impurity atoms are Secondary-ion mass spectroscopy (SIMS)¹ and Auger electron spectroscopy (AES).² These methods, like GDOS, destructively sputter the sample during analysis. Unlike GDOS,³⁻⁵ however, these methods require rather elaborate equipment and experimental setups. Electrical methods⁶⁻⁸ can also be used to measure the impurity profiles of implanted semiconductors. However, information gathered using such techniques do not provide the total atomic distribution since only the electrically active impurities are observed.

In this paper, the results of experiments to determine the impurity distributions of implanted B, Ge, and Mg in GaAs substrates are reported. Furthermore, the redistribution of these implants for several different annealing temperatures has been studied. Although GDOS has been successfully employed previously in profiling B and other species in Si substrates,^{9,10} this study constitutes the first such measurements of the dopant distributions in ion-implanted GaAs.

II. EXPERIMENTAL PROCEDURE

Since GDOS and the method of its application are described in detail elsewhere,³⁻⁵ only a brief description is presented here. In the use of GDOS, a dc glow discharge is

excited between two electrodes in the Pyrex vacuum chamber which is back filled with Ar. The sample, which is placed on the cathode, is slowly sputtered by the ionized Ar atoms striking its surface. The atoms sputtered from the sample are collisionally excited in the cathode-glow region of the discharge and emit characteristic emission lines. The resulting emission intensity may be assumed to be proportional to the concentration of atoms present in the discharge and, hence, at that particular depth in the sample.

The GDOS system used in this experiment is similar to the system used by other investigators.^{9,10} The sputtering chamber, shown by Fig. 1, consists of a Pyrex cylinder, 9.53-cm I.D., with three quartz windows. The anode was made of

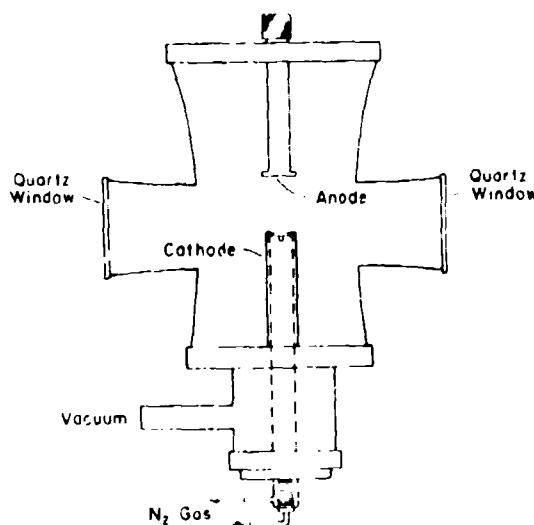


FIG. 1. Sputtering chamber of the GDOS apparatus.

^{a)} Author was resident scientist for the summer of 1977-1978 under Contract F33615-77-C-5003 with the Southeastern Center for Electrical Engineering Education, Inc. Present address: Dept. of Physics, Ohio University, Athens, Ohio.

^{b)} Work performed at the Air Force Avionics Laboratory under Contract F33615-76-C-1166.

TABLE I. Calibration constants used for the determination of the absolute concentration of the implants in GaAs.

Element	M (counts)	Wavelength (Å)	ρ (atoms/cc)	k (A/min)	C (atoms/count)
B	1.19×10^7	2497.73	1.30×10^{21}	1070	1.46×10^{19}
Ge	4.4×10^6	3039.06	4.42×10^{21}	1197	1.56×10^{19}
Mg	4.23×10^7	2852.13	4.36×10^{21}	1324	1.4×10^{19}
GaAs	—	—	2.2×10^{22}	1150	—
Si_3N_4	—	—	—	628	—

aluminum and was ~ 2.54 cm in diameter. The separation of anode and cathode could be varied, but uniform sputtering was achieved when the anode was placed 2.5 cm above the cathode. The cathode was constructed of copper with a removable aluminum top plate. Tungsten foil was silver epoxied to the surface of the cathode to minimize erosion. A glass envelope was used to insulate the base of the cathode to prevent arcing. Before each experiment, the system was cleaned by exciting a discharge without a sample. The sample was then placed on the cathode and the entire system evacuated to 5×10^{-7} Torr. After back filling the chamber with high-purity Ar to 20 μm , a voltage of 2.3 kV was applied to the electrodes through an external series resistance of 180 k Ω . A sputtering rate of 0.12 $\mu\text{m}/\text{min}$ for undoped GaAs was obtained. This rate was determined by partially shielding the sample in such a way that a step was formed between the sputtered and shielded areas. The step height was measured with a Sloan Dektak surface profiler. Light from the cathode-glow region was imaged by a quartz lens onto the slit of a Spex Model 1424 spectrometer having a diffraction grating blazed at 3000 Å with 1200 lines/mm. The spectrometer was set to the wavelength corresponding to the strongest characteristic emission line of the impurity. The intensity was determined by photon counting using a cooled RCA C3103404 photomultiplier tube and an SSR Model 1108 photon counter.

In order to enhance the collection of light, a concave mirror was placed opposite the spectrometer, thus reflecting light through the second optical window back to the spectrometer. From the sputtering rate of the sample, the resultant intensity data of the selected wavelength versus time could be translated to concentration versus depth into the sample.

A second spectrometer was used to monitor the discharge through the third optical window. It was tuned to the emission of Ga at 4172.0 Å. Monitoring of this line makes it possible to observe any change in the amount of Ga arising from fluctuations in the discharge. The discharge was observed to be unstable when the high voltage was first turned on. To protect the sample during this transient period, it was covered with a Si_3N_4 film ~ 1000 Å thick. Monitoring of the Ga line makes it possible to determine the exact time when the Si_3N_4 is removed and the sample sputtering begins. This, in turn, provides the starting point for the profile of the implanted impurity being monitored by the other spectrometer. The Si_3N_4 encapsulant was also used to protect the GaAs substrate during annealing which was performed on several samples.

The samples used in this study were undoped GaAs oriented in the (100) direction, which were cut into 0.5-cm squares and implanted at an energy of 60 or 120 keV with fluences of $(1-5) \times 10^{17}$ ions/cm². The implantation was performed $\sim 7^\circ$ off the (100) direction of the GaAs in order to avoid channeling and to make the crystal appear amorphous. The results were compared to the range predictions of Lindhard, Sharff, and Schiott (LSS)¹¹ which assume an amorphous target.

III. CALIBRATION OF DISTRIBUTION PROFILES

A scheme was devised for calibration of the GEDOS system which did not require the use of "known" implantation fluences of the impurity of interest into GaAs. If the implantation technique had been chosen, only a comparison between the impurity level and the standard implant would have been possible, calibration being dependent upon the dose accuracy of the standard. When comparing any implant to a standard implant, calibration is meaningless since inaccuracies in dose are the same. The use of bulk-doped GaAs was also considered but abandoned due to nonavailability. By using elemental standards and making certain assumptions, a reasonably accurate calibration was obtained as evidenced by the favorable match between the implanted impurity distribution and the predicted LSS profiles.

The method used for calibration involved sputtering pure elemental standards of B, Ge, and Mg. It may be assumed that the intensity of the line associated with the implanted impurity is proportional to the number of impurity atoms in the discharge. Hidden in the constant of proportionality C are the number of ions that sputter into the discharge, the proportion of that number which are excited, and the proportion of those excited which relax and emit the characteristic photon to which the spectrometer is set. In addition, the sensitivity of the instrument at this particular wavelength may be considered as being included in C .

Since photon counting is employed, let M be the number of counts in Δt when the elemental standard is probed. The quantity $M/\Delta t$ may thus be considered to be the count rate. Δt was typically 0.5 sec, and sample area $\sim 2 \times 0.25$ cm². The number of counts may be assumed to be proportional to the number of N atoms removed, i.e.,

$$N = CM, \quad (1)$$

which, in turn, may be expressed in terms of the atomic density of the standard ρ

$$N = \rho \Delta V = C \Delta V, \quad (2)$$

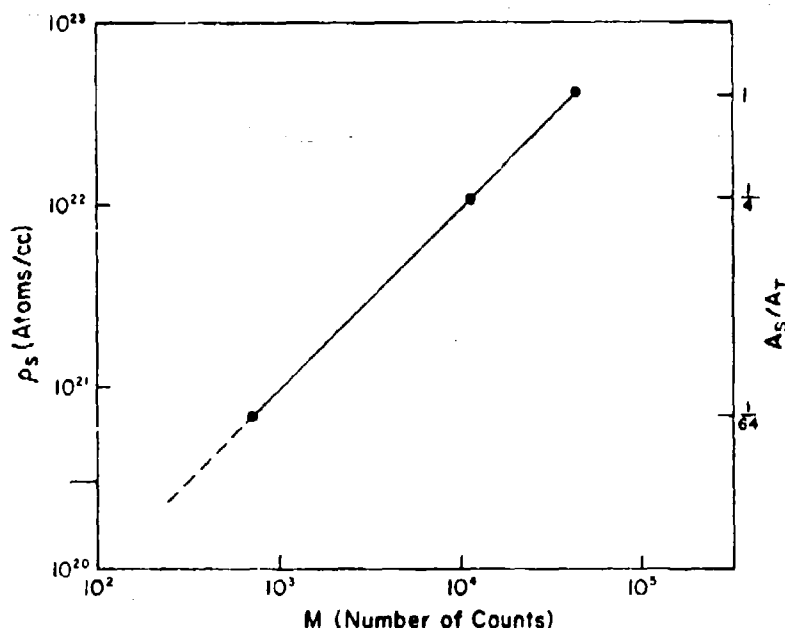


FIG. 2. The response of the GDOS photon-counting system to various densities of an elemental Ge standard. A_s is the area of the elemental standard, A_t is the total sample area, and the ratio A_s/A_t represents the proportion of the sample composed of elemental Ge (the remainder being GaAs) which corresponds to an effective density ρ_s as indicated. The dashed line shows an extrapolation to implantation densities which were investigated.

where Δx is the amount of material removed in Δt . Since the sputter rate $R_s = \Delta x/\Delta t$ can be determined as described earlier, the constant C may be written

$$C = \rho_s AR_s / \left(\frac{M}{\Delta t} \right) \quad (3)$$

These values were recorded in Table I for Ge, Mg, and B standards.

This calibration constant C may be used in profiling implanted samples. Since the distribution is constantly

changing, let m be the counts in Δt at some time t . The number of impurity atoms removed n may be assumed to follow Eq. (1). Since this is only a portion of the atoms being removed from the volume $A\Delta x$ at time t (the remainder being Ga and As), this total impurity concentration N_i may be expressed by

$$N_i = n/(\Delta x A) = C m / (\Delta x A) = C \left(\frac{m}{\Delta t} \right) / AR_s \quad (4)$$

where R_s is the sputtering rate of the implanted GaAs sample

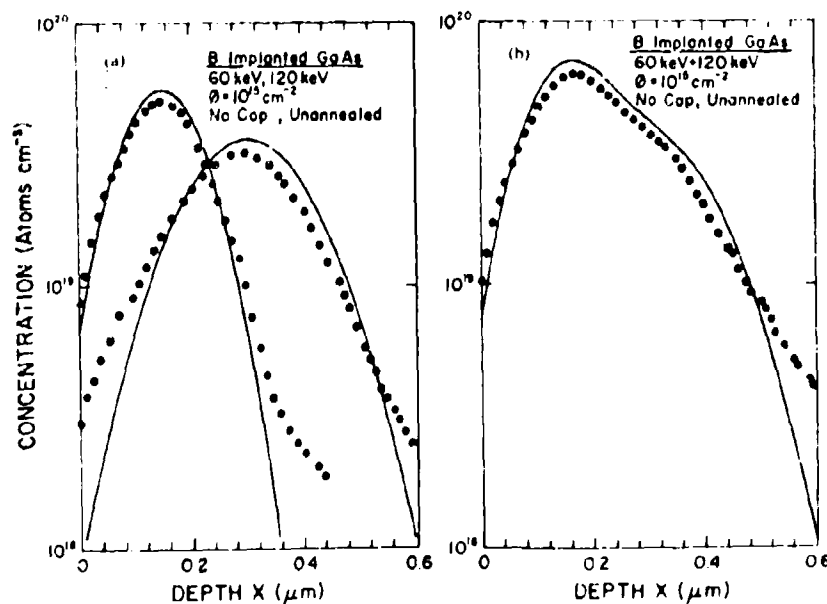


FIG. 3. Resolution capabilities of GDOS for multiple implants of B in GaAs. (a) Implants of 60 and 120 keV. (b) Multiple energy implantation of both 60 and 120 keV.

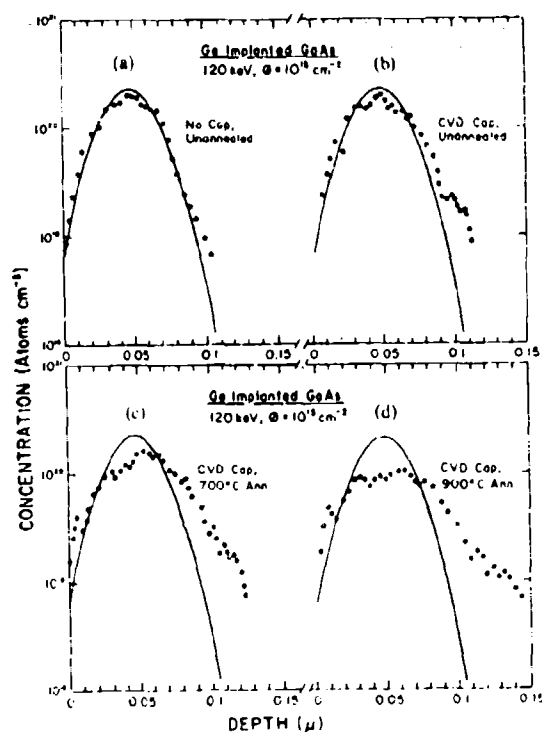


FIG. 4. Distribution of the Ge implant in GaAs as a function of annealing temperature. (a) As-implanted profile, (b) After encapsulation, (c) After 700°C anneal for 15 min, (d) After 900°C anneal for 15 min.

Implanted peak densities are lower than those of the pure element by several orders of magnitude. The degree to which C remains constant was explored as a function of the effective density by using smaller elemental standards. To maintain the same geometry as much as possible, total sample size was held constant with GaAs (in the form of chips along the edges) being substituted for the difference. Since GDOS profiles the entire plane, this simulated an implant with density proportional to the area of the standard A_s , divided by the total sample area A_t . Linearity between the number of counts and the effective impurity density formed with this technique was observed over two orders of magnitude, as shown in Fig. 2. This indicates that C is constant and is neither altered by decreasing the effective concentration, nor affected by increasing the concentration of Ga and As in the discharge. Since the implants of interest are at still lower concentrations, the linearity of C was extrapolated to these concentrations.

If analysis techniques such as GDOS are to be useful, they must not exhibit strong matrix effects. These effects may arise from two sources. The first is that the emission probabilities of the element of interest may be altered by the presence of other atomic species in the discharge. This condition was explored by introducing perimeter chips of GaAs which sputtered with the elemental standards. The linearity of the data shown in Fig. 2 ensures that increasing the amount of Ga and As present in the discharge will not alter the emission probability of the element (the relative Ga and

As concentration is inversely related to that of the element of interest). The other source of matrix effects may arise from the difference in sputtering impurities in the GaAs matrix as opposed to the pure standard. For ion-implanted specimens, the concentration of the impurity is small, as a result, the sputtering rate is determined entirely by the GaAs substrate. Differences between the sputtering rates of the GaAs and the standards are approximately 15% or less and, thus, are ignored. The value of 1150 Å/mm was used in all calibrations for the sputtering rate.

The values of C which were determined for B, Ge, and Mg are included in Table I. With respect to the assumptions made, these values represent the number of atoms being removed in time Δt which will result in a count recorded by the photon-counting system employed in the experiment. The test concerning the accuracy of this calibration lies in its comparison to predicted profiles for ion implantation or by comparison with profiling by other means. The latter experiment is currently being undertaken and a direct comparison of profiles obtained by GDOS is being made with profiles obtained by AES and SIMS.

IV. EXPERIMENTAL RESULTS AND DISCUSSION

The purpose of the experiment was to determine the

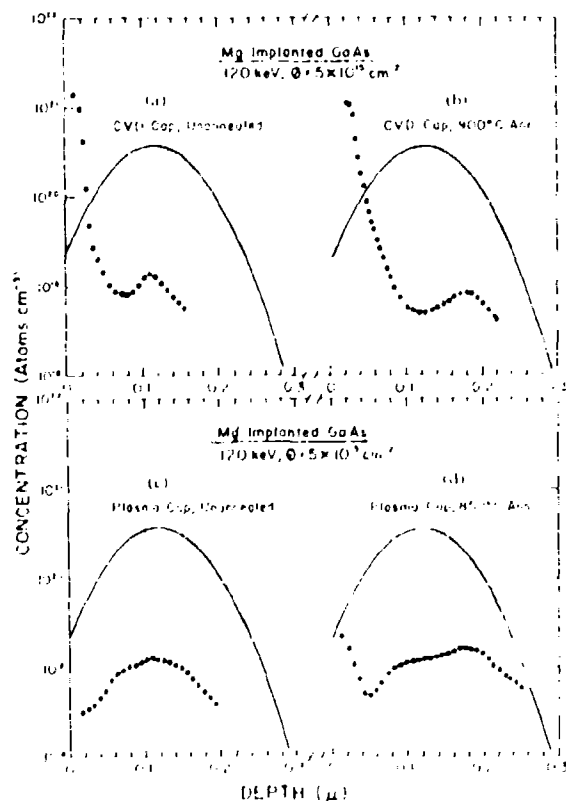


FIG. 5. Distribution of the Mg implant in GaAs with two different encapsulation methods. (a) CVD encapsulant before anneal, (b) After 900°C anneal for 15 min, (c) Plasma deposited encapsulant before anneal, (d) After 900°C anneal for 15 min.

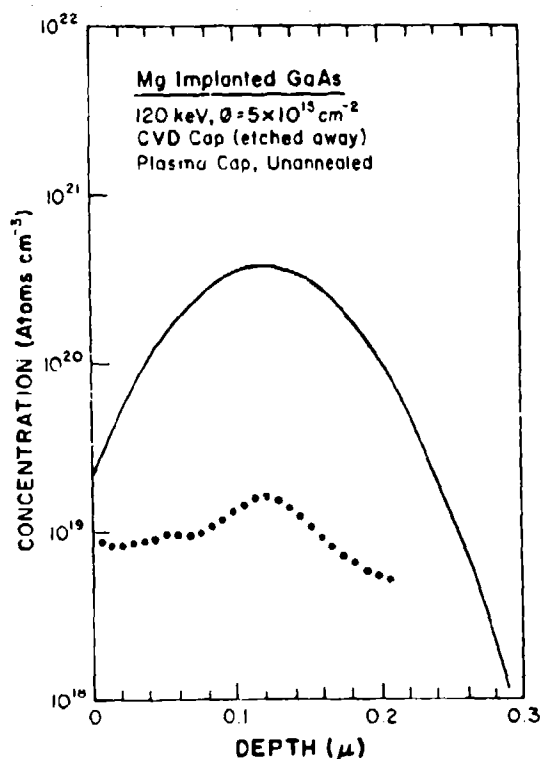


FIG. 6. Distribution of the Mg implant in GaAs after removal of CVD encapsulant with HF acid. Sample was re-encapsulated with PED Si_3N_4 and profiled.

depth distribution of the implanted impurity. The distribution was studied as a function of annealing temperature and method of deposition of the Si_3N_4 encapsulant. The projected range R_p and maximum concentration N_p can be predicted by LSS theory for each of the implants investigated (R_p being dependent upon the stopping power of the target¹¹). A Gaussian distribution is expected, with N_p being proportional to the fluence ϕ (ions/cm²), i.e.,

$$N_p \approx \phi / (2\pi)^{1/2} \Delta R_p \quad (5)$$

where ΔR_p is the standard deviation.

The resolving capability of GDOS was demonstrated using B implants into GaAs. Figure 3(a) shows implants with energies of 60 and 120 keV which closely followed the LSS predictions. A multiple-energy implantation is shown in Fig. 3(b). The location of the two peaks is resolved and follows the LSS prediction.

An annealing study was performed on the Ge implants. A Si_3N_4 encapsulant was used to protect the sample during high temperature annealing. The nitride was grown by pyrolytic chemical-vapor deposition (CVD) utilizing silane and ammonia gases at an elevated sample temperature of $\sim 725^\circ\text{C}$ for 45 sec. Approximately 1000 Å of Si_3N_4 was deposited on the sample. Figure 4(a) shows the Ge implant before any processing steps. Figure 4(b) shows that indiffusion has occurred after sample encapsulation. The enhancement of this indiffusion by the 700 and 900 $^\circ\text{C}$ anneals is

shown in Figs. 4(c) and 4(d), respectively. There is an associated decrease in peak height as this diffusion occurs.

The CVD encapsulant was also employed on Mg implants. The samples were implanted to a fluence of 5×10^{15} ions/cm² at an energy of 120 keV. (A similar implant at 60 keV was also investigated, but the results follow those at 120 keV and are not included.) The results in Fig. 5(a) exhibit a considerable concentration of Mg just below the surface of the sample after encapsulation. A peak is observed at the predicted depth but is several orders of magnitude smaller than the one occurring near the surface. A possible explanation is that the Mg diffused outwardly to the region of high damage when exposed to the temperature at which the CVD encapsulant is grown ($\sim 725^\circ\text{C}$). Similar behavior is observed for Be in Si.¹² An anneal of 700 $^\circ\text{C}$ for 15 min did not alter the Mg distribution. For the 900 $^\circ\text{C}$ anneal shown in Fig. 5(b), the peak has shifted deeper by about 0.06 μm . This indicates that an in-diffusion process occurs at this temperature, with no further enlargement of the Mg concentration located near the surface.

Another encapsulation method was attempted in order to minimize the redistribution. In this case the Si_3N_4 was grown from silane and nitrogen at a temperature of $\sim 200^\circ\text{C}$. The energy for the reaction was provided by exciting an RF plasma in the chamber containing the gases. Figure 5(c) shows the results for plasma-enhanced deposition (PED) Si_3N_4 after the cap has been grown, and Fig. 5(d) shows results after an anneal of 850 $^\circ\text{C}$ for 15 min. The reason for the apparent discrepancy between the magnitude of the profile [see especially Fig. 5(c)] and theoretical prediction is not known. Since the sputter rate of the Mg standard differs from that of the GaAs by 15% (as opposed to the other standards which differ at most by 7%), matrix effects may not be negligible for Mg. This would appear as an error in the calibration constant C for Mg. Alternately, the Mg standard is a metal (as opposed to B and Ge). The effect of covering the cathode with a metal rather than an insulator or semiconductor would be to alter the electric fields in the GDOS sputtering chamber and change the geometry of the experiment. Further experimentation is planned to clarify the results for Mg-implanted GaAs. The results after the anneal resemble those for the CVD encapsulant, Mg diffused to a region of high damage nearer the surface and the peak moved inwardly.

One further observation was made concerning encapsulation of Mg implants: the CVD nitride was removed from an unannealed Mg-implanted sample using HF acid. This is the removal method commonly used to obtain bare GaAs substrates for contacts in electrical measurements. The sample was then capped with PED nitride and profiled using GDOS. The results are shown in Fig. 6. The large surface accumulation as observed in Fig. 5(a) was not detected. This would explain the electrical measurements performed using CVD encapsulants which show a peak carrier concentration of $1 \times 10^{17}/\text{cm}^3$ but no surface accumulation. This agrees in magnitude with the GDOS data in Fig. 6, indicating removal of the surface Mg. It is interesting to note that a fluence of $1 \times 10^{17}/\text{cm}^2$ exhibits surface accumulation. (No corresponding GDOS data are available due to sensitivity limita-

tions.) This leads one to believe that surface accumulation is present at all fluences but may be removed by HF only when high damage is present.

V. SUMMARY

GDOS has been successfully employed to profile the depth distribution of B, Ge, and Mg implants in GaAs and to study their annealing behavior. The resolving capability of GDOS was demonstrated using a multiple-energy implantation of B. Excellent agreement was obtained between the absolute-concentration profiles determined by calibration of the system against elemental standards and the predictions of the LSS theory, except for Mg. Reasons for the discrepancy in the Mg data are not clear.

Minor redistribution of the Ge implant occurred when the samples were encapsulated with CVD Si_3N_4 or annealed at temperatures between 700 and 900 °C for 15 min. This is in contrast to the large redistributions observed for the Mg implants.

During CVD encapsulation, at a temperature of 725 °C, a large portion of the Mg diffused to the region of high damage at the surface of the sample. Furthermore, these atoms can be removed if the nitride is stripped by soaking in HF acid. Another method of encapsulation, PED Si_3N_4 , appeared to reduce the surface accumulation, even after an 850 °C anneal. For both encapsulants, the predicted peak in the distribution shifts inwardly at high-annealing temperatures, indicating diffusion into the sample.

Comparison with published results of electrical measurements for high-fluence Mg implants ($\sim 1 \times 10^{15}/\text{cm}^2$) in GaAs indicates that the surface Mg did not contribute to the electrical activity. This may be due to its removal by HF

acid. The reason for the anomalous diffusion of the Mg implants in GaAs is not clear but probably is not due to exceeding the solid-solubility limit since the low-fluence ($\sim 1 \times 10^{13}/\text{cm}^2$) Hall data also displayed surface accumulation. The mechanism governing this diffusion is not known, and further study is warranted.

ACKNOWLEDGMENTS

The authors are grateful for the assistance of M. Whitaker and G. Johnson and to Professor B.G. Streetman of the University of Illinois for many helpful discussions in the early stage of the experiment. We are also indebted to W.J. Anderson of the Air Force Academy for his contribution.

- See, for example, A. Edlow, J.E. Gibbons, V.R. Deane, and C.A. Evans Jr., *Appl. Phys. Lett.* **32**, 15 (1978).
- See, for example, Y.S. Park, J.T. Grant, and T.W. Haas, *J. Appl. Phys.* **50**, 809 (1979).
- J.E. Greene, F. Sequeda-Osorio, and B.R. Natarajan, *J. Appl. Phys.* **46**, 2701 (1975).
- J.E. Greene, F. Sequeda-Osorio, B.G. Streetman, J.R. Noonan, and C.G. Kirkpatrick, *Appl. Phys. Lett.* **25**, 435 (1974).
- J.E. Green and J.M. Whelan, *J. Appl. Phys.* **44**, 2509 (1973).
- See, for example, J.W. Mayer, I. Eriksson, and J.A. Davies, *Ion Implantation in Semiconductors* (Academic, New York, 1970), p. 18.
- See, for example, Y.K. Yeo, Y.S. Park, and P.W. Yu, *J. Appl. Phys.* **50**, 3274 (1979).
- G.T. Marcyk and B.G. Streetman, *J. Electrochem. Soc.* **123**, 1388 (1976).
- G.T. Marcyk and B.G. Streetman, *J. Vac. Sci. Technol.* **14**, 1165 (1977).
- J.E. Green and F. Sequeda-Osorio, *J. Vac. Sci. Technol.* **10**, 1144 (1973).
- J. Lindhard, M. Schott, and H. Schott, *Mat. Fys. Medd. Dan Vid. Selsk.* **33**, 1 (1963).
- R.G. Wilson and J. Comas, *Proc. of the International Conference on Ion Beam Modification of Materials* (to be published).

APPENDIX D
COMPUTER PROGRAM OF ELECTRICAL DEPTH PROFILING

```

TYPE OTOPV2.
C
PROGRAM OTOPV2
C
SUBROUTINES DATA,SURFAC,PROFIL ARE OVERLAYES
C
INTEGER ECHTIM(25)
REAL EFF(25),MUH(25),NS(25)
DIMENSION DEPTH(25),HI(25),RHOS(25),RHS(25),RI1(4),
1KI2(4),THICK(25),V1(4),V2(4),VNO(4),VNB(4),
1VRO(4),VRB(4)
COMMON /BLK1/ HI,RI1,RI2,T,V1,V2,VNO,VNB,VRO,VRB
COMMON /BLK2/ B,DEPTH,DOSE,ECHTIM,EFF,MUH,NS,RHOS,RHS,
1STHICK,THICK,I,NTIME
BYTE TIM(8),FLNAM(11)
C
FORMAT (A1)
10 FORMAT(11A1)
C
DEFINE FILE 1(25,8,U,NXREC)
TYPE*, 'ENTER FILE NAME (10 CHAR MAX)'
ACCEPT 10, FLNAM
OPEN(UNIT=1,NAME=FLNAM,TYPE='NEW',ACCESS='DIRECT',
1RECORDSIZE=4,INITIALSIZE=2)
DO 15 N=1,25
WRITE(1'N)0,0,0,0,0.
15 CONTINUE
C
CLOSE(UNIT=1)
DEFINE FILE 1(25,8,U,NXREC)
C
TYPE*, 'DOSE?'
ACCEPT*, DOSE
TYPE*, 'B (GAUSS)'
ACCEPT*, B
NTIME=0.0
STHICK =0.0
TYPE*, 'ETCH RATE/SEC IN ANGSTROMS'
ACCEPT*, ERATE
I=0
20 IF(I.NE.0) PAUSE 'ETCH SAMPLE'
C
CALL TIME(TIM)
TYPE 25, TIM
25 FORMAT (1X,'PRESENT TIME = ',8A1)
C
TYPE*, 'ETCH # =?, TIME =?'
ACCEPT*, I,ECHTIM(I+1)
TYPE*, 'DATA OK ? Y OR N'
ACCEPT 5, ANS
IF(ANS.EQ.'N') GOTO 20
C
I=I+1
IF(LASTI.EQ.I) GOTO 30
THICK(I)=ERATE*FLOAT(ECHTIM(I))
STHICK=STHICK + THICK(I)
DEPTH(I) = STHICK
NTIME = NTIME + ECHTIM(I)
C
30 CALL DATA
C
IT=T
IF(IT.EQ.1) GOTO 50      IT SET. IN DATA TO SHOW NO MEASUREMENT

```

```

      LASTI = I
      PAUSE 'SET PAGE'
C
      CALL SURFAC
C
      OPEN(UNIT=1,NAME=FLNAM,TYPE='OLD',ACCESS='DIRECT',
      1RECORDSIZE=4)
      WRITE(1'I')I,ECHTIM(I),RHOS(I),RHS(I)
      CLOSE(UNIT=1)
      IF(I.EQ.1) GOTO 20
C
      CALL PROFIL
C
      IF(IT.NE.1) GOTO 60
150    TYPE*, 'DATA CANNOT BE MEASURED'
      GOTO 70
60     TYPE*, 'CONTINUE MEASUREMENT? Y OR N'
      ACCEPT 5, ANS
      IF(ANS.EQ.'Y') GOTO 20
      IF(ANS.NE.'Y') TYPE*, 'ARE YOU SURE/'
      ACCEPT 5, ANS
      IF(ANS.EQ.'Y') GOTO 70
      GOTO 60
70     PAUSE 'NEW PAGE -- FINAL PROFILE PRINTOUT'
      TYPE*, 'FINAL PROFILE'
      TYPE 74, FLNAM
74     FORMAT(/,2X,'DATA FILE NAME IS ',11A1)
      TYPE 75, STHICK,NTIME
75     FORMAT(/,2X,'TOTAL DEPTH = ',F7.1,' ANGSTROMS',12X,
      1'TOTAL ETCH TIME = ',I6,2X,' SEC'/)
      TYPE 80
80     FORMAT(2X,'ETCH #',3X,'ETCH TIME(SEC)',3X,'AVG SHEET RHO'
      1,3X,'AVG SHEET HALL COEFF',3X,'AVG MOBILITY',5X,'AVG SH
      1EET NS',6X,'ACT EFF(%)'/)
      DO 100 M=1,I
          TYPE 90, M-1,ECHTIM(M),RHOS(M),RHS(M),MUH(M),NS(M),
      1EFF(M)
90     FORMAT(4X,I2,9X,I4,9X,E12.5,7X,E12.5,9X,F8.2
      1,8X,E12.5,7X,F6.2/)
100    CONTINUE
C
      CALL EXIT
      END

```

TYPE DATA.

```

SUBROUTINE DATA
  DIMENSION HI(4),RI1(4),RI2(4),S(4),SW(4),V1(4),
  V2(4),VNO(4),VNB(4),URO(4),URB(4),W(4)
  COMMON /BLK1/ HI,RI1,RI2,T,V1,V2,VNO,VNB,URO,URB
  BYTE MSGI(16),MSGV(15)

C
C  -INITIALIZING INSTRUMENTS-----
  CALL IRSEND('SF0C10X',,1,201)
  CALL IRSEND('DOMOZ1TOROX',,1,202)

C
C  PAUSE 'ZERO 616'

  CALL IRSEND('ZOX',,1,202)
  CALL IRSEND('DOM.',,9)
  CALL IRSEND('SX',,1,201)
  CALL IRECV(MSGV,15,9)
5  FORMAT(A1)
22  FORMAT (6X,E10.3)
26  FORMAT (2X,'I= ',E10.3,' AMPS')
30  FORMAT (5X,E10.3)
35  FORMAT (F10.7)
36  FORMAT (2X,'V= ',F10.6,' VOLT')
C
10  PAUSE 'SW 'A', ZERO DVM'
    I=1
    J=0
    K=0
    T=0.0

C
    SW(1)='A'
    SW(2)='B'
    SW(3)='C'
    SW(4)='D'
    S(1)='E'
    S(2)='E'
    S(3)='F'
    S(4)='F'
    W(1)='+'
    W(2)='-'
    W(3)='+'
    W(4)='-'
15  TYPE*, '-----ADJUSTING I----'
    CALL IRSEND('SR60X',,1,201)
    CALL IRSEND('1=0999000',,2)

C
    TYPE*, 'PROPER I? Y OR N'
    ACCEPT 5, ANS
    IF(ANS.EQ.'Y') GOTO 100

C
    TYPE*, 'BIG OR SMALL I? B OR S'
    ACCEPT 5, ANS
    IF(ANS.EQ.'S') GOTO 20

C
    '-----RINGER CURRENT-----'
    CALL IRSEND('SR50X',,1,201)
    TYPE*, 'INCREASE I? Y OR N'
    ACCEPT 5, ANS
    IF(ANS.EQ.'N') GOTO 100

C
    CALL IRSEND('SR40X',,1,201)
    TYPE*, 'INCREASE I? Y OR N'
    ACCEPT 5, ANS
    IF(ANS.EQ.'N') GOTO 100

C

```

```

CALL IRSEND('SR30X',,1,201)
GOTO 100

C
C
20 '-----SMALLER CURRENT-----'
CALL IRSEND('SR70X',,1,201)
TYPE*, 'DECREASE I? Y OR N'
ACCEPT 5, ANS
IF(ANS.EQ.'N') GOTO 100

C
CALL IRSEND('SX',,1,201)
CALL IRSEND('I=0099000',,2)
CALL IRSEND('OX',,1,201)

C
TYPE*, 'DECREASE I? Y OR N'
ACCEPT 5, ANS
IF(ANS.EQ.'N') GOTO 100

C
CALL IRSEND('SX',,1,201)
CALL IRSEND('I=0009000',,2)
CALL IRSEND('OX',,1,201)

C
100 TYPE*, 'U SURE I OK? Y OR N'
ACCEPT 5, ANS
IF(ANS.EQ.'N') GOTO 25
IF(N.EQ.1) GOTO 350 !350 INIT. TAKING HALL DATA
GOTO 199

C
25 TYPE*, 'TRY AGAIN? OR GIVE UP? A OR G'
ACCEPT 5, ANS
IF(ANS.EQ.'A') GOTO 15
GOTO 430

C
199 TYPE*, '---TAKING RESIST DATA---'
200 TYPE 205,SW(I)
205 FORMAT(2X,'SW = ',A1,/)
CALL IRSEND('SFOOX',,1,201)
FAUSE '+I'
CALL IRECV(MSGI,16,1,202)
CALL IRSEND(' ',,1,217)
DECODE(15,30,MSGI,ERR=31)RI1(I)
GO TO 105

31 DECODE(16,22,MSGI)RI1(I)
105 CALL IRECV(MSGV,15,9)
DECODE(10,35,MSGV)V1(I)
CALL IRSEND('SX',,1,201)

C
CALL IRSEND('F10X',,1,201)
FAUSE '-I'
CALL IRECV(MSGI,16,1,202)
CALL IRSEND(' ',,1,217)
DECODE(15,30,MSGI,ERR=32)RI2(I)
GO TO 110

32 DECODE(16,22,MSGI)RI2(I)
110 CALL IRECV(MSGV,15,9)
DECODE(10,35,MSGV)V2(I)
CALL IRSEND('SX',,1,201)
CALL IRECV(MSGV,15,9)
IF(I.EQ.1) GO TO 250
IF(I.EQ.4) GOTO 39

C
PAUSE 'CHANGE SW, ZERO DVM'
39 I=I+1
GO TO(200,40,260,200,250),I
40 CALL IRSEND('SFOOX',,1,201)
PAUSE 'I CHURN FOR *R* OR *E*'
CALL IRECV(MSGI,16,1,202)

```



```

CALL IRSEND(' ',1,217)
DECODE(15,30,MSGI,ERR=33)RI
GO TO 115
33 DECODE(16,22,MSGI)RI
115 TYPE 26,RI
CALL IRRECV(MSGV,15,9)
DECODE(10,35,MSGV)VV
TYPE 36, VV
CALL IRSEND('SX',,1,201)
CALL IRRECV(MSGV,15,9)
TYPE*, 'IS I ON HERE? Y OR N'
ACCEPT 5, ANS
IF(ANS.EQ.'N') GO TO 45
IF(N.EQ.1) GO TO 350
IF(I.EQ.2) GO TO 200
45 TYPE*, 'WRONG I TRY AGAIN'
IF(N.EQ.1) GO TO 15
GO TO 10

C
250 TYPE*, '----INTERMEDIATE DATA ----'
TYPE 50
50 FORMAT(/,2X,'SW',1X,'+',6X,'I+',7X,'VOLT AT I+'
1,9X,'I-',7X,'VOLT AT I-')
DO 60 N=1,4
TYPE 55,SW(N),N,RI1(N),V1(N),RI2(N),V2(N)
55 FORMAT(3X,A1,'=',I1,2X,E10.3,3X,F10.7,5X,E10.3
1,3X,F10.7)
60 CONTINUE
TYPE*, '----CORRECTING ----'
300 TYPE*, 'DATA REPEAT? Y OR N'
ACCEPT 5, ANS
IF(ANS.EQ.'N') GO TO 70
TYPE*, 'ENTER SW # OF MEAS.'
ACCEPT 65,I
65 FORMAT(I1)
PAUSE 'CHANGE SW, ZERO DVM'
J=1
GO TO 200
70 I=1
J=0
K=1
TYPE*, '----CHECKING HALL I----'
CALL IRRECV(MSGV,15,9)
PAUSE 'SW TO "E", ZERO DVM'
GO TO 40
350 L=1
M=0
IM IS SET AFTER ONCE THROUGH PROG
400 TYPE*, 'TAKING HALL DATA'
405 TYPE 407,S(L),W(L)
407 FORMAT(/,2X,'SW = ',A1,' AND ',A1,' I'/)
CALL IRSEND('SX',,1,201)
CALL IRRECV(MSGV,15,9)
PAUSE 'SW @ E OR F, NDR-0-B, ZERO DVM'
CALL IRSEND('POOX',,1,201)
PAUSE 'I READY?'
410 CALL IRRECV(MSGI,16,1,202)
CALL IRSEND(' ',,1,217)
DECODE(15,30,MSGI,ERR=411)HI(L)
GO TO 412
411 DECODE(16,22,MSGI)HI(L)
412 CALL IRRECV(MSGV,15,9)
DECODE(10,35,MSGV)VNO(L)
PAUSE 'APPLY NDR B'
CALL IRRECV(MSGV,15,9)
DECODE(10,35,MSGV)VNB(L)
PAUSE 'ZERO B, SW TO 0 REV'

```

```

CALL IRRCV(MSGV,15,9)
DECODE(10,35,MSGV)URO(L)
PAUSE 'APPLY REV B'
CALL IRRCV(MSGV,15,9)
DECODE(10,35,MSGV)URB(L)
CALL ISEND('SX',,1,201)
TYPE*, 'ZERO B, SW TO 0 NOR'
IF(M.EQ.1) GO TO 417
L=L+1
GO TO(400,415,405,415,417),L
415 TYPE 407,S(L),W(L)
CALL ISEND('F10X',,1,201)
GO TO 410

C
417 TYPE*, '---INTERMEDIATE DATA---'
TYPE 80
80 FORMAT(/,2X,'SW',1X,'I',7X,'I',10X,'UNO',9X,'UNB'
1,9X,'DUN',9X,'URO',9X,'URB',9X,'DUR')
DO 90 N=1,3,2
DUN=UNO(N)-UNB(N)
DUR=URO(N)-URB(N)
TYPE 85, S(N),W(N),N,HI(N),UNO(N),UNB(N),
1 DUN,URO(N),URB(N),DUR
85 FORMAT(2X,A1,A1,'=',I1,2X,E10.3,6(2X,F10.7))
90 CONTINUE
DO 95 N=2,4,2
DUN=UNO(N)-UNB(N)
DUR=URO(N)-URB(N)
TYPE 85, S(N),W(N),N,HI(N),UNO(N),UNB(N),
1 DUN,URO(N),URB(N),DUR
95 CONTINUE
420 TYPE*, '----CORRECTING ----'
C
TYPE*, 'REPEAT DATA? Y OR N'
ACCEPT 5, ANS
IF(ANS.EQ.'N') GOTO 440
TYPE*, 'ENTER SW # OF MEAS'
ACCEPT 65, L
PAUSE 'CHANGE VDP SW, NOR-0-B, ZERO DVM'
M=1
GOTO(405,415,405,415),L
430 T=1.0 ' INDICATES NO MEAS
CALL ISEND('SX',,1,201)
440 RETURN
END

```

TYPE SURFAC.

C

SUBROUTINE SURFAC

C

```

INTEGER ECHTIM(25)
REAL EFF(25),MUH(25),NS(25)
DIMENSION DEPTH(25),DRN(4),DRR(4),HI(4),RHOS(25),RHS(25)
1,R11(4),R12(4),THICK(25),V1(4),V2(4),VNO(4),VNB(4),
1VR0(4),VRB(4)
COMMON /BLN1/ HI,R11,R12,T,V1,V2,VNO,VNB,VR0,VRB
COMMON /BLN2/B,DEPTH,DOSE,ECHTIM,EFF,MUH,NS,RHOS,
1RHS,STHICK,THICK,I,NTIME

```

C

```

DO 45 J=1,4
  R1(J)=ABS(V1(J)/R11(J))
  R2(J)=ABS(V2(J)/R12(J))
  DUN=VNO(J)-VNB(J)
  DVR=VR0(J)-VRB(J)
  DRN(J)=ABS(DUN/HI(J))
  DRR(J)=ABS(DVR/HI(J))

```

45

```

  CONTINUE
  RTO=ABS(R1(1)/R1(2))
  IF(RTO.LT.1.0) RTO=1.0/RTO
  IF(RTO.LT.1.4) GOTO 60
  IF(RTO.GT.5.0) GOTO 50
  F=.99-((RTO-1.4)*.05)
  GOTO 65
50  TYPE 55, RTO
55  FORMAT(1X,'RESIS RATIO = ',F9.2)
  TYPE*, 'FACTOR 'F'?'
  ACCEPT*, F
  GOTO 65
60  F=1.0
65  RAUG1=(R1(1)+R1(2)+R1(3)+R1(4))/4.0
  RAUG2=(R2(1)+R2(2)+R2(3)+R2(4))/4.0
  RAUG=(RAUG1+RAUG2)/2.0
  DR1=(DRN(1)+DRR(1)+DRN(3)+DRR(3))/4.0
  DR2=(DRN(2)+DRR(2)+DRN(4)+DRR(4))/4.0
  DRAUG=(DR1+DR2)/2.0
  RHUS(I)=4.5324*RAUG*F
  RHS(I)=1.0E8*DRAUG/B
  MUH(I)=RHS(I)/RHOS(I)
  NS(I)=6.2415E18/RHS(I)
  EFF(I)=(NS(I)/DOSE)*100.0
70  TYPE*, 'SURFACE RESULTS'
  TYPE 75,I-1,ECHTIM(I)
75  FORMAT(/,2X,'ETCH # = ',I2,' TIME = ',I4,' SEC'//)
  TYPE 80
80  FORMAT(6X,'I+',7X,'VOLT AT I+',9X,'I-',6X,'VOLT AT I-')
  DO 90 J=1,4
    TYPE 85,R11(J),V1(J),R12(J),V2(J)
    FORMAT(2X,E10.3,2X,F10.7,5X,E10.3,2X,F10.7)

```

85

90

95

96

97

98

99

100

```

  CONTINUE
  TYPE 95,RAUG1,DR1
  FORMAT(/,1X,'AVE R AT I+ = ',E12.5,' OHMS',T45,'AVE DELTA
  1R AT I+ = ',E12.5,' OHMS')
  TYPE 96, RAUG2,DR2
  FORMAT(1X,'AVE R AT I- = ',E12.5,' OHMS',T45,'AVE DELTA
  1R AT I- = ',E12.5,' OHMS')
  TYPE 97, RAUG,DRAUG
  FORMAT(1X,'AVE R = ',6X,E12.5,' OHMS',T45,'AVE DELTA R
  1= ',6X,E12.5,' OHMS'//)
  TYPE 100
  FORMAT(8X,'I+',7X,'VOLT@B=0,NOR',2X,'VOLT@B=B,NOR',2X,'DELTA
  1 V,NOR',3X,'VOLT@B=0,REV',2X,'VOLT@B=B,REV',2X,'DELTA V,

```

```

2REV'/)
DO 110 J=1,3,2
    DVN=VNO(J)-VNB(J)
    DVR=VRO(J)-VRB(J)
    TYPE 105,HI(J),VNO(J),VNB(J),DVN,VRO(J),VRB(J),DVR
105    FORMAT(2X,E12.5,2X,6(F10.6,4X))
110    CONTINUE
    DO 115 J=2,4,2
        DVN=VNO(J)-VNB(J)
        DVR=VRO(J)-VRB(J)
        TYPE 105,HI(J),VNO(J),VNB(J),DVN,VRO(J),VRB(J),DVR
115    CONTINUE
    TYPE 125,RT0,F
125    FORMAT(/,1X,'RES RATIO = ',F9.2,12X,'COR FACTOR = ',F7.2/)
    TYPE 130
130    FORMAT(2X,'ETCH #',5X,'TIME(SEC)',10X,'RHOS'
    1,16X,'RHS',16X,'MUH',15X,'NS',13X,'ACT. EFF(%)'/)
    TYPE 135,I-1,ECHTIM(I),RHOS(I),RHS(I),MUH(I),NS(I),EFF(I)
135    FORMAT(4X,I2,9X,I4,9X,E12.5,7X,E12.5,9X,F8.2,8X,E12.5
    1,7X,F6.2/)
    RETURN
    END

```

TYPE PROFIL.

C

SUBROUTINE PROFIL

C

INTEGER ECHTIM(25)
REAL EFF(25),MUH(25),MUI(25),NI(25),NS(25)
DIMENSION DELNS(25),DEPTH(25),RHOS(25),RHS(25),THICK(25)
1,X(25),EFMU(25)
COMMON /BLK2/ B,DEPTH,DOSE,ECHTIM,EFF,MUH,NS,RHOS,RHS,
1STHICK,THICK,I,NTIME

C

139

DO 140 M=1,(I-1)
DELX=(RHS(M)/RHOS(M)**2)-(RHS(M+1)/RHOS(M+1)**2)
DELY=(1.0/RHOS(M))-(1.0/RHOS(M+1))
IF(RHOS(M).EQ.RHOS(M+1))DELY=1.E-20
MUI(M)=DELX/DELY
NI(M)=DELY/(1.6022E-19*MUI(M)*THICK(M+1)*1.0E-8)
DELNS(M)=NS(M)-NS(M+1)
X(M)=DEPTH(M+1)-(THICK(M+1)*.5)
EFMU(M)=6.2415E18*((1.0/RHOS(M))-(1.0/RHOS(M+1)))/
1 DELNS(M)

140

CONTINUE
TYPE*, '***** PROFILE RESULTS (INTER) *****'
TYPE 150,STHICK,NTIME

150

FORMAT(/,2X,'TOTAL DEPTH = ',F7.1,' ANGSTROMS',12X,
1'TOTAL ETCHED TIME = ',16,2X,' SEC'/)
TYPE 155

155

FORMAT(1X,'ETCH * ',3X,'ETCH TIME',3X,'AVG SHEET NS',3X,
1'ACT EFF',5X,'DELTA NS',6X,'MOBILITY',4X,'VOL CONCENTR'
1,3X,'AT DEPTH',5X,'EFF MOBILITY')

FLAG=0.0

DO 190 M=1,I

TYPE 160, M-1,ECHTIM(M),NS(M),EFF(M)

IF(M.EQ.1) TYPE*, ' '

IF(M.EQ.1) GOTO 190

TYPE 180, DELNS(M-1),MUI(M-1),NI(M-1),X(M-1),EFMU(M-1)

160

FORMAT(3X,I2,7X,14,6X,E12.5,4X,F6.2,8)

180

FORMAT(3X,2(E12.5,3X,F10.2,3X),F10.2)

190

CONTINUE

TYPE*, ' '

RETURN

END

APPENDIX E

DEFECT STUDIES IN MULTILAYER EPITAXIAL
GaAs BY TRANSIENT CAPACITANCE

Defect studies in multilayer epitaxial GaAs by transient capacitance

E. T. Rodine

Systems Research Laboratories, Inc., 2800 Indian Ripple Road, Dayton, Ohio 45440

J. W. Farmer

University of Dayton, Department of Physics, Dayton, Ohio 45409

D. W. Langer

Air Force Avionics Laboratory, AFAL/DHR, Wright-Patterson Air Force Base, Ohio 45433

(Received 25 January 1979; accepted for publication 3 April 1979)

Majority-carrier defects, induced by 1-MeV-electron irradiation in *n*-type epitaxial GaAs were studied by deep-level-trap spectroscopy. The samples were fabricated in the form of FET-like devices on the epitaxial active and buffer layers. Anomalies in the DLTS response such as the appearance of double peaks, a rapid growth of transient response, and lack of exponential behavior as the depletion width extends into the buffer are discussed in terms of the planar geometry, the series resistance, and the multilayer nature of the devices.

PACS numbers: 61.80. - x, 61.70. - r, 73.60.Fw, 85.30.Tv

Numerous electronic devices are being fabricated by vapor-phase epitaxy (VPE) of GaAs on a semi-insulating substrate with a VPE buffer between the active layer and the substrate. Some defects in *n*-type VPE material, similar to device-grade layers, have been studied in this laboratory. Of particular interest were the samples having a Schottky-gate FET-like structure. The planar geometry of this structure and the multilayer nature of the active layer, buffer, and substrate contributed to the unusual behavior which must be considered for complete analysis.

Deep-level-trap spectroscopy (DLTS) was used to characterize the defects. No native deep-level majority-carrier traps were observed in the material after device processing. Deep levels were induced in the samples by 1-MeV-electron irradiation.

DLTS has been applied to GaAs by several investigators.¹⁻⁴ Numerous defects have been observed that are either native or induced by irradiation. Lang and Kimerling,^{1,2} as well as Lang and Logan,³ reported the results of electron irradiation as well as some other forms of irradiation. Wang and Ewaryne⁴ reported an application of DLTS to IGFET structures in Si. Lang and Logan³ applied DLTS to GaAs/Al_{0.3}Ga_{0.7}As heterojunctions, and Huang⁵ reported the presence of interface states between VPE GaAs and a Cr-doped substrate.

The primary samples in this study consisted of a 1- μ VPE *n*-type active layer doped to 2×10^{16} cm⁻³, atop a 3- μ "buffer" layer doped to 10^{15} cm⁻³ grown on a Cr-doped semi-insulating substrate. Processing consisted of mesa etching for isolation and the formation of a 1-mil-gate-length FET test pattern with Al Schottky and AuGe Ohmic contacts. Dies were mounted on TO5 headers and ultrasonically wire bonded. (*C-V*, *N-W*, and *I-V* curves were generated to check consistency, and FET modulation was observed.) The VPE layers were grown in this laboratory by the AsCl₃ process. The multilayers were formed *in situ* by varying the growth parameters.

The electron irradiation was performed with a 1-MeV Van de Graaff accelerator at a flux of $\sim 0.3 \mu\text{A}/\text{cm}^2$. The carrier-removal rate was determined to be linear by means of

an automated *C-V* profiler. After electron irradiation to a dose of 5×10^{15} cm⁻², the carrier concentration for the active and buffer layers were 1×10^{15} and 5×10^{12} cm⁻³, respectively.

The DLTS measurements were carried out at 1 MHz using a Boonton 72BD capacitance meter, a Systron-Donner 110B pulse generator, and a PAR 162 double boxcar. The sample temperature was varied from 15 to 450 °K using an Air Products Helitran. The chrome versus gold (0.7% Fe) thermocouple was mounted directly on the can of the TO5

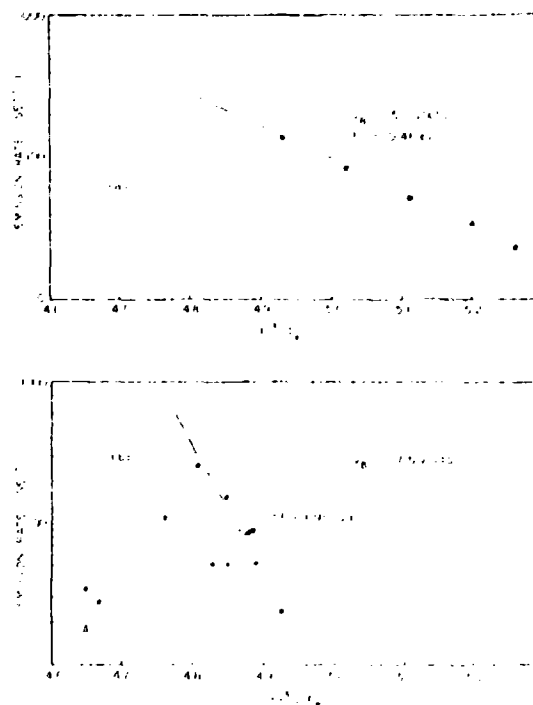


FIG. 1. Plot of uncorrected emission rate as function of $1/T$ for DLTS peak E3 in electron-irradiated *n*-type GaAs. (a) Emission rate versus $1/T$ at $V_g = 5$ V. (b) Emission rate versus $1/T$ at $V_g = 7.5$ V.

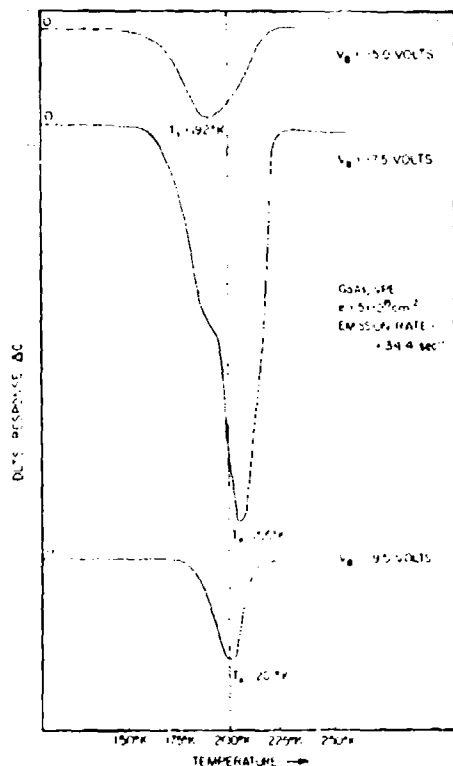


FIG. 2. Plot of DLTS response ΔC as a function of temperature for electron-irradiated VPE GaAs at three reverse biases.

header. Majority-carrier traps were filled to saturation by pulsing to zero bias. The pulses were achieved via the offset capabilities of the pulse generator and the bias network of the capacitance meter. Boxcar gates were generally 0.5 ms wide on a 50-ms time base.

At small bias levels ($V_H = -5$ V or less) where the depletion region was entirely in the active epitaxial layer (the top $1\ \mu\text{m}$), the DLTS results were normal. The electron-induced defects E1, E2, and E3 (using the nomenclature of Lang¹), in addition to a large signal from a deep center, were observed. The temperature dependence of these DLTS peaks, their relative magnitudes, and their thermal activation energies were nearly identical to the spectra obtained in this laboratory from similar epitaxial layers on conducting substrates and are in excellent agreement with data published by other laboratories.^{1,11} The uncorrected activation energies for E2 and E3 were 0.16 and 0.46 eV, respectively. Figure 1(a) is a plot of the electron emission rates obtained at $V_H = -5$ V as a function of reciprocal temperature, which yields the thermal activation energy for E3. The DLTS rate window was varied over an order of magnitude by adjusting the boxcar delay times.

The defect production rate for E3 was measured for electron doses ranging over several orders of magnitude and found to be linear with dose. For a moderately high electron dose $\phi = 5 \times 10^{15}\ \text{cm}^{-2}$ and a small reverse bias, the total number of traps N_t was $3.5 \times 10^{15}\ \text{cm}^{-2}$, yielding a production rate of $0.7\ \text{cm}^{-2}\ \text{s}^{-1}$.

At large reverse biases ($V_H > 6$ V), and with the same electron dose ($5 \times 10^{15}\ \text{cm}^{-2}$), the DLTS results are quite anomalous. There is an apparent large increase in N_t as exhibited by a large increase in the DLTS response. The trap concentration is normally proportional to $\Delta C/C$, which also increases sharply as the bias is increased. The peak temperature T also shifts with slight changes of V_H . In general, the peak temperatures observed using a reverse bias of more than 6 V are 10 to 15 °K higher than the peak temperatures observed for $V_H \leq 5$ V.

For some conditions a second peak occurs which is only slightly separated from the original peak. Figure 2 shows three DLTS response curves drawn to the same scale. The same DLTS rate window was used for three different reverse-bias conditions. For $V_H = -5$ V a normal single peak is observed at 192 °K. At $V_H = -7$ V a very large peak is observed at 205 °K, with a lower temperature shoulder which is very similar to the peak in curve (a). At $V_H = -9$ V, only a peak at 201 °K is observed. These curves are drawn to the same vertical scale.

Attempts were made to determine the thermal activation energies for the peaks at a large reverse-bias condition of $V_H = -7.5$ V, and the results are shown in Fig. 1(b). No further separation of the two peaks was observed, nor can a

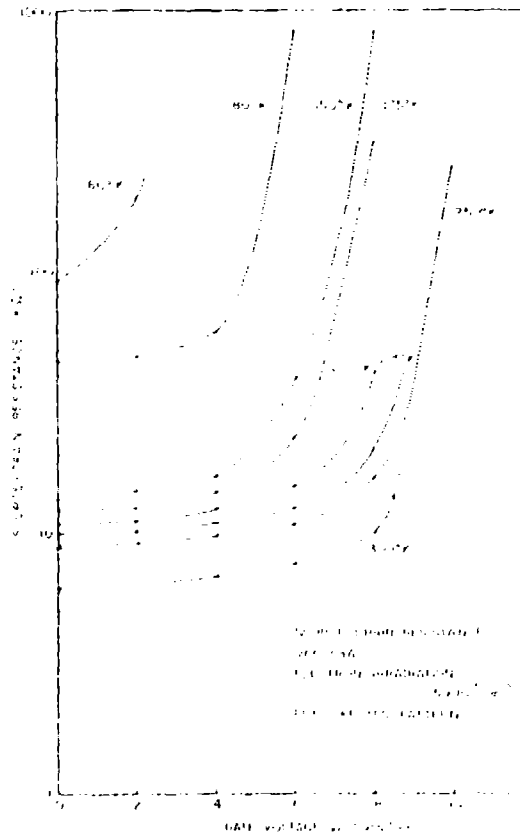


FIG. 3. Plot of source-drain resistance as a function of Schottky gate voltage at several temperatures for electron-irradiated n-type VPE GaAs LEU-like test pattern.

clear activation energy be determined from Fig. 1(b). Similar results are found at $V_B = -6.5$ and -9 V. The series at $V_B = -6.5$ V yielded a more coherent Arrhenius plot than either the -7.5 and -9 V curves; but the deviations were quite large, and no reasonable activation energy could be determined. Hence, the fit of the emission data to an exponential model becomes progressively worse with increasing reverse bias.

The transient decays appear to be nonexponential. The oscilloscope traces become very flat after a delay of > 20 ms. Nonexponential decay could account for the scatter in the results in Fig. 1(b). The two points in Fig. 1(b) labeled A were taken with the boxcar gates placed as far away from the pulse as possible.

The series resistance of the FET-like devices shown in Fig. 3 was measured as a function of temperature for gate voltages ranging from 0 to 10 V using a transistor curve tracer. At 200 °K the source-to-drain resistance as a function of gate voltage was relatively constant at about $10^4 \Omega$ between 0 and -5 V. For $V_B > -5$ V, pinch off was rapidly achieved with a resistance $> 10^5 \Omega$ for $V_B = -9$ V.

The quiescent capacitance was also measured as a function of reverse bias and temperature. The depletion width was found to be a strong function of temperature as shown in Fig. 4. This strong temperature dependence of the depletion width is caused by the carrier freeze out at this relatively high electron dose.

The low-bias data are quite consistent in all respects, both with data on single-layer systems in the present study and with results reported in the literature. C - V measurements (and hence concentration profiles) indicate that the large apparent increase of trap concentration $\Delta C/C$ is coincident with entry of the depletion region into the "buffer" material. At 200 °K a reverse bias of 5 V produces a depletion width of slightly less than 1μ (nearly equal to the thickness

of the active epilayer), whereas a reverse bias of 7.5 V produces a depletion width significantly greater than 1μ , i.e., penetration of the buffer. The increase of ΔC is shown in Fig. 2.

The effect of the abrupt change in donor density can be qualitatively seen in the following manner. In a single-layer system the change in capacitance is given by

$$\Delta C/C = [1 + (N_T/N_D)]^{1/2} - 1, \quad (1)$$

where N_D and N_T are the donor and electron-trap concentration, respectively. In the multilayer system the relationship is more complicated; however, it can be shown that in two limiting cases (low and high bias) the change in the capacitance is given by

$$\Delta C/C = [1 + (N_T/N_D^*)]^{1/2} - 1,$$

where N_D^* represents the donor concentration in the epilayer (small-bias limit) or in the buffer (large-bias limit). For 1-MeV-electron irradiation N_T will be nearly constant throughout both layers and C will change by only a factor of 2 or 3. Clearly, ΔC and $\Delta C/C$ will grow rapidly in the transition from the low-bias limit to the high-bias limit. Because C is a strong function of temperature in the present case, meaningful quantitative calculations of the actual trap density cannot be made.

The shift of the peak temperature T_* with reverse bias may be due to the series resistance and pinch off of the FET. The effect of series resistance on the quiescent-capacitance measurement has been discussed by Wiley and Miller.¹⁰ For E3 at about 200 °K, using the measured values of series resistance and capacitance, the measured value of capacitance at $V_B = -7.5$ V is nearly unaffected. At $V_B = -9$ V, the series resistance causes significant suppression of the capacitance and may also cause some shift of the DLTS peak temperature.

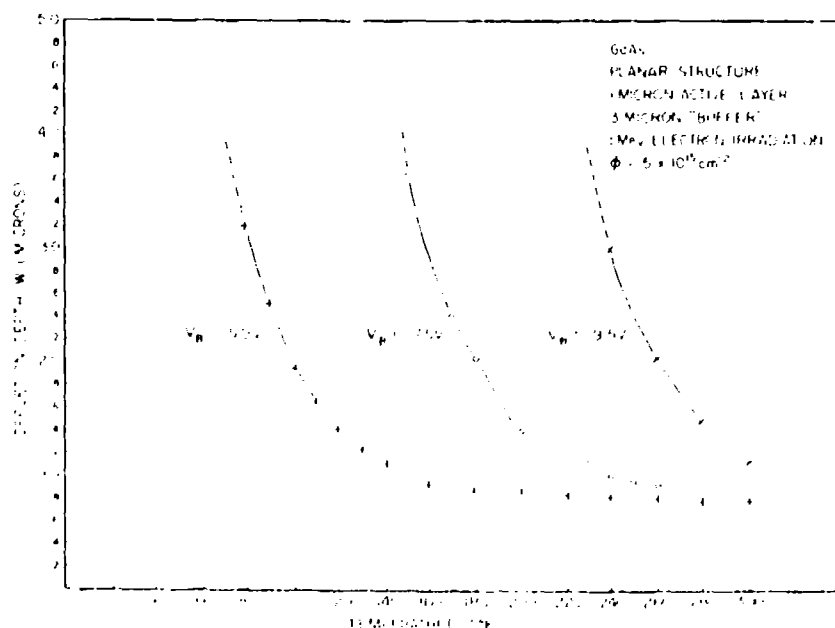


FIG. 4 Plot of depletion depth as a function of temperature for three reverse biases as calculated from C - V measurements.

The double peaks may arise from a fortuitous combination of the suppression of the measured capacitance due to series resistance and the enhancement of ΔC due to the abrupt decrease of N_D across the interface. The analytical verification of such behavior would be very difficult; however, qualitatively, calculations show such an explanation to be unlikely. The experimental verification would be more fruitful on a wafer grown on a conducting substrate which would eliminate the problem of series resistance.

The double peaks may also be due to the same defect with slightly different activation energies and/or emission rates in the two types of material (active and buffer layers). The two peaks could not be separated further than they are in Fig. 2, nor could they be studied separately. The multilayer system made possible the study of the buffer under conditions where $N_A > N_D$ (a condition not amenable to investigation in single-layer systems). One effect of the high density with respect to N_D is that the Fermi level is pinned near E_3 . It is possible that the high trap density in the buffer could result in anomalous DLTS responses for as-yet-unknown reasons.

The appearance of a double peak where only one is usually observed may be due to interface states or the presence of a new defect in the buffer. Although some data indicated these possibilities, data obtained from similar irradiated single-layer doped epilayer material on a conducting substrate and also from an irradiated buffer layer on a semi-insulating substrate did not indicate the presence of a new defect or interface states.

The multilayer architecture of the FET-like devices discussed here yields surprising and anomalous results. The planar geometry and associated series resistance complicate the analysis of the data. The large apparent increase of trap

density near the interface, the shift of peak temperature with reverse bias, and the appearance of double peaks under certain conditions can, to a large extent, be rationalized in terms of the multilayer planar geometry. The possibility still exists that the electron-damage defects are intrinsically different in the active and buffer layers or that the properties of the defects as measured by DLTS only appear to be different.

Further study is required to analyze this behavior. Until such a study has been performed, caution must be exercised in the analysis of DLTS data from multilayer devices.

Work was performed at the Air Force Avionics Laboratory, AFAL/DHR, Wright-Patterson Air Force Base, Ohio, under AF Contracts F33615-76-C-1166 and F33615-76-C-1207. The authors wish to thank Gary McCoy, AFAL/DHR, for growing the epitaxial layers. The authors also thank Jim Skalski and his staff of AFAL/DHE for fabricating the FET-like structures.

¹D. V. Lang, *J. Appl. Phys.* **45**, 3023 (1974).

²D. V. Lang and R. A. Logan, *Appl. Phys. Lett.* **31**, 683 (1977).

³A. Mircea and A. Mitonneau, *Appl. Phys.* **8**, 15 (1975).

⁴O. Wada, S. Yanagisawa, and H. Takanashi, *Appl. Phys.* **13**, 5 (1977).

⁵D. V. Lang and L. C. Kimerling, *Inst. Phys. Conf. Ser.* **23**, 581 (1975).

⁶D. V. Lang and R. A. Logan, *J. Electron. Mater.* **4**, 1053 (1975).

⁷K. L. Wang and A. O. Eswaraye, *J. Appl. Phys.* **47**, 4574 (1976).

⁸Y. M. Houng and G. L. Pearson, *J. Appl. Phys.* **49**, 3348 (1978).

⁹G. M. Martin, A. Mitonneau, and A. Mircea, *Electron. Lett.* **13**, 191 (1977).

¹⁰J. D. Wiley and G. L. Miller, *IEEE Trans. Electron Devices* ED-12, 191 (1977).

¹¹G. L. Miller, D. V. Lang, and L. C. Kimerling, *Annual Review of Materials Science* (Annual Reviews, Inc., Palo Alto, Calif., 1977), Vol. 7, p. 377.